



HAL
open science

Études électrochimiques des interfaces fonctionnelles et nanomatériaux pour le stockage de l'énergie : du supercatterie au water splitting

Christine Ranjan

► **To cite this version:**

Christine Ranjan. Études électrochimiques des interfaces fonctionnelles et nanomatériaux pour le stockage de l'énergie : du supercatterie au water splitting. Material chemistry. Université Paris Cité, 2022. English. NNT : 2022UNIP7309 . tel-04498114

HAL Id: tel-04498114

<https://theses.hal.science/tel-04498114>

Submitted on 11 Mar 2024

HAL is a multi-disciplinary open access archive for the deposit and dissemination of scientific research documents, whether they are published or not. The documents may come from teaching and research institutions in France or abroad, or from public or private research centers.

L'archive ouverte pluridisciplinaire **HAL**, est destinée au dépôt et à la diffusion de documents scientifiques de niveau recherche, publiés ou non, émanant des établissements d'enseignement et de recherche français ou étrangers, des laboratoires publics ou privés.

**Université Paris Cité
Thesis in Chemistry****Electrochemical investigation of functional interfaces and
nanomaterials for energy storage:
From supercabattery to water splitting**

Written and defended by

Christine RANJAN

25th October 2022

Specialty: Electrochemistry

Supervisor: Professor Hyacinthe RANDRIAMAHAZAKA

École Doctorale de Chimie Physique et Chimie Analytique de Paris Centre – ED388

Interfaces Traitements Organisation et Dynamique des Systèmes (ITODYS) – UMR 7086

Surfaces Ionic Liquid Electrochemistry Energy (SIELE)

Jury members:

| | | |
|------------------------------------|--|-------------------|
| Prof. Sara CAVALIERE | University of Montpellier | Reviewer |
| Prof. Dodzi ZIGAH | University of Poitiers | Reviewer |
| Dr. Corinne LAGROST | University of Rennes I | Jury president |
| Prof. EunAe CHO | Korean Advanced Institute of Science and Technology | Examiner |
| Prof. Hyacinthe RANDRIAMAHAZAKA | Paris Cité University | Supervisor |

**Université Paris Cité
Thèse en Chimie**

**Études électrochimiques des interfaces fonctionnelles et
nanomatériaux pour le stockage de l'énergie :
Du supercatterie au water splitting**

Écrite et soutenue par

Christine RANJAN

Le 25 Octobre 2022

Spécialité: Électrochimie

Directeur de Thèse: Professeur Hyacinthe RANDRIAMAHAZAKA

École Doctorale de Chimie Physique et Chimie Analytique de Paris Centre – ED388

Interfaces Traitements Organisation et Dynamique des Systèmes (ITODYS) – UMR 7086

Surfaces Ionic Liquid Electrochemistry Energy (SIELE)

Membres du jury :

| | | |
|------------------------------------|--|-----------------------|
| Prof. Sara CAVALIERE | Université de Montpellier | Rapportrice |
| Prof. Dodzi ZIGAH | Université de Poitiers | Rapporteur |
| Dr. Corinne LAGROST | Université de Rennes I | Présidente du jury |
| Prof. EunAe CHO | Korean Advanced Institute of Science and Technology | Examinatrice |
| Prof. Hyacinthe RANDRIAMAHAZAKA | Université Paris Cité | Directeur de thèse |

Electrochemical investigation of functional interfaces and nanomaterials for energy storage : from supercabattery to water splitting



During these four years of the thesis, I learned a lot and matured professionally and personally. A PhD is like a marathon, which requires preparation and patience. These four years combined the transport strikes, the Yellow vests protest, and the famous Covid, which changed our lives. Despite all this, I complete my thesis despite last-minute unforeseen events.

Through this page, I would like to thank the people who have contributed or helped me during this period.

I would first like to thank all the jury members for agreeing to participate in my defense thesis. I am grateful to you for agreeing to participate despite the defense's delay. Thank you to Prof. Cavaliere and Prof. Zigah for agreeing to be the reviewers. I want to thank Dr. Lagrost for agreeing to be the jury president. And the last jury member, Prof. Cho too. Prof. Cho, I was honoured to work with you, and Hyacinthe and I are pretty proud of the results obtained. The discussion that we had during the defense was very useful and rewarding.

I also wanted to thank my supervisor, Prof. Randriamahazaka, for these six years, including my master's internships and the thesis. I thank you for your advice, guidance, and kindness. Despite all our problems (change of subject and last-minute accidents), we made it. As they say, the best stories always have twists and surprises.

I also wanted to thank all the people who carried out the analyses.

First of all, Dr Decorse, for the quality XPS analyses and exceptional speed. Then Dr Lau for the Raman spectra and her expert advice, and Dr Gam-Derouich for her beautiful SEM images.

And finally, Dr Nowak, with whom we exchanged a lot for the XRD investigations. Thanks, Sophie, for all the advice and proposals, which have helped me enormously.

I also wanted to thank the Director of the Doctoral School and the Co-Director, Prof. Courty and Prof. Limoges, for their listening and indulgence concerning the defense.

I also wanted to thank my teaching colleague Mr Corré who helped me during mentoring. Thank you for your advice and patience, which allowed me to give the lessons in peace.

I would also like to thank my colleagues who quickly became friends and supporters who encouraged me during my thesis. Thank my future doctors from office 467, who were of un-failing support. Hao-Zheng, with his exemplary patience, or Nga (my favourite troublemaker) with her joie de vivre, I was happy to work with you and also wanted to thank Van for all her advice and kindness. You are a wonderful person, and I hope the best for you. Also, a big thanks to Zaynab, you have such a kind heart, and I hope for the best. A lot of articles and a beautiful thesis.

I have a particular thought for Selma and Célia. Both of you helped me enormously. Selma and Célia, thank you from the bottom of my heart for all your support. And you will soon be a doctor too, and I will be there for you. And Célia, I hope all your dreams and accomplishments will become true. All your motivation and kindness helped me a lot, my Che.

I have a special thought to Juliette who was a really help during this period. I also have a thought for my friends who have been of steel support to me : Iman for wise pieces of advice, Loren and Marie for our long hours of discussions which helped me so much; Damien, who

illuminated my first year and Jung Eun (Dr Lee) for the advice and our exchanges of experience as a doctoral student.

I also want to thank my following friends who were real support and comfort during this period of my life : Myriam, Emilie, Alexandre (Dr Da Silva), Hasna, Justine, Gwendoline and Mathieu.

I have a special thought for Jessica and Anahide, who helped me write my dissertation. First, Anahide, for your help with English and kindness ; that has never changed since high school. And finally, Jessica, for all your help, throughout my thesis, with your listening and your advices, which have always helped. And I'm so Thankful that your teachings on Latex have paid off..

Finally, my last words will be for my family.

First, my sisters Sophie and Stéphanie, for your unfailing support. Sophie, for your advice and patience. And Stéphanie, your support and motivation always cheer me up even in the lowest moment. This year was particularly rude for both of us, you in medicine and me, with the thesis, but we made it.

Finally, to my parents for all their love and support that allowed me to become the person I am, and I love you.

GLOSSARY

A : Electrode surface area
AC : Alternating current
AEM : Anion exchange membrane
AQD : 9,10-dioxo-9,10-dihydroanthracene-1-diazonium tetrafluoroborate
BSH :Battery-supercapacitor hybrid device
C : Capacitance
CC : Carbon Cloth
CE : Coulombic Efficiency
COP21 : 2015 United Nations Climate Change Conference
CV : Cyclic voltammogram
DC : Direct current
DFT : Density Functional Theory
E : Energy
ECSA : Electrochemical active surface area
EDL : Electric double layer
EDLC :Electric double layer capacitance
EDS : Energy dispersive spectroscopy
EE : Energy Efficiency
EES : Electrochemical energy storage
EESD :Electrochemical energy storage device
EIS : Electrochemical Impedance Spectroscopy
ESW : Electrochemical stability window
EVs : Electric vehicles
FWHM : Fill width at half maximum
G : Conductance
GCDs : Galvanostatic charge-discharge curves
GHGs : Greenhouse gases

HBE : Hydrogen binding energy
HER : Hydrogen Evolution Reaction
HEVs : Hybrid electric vehicles
HF : High-frequency
HOR : Hydrogen Oxidation Reaction
HVs : Heavy vehicles
I or i : Current
IHP : Inner Helmholtz plane
IUPAC : International Union of Pure and Applied Chemistry
J or j : Current density
KAIST : Korean Advanced Institute of Science and Technology
K-L : Koutecky-Levich
L : Inductance
LF : Low frequency
LIB : Lithium-ion battery
LSV : Linear sweep voltammetry
MAB : Metal-air battery
MAUD : Material Analysis Using Diffraction
MO : Metal oxides
MOFs : Metal-organic frameworks
 M_W : molecular weight
 M_xO_y : metal oxide
N : collection rate
NIST : National Institute of Standards and Technology
OER : Oxygen Evolution Reaction
OHP : Outer Helmholtz plane
ORR : Oxygen Reduction Reaction
P : power
PE : Power Efficiency
PEM : Proton exchange membrane
PEMFC : Proton Exchange Membrane Fuel Cell
PGMs : Platinum-group metals
PhD : Doctor of Philosophy
PVP : Polyvinylpyrrolidone
PXRD : Powder X-ray diffraction
Q : Charge
R : Resistance
RDE : Rotating disk electrode
RDS : Rate-determining step

RRDE : Rotating ring disk electrode
S : Elastance
SCAP : Supercapattery
SEM : Scanning Electron Microscopy
sig or X^2 : Goodness of Fit
TMOs : Transition metal oxides
TMs : Transition metals
TOF : Turnover frequency
U or V : Voltage
UPD : Low-potential deposition
V : Applied voltage
XDR : X-ray diffraction
XPS : X-ray photoelectron spectroscopy
Y : Admittance
Z : Impedance
 α : Electron transfer coefficient
 Δ_E : Potential window
 Δ_G : Gibbs free energy
 ε : Dielectric constant
 η : Overpotential
 ν : Scan rate
 φ : Electrical flux

Summary

The use of non-noble electrocatalysts is an interesting pathway for the development of sustainable energy. In this PhD thesis, the electrocatalytic properties of manganese oxide nanomaterial and doped nickel oxide are investigated for important reactions around oxygen (oxygen evolution reaction, and oxygen reduction reaction) and hydrogen (hydrogen evolution reaction) electrochemistry. Indeed, water splitting is an effective approach to producing hydrogen, which is a form of sustainable chemical energy storage. These electrocatalysts are abundant and stable in alkaline media. Also, a supercabattery, an electrochemical energy storage system issued from the marriage of supercapacitor and battery, is studied. Particularly, doped nickel oxide can be viewed as a trifunctional material able to catalyze oxygen evolution and hydrogen evolution reactions and as electrode material for supercabattery.

Keywords: nanomaterials, energy storage, water splitting, electrocatalysis, oxygen evolution reaction, oxygen reduction reaction, hydrogen evolution reaction, supercabattery.

Résumé

L'utilisation d'électrocatalyseurs non nobles est une approche intéressante pour le développement de l'énergie durable. Dans cette thèse de doctorat, les propriétés électrocatalytiques de nanomatériaux à base d'oxyde de manganèse et de l'oxyde de nickel dopé sont étudiées pour des réactions importantes autour de l'électrochimie de l'oxygène (réaction de dégagement d'oxygène et réaction de réduction de l'oxygène) et de l'hydrogène (réaction de dégagement d'hydrogène). En effet, la production d'hydrogène qui est une forme de stockage d'énergie chimique durable via l'électrolyse de l'eau est une approche efficace. Ces électrocatalyseurs sont abondants et stables en milieu alcalin. De même, une supercabatterie qui est un système électrochimique de stockage d'énergie issu du mariage d'un supercondensateur et d'une batterie est étudiée. En particulier, nous montrons que l'oxyde de nickel dopé peut être considéré comme un matériau trifonctionnel apte non seulement à catalyser la réaction de dégagement d'oxygène et la réaction de production d'hydrogène mais également comme matériau d'électrode pour les supercabatteries.

Mots-clés: nanomatériaux, stockage de l'énergie, électrolyse de l'eau, électrocatalyse, réaction de libération d'oxygène, réaction de réduction de l'oxygène, réduction des protons, supercabatterie.

Résumé substantiel

Le défi important du XXI^e siècle est le réchauffement climatique dû à des décennies d'industrialisation massive en utilisant des énergies fossiles. Cette prise de conscience sur ces questions environnementales s'est traduite par les engagements politiques pris lors de la conférence de Paris de 2015 sur les changements climatiques (COP21). Ainsi, le développement des énergies renouvelables devient une priorité absolue pour notre société. Dans ce contexte, il est primordial de développer d'une manière durable des systèmes de production et de stockage d'énergie. Parmi les dispositifs pouvant répondre à ce défi, les systèmes de stockage d'énergie électrochimique comme les batteries, les piles à combustible et les supercondensateurs jouent un rôle important. L'élément clé pour le développement du stockage d'énergie durable est l'étude des matériaux utilisés pour l'élaboration de l'électrode, car la nature des matériaux conditionne l'efficacité du dispositif. En effet, les systèmes de stockage d'énergie électrochimique mettent en jeu des réactions électrochimiques se déroulant sur les électrodes. Il est alors important d'optimiser les performances telle la capacité à stocker des charges et les propriétés catalytiques. De plus, les matériaux choisis doivent être non seulement abondants et peu onéreux, mais également respectant les contraintes environnementales.

Afin d'améliorer les performances des systèmes électrochimiques de stockage d'énergie, on assiste à l'émergence d'un dispositif hybride combinant les propriétés des batteries (énergie élevée, mais faible puissance) et des supercondensateurs (forte puissance, mais faible énergie). Il s'agit de la supercatterie qui permet d'obtenir une puissance et une énergie élevées. Ces propriétés permettront d'obtenir un appareil doté d'une durée de vie et d'une puissance d'impulsion plus longues. L'application de la supercatterie est principalement les véhicules électriques ou hybrides.

Toujours dans le besoin d'énergie pour le transport, on peut citer les piles à combustible à l'hydrogène qui nécessitent une approche durable pour la production de l'hydrogène. L'électrolyse de l'eau est une approche intéressante pour la production d'hydrogène en utilisant le surplus d'énergie obtenue par des sources d'énergie renouvelables telles que l'énergie solaire ou éolienne. Cependant, les cinétiques sont lentes et demandent une énergie d'activation élevée. Ainsi, il est important de développer des catalyseurs pour la réaction de dégagement d'hydrogène (HER) et la réaction de dégagement d'oxygène (OER) qui sont les réactions impliquées dans l'électrolyse de l'eau. Une autre réaction très étudiée est la réaction de réduction de l'oxygène (ORR) pour l'application de batteries de type métal-air.

Cette thèse de Doctorat est centrée sur les études de catalyseurs à base de métaux non nobles tels que l'oxyde de manganèse pour la réaction de réduction de l'oxygène (ORR) et l'oxyde de nickel pour la réaction de dégagement d'hydrogène (HER) et la réaction de dégagement d'oxygène (OER). L'utilisation de métaux non nobles est l'une des clés de l'énergie durable.

Le manuscrit de thèse est divisé en quatre parties qui seront détaillées dans les paragraphes suivants.

La première qui est une introduction générale donne une vue d'ensemble des systèmes électrochimiques associés au stockage d'énergie. Dans l'étude de ces systèmes, nous allons nous focaliser sur les batteries, les supercondensateurs et les piles à combustible, qui sont les acteurs majeurs dans ce type de système. À travers cette étude, nous allons voir les variétés de ces systèmes cités, ainsi que leurs impacts et rôles joués dans la course aux énergies renouvelables, notamment via la composition des matériaux utilisés pour leurs conceptions. Les études sur les batteries et les supercondensateurs vont permettre d'introduire les superbatteries. En effet, la superbatterie est un système hybride qui combine les propriétés des batteries et des supercondensateurs. Ce système hybride qui est un système émergent, c'est pour cela que nous avons moins d'études comparées aux batteries et supercondensateurs. Cette introduction va nous permettre de nous familiariser avec l'état de l'art des superbatteries. Durant cette thèse, nous avons développé une superbatterie que nous allons développer dans le cinquième chapitre.

Toujours dans le premier chapitre, nous allons décrire en détail les réactions associées au dégagement d'hydrogène (HER) et au dégagement d'oxygène (OER) en milieu acide et basique. De même, nous allons également nous intéresser à la réaction de réduction de l'oxygène (ORR) dans les conditions alcalines. Ces études sont essentielles pour comprendre les systèmes catalytiques étudiés durant ces travaux de thèse. Cette étape va permettre aux lecteurs de comprendre ces réactions et voir les implications dans les parties suivantes. La deuxième et troisième parties vont porter sur les catalyseurs développés et les applications pour les réactions catalytiques vues dans la première partie. Par exemple, dans la deuxième partie, nous allons nous focaliser sur la réaction de réduction de l'oxygène (ORR) dans le milieu basique. Cette réaction peut prendre deux chemins possibles. Le premier chemin est la réduction à quatre électrons qui conduit à la formation de HO^- et le deuxième est le chemin à deux électrons qui conduit à la formation de HO_2^- .

Dans ce deuxième chapitre, nous avons développé une série de nanoparticules catalytiques à base de manganèse d'oxyde. Pour obtenir ces catalyseurs, nous avons utilisé l'électrofilage pour élaborer les films de polymères dopés par du manganèse, qui seront à la base de nos catalyseurs. La transformation des films en nanoparticules se fait par le biais de traitement thermique à différentes températures qui va conduire à des poudres catalytiques de différentes propriétés. Nous avons joué sur la variation de la température pour élaborer différentes séries et les étudier. Par le biais de différentes techniques spectroscopiques telles que la spectrométrie de photoélectrons induits par rayons X (XPS), la diffractométrie de rayons X (DRX), le Raman et la microscopie électronique à balayage (MEB), nous avons pu déterminer les compositions chimiques de nos poudres catalytiques. Nous avons identifié la nature du manganèse d'oxyde

synthétisée ; dans la majorité des cas, nous avons $\alpha\text{-Mn}_2\text{O}_3$. $\alpha\text{-Mn}_2\text{O}_3$ peut être sous deux formes qui sont la forme cubique ou la forme orthorhombique. Cette différence peut avoir un impact sur les propriétés catalytiques du $\alpha\text{-Mn}_2\text{O}_3$. Lors de l'étude des propriétés électrochimiques de chaque série, nous avons utilisé une électrode à anneau-disque tournant (rotating ring-disk electrode ou RRDE en anglais). La RRDE est un outil très puissant qui nous permet de remonter au chemin pris par le catalyseur durant la réaction de réduction de l'oxygène (ORR). Pour les catalyseurs étudiés, cette investigation électrochimique a permis de mettre en valeur une série de catalyseurs présentant une sélectivité exceptionnelle pour la réaction de réduction de l'oxygène (ORR). C'est la série de poudres traitée à 500°C qui se démarque avec une sélectivité pour le chemin à quatre électrons qui correspond à la formation de HO^- . Nous avons mené des études micro-cinétique pour comprendre les mécanismes suivis par ces catalyseurs.

Dans la troisième partie, nous allons trouver le troisième, quatrième et cinquième chapitre. Cette partie va porter sur l'électrode de nickel d'oxyde dopé au fer et au phosphore. Cette étude est en collaboration internationale menée avec la Professeure Cho du Korean Advanced Institute of Science and Technology (KAIST, Corée du Sud). Cette électrode a des usages multiples et variés. Elle peut être un catalyseur pour la réaction de dégagement d'hydrogène (HER) comme la réaction de dégagement d'oxygène (OER). De plus, elle peut être utilisée comme anode dans un système de supercapacité. Cette partie souligne la versatilité de l'application de ce matériau et nous permet de souligner des qualités exceptionnelles.

Si nous prenons le cas de la réaction de dégagement d'hydrogène (HER) vue dans le troisième chapitre, nous pouvons voir que notre électrode d'oxyde de nickel dopé présente de bonnes performances catalytiques vis-à-vis de la réaction de dégagement d'hydrogène (HER). Durant l'étude électrochimique menée par la voltampérométrie à balayage linéaire (LSV), nous avons démontré que les réponses électrochimiques dépendent du potentiel. Nous avons remarqué l'existence de deux zones de surtensions qui vont influencer le comportement de l'électrode par rapport à la réaction de dégagement d'hydrogène (HER). Nous avons aussi conduit des études par spectroscopie d'impédance électrochimique qui nous a permis de définir des résistances propres au système étudié telles que la résistance de transfert de charge R_{ct} , la résistance de polarisation de l'électrode R_p , et la résistance du circuit électrique R'_θ . Nous trouvons une corrélation entre les résultats obtenus avec l'impédance et voltampérométrie à balayage linéaire (LSV) qui montrent une dépendance au courant et l'existence de deux zones de surtensions.

Dans le cas du quatrième chapitre, nous nous sommes intéressés à la réaction de dégagement d'oxygène (OER) et à la réponse catalytique de notre électrode d'oxyde nickel par rapport à la réaction de dégagement d'oxygène (OER). Nous avons mené une investigation électrochimie

par le biais de la voltampérométrie à balayage linéaire (LSV) pour analyser les réponses catalytiques. L'oxyde de nickel présente un excellent catalyseur vis-à-vis de la réaction de dégagement d'oxygène (OER). Tout comme dans le troisième chapitre, nous avons deux zones de surtensions qui vont influencer le comportement de l'électrode par rapport à la réaction de dégagement d'oxygène (OER). De plus, la spectroscopie d'impédance électrochimique nous a permis de définir des résistances propres au système étudié. En combinant les résultats du troisième et quatrième chapitre, nous pouvons montrer les effets catalytiques de l'oxyde de nickel pour la réaction de dégagement d'hydrogène (HER) et la réaction de dégagement d'oxygène (OER) par le biais de l'électrolyse de l'eau. Enfin, nous avons mené une électrolyse de l'eau en utilisant un système à deux électrodes, composé de deux électrodes d'oxyde de nickel dopé pour l'anode et la cathode. Les résultats obtenus par cette expérience sont encourageants pour un matériau non-noble et souligne d'autant plus le rôle catalytique de l'oxyde de nickel dopé.

La troisième partie se termine avec le cinquième chapitre. Ce chapitre correspond à l'élaboration de la supercatterie. Dans ce chapitre, nous avons voulu souligner le rôle joué par l'oxyde de nickel comme l'anode de notre système élaboré. Le système élaboré est composé de l'oxyde de nickel (anode et jouant le rôle de l'électrode de type batterie) et d'un tissu de carbone modifié et activé (cathode et jouant le rôle de l'électrode de type pseudo-capacitive). Nous avons augmenté la réponse électrochimique du tissu de carbone en l'activant dans un premier temps, et nous avons effectué au greffage d'un sel de diazonium (9,10-Dioxo-9,10-dihydroanthracene-1-diazonium tetrafluoroborate). Nous nous sommes intéressés aux cycles de charges et décharges. La non-linéarité des réponses électrochimiques obtenues, à savoir la variation du potentiel en fonction du temps, nous a conduit à développer une nouvelle méthodologie pour analyser ces réponses en calculant le flux électrique. A travers ces cycles de charge/décharge, nous avons pu via le flux électrique des paramètres caractéristiques tels que l'énergie et la puissance. De plus, nous avons introduit les notions peu utilisées dans le domaine des batteries ou supercondensateurs telles que l'élastance S et la conductance G . Enfin, nous avons apporté notre révision au diagramme de Ragone.

La quatrième partie correspond au sixième et dernier chapitre. Ce chapitre va porter sur la conclusion globale des travaux présentés à travers ce mémoire. Et nous allons terminer ce dernier chapitre par les perspectives liées à chaque travaux présentés dans ce manuscrit.

CONTENTS

| | |
|--|-------------|
| Acknowledgements | III |
| Glossary | V |
| Summary | IX |
| Résumé substantiel | XI |
| Contents | XV |
| List of figures | XVII |
| List of Tables | XXV |
| General introduction | 1 |
| 1 Introduction - an overview of Energy Storage Systems | 3 |
| 1.1 Different energy storage systems | 4 |
| 1.2 Energy production | 33 |
| 1.3 Conclusion of the first chapter | 53 |
| References | 53 |
| 2 Manganese oxide for Oxygen Reduction Reaction | 65 |
| 2.1 Elaboration of the catalyst: Carbon film to powder Manganese oxide | 66 |
| 2.2 Spectroscopic investigation | 70 |
| 2.3 Electrochemical investigation | 87 |
| 2.4 Conclusion | 106 |

| | |
|--|------------|
| References | 108 |
| 3 NiOx system, hybrid materials. : catalyst for HER | 115 |
| 3.1 General properties: Nickel oxide | 116 |
| 3.2 Electrochemical investigation | 125 |
| 3.3 Conclusion: Correlation between LSV and EIS | 140 |
| References | 141 |
| 4 NiOx system, hybrid materials : catalyst for OER | 151 |
| 4.1 Mechanism and catalyst for Oxygen evolution reaction (OER) | 151 |
| 4.2 Experimental section | 154 |
| 4.3 Oxygen evolution reaction response | 155 |
| 4.4 Conclusion Water splitting | 167 |
| References | 169 |
| 5 Supercabattery | 177 |
| 5.1 Introduction | 177 |
| 5.2 Experimental section | 179 |
| 5.3 Electrochemical responses of the supercabattery | 181 |
| 5.4 Conclusion | 196 |
| References | 196 |
| 6 Conclusions et perspectives | 199 |
| 6.1 Conclusion | 199 |
| 6.2 Perspectives | 200 |

LIST OF FIGURES

| | | |
|------|---|----|
| 1.1 | Illustration of the structure and electrochemical behavior of supercapacitors and batteries. ^[9] | 5 |
| 1.2 | Energy storage mechanisms for electric double layer capacitance and pseudocapacitor ^[11] | 7 |
| 1.3 | Stern model at electric double layer at the positive electrode ^[16] | 8 |
| 1.4 | Cyclic voltammogram of modified NiO recorded at various scan rate (seen in chapter 4) | 9 |
| 1.5 | Charge and Discharge process of electric double layer capacitance ^[11] | 10 |
| 1.6 | Electrical circuit model of electric double layer capacitance | 10 |
| 1.7 | The accurate electrical circuit of an electric double layer capacitance | 11 |
| 1.8 | Charge storage mechanisms of pseudocapacitor ^[17] | 12 |
| 1.9 | Electrical circuit of a pseudocapacitor | 12 |
| 1.10 | Underpotential deposition process | 13 |
| 1.11 | Redox pseudocapacitance process | 14 |
| 1.12 | Intercalation pseudocapacitance process | 14 |
| 1.13 | Charge / Discharge process for the lithium-ion batterie ^[20] | 17 |
| 1.14 | Ragone plot of different electrochemical energy storage devices. ^[29] | 20 |
| 1.15 | Three charging storing mechanisms ^[33] | 21 |
| 1.16 | Comparison between metal-air battery and lithium-ion battery ^[38] | 22 |
| 1.17 | Zoom at the air electrode and three-phase ^[38] | 23 |
| 1.18 | Crystal structures various manganese oxides. ^[41] | 24 |
| 1.19 | Pourbaix diagram of Mn–O–H phases ^[40] | 25 |
| 1.20 | Bode diagram of nickel hydroxides. ^[42] | 26 |
| 1.21 | Ragone plot with position of supercapattery relative to other energy technologies ^[9] | 28 |
| 1.22 | Schematic diagram of charge storage for ELDC (A), pseudocapacitor (B), and Supercapattery (C) ^[11] | 29 |

| | | |
|------|---|----|
| 1.23 | Cyclic voltammograms of a battery (A), capacitor (B), a Supercabattery (C), and Supercapattery (D) ^[47] | 30 |
| 1.24 | Galvanostatic charge-discharge (GCD) and the current response versus potential from cyclic voltammograms of (a) a rechargeable battery, (b) a supercapacitor, and (c) a supercapattery. ^[48] | 31 |
| 1.25 | Galvanostatic charge-discharge (GCD) and the current response versus potential from cyclic voltammograms of a supercabattery ^[51] | 32 |
| 1.26 | Schema of supercapacitor and battery to explain our supercabattery made | 33 |
| 1.27 | Classification of the fuel cell system ^[56] | 34 |
| 1.28 | Simplify Proton exchange membrane fuel cell (PEMFC) mechanism ^[59] | 36 |
| 1.29 | Hydrogen and oxygen cycle for energy storage and energy conversion. ^[60] | 37 |
| 1.30 | Scheme of the water electrolysis process ^[61] | 38 |
| 1.31 | 3 pathways for hydrogen evolution reaction under alkaline conditions ^[68] | 41 |
| 1.32 | A volcano plot of hydrogen evolution reaction ^[73] | 43 |
| 1.33 | 3 pathways for hydrogen evolution reaction under acidic conditions ^[68] | 44 |
| 1.34 | Simplified oxygen evolution reaction mechanisms pathways in alkaline media ^[78] | 46 |
| 1.35 | Volcano plot for oxygen evolution reaction ^[78] | 47 |
| 1.36 | Hydrogen oxidation reaction pathways in alkaline media. (a) Tafel-Volmer and (b) Heyrovsky-Volmer mechanism with OH ⁻ only in the electrolyte.(c) Volmer step with OH ⁻ adsorbed on the catalyst surface. ^[81] | 48 |
| 1.37 | 4 pathways of oxygen reduction reaction mechanism ^[83] with black, red, and white spheres are oxygen atoms and hydrogen atoms in yellow arrows are the O-O bond cleavage and blue arrows are proton or electron transfer | 51 |
| 1.38 | Oxygen reduction reaction volcano plot ^[84] | 52 |
| 2.1 | Electrospinning setup ^[5] | 66 |
| 2.2 | Photo of the film made | 68 |
| 2.3 | SEM of the film | 68 |
| 2.4 | Mn 2p XPS spectra for five manganese oxide powder synthesized with (1) powder made with the thermic treatment at 500° C, (2) 600° C, (3) 700° C, (4) 800° C and (5) 900° C | 70 |
| 2.5 | O 1s XPS spectra for five manganese oxide powder synthesized | 71 |
| 2.6 | Raman spectra for 500°C (black), 600°C (red), 700 °C (blue), 800°C (green) and 900°C (pink) | 72 |
| 2.7 | SEM images of E500 deposited onto ITO | 73 |
| 2.8 | SEM images of E900 deposited onto ITO | 73 |
| 2.9 | X-ray diffraction patterns of α -Mn ₂ O ₃ were obtained at different temperatures 500°C (black), 600°C (red),700°C (blue), 800°C (green), and 900°C (pink) | 74 |
| 2.10 | CRISTAL synoptic ^[12] | 75 |

| | | |
|------|---|-----|
| 2.11 | PXDR patterns of α -Mn ₂ O ₃ was obtained at 500°C around 12° and 16° with MAUD | 77 |
| 2.12 | PXDR patterns of α -Mn ₂ O ₃ was obtained at 500°C around 16° and 20° with MAUD | 77 |
| 2.13 | PXDR patterns of α -Mn ₂ O ₃ was obtained at 600°C around 12° and 16° with MAUD | 79 |
| 2.14 | PXDR patterns of α -Mn ₂ O ₃ was obtained at 600°C around 19° and 20° with MAUD | 79 |
| 2.15 | PXDR patterns of α -Mn ₂ O ₃ was obtained at 700°C around 12° and 16° with MAUD | 80 |
| 2.16 | PXDR patterns of α -Mn ₂ O ₃ was obtained at 800°C around 13° and 15° with MAUD | 82 |
| 2.17 | PXDR patterns of α -Mn ₂ O ₃ was obtained at 800°C around 18° and 20° with MAUD | 82 |
| 2.18 | PXDR patterns of α -Mn ₂ O ₃ was obtained at 900°C around 17.4° and 18.2° with MAUD | 83 |
| 2.19 | PXDR patterns of α -Mn ₂ O ₃ was obtained at 900°C around 22.4° and 23.2° with MAUD | 84 |
| 2.20 | (a) Evolution of the average crystallite sizes L (nm) as function of the temperature (C°) (b) Evolution of the Phases of α -Mn ₂ O ₃ 's Proportion (%) as function of the temperature (C°) | 85 |
| 2.21 | Orthorhombic and cubic α -Mn ₂ O ₃ structures ^[14] | 85 |
| 2.22 | Crystal structures of α -Mn ₂ O ₃ ^[17] With Mn ^(III) and O a brown and red sphere | 86 |
| 2.23 | Jahn-Teller distortion for Mn ^(III) O ₆ octahedra ^[20] | 87 |
| 2.24 | Schema of Rotating ring-disk electrode | 88 |
| 2.25 | LSV comparison of ORR polarization curves between the blank (black) and the catalytic ink E500 (red), in O ₂ saturated 0.1 M KOH solution, using RRDE at rotation 1600 rpm with 10 mV/s scan rate | 89 |
| 2.26 | ORR polarization curves in O ₂ -saturated 0.1 M KOH solution using RRDE for powder made at 500°C in ink form | 90 |
| 2.27 | Variation of the electron number and the % HO ₂ ⁻ as function of Applied potential (V) RHE for the powder made at 500°C in ink form | 92 |
| 2.28 | (a) Evolution of electron number exchanged as function of applied potential E (V) RHE (b) Evolution of HO ₂ ⁻ produced as a function of applied potential E (V) RHE | 93 |
| 2.29 | Possible mechanisms for oxygen reduction reaction ^[24] | 94 |
| 2.30 | Representation of crystal structure and d-orbital electronic configuration of Mn ₂ O ₃ ^[17] | 96 |
| 2.31 | Representation of lattice structure of Mn ₅ O ₈ ^[36] | 98 |
| 2.32 | Oxygen reduction reaction mechanism for Mn oxides ^[27] | 98 |
| 2.33 | (a) ORR polarization curves in O ₂ -saturated 0.1 M KOH solution using RRDE for powder made at 500°C in ink form (b) Linear Tafel plot for powder made at 500°C in ink form (K-L 1 zone) | 102 |
| 2.34 | Evolution of the transfer coefficient (n' + α) as function of the size of powder made at different temperatures (nm) | 103 |

| | | |
|------|--|-----|
| 2.35 | Evolution of (a) electron number exchanged and (b) % HO_2^- in K-L 1 zone as function of the size of powder made at different temperatures (nm) | 104 |
| 2.36 | (a) ORR polarization curves in O_2^- saturated 0.1 M KOH solution using RRDE for powder made at 500°C in ink form (b) Linear Tafel plot for powder made at 500°C in ink form (K-L 2 zone) | 104 |
| 2.37 | Evolution of the transfer coefficient (K-L 2 zone) as function of the size of powder made at different temperatures (nm) | 105 |
| 2.38 | Evolution of (a) electron number exchanged and (b) % HO_2^- in K-L 2 zone as function of the size of powder made at different temperatures (nm) | 105 |
| 2.39 | Evolution of the transfer coefficient for K-L 1 (green) and K-L 2 (red) as function the size of powder made at different temperatures (nm) | 107 |
| 2.40 | Evolution of (a) electron number exchanged and (b) HO_2^- % for K-L 1 and K-L 2 as function of the size of powder made at different temperatures (nm) | 107 |
| 2.41 | Comparison Mn-based oxides and noble metal catalysts for ORR ^[44] | 108 |
| 3.1 | Mechanism of hydrogen evolution reaction in acidic (left) and alkaline (right) solutions ^[8] | 117 |
| 3.2 | Volcano plot for hydrogen evolution reaction in the alkaline medium for various metals ^[12] | 118 |
| 3.3 | XPS spectra of (a) Ni 2p, (b) O 1s, (c) Fe 2p and (d) P 2p of NiO foam electrode | 121 |
| 3.4 | SEM image of NiOx/Ni | 123 |
| 3.5 | EDS of the NiOx/Ni | 123 |
| 3.6 | Elemental mappings of the edge of NiOx | 124 |
| 3.7 | (a) Cyclic voltammogram of modified NiOx recorded at various scan rates (b) Evolution of the charging current (A) as a function of the scan rate ($\text{V}\cdot\text{s}^{-1}$) . . . | 126 |
| 3.8 | Evolution of the inverse of the real part as a function the inverse of frequency | 127 |
| 3.9 | Linear sweep voltammetry (LSV) of modified NiOx recorded at $\nu = 2 \text{ mV/s}$ in 1 M KOH | 128 |
| 3.10 | Evolution of overpotentials (mV) at various density current as function of the KOH concentration (mol/L) | 129 |
| 3.11 | (a) Linear sweep voltammetry (LSV) of modified NiOx recorded at $\nu = 2 \text{ mV/s}$ in 1 M KOH and (b) Tafel slope of 3.11a | 130 |
| 3.12 | (a)Evolution of the Tafel slope for low overpotential, (b) and large overpotential for different KOH concentration | 131 |
| 3.13 | Nyquist plot for NiOx at different potential (1M KOH) | 131 |
| 3.14 | Equivalent circuit for analyzing EIS responses during HER with NiOx electrode ^[53] | 132 |
| 3.15 | (a) Nyquist plot for NiOx at 1 M KOH. (b) Nyquist plot at Low overpotential zone. (c) Nyquist plot for NiOx at large overpotential zone | 135 |

| | | |
|------|---|-----|
| 3.16 | (a) Nyquist plot for NiOx at 1 KOH M (low overpotential zone) (b) Nyquist plot for NiOx at 1 KOH M (large overpotential zone) | 136 |
| 3.17 | (a) Experimental recorded Bode plot for -0.17 V (b) Fitting for -0.17 V (low overpotential zone) (c) Experimental recorded Bode plot for -0.23 V (b) Fitting for -0.23 V (large overpotential zone) | 136 |
| 3.18 | Evolution of the Charge transfer resistance R_{ct} (Ω) as function of the overpotential η (V) | 137 |
| 3.19 | Evolution of the polarization resistance R_p (Ω) as function of the overpotential η (V) | 137 |
| 3.20 | Evolution of the electrical circuit resistance $R'\theta$ (Ω) as function of the overpotential η (V) | 138 |
| 3.21 | (a) Evolution of the charge transfer resistance R_{ct} (Ω) as function the polarization resistance R_p (Ω), (b) Evolution of the electrical circuit resistance $R'\theta$ (Ω) as function the polarization resistance R_p (Ω) and (c) Evolution of the charge transfer resistance R_{ct} (Ω) as function the electrical circuit resistance $R'\theta$ (Ω) . | 139 |
| 3.22 | (a) Evolution of $\ln(i/A.cm^{-2})$ as function of the overpotential (V), (b) Evolution of $\ln(1/R_{ct})$ as function of the overpotential (V), (c) Evolution of $\ln(1/R_p)$ as function of the overpotential (V) | 140 |
| 4.1 | Simplified Oxygen evolution reaction mechanisms pathways in alkaline media ^[7] | 152 |
| 4.2 | Volcano plot for Oxygen evolution reaction ^[7] | 153 |
| 4.3 | Cyclic voltammogram of modified NiO recorded at $\nu = 100$ mV/s in 1 M KOH . | 155 |
| 4.4 | (a) Cyclic voltammogram of modified NiO recorded at $\nu = 100$ mV/s in 1 M KOH saturated in oxygen (b) Bode diagram of nickel hydroxides | 156 |
| 4.5 | Linear sweep voltammetry (LSV) of modified NiO for oxygen evolution reaction recorded at $\nu = 2$ mV/s in 1 M KOH saturated in O_2 | 157 |
| 4.6 | Evolution of the overpotentials (V) at various density currents as function of the KOH concentration (mol/L) | 158 |
| 4.7 | a) Linear sweep voltammetry (LSV) of modified NiO recorded at $\nu = 2$ mV/s in 1 M KOH, (b) Tafel plot of the studies made with 1 M KOH | 159 |
| 4.8 | Evolution of the Tafel slope for low overpotential and large overpotential for different KOH concentration | 159 |
| 4.9 | Evolution of the transfer coefficient α_a for low overpotential and large overpotential for different KOH concentration | 161 |
| 4.10 | Proposition of mechanism for oxygen evolution reaction involving two adjacent oxidized Ni sites ^[38] | 162 |
| 4.11 | (a) Nyquist plot for NiOx obtained with EIS measurement at 1 M KOH, (b) Nyquist plot for NiOx with fitting at 1 M KOH | 163 |
| 4.12 | Equivalent circuit for analyzing EIS responses during OER with NiO _x electrode | 163 |

| | | |
|------|--|-----|
| 4.13 | Evolution of the Charge transfer resistance R_{ct} (Ω) as function of the overpotential (V) | 164 |
| 4.14 | Evolution of the adsorption resistance R_a (Ω) as function of the overpotential (V) | 164 |
| 4.15 | Evolution of the adsorption capacitance C_a (H) as function of the overpotential (V) | 165 |
| 4.16 | Evolution of the charge transfer resistance R_{ct} (Ω) as function of the adsorption resistance R_a (Ω) | 165 |
| 4.17 | a) Evolution of $\ln i$ (A/cm^2) as function of the overpotential (V), (b) Evolution of $\ln (1/R_{ct})$ as function of the overpotential (V), (c) Evolution of $\ln (1/R_a)$ as function of the overpotential (V) | 166 |
| 4.18 | Polarization curves in a two-electrode system with NiO _x (+) NiO _x (-) in 1M KOH | 167 |
| 4.19 | Evaluation of the energy efficiency based on thermoneutral potential | 169 |
| 4.20 | Comparisons of cell voltages (A) at 10 mA/cm ² and (B) 100 mA/cm ² among different alkaline water electrolyzers ^[48] | 169 |
| 5.1 | Classification of the battery-supercapacitor hybrid device ^[6] | 178 |
| 5.2 | Energy storage mechanism for the battery-supercapacitor hybrid device ^[6] | 179 |
| 5.3 | Electrografting of AQD to Carbon cloth | 180 |
| 5.4 | Photo of the supercabattery made | 181 |
| 5.5 | Galvanostatic charge-discharge curves at different currents of NiO/CC-AQD supercabattery | 182 |
| 5.6 | (a)Galvanostatic discharge curves at different currents of NiO/CC-AQD supercabattery , (b) Galvanostatic charge curves at 0.5 mA and 1.5 mA of NiO/CC-AQD supercabattery , (c) Evolution of the charging time (s) as function of the applied current (mA) | 183 |
| 5.7 | (a) Evolution of the charging electrical flux (V.s) as function of the applied current (mA) , (b) Evolution of the charging electrical flux/charging time (V) as function of the applied current (mA) | 184 |
| 5.8 | (a) Galvanostatic discharge curves at different currents of NiO/CC-AQD supercabattery , (b) Galvanostatic discharge curves at 0.5 mA and 1.5 mA of NiO/CC-AQD supercabattery , (c) Evolution of the discharging time (s) as function of the applied current (mA) | 185 |
| 5.9 | (a) Evolution of the discharging electrical flux (V.s) as function of the applied current (mA) , (b) Evolution of the discharging electrical flux/discharging time (V) as function of the applied current (mA) | 185 |
| 5.10 | (a) Evolution of the charging electrical flux/charging time (V) as function of the applied current (mA) , (b) Evolution of the discharging electrical flux/discharging time (V) as function of the applied current (mA) | 186 |

| | | |
|------|--|-----|
| 5.11 | GCDs of charge-discharge profiles of a hybrid supercapacitor with capacitive Faradaic charge storage (CFS) and non-capacitive Faradaic charge storage (NCFS) processes. ^[15] | 187 |
| 5.12 | Evolution of the stored energy (J) as function of the applied current (mA) . . . | 188 |
| 5.13 | Evolution of the stored charge (C) as function of the the applied current (mA) | 188 |
| 5.14 | Evolution of the stored power (W) as function of the applied current (mA) . . | 189 |
| 5.15 | (a) Evolution of the useable energy (J) as function of the applied current (mA) (b) Evolution of the useable charge (C) as function of the applied current (mA) (c) Evolution of the useable power (W) as function of the applied current (mA) | 190 |
| 5.16 | (a) Evolution of the useable energy/stored charge (V) as function of the stored charge (C), (b) Evolution of the useable energy/stored charge (V) as function of the useable charge (C) | 191 |
| 5.17 | Evolution of the useable power/stored charge (V/s) as function of applied current (A) | 192 |
| 5.18 | Comparaison of Elastance S | 193 |
| 5.19 | Evolution of the efficiency metrics as function of the applied current (mA) . . | 194 |
| 5.20 | (a) Ragone plot, (b) Modified Ragone plot | 195 |
| 5.21 | (a) Galvanostatic charge-discharge curves at different currents of NiO/CC-AQD supercabattery , (b) Modified Ragone plot | 196 |

LIST OF TABLES

| | | |
|-----|---|-----|
| 1.1 | Table of various EESD according to their charge storage mechanism ^[10] | 6 |
| 1.2 | Comparisons of alkaline water electrolyzers and acidic PEM water electrolyzers ^[63] | 39 |
| 1.3 | Tafel mechanism and slope | 41 |
| 1.4 | Possible mechanisms for oxygen evolution reaction in alkaline media ^[77] | 45 |
| 1.5 | Kinetic expressions and Tafel slope for hydrogen oxidation reaction in acidic media ^[82] | 49 |
| 1.6 | Oxygen reduction reaction mechanisms in alkaline media ^[76] | 51 |
| 2.1 | Processing parameters involved in electrospinning | 67 |
| 2.2 | Presentation of the different temperatures evaluated for thermic treatment during 2 H | 69 |
| 2.3 | Average crystallite sizes of the powder made at different temperature | 75 |
| 2.4 | Measured obtained with the Cristal line for the powder made at 500°C with a, b and c:lattice parameters; L: average crystallite sizes and sig or X ² : Goodness of Fit | 78 |
| 2.5 | Measured obtained with the Cristal line for the powder made at 600°C | 80 |
| 2.6 | Measured obtained with the Cristal line for the powder made at 700°C | 81 |
| 2.7 | Measured obtained with the Cristal line for the powder made at 800°C | 83 |
| 2.8 | Measured obtained with the Cristal line for the powder made at 900°C | 84 |
| 3.1 | Comparison of hydrogen evolution reaction electrochemical activity parameters for selected materials in alkaline (1M KOH) for Nickel foam (NF) with Iron and Phosphor doped ^[40] | 120 |
| 3.2 | Table of the Ratio of slopes for the evolution's curves studied in figure 3.22 | 141 |

| | | |
|-----|---|-----|
| 4.1 | Comparison of Oxygen evolution reaction electrochemical activity parameters for selected materials in alkaline (1M KOH) for Nickel foam (NF) with Iron and Phosphor doped ^[20] | 154 |
| 4.2 | Value of the overpotentials (V) for selected current density (mA/cm ²) | 157 |
| 4.3 | Correlation between the values of transfer coefficient and the Tafel slope | 160 |
| 4.4 | Table of the Ratio of slopes for the evolution's curves studied in figure 4.17 | 167 |
| 4.5 | Table of the potential difference Δ_E (V vs RHE) | 168 |

INTRODUCTION

The main problem of the twenty-first century is global warming due to decades of massive industrialization and the development of emergent countries. Then, it is urgent to find an alternative to fossil energies and to develop sustainable energy. One of the main turning points in the importance of the environmental issue is the COP21 which took place in 2015 in Paris. In this context, developing electrochemical energy storage such as batteries, fuel cells, and supercapacitors using non-noble metal is an exciting way to respond to this demand.

The key element for developing sustainable energy storage is investigating the material used for elaborating the electrode of the device design. The nature of the material can influence efficiency. We have an electrochemical reaction at each electrode in the electrochemical energy storage device. To improve the system, it is common to play on one of the electrode's nature and/or structures to improve the electrocatalytic properties. For example, in the case of the reversible fuel cell, water splitting is the key reaction that implies both of the electrodes. However, the problem is the slow kinetics in oxygen electrochemistry. Then, it is necessary to find stable, abundant, and good catalysts for hydrogen evolution reaction (HER) and oxygen evolution reaction (OER), both of the reactions implied in the water-splitting. The other highly studied reaction is the oxygen reduction reaction (ORR) for the application of batteries such as Metal-air batteries. The emergence of a hybrid device that combines the battery and supercapacitors is an interesting approach. This hybrid device is called a *supercabattery*, a marriage of *supercapacitor* and *battery*. It has high power and energy; these proprieties allow us to obtain a device with longer life and pulse power. The application supercabattery is mainly used for electric or hybrid vehicles.

During my PhD studies, we focused on the studies of catalysts based on non-noble metals such as manganese oxide for ORR and doped nickel oxide for HER and OER. Based on the electrochemical properties of doped nickel oxide, we analyzed an electrochemical energy storage system, a supercabattery, by combining doped nickel oxide and modified carbon cloth. To this

end, we combined various spectroscopy techniques (X-ray photoelectron spectroscopy, Raman spectroscopy, X-ray diffraction, Scanning Electron Microscopy, energy dispersive spectroscopy), and electrochemical techniques (cyclic voltammetry, rotating ring disk, galvanostatic charging/discharging, electrochemical impedance spectroscopy). This PhD thesis contains five chapters:

- Chapter 1 is a general introduction in which we focus on the different reactions that will be investigated, like HER, OER, and ORR, and the different energy storage systems such as supercapacitors and batteries to introduce the supercabattery.
- Chapter 2 will be devoted to the powder composed of nanomaterials based on manganese oxide produced by electrospinning followed by a thermal treatment. We will analyze the structure and composition of manganese oxide by combining various spectroscopy techniques and investigate the ORR mechanism.
- Chapter 3 and Chapter 4 are focused on the electrochemical properties of doped nickel oxide for HER and OER, respectively. The water-splitting ability of doped nickel oxide in alkaline media is highlighted.
- Chapter 5 is devoted to the supercabattery, which is a two-electrode device based on doped nickel oxide and modified carbon cloth electrode. To consider the non-linear response of the device, we introduce a new approach for determining the energy, the charge (capacity), and the power by using the electrical flux. In the same way, we introduce the notion of the device's elastance and conductance. Also, a modified Ragone plot is presented.

One can emphasize that chapters 3-5 in which a doped nickel oxide electrode used are parts of an international collaboration common project focused on the development of non-noble electrocatalysts for energy application between Professor Cho from Korean Advanced Institute of Science and Technology (KAIST, South Korea) and my supervisor Professor Randriamahazaka (Université Paris Cité, France). A short general conclusion is given in the last part of this PhD thesis, in which we summarize the most important results from different perspectives related to the electrode materials.

CHAPTER 1

INTRODUCTION - AN OVERVIEW OF ENERGY STORAGE SYSTEMS

60

Contents

| | | |
|------------|--|-----------|
| 1.1 | Different energy storage systems | 4 |
| 1.1.1 | Supercapacitor | 6 |
| 65 | a) Electrical double-layer capacitor | 7 |
| | b) Pseudocapacitor | 11 |
| 1.1.2 | Battery | 15 |
| | a) Li-ion battery | 18 |
| | b) Metal-air battery | 22 |
| 70 | 1.1.3 Supercapattery (SCAP) | 27 |
| | a) Charge storage of the supercapattery | 29 |
| | b) Focus on the Supercabattery | 32 |
| 1.2 | Energy production | 33 |
| 1.2.1 | Chemical Energy conversion by Fuel Cell | 33 |
| 75 | 1.2.2 Chemical Energy storage by water splitting | 37 |
| | a) Hydrogen evolution reaction: HER | 40 |
| | b) Oxygen evolution reaction OER | 44 |
| | c) Hydrogen oxidation reaction HOR | 47 |
| | d) Oxygen reduction reaction ORR | 50 |
| 80 | 1.3 Conclusion of the first chapter | 53 |
| | References | 53 |

1.1 Different energy storage systems

Since the beginning of industrialization, Men have used fossil energies to supply social needs. During the past decade, we had an emergence of alternative energy systems to reduce the use of fossil energies and their impact on the environment. The effect on the environment and global warming is the central issue of the 21st century and will impact the future. During the Conference of the Parties (COP21) in Paris in 2015, the participants unanimously agreed that all of them would try to limit climate change by decreasing emissions of greenhouse gases (GHGs). One key point defined was limiting global temperatures to 2°C above the pre-industrial era. In this agreement, they defined a guideline to adopt to limit the harmful impact of climate change.^[1]

This first chapter will focus on different storage and alternative energy systems. To begin this part, we will introduce other trends of the progress in energy storage technology to identify with which we deal. After that, we will focus on different electrochemical systems such as batteries, supercapacitors, Supercapbattery (a hybrid system), and fuel cells. We can divide the energy storage system into five categories: mechanical energy storage, heat-energy storage, electrochemical energy storage, magnetic energy storage, and chemical energy storage. We will focus on electrochemical energy storage and chemical energy storage.^[2]

We can find supercapacitors and rechargeable batteries in the field of Electrochemical energy storage devices (EESD). EESD can store and release electricity through electrochemical processes in a reversible, efficient and convenient way.^[3] Electrochemical energy storage systems have various applications like portable electronics, electrical vehicles, and aviation/aerospace equipment.^[4-8]

In figure 1.1, we can see the typical structure of supercapacitors and batteries. In both systems, we have a positive and negative electrode, a separator, and an electrolyte that can be in a liquid or gel state.

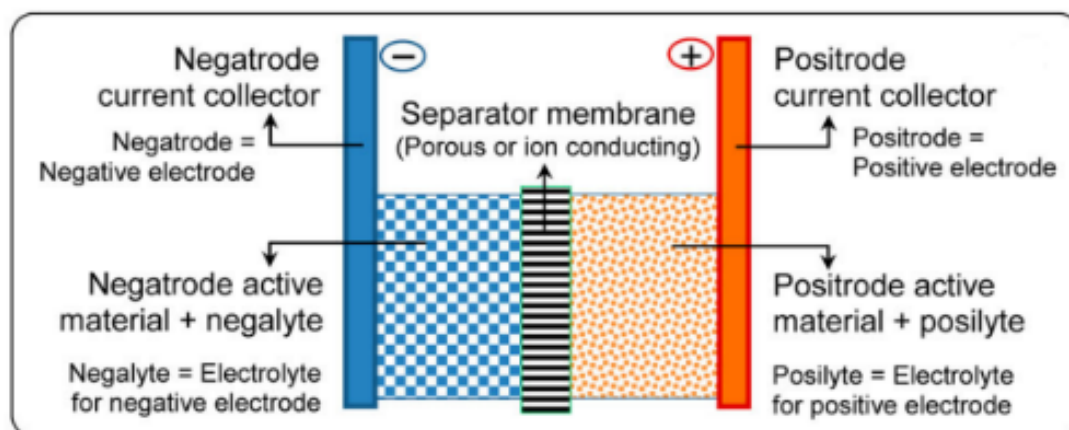


Figure 1.1 – Illustration of the structure and electrochemical behavior of supercapacitors and batteries.^[9]

Optimizing various parameters, such as the electrolyte and the electrode, it is possible to improve the system's performance. Replacing the liquid electrolyte with a gel or solid film can supply less leaking and simplify the construction of storage systems. Furthermore, the flexibility in device fabrication and safety is improved. Usually, the working electrodes are made with a layer containing active materials, polymer binders, and electrically conductive agents on a metallic foil or foam that acts as a current collector. In some instances, the binders and conductive agents can be replaced by active materials like carbon nanotubes and graphene. In the following part, we will focus on supercapacitors and batteries to understand their difference and their similarities. Table 1.1 shows different types of supercapattery, including hybrid device battery- supercapacitor.

| | | | | | | | | | | |
|--------------------|----------------|------|------|-----------------|-----|--------|------|-----------------|---------|--|
| Device | Supercapattery | | | | | | | | | |
| | Supercapacitor | | | | | Hybrid | | Super-cabattery | Battery | |
| Electrode Material | EDLC | | | Pseudocapacitor | | | | | | |
| | NFCS | NFCS | NFCS | CFS | CFS | NFCS | CFS | NCFS | NCFS | |
| | 1+1 | 1+2 | 1+3 | 1+1 | 1+2 | 1+3 | 1+2 | 1+1 | 1+2 | |
| | NFCS | NFCS | CFS | CFS | CFS | NCFS | NCFS | NCFC | NCFS | |

NFCS: Non-Faradaic Capacitive Storage = EDLC Storage
 CFS: Capacitive Faradaic Storage = Pseudocapacitive Storage
 NCFS: Non-Capacitive Faradaic Storage = Battery-Type Storage
 1+1: Symmetrical device of the same electrode material
 1+2: Asymmetrical device of different materials with the same storage mechanism
 1+3: Asymmetrical device of different materials with different storage mechanisms

Table 1.1 – Table of various EESD according to their charge storage mechanism^[10]

1.1.1 Supercapacitor

There are two types of supercapacitors: electric double-layer capacitance and pseudocapacitance (Figure 1.2). Firstly, we will introduce an electrical double-layer capacitor and its storage mechanism. After that, we will focus on pseudocapacitor in detail.

– Electrical dual-layer capacitors, also called supercapacitors, can store and release electrical energy through fast charge transfer during the charge and discharge processes. Since the energy is stored by adsorption of physical ionic species, the supercapacitor can generate high power.^[11] It can be charged very quickly 10^6 times without power deficiency with a high-specific power density. Supercapacitors can be used in various areas like hybrid electric vehicles (HEVs), plug-in hybrids, and everyday devices, like laptops and smartphones.

In figure 1.2, we have two systems: electric double layer (EDL) capacitance and pseudocapacitance. In an electric double layer capacitance (EDLC), one has a fast absorption/desorption of electrolyte ions on the surface of the active material during the charging/discharging processes^[12]. The charge storage is in double electrical layers formed near the electrode/electrolyte interfaces. The electrochemical response is high reversibility, and the durability in time is limitless in theory.

– On the other hand, for the pseudocapacitance, a fast redox reactions occurs on and near the surface of active materials during the charging/discharging processes.^[13] Compared to EDLC, the charge is stored not only by the electrical double layer but also by the fast oxidation-reduction reactions at the electrode surface and/or the intercalation of ions within the electrode materials.

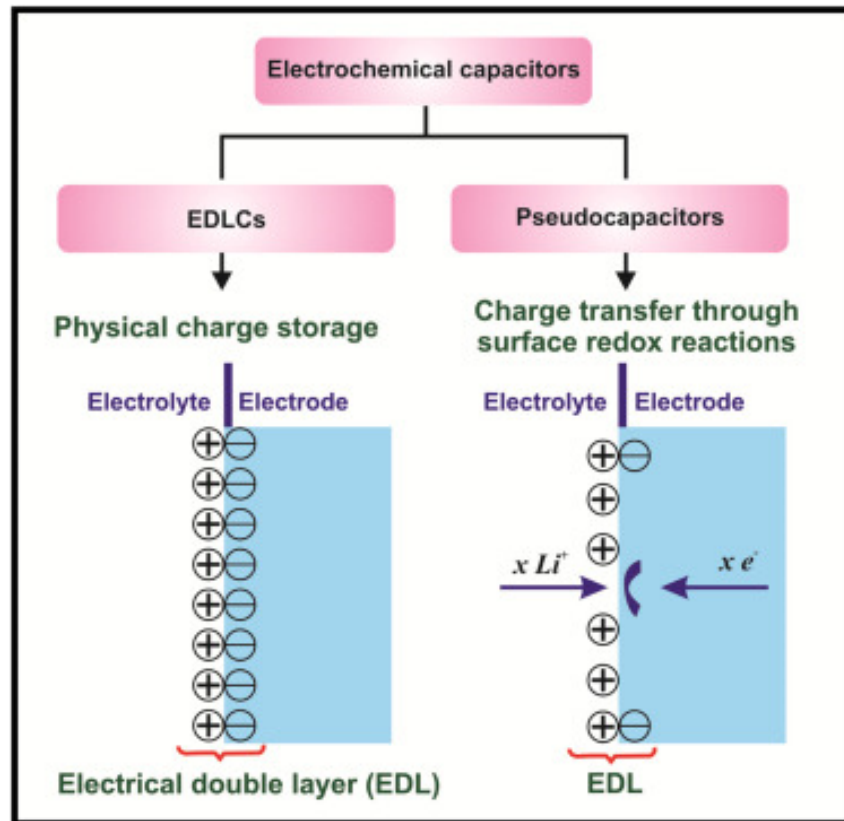


Figure 1.2 – Energy storage mechanisms for electric double layer capacitance and pseudocapacitor^[11]

145 a) Electrical double-layer capacitor

In this part, we will focus on the charge storage mechanism of Electrical double-layer capacitors. In this system, the energy can be stored without faradaic reaction thanks to loading adsorption on the electrode surface^[14,15]. One has a double layer formation at the interface electrode-electrolyte, with one layer sided to the conductor (here, the electrode) and the other layer sided to the electrolyte. The nature of electrode surface structure and electrolyte plays an essential role in the charging processing at the interface.

Let us look at the Helmholtz model to understand the charging and discharging processes. In this model, the charge is on each side of the electrode depending on the charge of the electrode. The following equation defines the capacitance:

$$C_{dl} = \frac{Q}{V} = \frac{\epsilon_r \epsilon_0 A}{d} \quad (1.1)$$

where C_{dl} is the capacitance of the electrode, Q is the total charge transferred at potential applied V , ϵ_r is the dielectric constant of the electrolyte, ϵ_0 is the dielectric constant of vacuum, d is the charge separation distance, and A is the electrode surface area. However, the Helmholtz model alone cannot explain many experimental results. Then, the more accurate models were

developed by Gouy and Chapman, and later by Stern. The continuous distribution of the electrolyte ions (both cations and anions) in the electrolyte solution, which corresponds to the diffusion layer is introduced in Gouy and Chapman's correction. In Stern's correction, one has two regions of ion distributions: the inner region called the compact layer or Stern layer, and the diffuse layer (Figure 1.3).

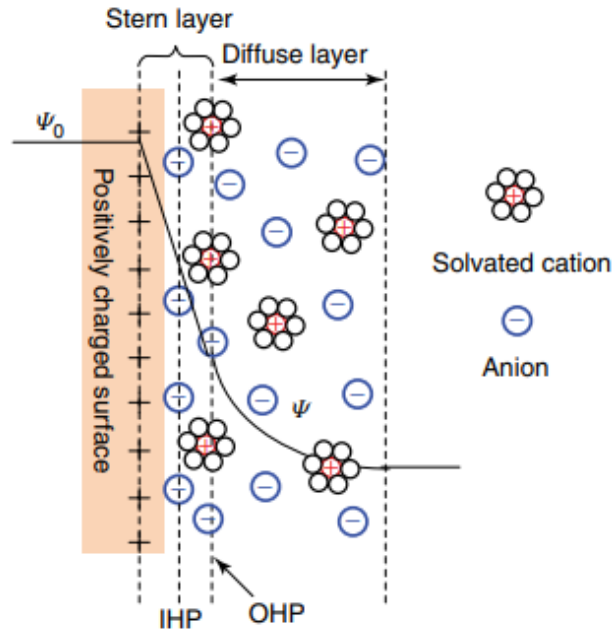


Figure 1.3 – Stern model at electric double layer at the positive electrode^[16]

One can observe the outer Helmholtz plane (OHP) and the inner Helmholtz plane (IHP). OHP is represented by adsorbed ions (often cations) near the electrolyte (solution). The interaction at the interface is due to coulombic interaction. In IHP, the closest adsorbed ions (regularly anions) are near the electrode. The chemical affinities of the ions to the surface and the field strength of the double layer play a key role in the adsorption process.^{[4], [16]} The differential capacitance C determines the electrical charge storage ability. The interfacial capacitance of the electrical double layer C_{dl} is given by the series combination of the capacitances from two regions: the Stern layer region capacitance C_H and the diffusion region capacitance C_{diff} as

$$\frac{1}{C_{dl}} = \frac{1}{C_H} + \frac{1}{C_{diff}} \quad (1.2)$$

If the capacitance C_{dl} is constant and does not vary with the voltage, one can link it with the response current I and the time of charge t :

$$I = \frac{dQ}{dt} = C_{dl} \frac{dV}{dt} \quad (1.3)$$

Using the cyclic voltammetry technique, one can find a simple relationship between the applied voltage V , the scan rate ν , the current I , and the capacitance C_{dl} . Since the voltage varies linearly with the time as :

$$V = V_0 + \nu t \quad (1.4)$$

With V_0 is the initial voltage and ν is the sweep rate (V/s) then

$$I = C_{dl}\nu \quad (1.5)$$

In Figure 1.4, we have different cyclic voltammograms at different scan rates for the electrode NiOx. One obtains a rectangular signal in the cyclic voltammogram. According to equation (1.5), the current charge I varies linearly with the scan rate ν , and the slope of I vs V gives the capacitance C_{dl} .

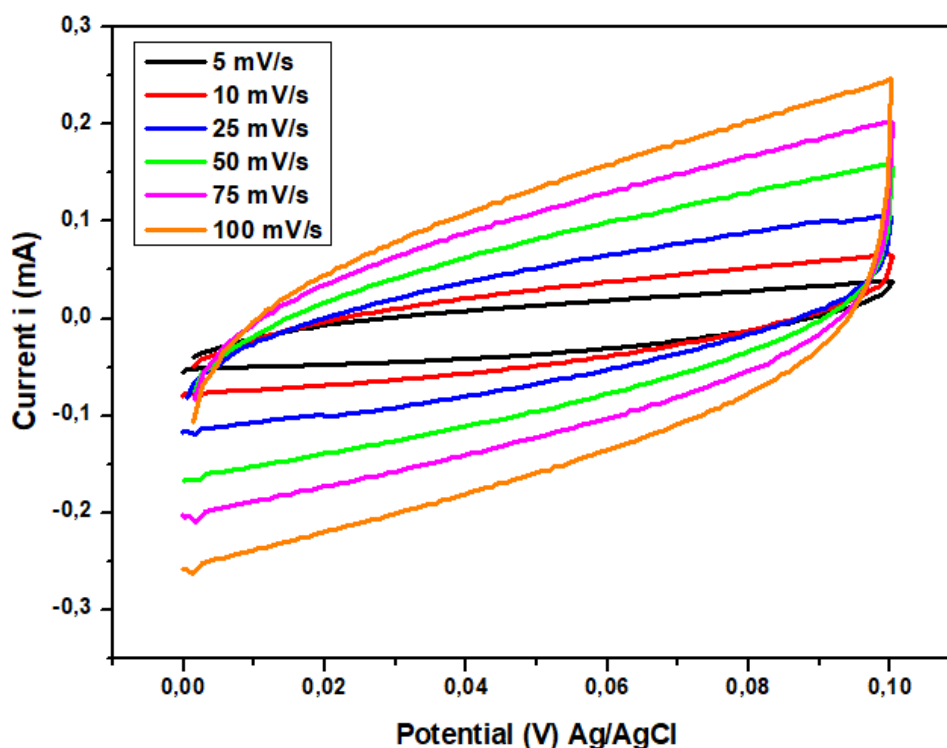


Figure 1.4 – Cyclic voltammogram of modified NiO recorded at various scan rate (seen in chapter 4)

In this part, we will focus on the working process of the EDLC. EDLC is composed of one cell with two electrodes divided by the electrolyte. At the interface electrode/electrolyte, we have charge stored. In the previous part, we saw that the charges are placed in two different layers, differing by the sign at the layer (Stern model). The electrolyte can be aqueous or organic and plays a crucial role in the voltage. It stabilizes the operating voltage of the system. And when we look at the double layer, we apply potential differences. If we look at the

195 charge/discharge of EDLC illustrated in figure 1.5, we can see that the voltage applied between our two-electrode, will influence the ions. Ions are absorbed into the electrode that had the opposite polarity sign and the double layer at each electrode is developed. During the loading of EDC, the double layer replaced the voltage source, and the ions returns to the electrolyte.

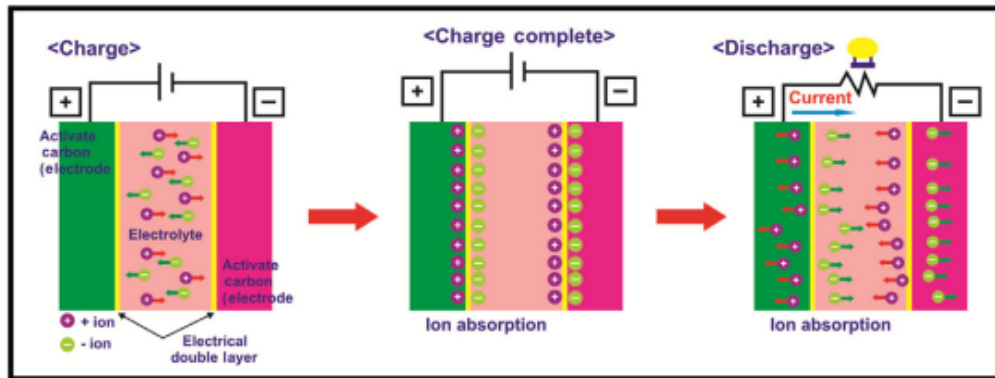


Figure 1.5 – Charge and Discharge process of electric double layer capacitance^[11]

To understand the voltage distribution during the charging process of EDLC, the equivalent electrical circuit shown in Fig. 1.6 can be used in which the capacitance contribution of each electrode is noted C_1 and C_2 . The two capacitances are connected by series. Also, the resistance R_E due to the contribution of each electrode is included. Furthermore, the electrolyte contribution with internal resistance due to the movement of ions inside the electrolyte R_i and R_{Leak} must be taken into account.

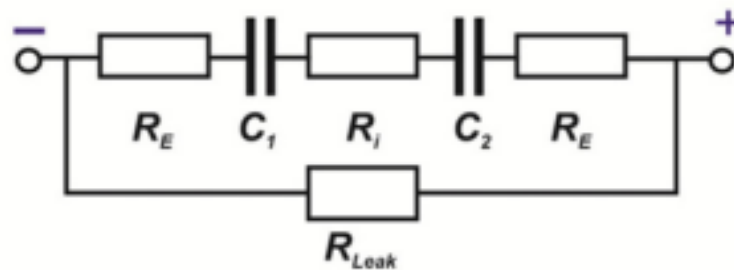


Figure 1.6 – Electrical circuit model of electric double layer capacitance

205 Figure 1.7 reports the accurate electrical circuit of an EDLC cell showing two parallel plate condensers at the electrodes of EDLC with two condensers connected in series. The significant difference with the previous model (Figure 1.6) is the resistance due to the layer noted R_p isolating layer's resistance. The parallel circuit of C_{dl} and R_p is explained by the presence of a capacitance and a resistance at the double layer of the electrode. These two parallel circuits of C_{dl} and R_p correspond to a double layer of each electrode separated by the resistance from

electrolyte denoted R_s .

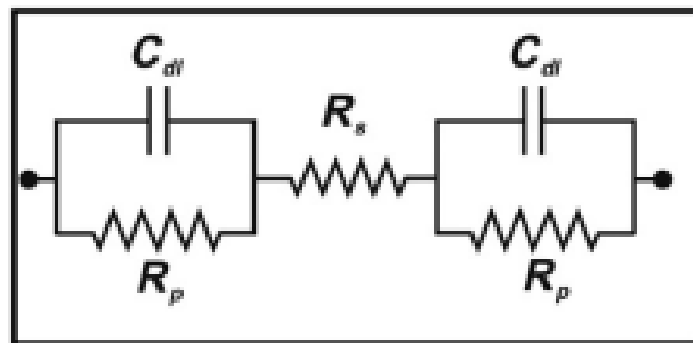


Figure 1.7 – The accurate electrical circuit of an electric double layer capacitance

b) Pseudocapacitor

In the case of the pseudocapacitor, the energy storage results from the insertion and adsorption of the ions from the electrolyte to the electrode surface due to the reduction/oxidation reactions involving the electrode materials. The magnitude of the charging and discharging rates are similar to those of the EDLC. The capacity is related to the oxidation/reduction reactions at the electrode interface. Herein, the charge storage is governed by the redox reactions and the electrostatic interaction.

Figure 1.8 shows the working principle of the pseudocapacitor. At the interface, there are various processes due to redox reactions leading to storing charge and energy while increasing the system's capacitance.

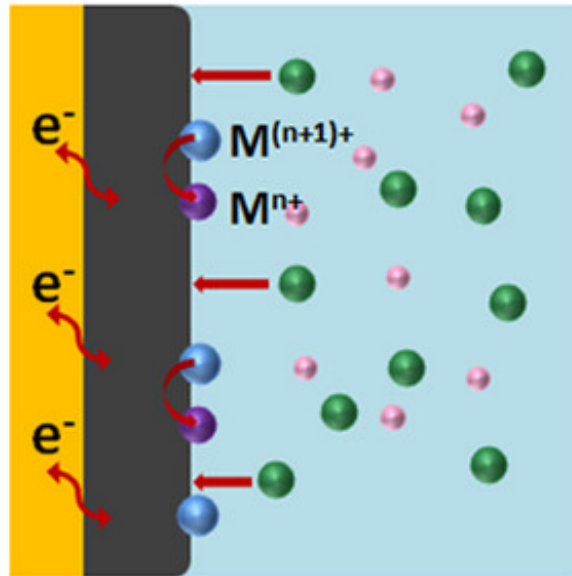


Figure 1.8 – Charge storage mechanisms of pseudocapacitor^[17]

The equivalent electrical circuit of pseudocapacitor is reported in Figure 1.9 where C_{dl} , and R_s are the capacitance of the double layer of electrode and resistance from the electrolyte, respectively. There are also the potential-dependent pseudo-capacitance C_ϕ , electrode-electrolyte resistance R_f , and Faradaic resistance R_D due to ion desorption. Sometimes, the potential-dependent pseudo-capacitance C_ϕ can be higher than the capacitance of the double layer C_{dl} depending on the applied potential.

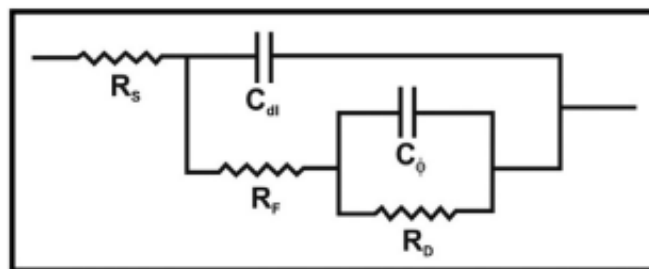


Figure 1.9 – Electrical circuit of a pseudocapacitor

There are three main types of pseudocapacitors:

- Underpotential deposition process
- Redox pseudocapacitance process
- Intercalation process

The first type of pseudocapacitor is underpotential deposition with a two-dimensional storage load process. In this case, the electrode had a positive potential in addition to Nernst's potential to deposit another metal (monolayer) onto the metal's electrode surface. In other words, the deposition process occurs at a higher potential than a reduction potential. Figure 1.10 illustrates the underpotential deposition process.

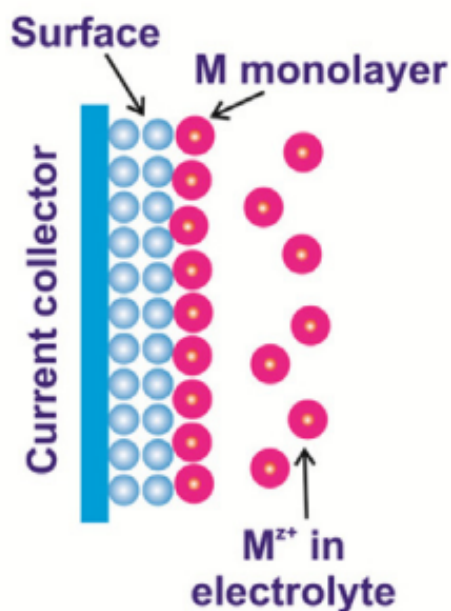


Figure 1.10 – Underpotential deposition process

For the second type of pseudocapacitor, faradaic reactions through the charge transfer occur between electrodes and electrolytes. The reversibility during partial charge transfer between the electrode and electrolyte plays an important role.^[18] Typical example is the charging process is the reduction of metal oxide electrodes like Mn_2O or RuO_2 concomitant to electrolytic cations adsorption.^[19] Figure 1.11 illustrates the redox pseudocapacitance process.

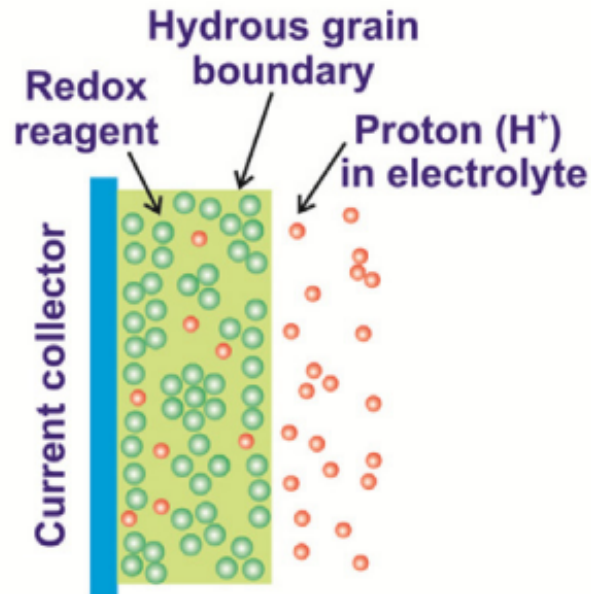


Figure 1.11 – Redox pseudocapacitance process

For the last type of pseudocapacitor, an intercalation pseudocapacitance process occurs. One has an insertion of cation into the solid electrode's bulk lattice. During this process, the electroneutrality of the electrode is maintained by considering the number of electrons transferred to the host. Also, there is fast reversibility during the charging/discharging process. For this type of device materials like molybdenum nitrides, niobium pentoxides, and titanium carbides have been investigated^[11]. Figure 1.12 illustrates the last pseudocapacitor seen.

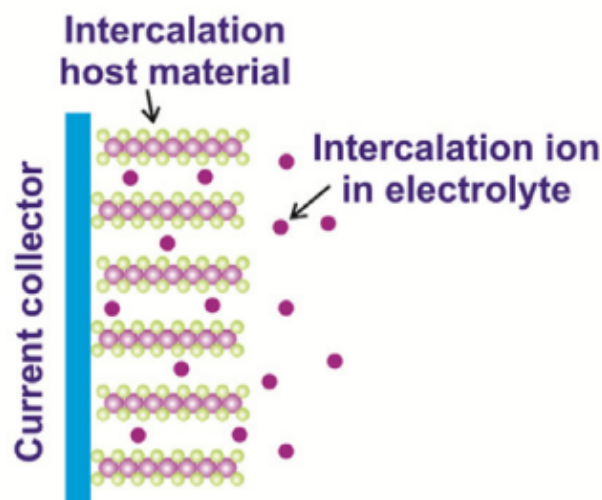


Figure 1.12 – Intercalation pseudocapacitance process

In the next section, we will look at the second type of electrochemical energy storage device (EESD) that we saw in the introduction, the battery system.

1.1.2 Battery

In this part, we will focus on the battery system divided into different sections.

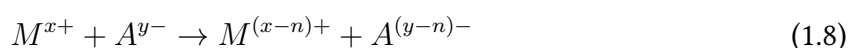
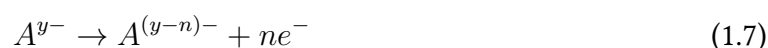
Firstly, the different parameters used to define the system are introduced. Secondly, one describes three main families of batteries. And finally, two types of positive electrodes are analyzed deeply, for instance, manganese and nickel oxides.

The battery store can convert chemical energy to electrical energy. During this energy transformation, reduction and oxidation processes occur in the system. Thermodynamic constraints determine the arrow of these redox reactions. Indeed, these reactions occur spontaneously during the discharging. The battery system can be divided into two compartments with two active electrodes composing the two-half cell. These two separated electrodes are connected by the electrical circuit (a metal conductor) and by an electrolyte (ion conductor). During the redox reactions, the electroneutrality condition is satisfied in both half-cells.

If we look at the electrode and electrolyte interface, we have a charge transfer process. This phenomenon translates the electron exchange at the two half-cells. And it is thanks to the external electrical circuit that we have the exchange of n electrons. And the electrolyte is the main key point in our system because it can restore local electroneutrality by ion con-

tions. The other components of the cells are the separators, the container, and the electrical terminals.

One can summarize the following spontaneous reactions during the discharging process at both electrodes by the following equations :



The first equation (1.6) (reduction reaction) corresponds to the reaction that happens at one of the half cells. This electrode is called the cathode. The second equation (1.7) corresponds to the oxidation process at the second half cell, which plays the role of the anode. And the third equation (1.8) is the global reaction happening in the cell. Each half-cell is physically separated. The specific notation to write the redox couple involved in the cell is : $A^{y-} | A^{(y-n)-} || M^{x+} | M^{(x-n)+}$

On the left side of the notation ($A^{y-} | A^{(y-n)-}$), we have the redox couples involved in the oxidation process. For the right side ($M^{x+} | M^{(x-n)+}$), we have the redox couples involved in the reduction process.

The single bar that describes the interface, and the double bars are used to symbolize the separation of the two half cells and are connected by the electrolyte.

The battery's goal is to give the system the required voltage and current. We can also quantify the power thanks to these two parameters. The working process of a battery can be divided into two parts. We have the charging and discharging parts. We look closely at the different parts in a few sections. The discharging part of the battery can be different depending on the type of batteries. We have the reversible chemistry due to reverse redox reaction processes and flow two types of ends; we have the one that is going to be discarded or the other that can be recharged thanks ions and electrons present.

We can look at the discharge process to find the different types of batteries. One can describe three main families of batteries:

1. the first one is the primary batteries or the electrochemical generators in which some components are discarded during the discharging process
2. the second type is the secondary batteries or accumulators where the loading can invert the oxidation-reduction process.
3. the third type is the fuel cell which is an open system, and thanks to the occurring redox processes the chemical energy of reactants given by the outside environment into electrical energy.

In the following part, we look at the battery's main components, which are the electrode materials and electrolytic solution.

The electrolytic solution plays a key role during the transport of ions to the electrode and maintenance of the electroneutrality at each electrode of the system. Depending on the charge of the ions present, they will go to the electrode with the opposite charge thanks to the electric field applied to the cell. And the flow is not the same, along with the battery life. The flow will switch, demining the charge-discharge process. Most of the time, the electrolyte used is a salt solution with a polar solvent; often, it is water. The composition of the electrolyte influences the behaviour at the electrochemical scale. High conductivity is essential to have good battery performance. The conductivity depends upon the electrolyte's concentration and the solvent's viscosity. Also, the solvent properties determine the "electrochemical stability window" (ESW). Furthermore, the electrolytic solution controls the stability of the redox properties of the various components in the electrochemical systems. The electrolyte had a redox couple, which will influence the redox couple present at each electrode. For example, in the case of an alkaline electrolyte, the reduction or the oxidation of the electrolytic solution may lead to the leak of gas like H_2 or O_2 and can be dangerous.

The charge transfer processes involving the electrolytic solution plays an important role in the control of the overpotentials; in real-life applications, the ESW can be larger than the theoretical value thanks to this phenomenon.

Now, look at the other components of the battery: the electrode materials. The electrode

characteristics, such as the materials' nature and surface area, play an essential role during the redox kinetic processes. The current will influence the surface delivered per surface that translates by the current density noted J ($A \cdot cm^{-2}$). The electrode also has a role in the charge and discharge process. We will focus on the secondary battery we studied during my PhD project.

The nature of the electrode and the value of equilibrium potential for each couple present at the electrode determine the role played by each electrode. The roles played by each electrode are different during the charging and discharging processes. During the charging process, the oxidation reaction occurs at the positive electrode, and the reduction reaction occurs the negative electrode. The electrons move from the positive electrode to the negative electrode through the external electrical circuit. During the discharging, the reverse reactions occur for each electrode. In the battery field, the positive and negative electrodes are called cathode and anode, respectively.

The main characteristic of the secondary batteries is that they have an external power supply that can apply a higher voltage than the voltage in the cell. This action conducts a spontaneous oxidation-reduction reaction that can reverse the reaction at each electrode and implies the charge-discharge process's switching.

In Figure 1.13, one can see the charging-discharging processes in a lithium-ion battery (LIB).

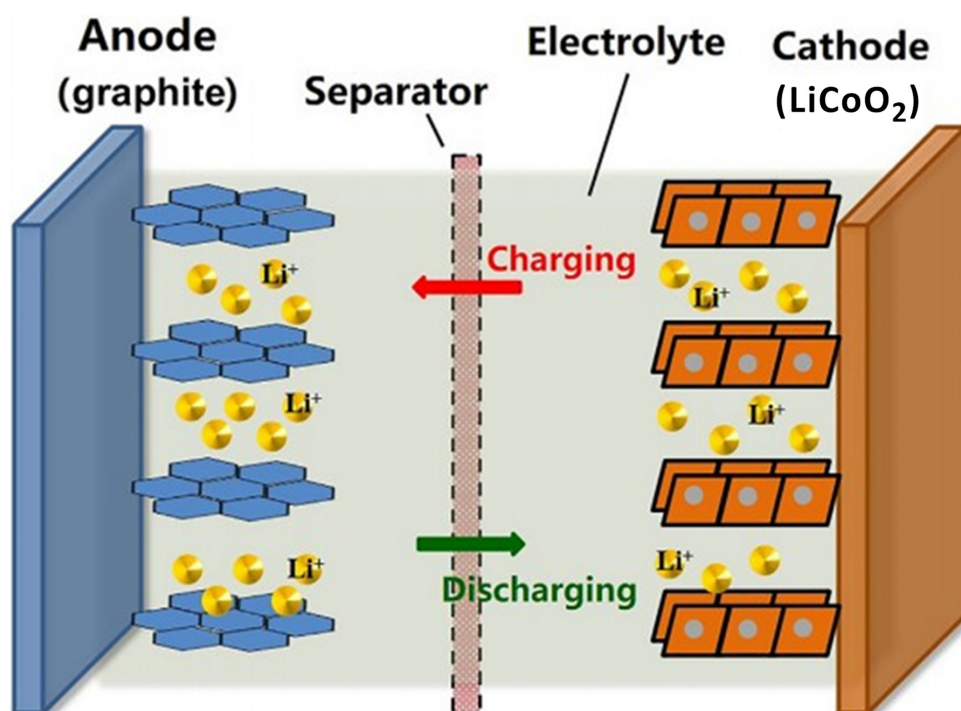


Figure 1.13 – Charge / Discharge process for the lithium-ion batterie^[20]

Despite LIB being the most famous model in the secondary battery for energy storage, its high cost may hinder the large-scale application, such as stationary batteries.^[21] One of the

alternatives studied is the use of the transition metal oxide as the positive electrode instead of lithium in this system. In this section, we will look at the lithium-ion battery and the alternatives proposed by the transition metal oxide. Notably, we will highlight the manganese oxide and nickel oxide electrodes because these electrode materials are mainly investigated in this PhD study.

a) Li-ion battery

In this section, we will look at the rechargeable lithium-ion battery (LIB), performance, and mechanism and look in detail at the cathode of its type of battery. The lithium-ion battery is one of the most used secondary batteries. It is widely used in technologies and impacts our daily use. It was essential in mobile applications such as cellular phones and laptops. The demand will increase by 15-16% in the future. If we value the increasing demand, it corresponds to USD 41.1 billion in 2021 to USD 116.6 billion \$ by 2030 if we look at the data from Marklines. The use of LIB is also used in electric vehicles (EVs). Nissan is one of the leaders in developing LIB of EV. For this type of LIB with a higher density is expected. At the beginning of 2010, LIB of EV delivered 24 kW h for maximum mileage of 200 km to 62 kW h in 2019 (maximum mileage of 458 km). (25) Even if it is a clear improvement, the energy density is lacking for heavy vehicles (HVs) like trains, buses, or trucks.^[22]

One of the approaches to increasing the energy density of LIB is to increase the storage capability of the anode. This deficit was due to the low specific capacity of carbon-based materials such as graphene used for the anode. The specific capacity of graphene is around 300 mA.h. g⁻¹. One of the investigations to resolve that issue is using of silicon for the anode.^[23] The specific capacity of silicon is around 2000–2500 mA.h. g⁻¹ which represents an increase of 70% compared to LIB.^[24,25] For the cathode materials, one can use a metal-oxide such as nickel-rich materials.^[26]

Now, one can focus on the performance of LIB and the parameters used to compare the data for optimizing the battery performance. The theoretical specific capacity (Q_{thSP}) is defined by the following equation (1.9):

$$Q_{thSP} = \frac{nF}{(3.6 \times M_w)} \quad (1.9)$$

where n is the number of reactive electrons per formula unit, F is the Faraday constant and M_w is the molecular weight of the element. The 3.6 corresponds to the conversion factor to obtain the theoretical specific capacity (Q_{thSP}) in mAh/g units. (1 Ah= 3600 C)

However, the value of specific capacity, estimated theoretically, is higher than measured. This difference is due to the limitation on the amount of extracted Li-ion. There is also instability in crystal structure during the Li-ion extraction.^[27]

The other important parameter is the energy of the cell given by this equation^[28] :

$$E = Q \cdot \Delta V \quad (1.10)$$

With E (J): Energy , Q (C): charge, and ΔV (V) : Potential window.

385 The charge and the energy are usually quantified by ampere-hour (1 Ah = 3600 C) and watt-hour (1 Wh= 3600 J); this indicates the device's operation time. One can normalize the energy to the volume or mass of the electrode materials or the overall volume or mass of the cell/battery. One can define these energies by the following equations:

$$E_d = \frac{E}{l} \quad (1.11)$$

390 With E_d (Wh.L⁻¹): Volumetric energy density, E: energy (Wh) and l:volume (L)

$$E_s = \frac{E}{m} \quad (1.12)$$

With E_s (Wh.kg⁻¹): Specific energy, E: energy (Wh) and m : mass (kg)

The battery needs to have a high energy density for application on heavy vehicles and devices with energy needs. Another important parameter is the power density (P_D) giving by the equation (1.13):

$$P_D = \left(\frac{E_D}{\Delta t} \right) \times 3600 \quad (1.13)$$

With E_D energy density and Δt the electrode time to completely be charged or discharged.

Thanks to energy density (E_D) and power density (P_D), one can compare the different performances of the electrochemical energy storage device (EESD) by using the Ragone plot (figure 1.14).

The Ragone plot allowed us to classify the different electrochemical energy storage devices (EESD). One observes a lower power density and a higher energy density for the battery system. Also, figure 1.14 highlights the faradaic and non-faradaic effect at the electrode and shows the main difference between these two devices. From an application point of view, battery stability is crucial point. The battery's durability can be defined as having the same response during repetitive cycling. The stability is linked to the Coulombic efficiency which is related to the charge of ion (in this case of the LIB, it's the Li⁺). Depending on the cycling step (charge or discharge), we will have an amount of charging ion or a loss. Usually, it is impossible to have an efficiency of 100% because of the loss of ions.^[30]

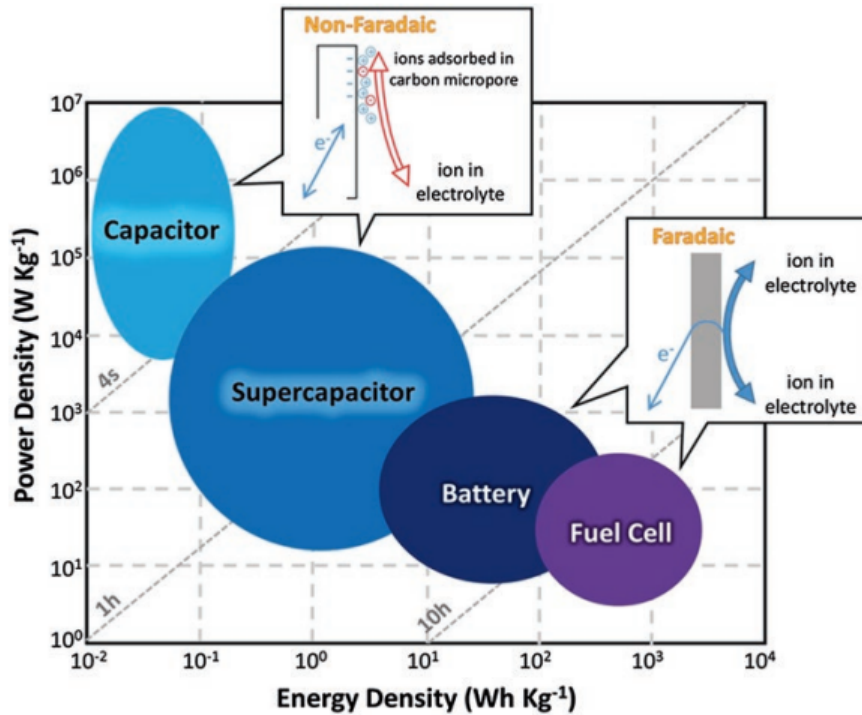
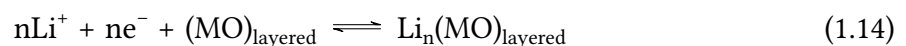


Figure 1.14 – Ragone plot of different electrochemical energy storage devices.^[29]

In this section, we will focus on the charge storing mechanism for the secondary batteries. In figure 1.15, there are three mechanisms: intercalation, conversion and alloying.

For the intercalation, we have the lithium-ion (Li⁺) and the transition metal oxides (TMOs) there are the alternative superposition of the ions and transition metal oxide in the interstitial space. Then, the crystal layer is composed of a TM - Li⁺ - TM. The intercalation can be described as (1.14):



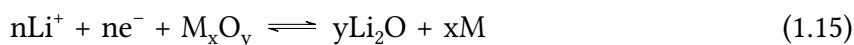
where (MO)_{layered} : layered metal oxide

Li⁺ ions go out of the interstitial space and take their original form during the discharge.

Usually, the graphite anode is used for intercalation systems. LiFePO₄ and LiMO₂ (where M is metal) are used as cathode materials for intercalation systems^[31]. Like the anode electrode, these materials exhibit good stability, but their specific capacity is limited. To solve the problem of the specific capacity, one can play on the nature of the metal, which can be a transition metal. This type of metal can improve performance because it stabilizes crystal structures. Also, the transition metal can be oxidized or reduced, which can influence the system's stability. This switch mode allowed it to keep the system during the cycling of the LIB.^[32]

The other mechanisms, conversion and alloying, are shown in Figure 1.15. For the conversion, Li⁺ ions became oxides thanks to the metal oxide ((M_xO_y)) presented. Li⁺ transformed to Li₂O. And during the discharging, the oxides go back to metal oxide. The following equation can

430 describe the conversion process:



For the alloy system, the electrodes can form Li alloy compounds. This reaction is due to the lithiation described as :

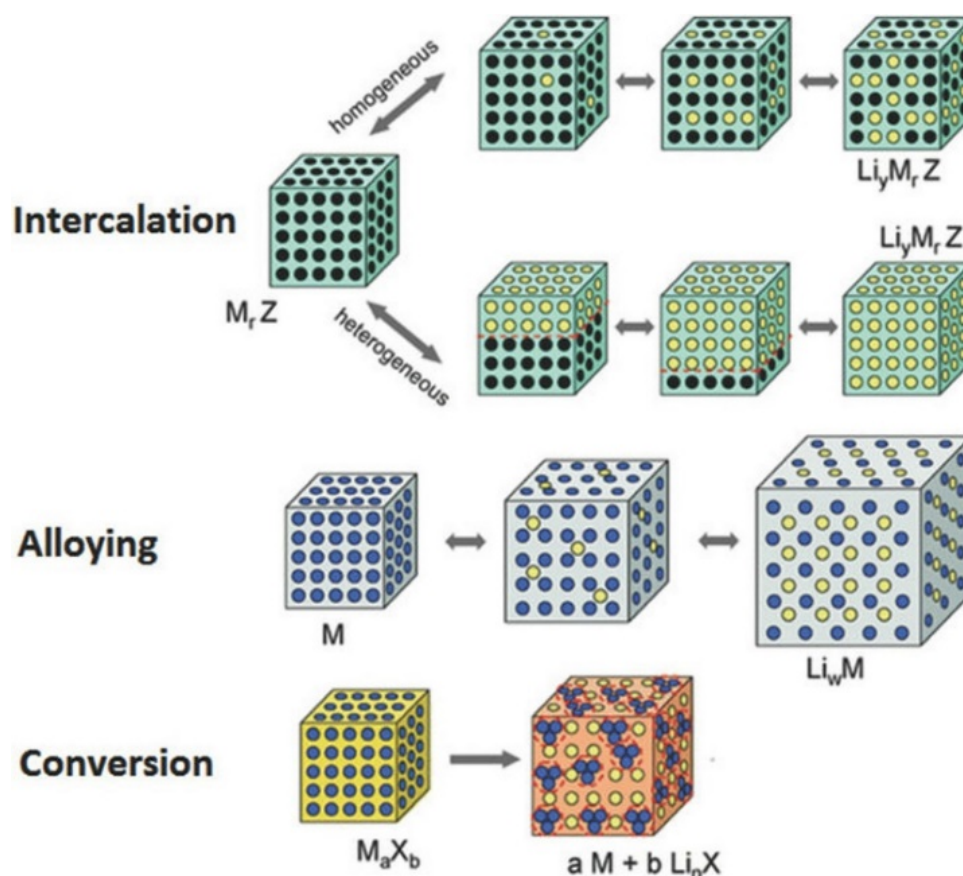


Figure 1.15 – Three charging storing mechanisms^[33]

435

If we look at the materials used in the second and third mechanisms, they offered more capacity than the ones used with the intercalation. Silicon is a material highly used for conversion and alloy. The theoretical specific capacity of silicon is 3600 mAh. g^{-1} . It is 10 times more than graphite used in the intercalation system.^[34,35]

440

Even if Si used in alloy system electrodes have an upper specific capacity, Si has low reaction kinetics with Li-ions. This behaviour can influence the stability and duration of LIB. The Coulombic efficiency is lower than 100%.

This lower efficiency is due to crystal defects in the materials and doesn't allow the Li-ion to transform back during the discharge. In the next section, we will look at nickel oxide and

445 manganese oxide as the cathode electrode for the metal-air battery.

b) Metal-air battery

One alternative to the lithium-ion battery is the metal-air battery (MAB). This type of battery is a serious candidate because it has many advantages like a high energy density and low cost due to abundant raw materials for fabrication. For example, looking at the theoretical
 450 specific energy densities of lithium-air and zinc-air batteries (two MABs well-known), one has 5928 and 1218 W.h.kg⁻¹^[36]. These high values are due to the specificities of the cathode. The cathode used for the MAB is different from the secondary battery seen previously.^[37] For the cathode here, it uses an air cathode. This type of cathode is using the oxygen present in air from the outside of the electrical cell. For MABs, the cathode does not take up a lot of
 455 space; a thin catalyst layer is enough. Thus, increasing the area for the anode (metal) in the cell is possible.

Figure 1.16 shows that the space management for MAB (left side) compared to LIB (right side) is different. The main difference is in the storage of the anode. The cathode is inexhaustible in the MAB case because the air is present in the atmosphere. Metal-air battery works until
 460 the anode is fully consumed.^[38]

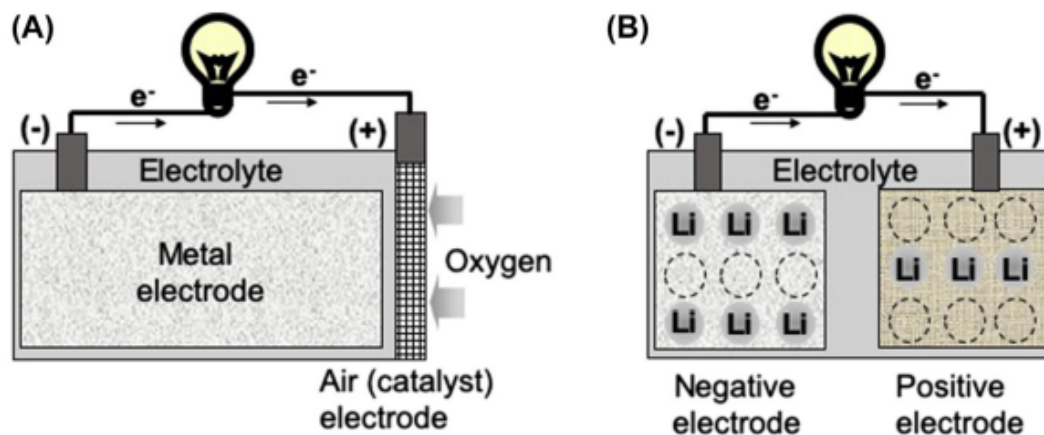


Figure 1.16 – Comparison between metal-air battery and lithium-ion battery^[38]

The metal used for the anode has strong reducing power, like lithium, zinc, sodium, and aluminium.^[39] Also, metal hydride alloys metals and organic compounds that can be used to activate the anode. We will focus more on details at the cathode during our studies.

465 In the following part, we look at the air electrode. We will quickly introduce this type of electrode and focus on two cases of oxide studied during this thesis.

The air electrode (Cathode) is a thin film where the outside oxygen is taken and reduced. The material used for the cathode is light, compact, cheap, and with large electrochemically active area.

470 In figure 1.17, one can see the air electrode in grey and the different processes occurring where there are triple-phase boundaries. The electrolyte played a significant role in the polarization and wettability of the electrode. The electrode must have be waterproof and electrolyte-proof to minimize the leaking due to the electrolyte.

475 Carbon and carbon materials are wildly used for the air electrode substrate due to the high surface area, high electrical conductivity, and controllable wettability of the carbon. The air electrode is also composed of a metal mesh added to the carbon substrate. The metal added can increase the electrical conductivity and mechanical stability. The metal mesh prevents the oxygen permeability of the electrode.^[38]

480 The metals used in acidic media are titanium, platinum and metal oxide like iridium or ruthenium. For the alkaline media, the metal used is carbon doped with metal.^[37]

Recently, transition metal oxides have taken an important part. Particularly, nickel and manganese are deeply analyzed in this PhD project.

For each electrode, we will see the mechanism in the chapter that we deal with them (chapter 2 for the manganese oxide and chapter 3 for the nickel oxide).

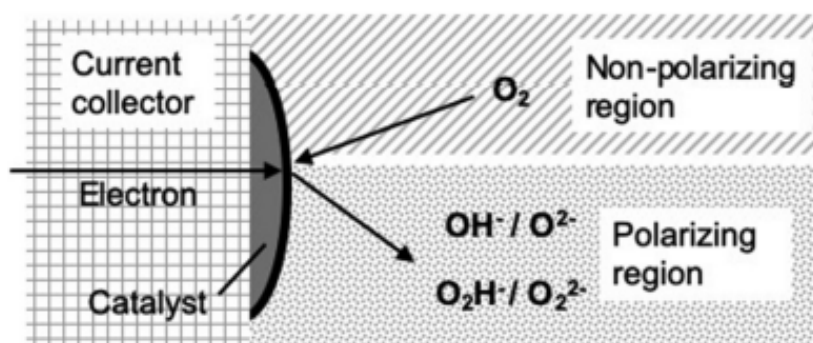


Figure 1.17 – Zoom at the air electrode and three-phase^[38]

485 In the past decade, manganese oxides have been studied as electrocatalysts for the oxygen evolution reaction (OER) and oxygen reduction reaction (ORR). They have a variety of oxides, with 30 phases with oxidation states going from Mn^{2+} to Mn^{7+} . This large variety of structures leads to various applications such as the use of λ - MnO_2 phase for the lithium-ion battery as

air electrode, ramsdellite- MnO_2 for the alkaline batteries, Mn^{3+} contains in as Hausmannite
 490 Mn_3O_4 and bixbyite $\alpha\text{-Mn}_2\text{O}_3$ can be used as precursor catalysts of the water-splitting.^[40] Figure 1.18 illustrated the variety of manganese oxides with ions of are $\text{Mn}^{(II)}$, $\text{Mn}^{(III)}$, $\text{Mn}^{(IV)}$, and O which are represented in purple, brown, black, and red spheres, respectively. These varieties of manganese oxide result from the crystallization pathways.

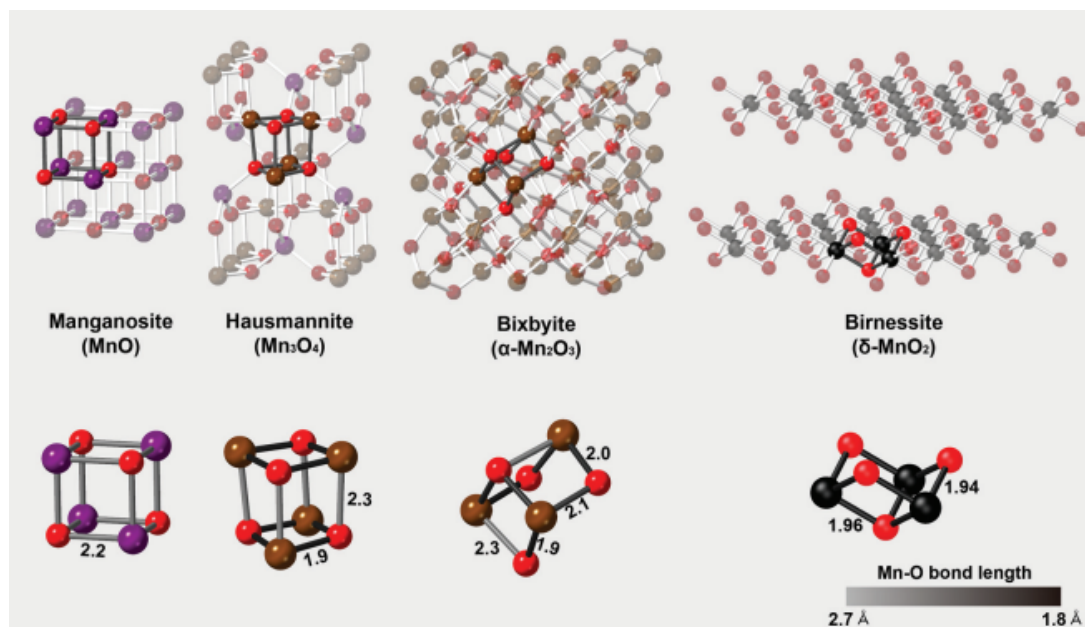


Figure 1.18 – Crystal structures various manganese oxides.^[41]

Sul and al^[40], introduced an alternative to the classic Pourbaix diagram by including the influence of size-dependent thermodynamics of metastable oxide nucleation and growth. In the classic diagram, one uses the Nernst equation to calculate E-pH boundaries between aqueous phases does not including free energy. This energy corresponds to surface energies and other forms of thermodynamic work to solid-aqueous stability analyses^[40].

The Pourbaix diagram allows us to find which materials can be used for a specific application. The diagram shows that manganese-based materials are stable in the large pH range under the redox potential window to -2 to 2 V. Not all the transition metal oxide had this behaviour and will be used only on the alkaline and neutral media. Figure 1.19 illustrates the Pourbaix diagram for Mn-O-H phases and limits for each phase.

Let's look at the $\alpha\text{-Mn}_2\text{O}_3$, which will be studied in this PhD project (Chapter 2). It is a suitable catalyst for OER and ORR due to its crystal structure and abundant defects.^[41]

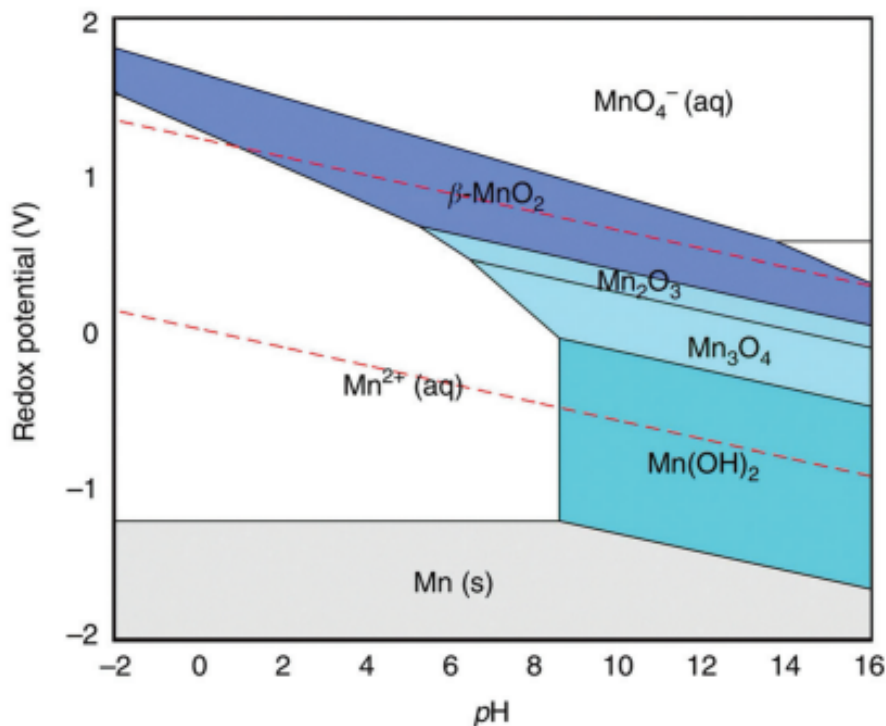


Figure 1.19 – Pourbaix diagram of Mn–O–H phases^[40]

For the nickel oxide electrode, we will focus mainly on the structural aspect of the different types of nickel oxide and how that play during the reaction at the electrode.

The nickel electrode is highly used as a positive electrode thanks to its rapid kinetic and good cycling. One can list the following nickel electrodes: Cd/Ni, Zn/Ni, Fe/Ni, H₂/Ni, O/Ni, and metal hydride/Ni. Particularly, it is interesting to analyze the phase transition occurring in the nickel electrode. These proprieties are due to the two ternary phases Ni(OH)₂ and NiOOH, during the insertion reaction between these two phases. Even if the mechanism and the thermodynamic aspect of this electrode are highly studied, many aspects are still unknown to fully understand the system. These different phases, the mechanism and thermodynamic aspect will be investigated in detail in chapter 3.

If we look at the nanostructures for the nickel electrode, one has a layer configuration. The hexagonally sheets of NiO₂ are lined in the layer where different spies can reside between each layer. The NiO₂ sheet is parallel with a hexagonal structure and O²⁻ ions between nickel. The nickel cations are in octahedral positions. The phase transition between Ni(OH)₂ and NiOOH plays an important role during the oxidation-reduction reaction. The two forms of hydroxide nickel during in the transition phase are the α -phase Ni(OH)₂ and β -phase Ni(OH)₂. They will be transforming into γ -phase NiOOH and β -phase NiOOH during the charging part of the battery. If we compare the theoretical electrochemical capacity of the two-phase of Ni(OH)₂, the α -phase, is higher than the β -phase (433 mAhg⁻¹ with an average oxidation number of 3.5 and with 289 mAhg⁻¹ for the β -phase). The α -phase Ni(OH)₂ is unstable in alkaline media

(media that we will study) and leading to a rapid transition to the β -phase (which is stable in alkane) media. The α -Ni(OH)₂ is dissolved and re-nucleated to the β -phase which participates in the charging process. When the electrode is overcharged, the β -phase Ni(OH)₂ will become γ -NiOOH. This transformation will give a larger surface area. During the discharging process, the γ -NiOOH phase is transformed into the α -Ni(OH)₂ phase as shown in figure 1.20 ([42])

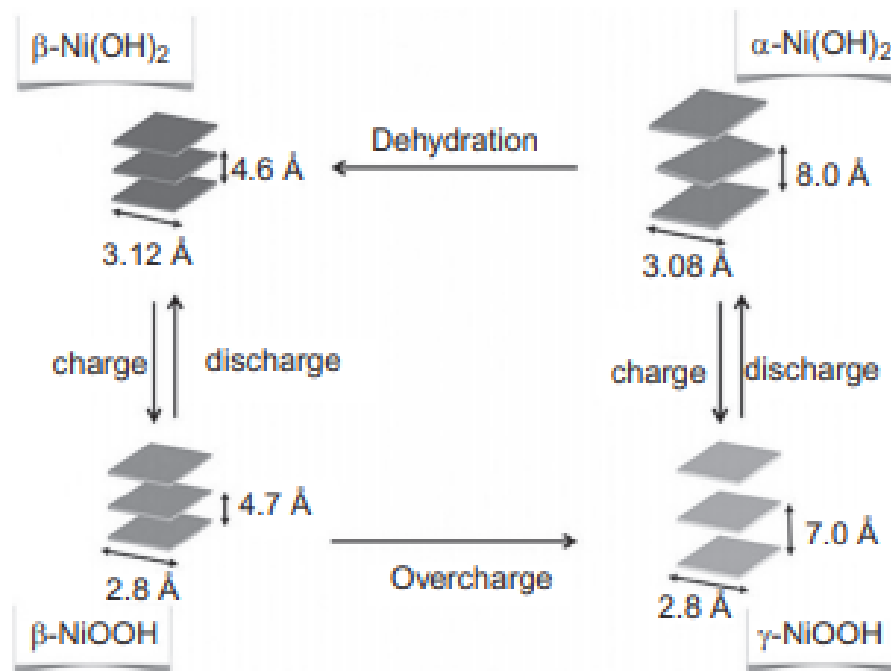


Figure 1.20 – Bode diagram of nickel hydroxides. [42]

The structure of the NiO₂ layer is formed in the edge-sharing of NiO₆ octahedra. The crystallization for both phases of Ni(OH)₂ is hexagonal symmetry with a brucite-type. The layered Ni(OH)₂ are stacked along the x-axis.

When the redox state of Ni(OH)₂ and NiOOH is compared, one observes that NiOOH is more oxidized. However, both redox states are semiconductors. In the nickel-metal hydride battery system, the negative electrode is a conductor. Also, one observes some changes in the electrode during the charging/discharging processes where the mechanical properties are modified, leading to increased electrical resistance and decreased capacity.

These electrode behaviours have a significant impact on the mechanism of the oxygen evolution reaction (OER):



where the electrode preparation, the morphology, and the particle size play a crucial role. The
545 mechanism and kinetic properties will be investigated deeply in chapters 3 and 4.

1.1.3 Supercapattery (SCAP)

Herein, the supercapattery system which belongs to EES technologies devices is described. It is well known that a battery system is able to store/deliver high energy density, but it has a low power density. This low power density is due to the slow kinetics involving Faradaic reactions and phase transition during the charge storage. On the other hand, the supercapacitor
550 has a high-power density thanks to the adsorption/desorption or surface-based Faradaic reactions, but the energy density is low. To improve the performance of EESD, since the mid-90 new topic of research was carried out to develop a hybrid electrochemical energy storage device combining the battery and supercapacitor properties. This type of hybrid should be able
555 not only to deliver high energy density and high-power density a high cycle life. This hybrid has a larger operating potential window due to the combination of the potential window of the capacitive and battery electrodes.^[43] In 1995, Varakin et al reported the first hybrid device. These authors combined a nickel oxide-based battery electrode with a carbon fiber capacitive electrode in a single device by combining two types of storage mechanisms (electrical double
560 layer and faradaic reactions).^[44] The device's performance was improved by 8-10 times. This type of hybrid device is obtained by combining different types of electrodes. One possibility is a combination of one capacitive electrode (typical of the electrical double layer) with another kind of capacitive electrode (typical of pseudocapacitive). The second possible combination is one battery electrode with a capacitive electrode. To characterize this second
565 combination, a new name was proposed as "Supercapattery". "Supercapa" is for the supercapacitor and "ttery" for the battery. The advantage of supercapattery is its high performance and longer cycle life thanks to the combination of capacitive and battery electrode materials.

1.21

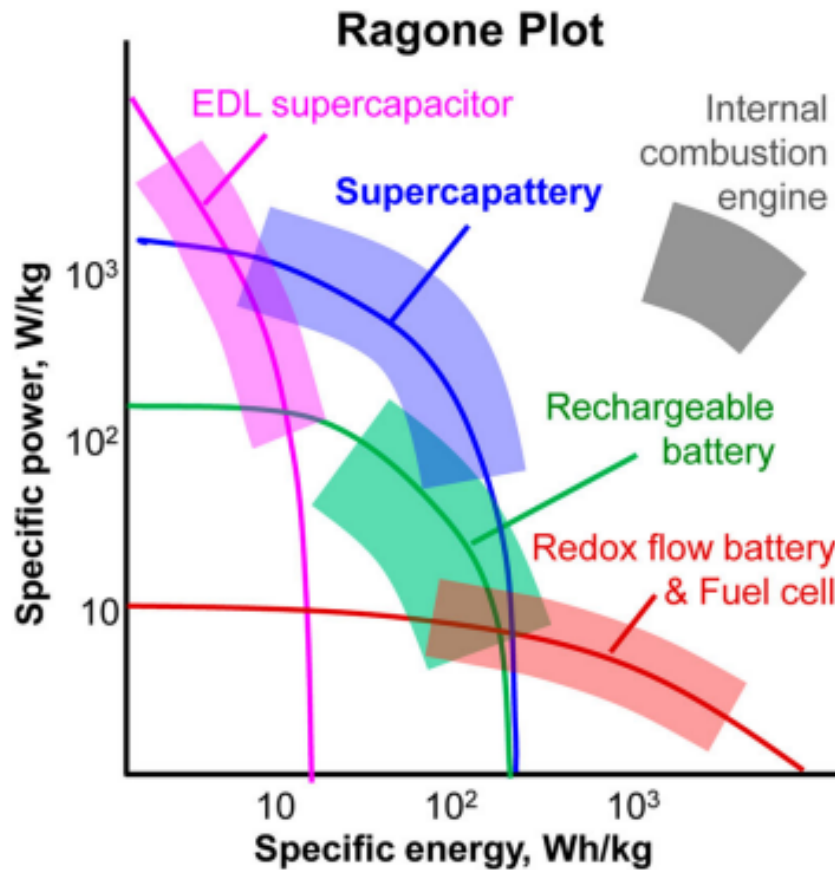


Figure 1.21 – Ragone plot with position of supercapattery relative to other energy technologies^[9]

Furthermore, this type of hybrid device offers a large flexibility in the choice of the electrode, we can play with the materials. We can look at the composition of electrode materials level or device level of the system. At the electrode material level, it is possible to combine capacitive and battery-grade materials to obtain a composite electrode. For example, one can combine an activated carbon known as a capacitive material and nickel oxide (NiOx), which has capacitive and Faradaic properties. Then, one can expect a high specific capacity and high-power density. In order to improve the performance of NiOx electrode, the design and nanostructure of the material can be optimized. At the device level of the system, we have to take a battery electrode and a capacitive electrode. This approach seems simple, but it is very complicated because we must match the performance of each electrode and, it is a very delicate task. A few case studies were very successfully made.^[45,46]

We have a capacitive and faradaic charge storage mechanism. Frequently, we use metal oxide to make supercabattery.^[45]

Table 1.1 shows that supercapattery family includes supercapacitor, hybrid, supercabattery, and battery.

585 a) **Charge storage of the supercapattery**

In the following part, we will look at the charge storage mechanism, which depends upon the electrode material. In the EESD, there are three kinds of electrode materials. The first type is the capacitive material, as shown in EDLC. There is no chemical reaction for this type of electrode; only a physical phenomenon (adsorption) occurs. The charge storage is due to the electrostatic attraction of charge between the electrode and electrolyte interface (Figure 1.22 (A)). The second type of material is pseudocapacitive material, in which the charge storage results from a concomitant interfacial faradaic reaction and physical adsorption (Figure 1.22 (B)). The kinetics of this type of system is rapid due to the faradaic reactions that take place at the surface of the electrode. The third and last type of electrode material is the battery-grade material. There are also Faradaic reactions associated with charge storage. Still, the main difference with the second electrode material is that the Faradaic reaction takes place at the surface and deep inside of the electrode material (Figure 1.22 (C)). This last action induces an alteration of the crystal structure of the material.

In figure 1.22 (C), we have a charge storage Supercapattery. We can see the two types of charge storage: electrostatically and electrochemically due to the electrode material used.

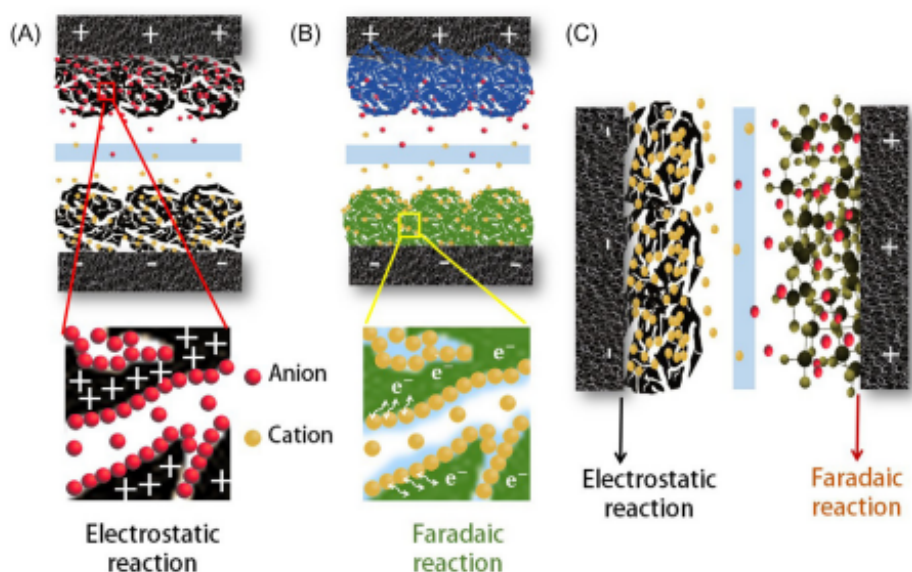


Figure 1.22 – Schematic diagram of charge storage for ELDC (A), pseudocapacitor (B), and Supercapattery (C)^[11]

In Figure 1.23, one can see the typical cyclic voltammogram (CV) in a three-electrode cell response to different EES for capacitive (EDL storage pseudocapacitance) or battery-like behaviours. Figure 1.23 (A) shows the typical response of battery material where the current peaks reflect the electron transfer (redox reaction). Figure 1.23 (B) indicates that we have the response of a supercapacitor where the CV shape is a rectangle. We observe a partial rectangle shape CV for the pseudocapacitive materials due to the faradaic and capacitive responses at the interface between the electrode and the electrolyte. In Figures, 1.23 (C) and (D), the responses of the supercapattery are reported, which is a mix of two types of behaviour seen before (battery and supercapacitor). In two CVs, one has localized and delocalized electrons in both cases. Figure 1.23 (C) shows a behaviour close to a battery; we have a supercabattery. On the other hand, in Figure 1.23 (D), we have a behaviour closer to a supercapacitor, we have a supercapattery. The difference in response is due to the electrode used to elaborate the device.^[47]

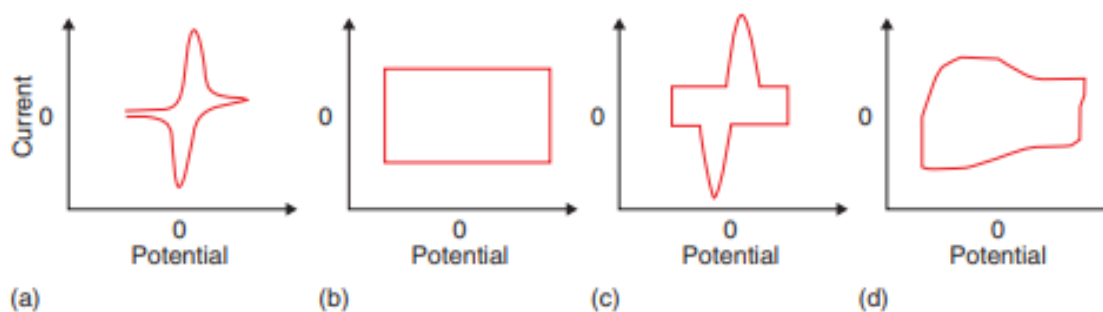


Figure 1.23 – Cyclic voltammograms of a battery (A), capacitor (B), a Supercabattery (C), and Supercapattery (D)^[47]

We can also analyze the difference between these three devices (two-electrode configuration) during the charging/discharging cycle. In Figure 1.24, we can see the different devices' cyclic voltammetry and galvanostatic charging/discharging responses. The important information underlined by this figure is that three different devices can store or release charge Q within the voltage range $U = U_{\max} - U_{\min}$ (delimited by the potential window). We can connect the capacitance, C , to the Q as seen in equation (1.1). If we look at U_{\min} for the supercapacitor (figure 1.24 (b)), it decreases to zero. Still, it is not the case for the battery due to the irreversibility of the battery system (figure 1.24 (a)). If we look at the GCV supercapacitor (figure 1.24 (b)), we have an ideal polarization and non-ideal for the battery (figure 1.24 (a)). For the case of the supercapattery (figure 1.24 (c)), we have both characterizations of battery and supercapacitor.^[48]

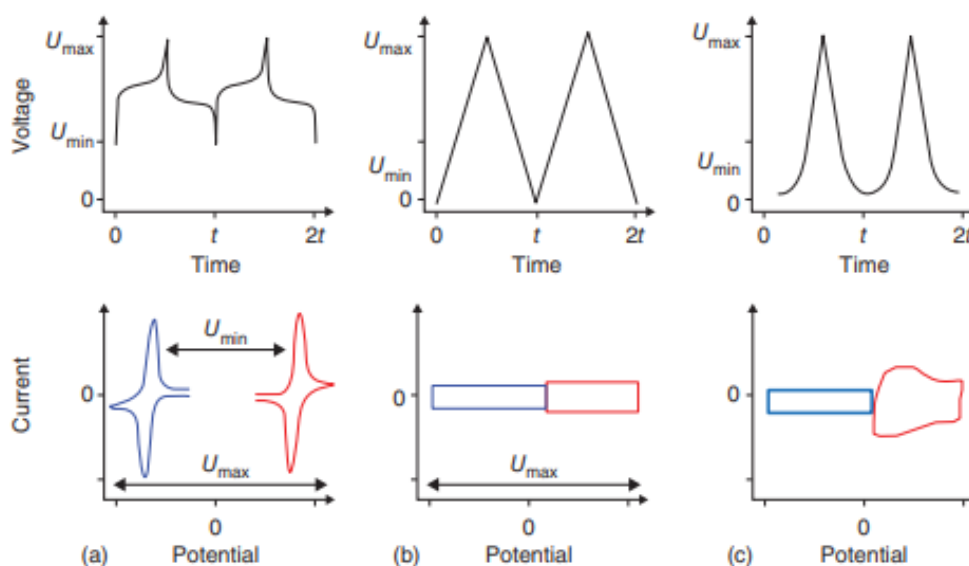


Figure 1.24 – Galvanostatic charge-discharge (GCD) and the current response versus potential from cyclic voltammograms of (a) a rechargeable battery, (b) a supercapacitor, and (c) a supercapattery.^[48]

In figure 1.25, we can find the typical response of a supercabattery, we have a different response compared to the supercapattery (figure 1.24 (c)). For the supercabattery, we have a battery material or electrode that is more important than the supercapacitor. For the supercabattery, if we look at the Q/U ratio, we have a high value, and the energy storage capacity is like a battery.^[9]

In the next section, we will see more details on supercabattery. In chapter 5, we will look closer at this type of system. Supercabattery is an application of supercapattery materials. Supercabatteries are mainly studied for commercial applications such as electric vehicles, hybrid electric drives for trucks, and electric rail vehicles.^[49,50]

We will just introduce the supercabattery in the following part.

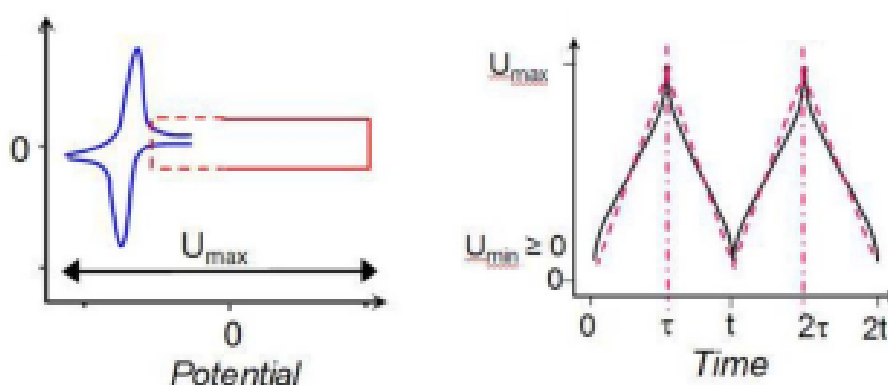


Figure 1.25 – Galvanostatic charge–discharge (GCD) and the current response versus potential from cyclic voltammograms of a supercabattery^[51]

b) Focus on the Supercabattery

Supercabattery is one kind of supercapattery. This system is an emerging energy storage device because it can supply high power and energy by combining battery proprieties and supercapacitor proprieties. To elaborate supercabattery, we use a carbon-based electrode for double-layer capacitor-type electrode and a redox-active transition metal oxides (TMOs) for the battery type electrode. Metal oxides (MO) and metal-organic frameworks (MOFs) are highly investigated due to their fast-redox kinetics and their high energy storage capacity.^[52]

The choice of transition metal oxides (TMOs) is due to their properties, such as a good surface that improves electron transfer kinetics. They are stable, less toxic, and cheaper than metal platinum oxide or iridium oxide. Also, they have high adsorption capacity, which makes them a good candidate to use as battery-electrode like in supercabattery.^[53]

In figure 1.26, we have the schema how explain the supercabattery. We used the NiOx electrode as the cathode and the carbon cloth with anthraquinone as the anode. The electrolyte used is KOH.

650 We added anthraquinone to the carbon cloth to increase the chemical response. NiO_x electrode as the battery-electrode and modified carbon as EDLC-electrode.

We look at chapter 5, the working process and the reaction imply in the system. In our investigations, we also studied the influence of electrolyte concentration and investigated this influence.

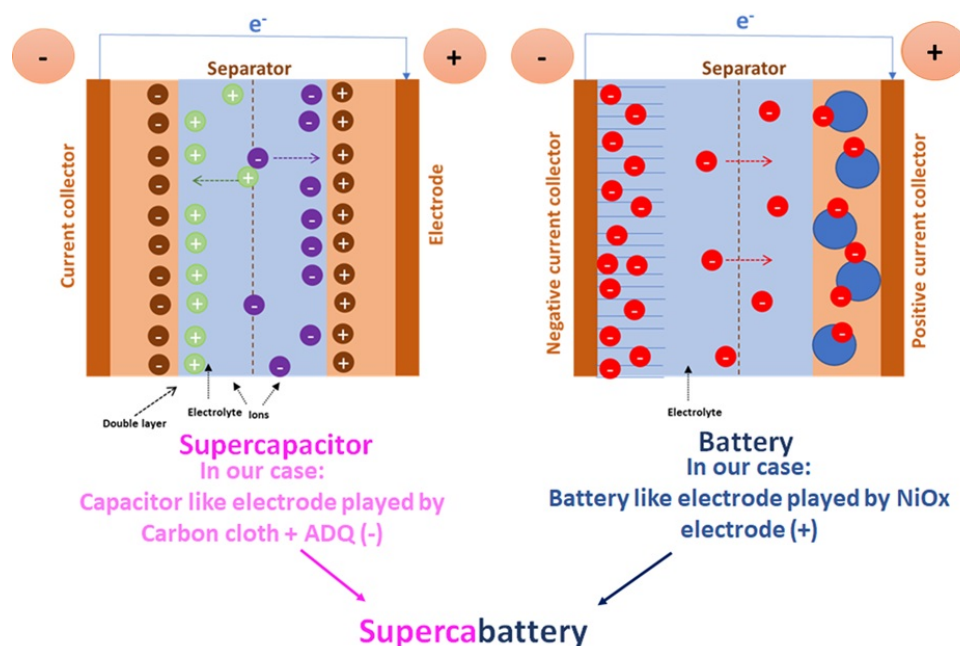


Figure 1.26 – Schema of supercapacitor and battery to explain our supercabattery made

655 1.2 Energy production

1.2.1 Chemical Energy conversion by Fuel Cell

In the next part, we will focus on the fuel cell. This device allows the use of the H₂ production for energy production. In this conversion system, hydrogen is useful for fuel cells and synthesising natural gas, such as methane, thanks to carbon dioxide. This type of device can be a significant actor in the development of green technology. We can produce large-scale energy (100 GWh) without pollution. But this system model has a few flaws, like the low energy conversion efficiency (between 40% and 50%) and needs large found to develop it. Meanwhile, the fuel cell's chemical energy conversion device has been highly studied in the past decade.^[2] The first fuel cell was made in 1802 by Sir Humphrey Davy, who introduced the concept of fuel cells and the chemical reactions that take place. But he did not completely understand the working process of the carbon cell (cathode). It was in 1839 that Sir William Grove made the first hydrogen-oxygen cell introduced as the "Gaseous Voltaic Battery". He demonstrated that

660

665

the reaction between the hydrogen and oxygen present in the cell carried out the production of water and electric current. One of his articles in 1842 highlighted the inverse phenomenon and described it as the "Decomposition of water through its composition" [54].

The fuel cell can be used in various fields like the automobile industry, the defense industry, or the remote area power supply. The critical element is hydrogen. The use of hydrogen fuel cells is a solution to sustainable energy. It became a real deal in the economic area, and we call it the "hydrogen economy." It is an economic area that highlights the link between sustainable energy technology and sustainable energy savings brought by the hydrogen storage system. [55]

We can classify the fuel cell based on the electrolyte or the temperature. In Figure 1.27, we have the different families of the fuel cell.

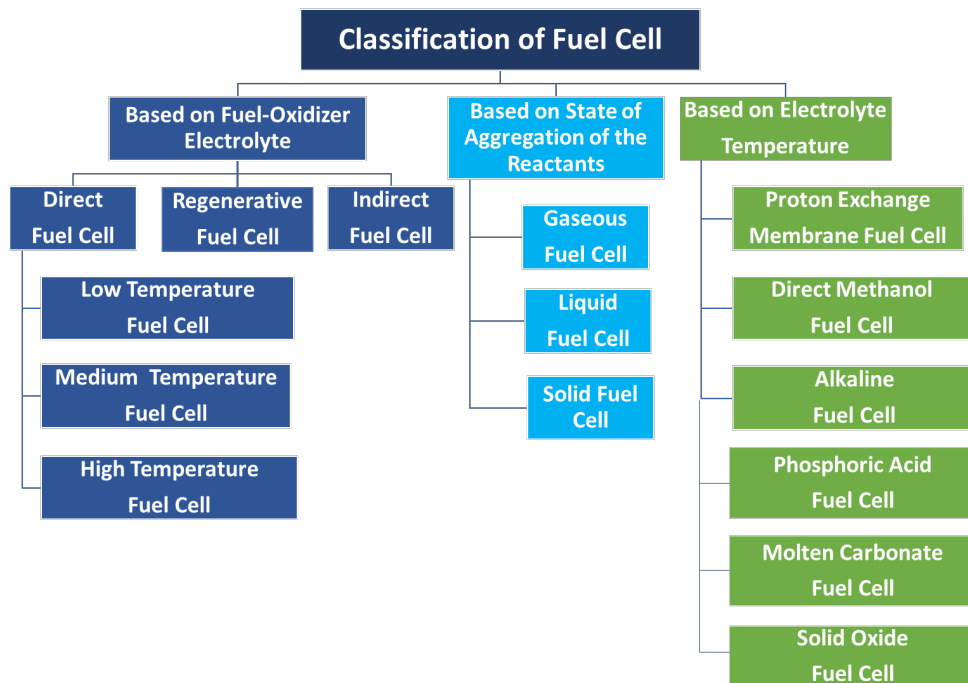


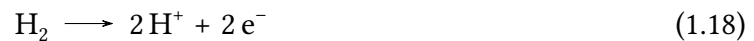
Figure 1.27 – Classification of the fuel cell system [56]

The fuel cell is composed of two electrodes which are an anode and a cathode. Both electrodes are separated by an electrolyte in solid or liquid form. The electrolyte will transport the ions from the electrode to achieve the electrochemical cycle system. These electrons will generate electricity and water as the by-product at electrodes. The amount of electric current produced will rely on the chemical reaction activity and the amount of fuel supplied. The anode is the negative electrode, and the cathode is the positive electrode.^[56,57]

The operation of the fuel cell also is dependent on temperature. When the temperature is decreasing, the rate of the chemical reaction produced by fuel and catalyst decreases. And when the temperature is high, the rate of the chemical reaction will increase but decrease the life of the components of the device.

To understand the mechanism of fuel cell, we look at the working process of one type of the fuel cell: Proton exchange membrane fuel cell (PEMFC) illustrate by Figure 1.28. PEMFC is composed of two electrodes, an anode and a cathode supplied with hydrogen and oxygen, respectively. The two electrodes are separated by an electrolyte. The first step is when the hydrogen is introduced into the system and the catalyst present in the anode will oxidize the hydrogen into proton and electrons. After that, the electrolyte (here the membrane is a proton exchange membrane) conducts the proton to cathode. The electrons will be conducted by the plates and will generate current. Finally, at the cathode, we will have the reduction of oxygen to water and heat.^[58] We can write the following equations how to take in the fuel cell:

At the anode:



At the cathode:



In the cell:



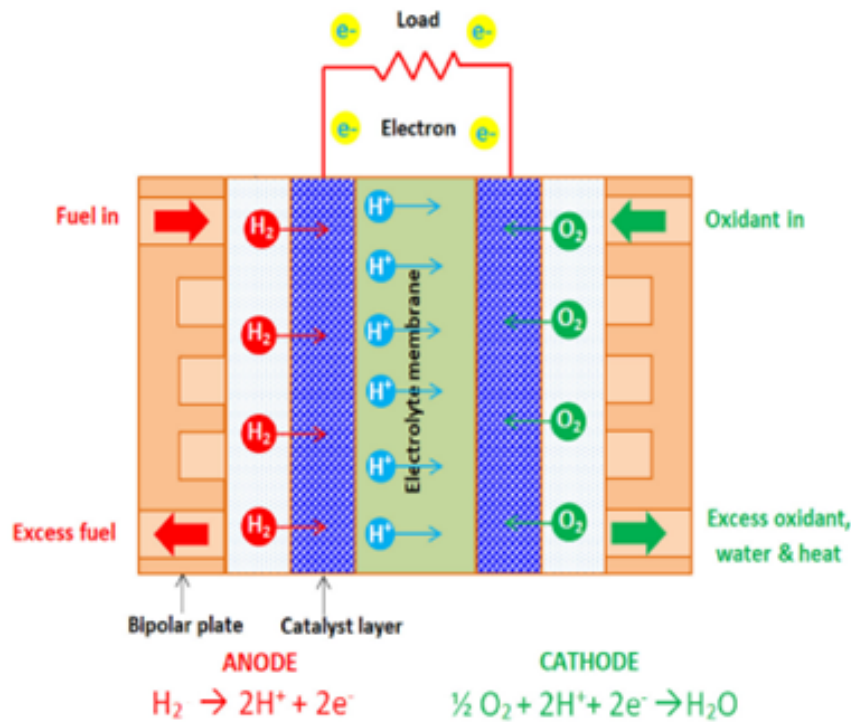


Figure 1.28 – Simplified Proton exchange membrane fuel cell (PEMFC) mechanism^[59]

705 The two-reactions used in the fuel cell are hydrogen oxidation reaction (at the anode) and oxygen reduction reaction (at the cathode). We will look forward to these reactions the few sections.

Oxygen and hydrogen are key elements for the energy storage (electrolyzer) and the energy production (fuel cells).

710 In figure 1.29; we can see the hydrogen and oxygen cycle for energy storage and energy conversion.

We can differentiate energy storage and energy production. In the case of the energy storage, we can look at water splitting. Splitting water electrochemically will take place at the two-half-cell present in the electrolyzers. We will have the water reduction how conduct to hydrogen (at the negative electrode). And will have the water oxidation how conduct to the oxygen (at the positive electrode). In figure 1.29, we have red arrows corresponding to the energy storage with the reactions associated. For the fuel cell, we have an energy production. We had seen in the previous part, the working process of it. In figure 1.29, the blue arrows corresponding to the energy production.^[60]

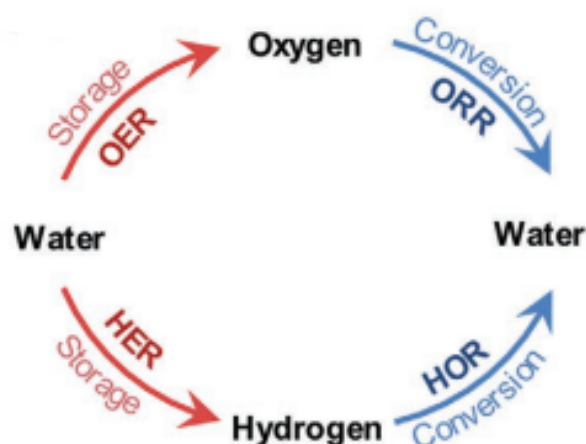
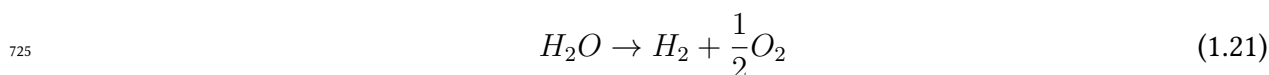


Figure 1.29 – Hydrogen and oxygen cycle for energy storage and energy conversion.^[60]

720 We can also introduce the water splitting linked to the reaction that we see in this section, such as hydrogen evolution reaction (HER) and oxygen evolution reaction (OER).

1.2.2 Chemical Energy storage by water splitting

The water-splitting is the hydrogen evolution reaction (HER) and the oxygen evolution reaction (OER). The water-splitting reaction is given by the following equation :



This reaction needs a minimum Gibbs free energy (ΔG) of $237.2 \text{ kJ mol}^{-1}$ and a standard potential of (ΔE) of 1.23 V . Theoretically, if we apply this voltage, we have OER and HER at each electrode. However, we do not have it for the practice because the OER and HER are difficult. To solve that problem, we have to apply overpotential to improve the reaction rate and cross the energy needed for the system. The overpotential is vital because it can cancel the intrinsic activation of the cathode ($\eta_{cathode}$) and anode (η_{anode}) materials and other resistances present like the solution's internal resistance.

The potential applied will be given by this equation :

$$E_{app} = 1.23 + \eta_{cathode} + \eta_{anode} \quad (1.22)$$

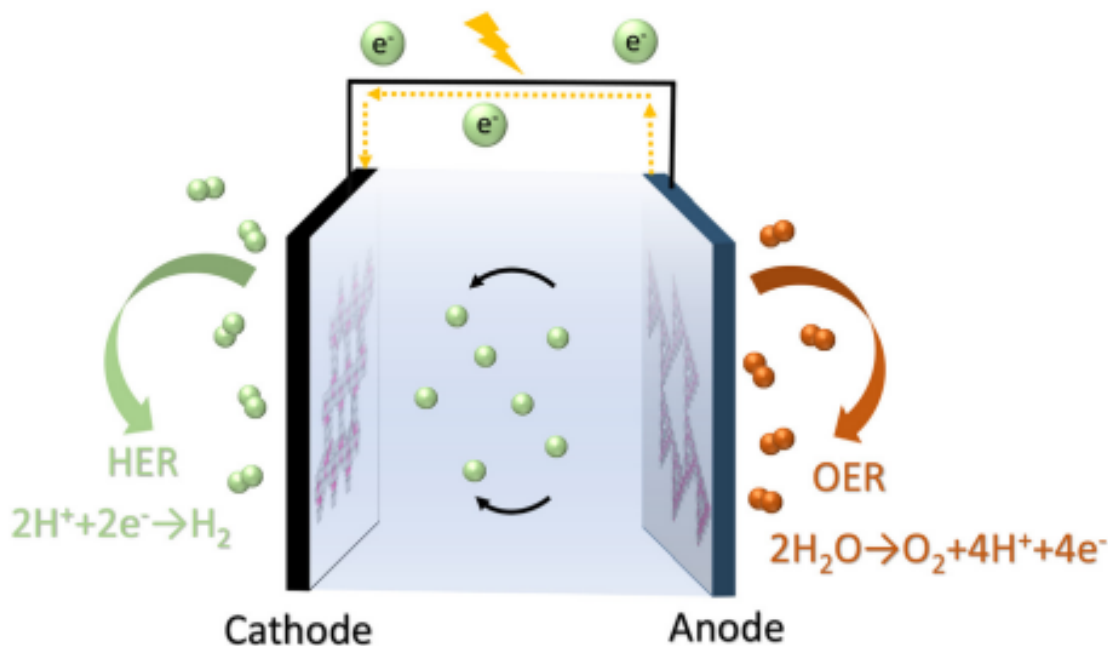


Figure 1.30 – Scheme of the water electrolysis process^[61]

735 To optimize the water-spilling, we can improve the HER and OER at each electrode by using catalysts. Precious metals such as Pt, Ir, and Ru are the best catalysts. However, their expensive cost prohibits their large-scale application. The development of high-performance and low-cost alternatives has been highly studied to resolve that issue in the past decade. One of the key solutions are metal oxides.

740 We will look at the alkaline water electrolyzers, the one we will study in chapter 3. And we compare it to acidic PEM water electrolyzers.

The emergence of the commercialization of water electrolysis in alkaline media for large-scale industrial applications highlights the use of the non-precious catalyst.^[62] Precious metal is used for acidic PEM water electrolysis and for small-scale applications.^[63] In Table 1.2, we can compare the operation parameters, advantages and disadvantages for alkaline water electrolyzers and acidic PEM water electrolyzers. We look closer to Table 1.2, we can see that the alkaline electrolyzers use a solution 20–40 wt. % KOH as the electrolyte. And the catalyst used is Ni-based transition metal catalysts used as the working electrodes.^[64] Thanks to the high stability of Ni-based catalysts in alkaline media, we will have lifetime of the system that will excess of 20 years.^[65]

755 The main problem of alkaline water electrolysis is the limited current density due to the increased Ohmic loss. In the other hand, a possible decrease of electroactive area can be observed due to the formation of gas bubbles on the electrode surface. This issue is always present in liquid electrolytes.^[63]

| Parameter | Alkaline water electrolysis | PEM water electrolysis |
|--|--|--|
| Catalysis | Ni-based catalysts | Pt-, Ru-, Ir-based catalysts |
| Electrolytes | 20–40 wt% KOH | Nafion membrane |
| Cell temperature [°C] | 50–80 | 50–80 |
| Cell voltage [V] | 1.8–2.4 | 1.8–2.2 |
| Current density [mA cm ⁻²] | 200–400 | 600–2000 |
| Voltage efficiency [%] | 60–80 | 60–80 |
| System lifetime [y] | 20–30 | 10–20 |
| Advantages | Non-noble metal catalysts Long-term stability Low capital cost Mature commercialization | High current density High-purity hydrogen Compact device |
| Disadvantages | Low current density Corrosive electrolyte Noncompact device | Noble metal catalysts Poor durability High capital cost Initial commercialization |

Table 1.2 – Comparisons of alkaline water electrolyzers and acidic PEM water electrolyzers^[63]

If we look at the PEM electrolyzer, we have a solid electrolyte using the Nafion membrane and the catalysts are coated to the membrane.^[66] This electrolyser delivers a very high current density of above 1000 mA/cm² with high voltage efficiency.

760 The main problem of the PEM electrolyzers is using noble metals, such as Pt, Ru, and Ir, as catalysts. Studies are carried out to find an alternative using cheap and sustainable transition-metal-based catalysts. However the problem related to the corrosion should be resolved.^[63]

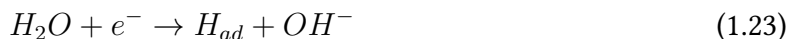
765 The International Renewable Energy Agency (IRENA) report compares the total capital expenditure of the PEM electrolysis and alkaline electrolysis. In 2017, the cost included the power supply and installation cost was around €750 per kW for alkaline electrolysis and around €1200 per kW for PEM electrolysis. We can see that we have a lower cost of the alkaline electrolysis. They estimate that we will have decrease by 2025, with cost around € 480 per kW for alkaline electrolysis and vs € 700 per kW for PEM electrolysis.^[67]

770 The following part will examine the HER mechanisms and the electrocatalyst used for these reactions.^[61]

a) Hydrogen evolution reaction: HER

We will look at the mechanism of HER just for the alkaline media. The mechanism of HER can follow one of three pathways where H_{ad} , hydroxyl adsorption (OH_{ad}) and water dissociation.

Volmer:



Heyrovsky:



Tafel:



Figure 1.31 shows the different pathways for HER.

The media used influences the HER. For example, if the concentration of hydrogen ions is low, the reaction rate will also be low. The dissociation of water in the alkaline HER brings hydrogen ions to the system. That phenomenon will increase water adsorption at the active site and improve HER performance.^[61]

Now, we look closer at the mechanism of HER. The Volmer step is the first step. It corresponds to the discharge reaction. The formation of the H_2 can follow two possible pathways: Heyrovsky and Tafel mechanisms. In the case of the Heyrovsky mechanism, we have a transfer of a second electron to an adsorbed hydrogen atom. This transfer results in the formation of protons with H_2 . For the Tafel mechanism, two adsorbed hydrogen atoms on the surface of the electrode conduct the formation of H_2 . One catalyst that uses this mechanism is the Platinum which is the best catalyst for HER. Figure 1.31 give use of all the mechanisms possible.

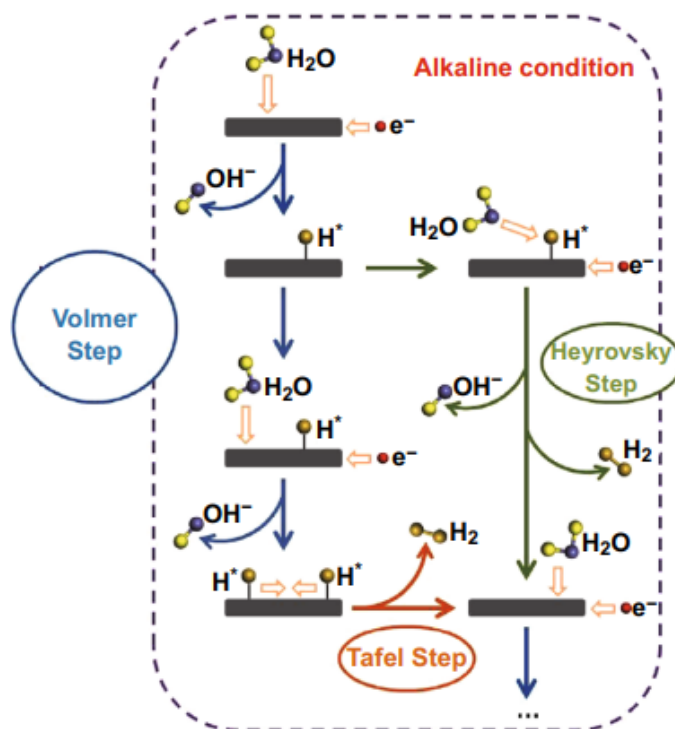


Figure 1.31 – 3 pathways for hydrogen evolution reaction under alkaline conditions^[68]

These three pathways are linked to the Tafel slopes, which give three limiting cases. In the table 1.3, linked to each mechanism to the slope value and reactions corresponding :

| Mechanism | Reaction observed | slope value |
|-----------|---|--|
| Tafel | - Fast discharge reaction - Formation of H_2 | $\frac{(2.3RT)}{2F} = 29 \text{ mV.dec}^{-1}$ |
| Heyrovsky | - Fast discharge reaction and H_2 | $\frac{(4.6RT)}{3F} = 38 \text{ mV.dec}^{-1}$ |
| Volmer | - Slow reaction - Formation combination reaction or the ion + atom reaction | $\frac{(2.3RT)}{2F} = 116 \text{ mV.dec}^{-1}$ |

Table 1.3 – Tafel mechanism and slope

The Tafel slope is linked to the overpotential and current density j and, j_0 is the exchange current density.

805 We can define overpotential by this equation: $\eta: \eta = b \log\left(\frac{j}{j_0}\right)$ with b is the Tafel slope.^[69]

In order to understand and estimate the activity of HER to catalytic materials, one can use DFT simulation (Density Functional theory). Thanks to the DFT calculations, we can link the activity of various HER catalysts to catalyst materials used like precious metals, transition metals, alloys, and eventually metal-free materials.^[70] DFT calculations highlighted that the reaction kinetics of the HER were connected by the Gibbs free energy of hydrogen adsorption ΔG_{H^*} .^[71] Depending on the hydrogen adsorption and ΔG_{H^*} , we can find the limited step. If $\Delta G_{H^*} > 0$, hydrogen adsorption is too weak, and the Volmer step is the limited step. If $\Delta G_{H^*} < 0$, that translate adsorption is too strong, so the Heyrovsky or Tafel step is the limited step. In this case, it is the desorption step.

815 Figure 1.32, which shows the volcano plot for HER, allows us to find the best catalyst for HER. When Gibbs free energy of hydrogen adsorption ΔG_{H^*} is close to 0 eV with the higher j_0 , that means we have the best catalyst for HER.^[69]

The Sabatier principle dictated that the strength of interaction between catalysts and reactive plays a role. If the interaction is too weak, we will have a few intermediates bind to the catalyst's surface and slow the reaction. If it is too strong, the reaction fails to dissociate. 820 The reaction will be stopped due to blocking the active sites. The Sabatier principle shows that under the ideal conditions, ΔG_{H^*} should be zero, and HER will be the highest HER j_0 .^[72] The Sabatier principle connected the experimentally measured activity (j_0) with ΔG_{H^*} and introduced the volcano plot.

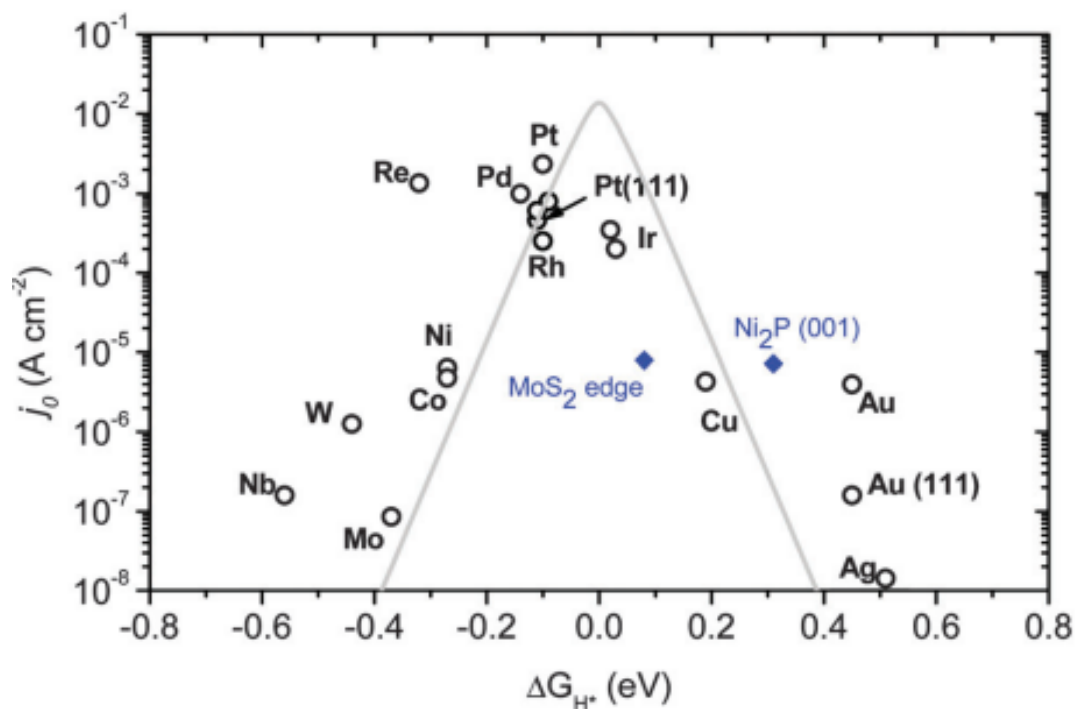
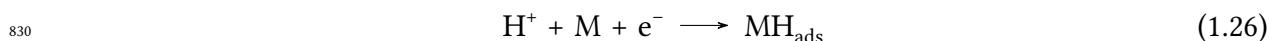
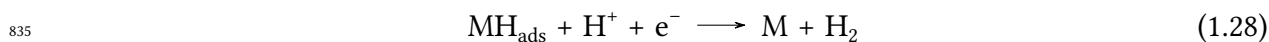


Figure 1.32 – A volcano plot of hydrogen evolution reaction^[73]

We can also look at the mechanism of HER in acidic media. Like in the alkaline media seen previously, in the acidic media, HER is divided into three-step. In both media, the Volmer reaction is the same. This step refers to electrochemical hydrogen adsorption as :



The second reaction possible is the Heyrovsky reaction which refers to the electrochemical desorption step given by the equation (1.28):



Moreover, the other reaction possible after the Volmer reaction is the Tafel reaction given by the equation (1.29):



840 The Tafel slope is the same as seen for the alkaline media, and we can go back to table 1.3 to see the value corresponding for each mechanism observed^[68]. Figure 1.33 gives us all the possible mechanisms.

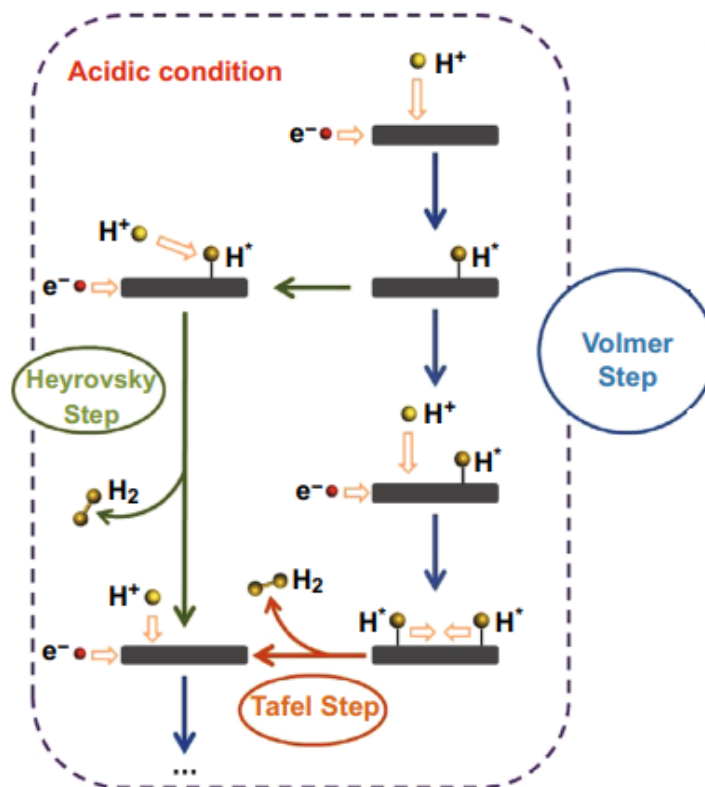


Figure 1.33 – 3 pathways for hydrogen evolution reaction under acidic conditions^[68]

The nature of the electrode used plays a role in the HER kinetics. According to the Volcano plot, the best catalyst is platinum, which will give the fastest electrocatalytic processes. The kinetic can also depend on the nature of the electrolyte or the crystalline nature and orientation of the electrode.^[74]

845

b) Oxygen evolution reaction OER

OER is highly studied in catalyzing in the past decade because of the complexity of the mechanism and the kinetic multistep.^[75] The kinetics of OER take into account the overpotential, η , j_0 , and Tafel slope to estimate their influence on the OER's mechanisms. To look at the performance of different catalysts, we take the overpotential η at the current density of 10 $mA \cdot cm^{-2}$.

850

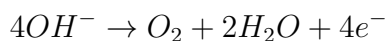
Tafel slope is an important parameter in understanding the system's kinetics and mechanisms. For example, if we have a smaller Tafel slope highlighting current density, we increase quickly and smaller overpotential η . We will have a faster reaction rate constant and a good kinetic. The Tafel slope is also useful to supply information about the mechanism by looking at the rate-determining step (RDS).^[76]

855

OER can be worked in acidic media and alkaline media. In our case, we look only at the alkaline media.

The global equilibrium for alkaline media is the following:

860



However, the mechanism can follow different pathways shown in figure 1.34. Furthermore, table 1.4 shows all the mechanisms possible for the OER in alkaline media. Table 1.4 shows us that OER comports four mechanisms possible in alkaline media depending on number exchange.

Table 2 The possible OER mechanisms in basic media^a

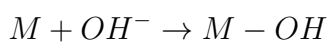
| Mechanism I | Mechanism II |
|---|--|
| 1. $2OH^- \rightarrow 2OH + 2e^-$ | 1. $2OH^- \rightarrow 2OH + 2e^-$ |
| 2. $2OH + 2OH^- \rightarrow 2O^- + 2H_2O$ | 2. $2OH + 2OH^- \rightarrow 2O^- + 2H_2O$ |
| 3. $2O^- \rightarrow 2O + 2e^-$ | 3. $2O^- + 2MO_x \rightarrow 2MO_{x+1} + 2e^-$ |
| 4. $2O \rightarrow O_2$ | 4. $2MO_{x+1} \rightarrow 2MO_x + O_2$ |
| Mechanism III | Mechanism IV |
| 1. $4OH^- + M \rightarrow 4M - OH + 4e^-$ | 1. $2OH^- \rightarrow 2OH + 2e^-$ |
| 2. $4M - OH \rightarrow 2MO + 2M + 2H_2O$ | 2. $2OH + 2OH^- \rightarrow 2H_2O_2^-$ |
| 3. $2MO \rightarrow 2M + O_2$ | 3. $2H_2O_2^- \rightarrow O_2^- + 2H_2O$ |
| | 4. $2O_2^- \rightarrow O_2 + 2e^-$ |

^a *M denotes the electrode surface.

Table 1.4 – Possible mechanisms for oxygen evolution reaction in alkaline media^[77]

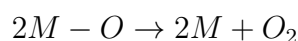
865

To understand the mechanism, we look at the figure 1.34, which brings us a simplified version of the mechanisms in alkaline media. The simplified mechanisms possible for the OER are:

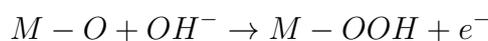


870

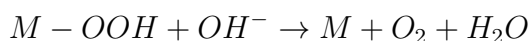
And can evolve in two pathways possible:



or



875



The intermediates species can be noted with * such as OH^* , OOH^* and O^* . Figure 1.34 highlights that we can have two pathways. The first one is the combination of two O^* to give O_2 . And the second one is the formation of the OOH^* intermediate. In two pathways, we can see that the bonding with the other intermediates is important ($\text{M}-\text{OH}$, $\text{M}-\text{O}$, and $\text{M}-\text{OOH}$). We can also take information on OER mechanisms thanks to the measured Tafel slope and, more precisely, the electron transfer coefficient (α).^[76]

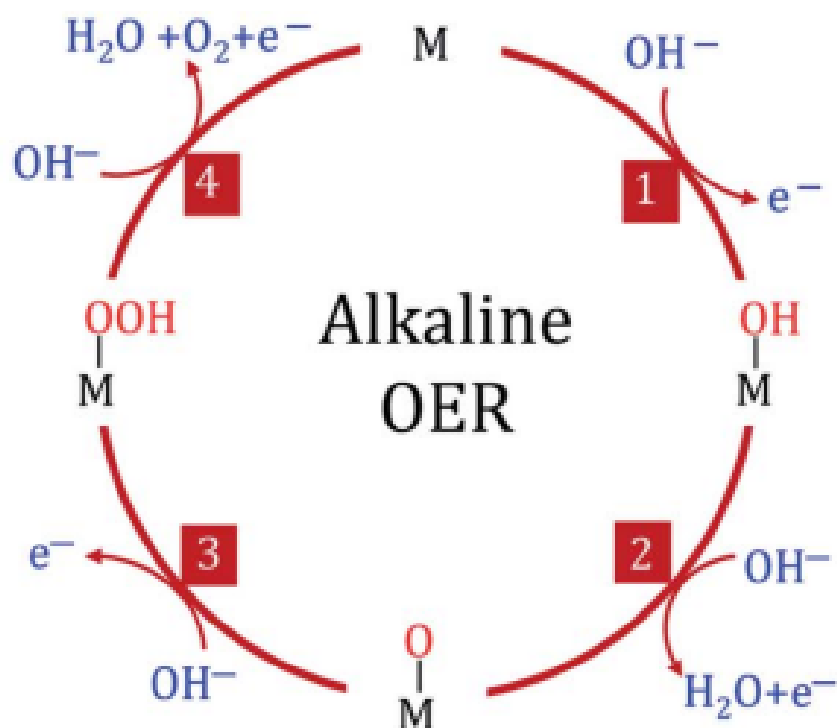


Figure 1.34 – Simplified oxygen evolution reaction mechanisms pathways in alkaline media^[78]

Density functional theory (DFT) calculations supply can provide information on the mechanism like what we have seen to HER. Nørskov et al.^[79] investigated OER kinetics for metal (hydro)oxide surfaces. The OER overpotential (η) and adsorption energy are important parameters in DFT calculation. To find the determining elementary step, we must look at the difference in the adsorption energy between two intermediates ($\Delta G_{\text{O}^*} - \Delta G_{\text{OH}^*}$). This information allows us to make energy diagrams to find thermodynamically rate-determining steps.^[78]

The difference in the adsorption energy between two intermediates and OER overpotential (η) are two parameters used to build the volcano plot. Figure 1.35. This information allows us to construct the volcano plot to find the best catalyst. The Sabatier principle can also explain

it. If the strength of interaction between catalysts and reactive is too strong (it can block H₂O desorption and active site oxygen adsorption) or too weak (it can limit the electron or proton transfer to the electrode).

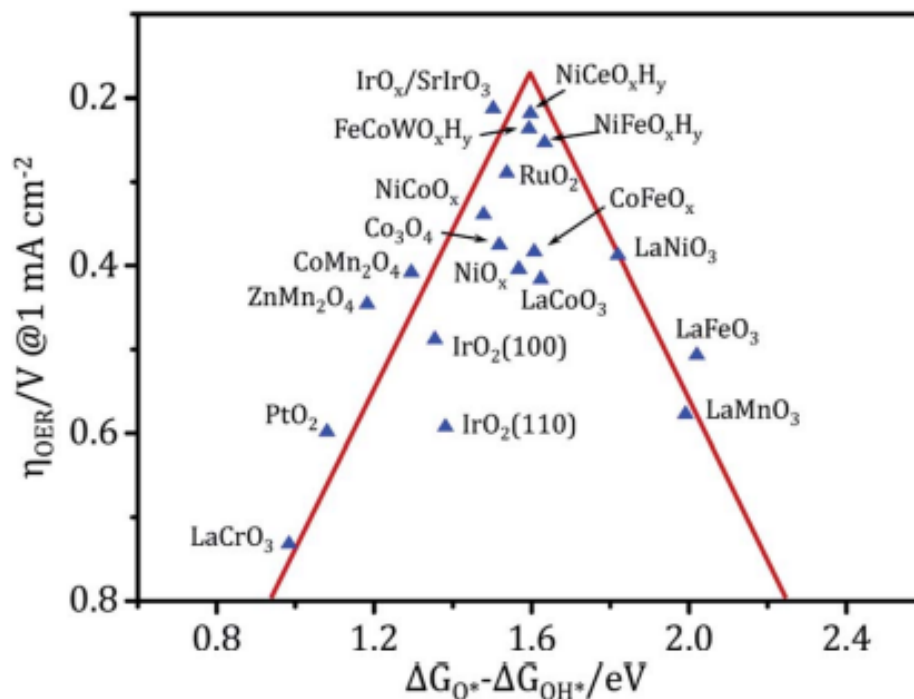


Figure 1.35 – Volcano plot for oxygen evolution reaction^[78]

895 c) Hydrogen oxidation reaction HOR

The following part will focus on Hydrogen Oxidation Reaction (HOR) in alkaline media. This reaction is highly used in fuel cell systems such as alkaline fuel cell. The fast kinetics for low concentration of Pt become an excellent candidate to boost performance. We can divide HOR into three-step given by the following equation^[80]: The Tafel reaction is given by the equation (1.30):



The Heyrovsky reaction is given by the equation (1.31):



And the Volmer reaction is given by equation (1.32):



We have H_{ad} intermediate formed during the Tafel or Heyrovsky step. After that, we have the Volmer step, which corresponds to water formation. During the Tafel reaction, the H_2 molecules will self-adsorb to the active sites and conduct the dissociation without electron transfer to give the chemically adsorbed H_{ad} . For the Heyrovsky reaction, the coordination of adjacent OH^- and H_2 molecules will break to give H_{ad} and water molecules. These reactions are coupled with electron transfer from H_2 to the catalyst. Furthermore, for the Volmer step, the H_{ad} is given by the above steps binds to OH^- to form H_2O and will release electrons.^[81] In figure 1.36, we can find the illustration of the HOR in alkaline media.

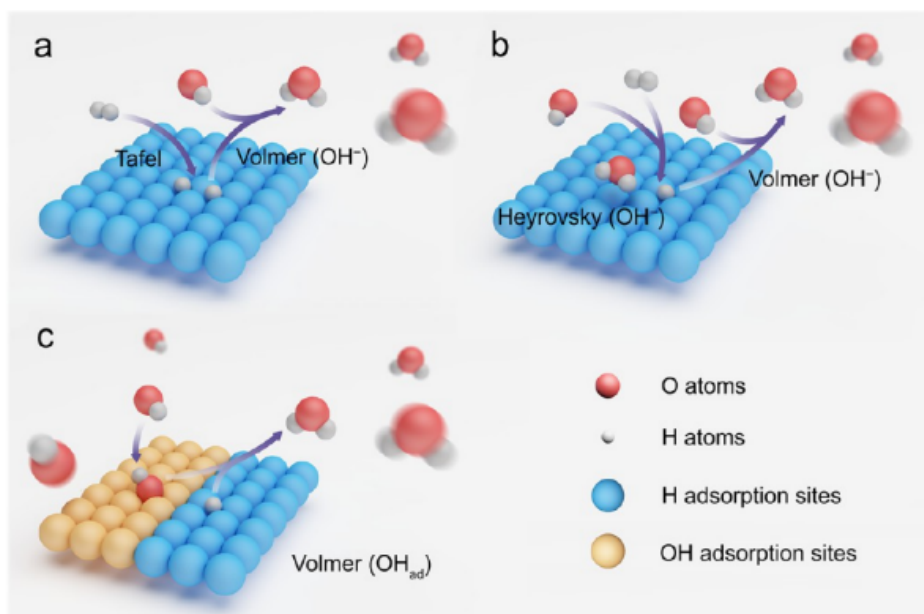


Figure 1.36 – Hydrogen oxidation reaction pathways in alkaline media. (a) Tafel-Volmer and (b) Heyrovsky-Volmer mechanism with OH^- only in the electrolyte. (c) Volmer step with OH_{ad} adsorbed on the catalyst surface.^[81]

The Volcano plot of the HER (Figure 1.32) is linked to the adsorption heat and, analogously, can be used for the activity descriptor in alkaline HOR.^[81] The main problem of the HOR is the strong H adsorption on the catalyst during the reversible H adsorption/desorption, which gives obstacles to reaction kinetics.

We can divide the alkaline HOR catalysts into three categories:

The first category is precious metals such as Pt, Ru, Pd, Ir, etc. The best catalyst is the platinum Pt. The second is also alloyed with precious and platinum-group metals (PGMs). Creating an alloyed structure is an alternative for the first category to decrease product cost. Moreover, the last category is PGMs-free catalysts with the mainly nickel-based catalyst^[81].

We can also look at the mechanism of HOR in acidic media. HOR proceeds through the reverse sequences of HER in acidic media. Like in the alkaline media seen previously, in the acidic media, HER is divided into three-step.^[82] The first step is the Volmer reaction given by the

following equation (1.33):



The second reaction possible is the Heyrovsky reaction given by equation (1.34) :



930 And the other reaction possible after the Volmer reaction is the Tafel reaction given by equation (1.35):



The slope value obtains thanks to the Tafel allows us to find which elementary step is the rate-determining step (RDS). In Table 1.5, we can find back the different values of slope and at which step it corresponds. We also see the form of the Butler-Volmer obtained for each step.^[82]

| Mechanism (RDS) | Kinetic expression | Tafel slope Anodic (HOR) | TS at 298 K [mV dec ⁻¹] (HOR) | B-V plot |
|-----------------------------|---|------------------------------|---|---|
| I: Volmer (RDS)–Tafel | $i = 2i_0 \left[-e^{\frac{-\alpha F}{RT}\eta} + e^{\frac{\beta F}{RT}\eta} \right]$ | $\frac{2.303RT}{\beta F}$ | 118 |  |
| II: Volmer–Tafel (RDS) | $\eta = \frac{RT}{2F} \ln\left(1 + \frac{i}{i_T}\right)$ | $\frac{2.303RT}{2F}$ | 30 | – |
| III: Volmer (RDS)–Heyrovsky | $i = 2i_0 \left[-e^{\frac{-\alpha F}{RT}\eta} + e^{\frac{(1+\beta)F}{RT}\eta} \right]$ | $\frac{2.303RT}{(1+\beta)F}$ | 39 |  |
| IV: Volmer–Heyrovsky (RDS) | $i = 2i_0 \left[-e^{\frac{-(1+\alpha)F}{RT}\eta} + e^{\frac{\beta F}{RT}\eta} \right]$ | $\frac{2.303RT}{\beta F}$ | 118 |  |
| V: Diffusion control | $\eta_d = -\frac{RT}{2F} \ln\left(1 - \frac{i_d}{i_{l,a}}\right)$ | $\frac{2.303RT}{2F}$ | 30 | – |

Table 1.5 – Kinetic expressions and Tafel slope for hydrogen oxidation reaction in acidic media^[82]

HOR in acidic media is highly studied in fuel cell systems for compact proton exchange membrane fuel cell (PEMFC). Pt is the best catalyst in acidic media for OER/ORR, but ultralow loading of Pt for HER makes it stand out compared to OER/ORR. The problem of HER/HOR studied in acidic media is that Pt or active Pt-group metals are the best catalysts. Moreover, the cost of the Pt explains the retard studied on HOR in acidic media. The other limitation is the strongly acidic environment, catalyst-based Pt-group metals, and no nonprecious metal will be limited compared to Pt.

In HOR studied in acidic media, we can find the notion of Hydrogen binding energy (HBE) in the literature. Hydrogen binding energy (HBE) is used as the sole descriptor for HER/HOR in acidic and alkaline media. We can trace the volcano type of relationship to link the reaction activity to the hydrogen adsorption energetics on metals and an ideal hydrogen binding energy with Gibbs free energy change. If the value of ideal hydrogen binding energy with Gibbs free energy change is zero, we will obtain a catalyst with the highest HER/HOR activity, and it is Pt.^[82]

d) Oxygen reduction reaction ORR

In the metal-air battery, we will look at the cathode part where we have the reduction of oxygen (ORR). The reaction how to takes place at the anode is the oxidation of oxygen that we see in the earlier part. The reaction of the reduction of oxygen can follow two pathways. We have the 2 electrons pathway or the 4 electrons pathway.

For the 2 electrons pathway, the oxygen will conduct to the formation of hydrogen peroxide H_2O_2 in the acidic media or HO_2^- in alkaline media. They can be intermediate species if we have the 4 electrons pathway. For the 4 electrons pathways conducted to the formation of water H_2O (in acidic media) or Hydroxide ion OH^- (in alkaline media). The catalyst used for the ORR will influence the selectivity of the pathways chosen. The adsorption energetics of the catalyst's intermediaries present on electrodes will influence reduction selectivity.

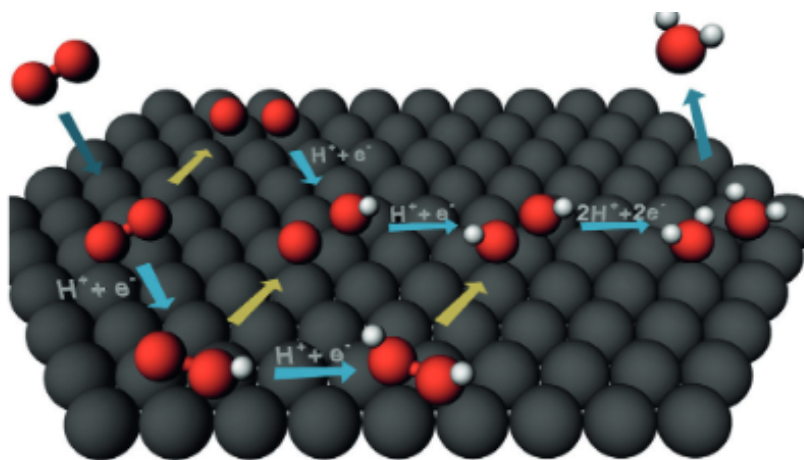
Table 1.6 shows that we have different mechanisms possible at the molecular level: dissociative and associative pathways. In these two different mechanisms, we can have 4 electrons pathway. The intermediates formed are the main differences in the mechanism for the dissociative or associative. For the dissociative is O^* and for associative: O^* , OOH^* , and OH^* . correspond to the active site of the catalyst.^[76]

Table 1. Mechanisms of the ORR in Alkaline Conditions

| mechanism | reactions |
|-------------------------|---|
| dissociative ($4e^-$) | $O_2 + 2^* \rightarrow 2O^*$ $2O^* + 2e^- + 2H_2O \rightarrow 2OH^* + 2OH^-$ $2OH^* + 2e^- \rightarrow 2OH^- + 2^*$ |
| associative ($4e^-$) | $O_2 + ^* \rightarrow O_2^*$ $O_2^* + H_2O + e^- \rightarrow OOH^* + OH^-$ $OOH^* + e^- \rightarrow O^* + OH^-$ $O^* + H_2O + e^- \rightarrow OH^* + OH^-$ $OH^* + e^- \rightarrow OH^- + ^*$ |
| associative ($2e^-$) | $O_2 + ^* \rightarrow O_2^*$ $O_2^* + H_2O + e^- \rightarrow OOH^* + OH^-$ $OOH^* + e^- \rightarrow OOH^- + ^*$ |

Table 1.6 – Oxygen reduction reaction mechanisms in alkaline media^[76]

With Figure 1.37, we will look at the mechanisms at the surface of the electrode. The first step of the oxygen molecule is the diffusion through the electrode, which leads to the formation of adsorbed oxygen molecule (O_2^*). After that, three pathways are possible. This pathway difference is due to O–O bond cleavage. The first choice of pathway is dissociation. It is when the O–O bond break immediately and conduct to the formation of O^* . O^* will finally be reduced to OH^* and to H_2O^* . The second pathway is associative. For this one, we have the formation of OOH^* and how to conduct O_2^* . O_2^* allowed the cleavage of O–O bond and created O^* and OH^* intermediates. Furthermore, the third choice of pathway is peroxy or second associative. We have the reduction of O_2^* to OOH^* and to $HOOH^*$ before O–O bond is cleaved.^[83]

**Figure 1.37** – 4 pathways of oxygen reduction reaction mechanism^[83] with black, red, and white spheres are oxygen atoms and hydrogen atoms in yellow arrows are the O–O bond cleavage and blue arrows are proton or electron transfer

Using DFT simulation, Nørskov et al.^[84], showed that the overpotential is linked to oxygen adsorption on the electrode. Also, the potential influences the stability of the adsorbed oxygen. For high potential, we will have very stable oxygen adsorbed on the electrode surface, but the reaction on the electrode will be blocked. To resolve that issue by decreasing the potential can resolve this issue and trouble the stability to allow the reaction.

The intermediates species involved in the ORR are vital in understanding the catalytic activity. The best catalyst must moderate binding to the intermediates involved in the reaction.

Like for HER and OER, Figure 1.38 shows the Volcano plot for ORR. Thanks to the volcano plot, the oxygen adsorption strength (ΔE_{O^*}) was used to look at the activity for ORR.^[75] We can see that Pt surface has bound to O^* , OOH^* , or OH^* and respect the characteristics to be a suitable catalyst for ORR.

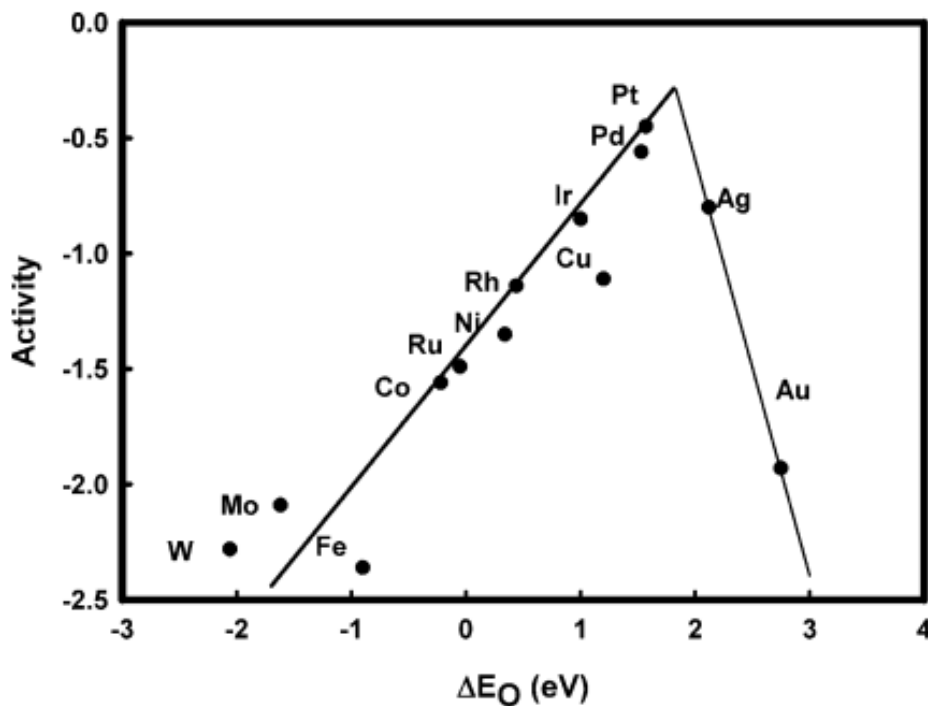


Figure 1.38 – Oxygen reduction reaction volcano plot^[84]

1.3 Conclusion of the first chapter

Environmental issues and the demand for an alternative to fossil energies are the main
990 problem of the twenty-first century linked to the massive industrialization conducted in the
past decades. In the past decade, universities and industries have reached out to find an alter-
native the fossil energy.

The development of electrochemical energy storage devices (EESD) such as batteries, super-
995 conductors, and fuel cells are widely conducted to develop more sustainable devices by elab-
orating these devices with more eco-friendly materials or components. We introduce the su-
percabattery, a hybrid device that combines the battery and superconductor proprieties.

We have seen in this chapter the different facets of these types of devices, and this allows
1000 us to focus on four catalytic reactions.

These four reactions are linked to hydrogen (HER and HOR) and oxygen (ORR and OER).
The investigation conducted on these four reactions will help us in the PhD studies that we
will investigate in the following chapters.

1005

In chapter 2, we will focus on the ORR using the Mn_2O_3 catalyst and look at the mechanism
obtained.

In chapters 3 and 4, we look at the HER and OER by catalytic effect and the mechanism con-
1010 ducted by the NiOx electrode.

Finally, in chapter 5, we will develop a supercabattery with the study of NiOx .

REFERENCES

- 1015 [1] Buhari Doğan, Daniel Balsalobre-Lorente, and Muhammad Ali Nasir. European commitment to COP21 and the role of energy consumption, FDI, trade and economic complexity in sustaining economic growth. *273:111146*. ISSN 0301-4797. doi: 10.1016/j.jenvman.2020.111146.
- [2] Liangzhong YAO, Bo YANG, Hongfen CUI, Jun ZHUANG, Jilei YE, and Jinhua XUE. Challenges and progresses of energy storage technology and its application in power systems. *Journal of Modern Power Systems and Clean Energy*, 4(4):519–528, October 2016. ISSN 2196-5420. doi: 10.1007/s40565-016-0248-x.
- 1020
- [3] Shaohua Chen, Ling Qiu, and Hui-Ming Cheng. Carbon-Based Fibers for Advanced Electrochemical Energy Storage Devices. *Chemical Reviews*, 120(5):2811–2878, March 2020. ISSN 0009-2665. doi: 10.1021/acs.chemrev.9b00466.
- 1025
- [4] Martin Winter and Ralph J. Brodd. What Are Batteries, Fuel Cells, and Supercapacitors? *Chemical Reviews*, 104(10):4245–4270, October 2004. ISSN 0009-2665, 1520-6890. doi: 10.1021/cr020730k.
- [5] William S. Wong and Alberto Salleo. *Flexible Electronics: Materials and Applications*. Springer Science & Business Media, April 2009. ISBN 978-0-387-74363-9.
- 1030
- [6] Arokia Nathan, Arman Ahnood, Matthew T. Cole, Sungsik Lee, Yuji Suzuki, Pritesh Hirralal, Francesco Bonaccorso, Tawfique Hasan, Luis Garcia-Gancedo, Andriy Dyadyusha, Samiul Haque, Piers Andrew, Stephan Hofmann, James Moultrie, Daping Chu, Andrew J. Flewitt, Andrea C. Ferrari, Michael J. Kelly, John Robertson, Gehan A. J. Amaratunga, and William I. Milne. Flexible Electronics: The Next Ubiquitous Platform. *Proceedings of the IEEE*, 100(Special Centennial Issue):1486–1517, May 2012. ISSN 1558-2256. doi: 10.1109/JPROC.2012.2190168.
- 1035

- [7] Matteo Stoppa and Alessandro Chiolerio. Wearable Electronics and Smart Textiles: A Critical Review. *Sensors*, 14(7):11957–11992, July 2014. ISSN 1424-8220. doi: 10.3390/s140711957.
- [8] Hiroyuki Nishide and Kenichi Oyaizu. Toward Flexible Batteries. *Science*, 319(5864):737–738, February 2008. doi: 10.1126/science.1151831.
- [9] George Z. Chen. Supercapacitor and supercapattery as emerging electrochemical energy stores. *International Materials Reviews*, 62(4):173–202, May 2017. ISSN 0950-6608. doi: 10.1080/09506608.2016.1240914.
- [10] Linpo Yu and George Z. Chen. Redox electrode materials for supercapatteries. *Journal of Power Sources*, 326:604–612, September 2016. ISSN 0378-7753. doi: 10.1016/j.jpowsour.2016.04.095.
- [11] Suresh Sagadevan, A. R. Marlinda, Zaira Zaman Chowdhury, Yasmin Binti Abdul Wahab, Nor Aliya Hamizi, M. M. Shahid, Faruq Mohammad, Jiban Podder, and Mohd Rafie Johan. Chapter two - Fundamental electrochemical energy storage systems. In Numan Arshid, Mohammad Khalid, and Andrews Nirmala Grace, editors, *Advances in Supercapacitor and Supercapattery*, pages 27–43. Elsevier, January 2021. ISBN 978-0-12-819897-1. doi: 10.1016/B978-0-12-819897-1.00001-X.
- [12] Atsushi Nishino. Capacitors: operating principles, current market and technical trends. *Journal of Power Sources*, 60(2):137–147, June 1996. ISSN 0378-7753. doi: 10.1016/S0378-7753(96)80003-6.
- [13] Patrice Simon and Yury Gogotsi. Materials for electrochemical capacitors. 7(11):845–854. ISSN 1476-1122. doi: 10.1038/nmat2297.
- [14] B. E. Conway. Transition from “Supercapacitor” to “Battery” Behavior in Electrochemical Energy Storage. *Journal of The Electrochemical Society*, 138(6):1539, June 1991. ISSN 1945-7111. doi: 10.1149/1.2085829.
- [15] Meryl D. Stoller and Rodney S. Ruoff. Best practice methods for determining an electrode material’s performance for ultracapacitors. *Energy & Environmental Science*, 3(9):1294–1301, August 2010. ISSN 1754-5706. doi: 10.1039/C0EE00074D.
- [16] Li Li Zhang, Zhibin Lei, Jintao Zhang, Xiaoning Tian, and Xiu Song Zhao. Supercapacitors: Electrode Materials Aspects. In *Encyclopedia of Inorganic Chemistry*. John Wiley & Sons, Ltd, 2011. ISBN 978-0-470-86210-0. doi: 10.1002/0470862106.ia816.
- [17] Yuqi Jiang and Jinping Liu. Definitions of Pseudocapacitive Materials: A Brief Review. *ENERGY & ENVIRONMENTAL MATERIALS*, 2(1):30–37, 2019. ISSN 2575-0356. doi: 10.1002/eem2.12028.

- [18] B. E. Conway. *Electrochemical Supercapacitors: Scientific Fundamentals and Technological Applications*. Springer Science & Business Media, April 2013. ISBN 978-1-4757-3058-6.
- [19] Jeffrey W. Long, Daniel Bélanger, Thierry Brousse, Wataru Sugimoto, Megan B. Sassin, and Olivier Crosnier. Asymmetric electrochemical capacitors—Stretching the limits of aqueous electrolytes. *MRS Bulletin*, 36(7):513–522, July 2011. ISSN 1938-1425, 0883-7694.
- [20] A. El Kharbachi, O. Zavorotynska, M. Latroche, F. Cuevas, V. Yartys, and M. Fichtner. Exploits, advances and challenges benefiting beyond Li-ion battery technologies. *Journal of Alloys and Compounds*, 817:153261, March 2020. ISSN 0925-8388. doi: 10.1016/j.jallcom.2019.153261.
- [21] Muhammad Rehman Asghar, Muhammad Tuoqeer Anwar, and Ahmad Naveed. A review on inorganic nanoparticles modified composite membranes for lithium-ion batteries: Recent progress and prospects. 9(7):78. ISSN 2077-0375. doi: 10.3390/membranes9070078.
- [22] Research {and} Markets Ltd. Lithium-ion battery market with COVID-19 impact analysis, by type (li-NMC, LFP, LCO, LTO, LMO, NCA), capacity, voltage, industry (consumer electronics, automotive, power, industrial), & region (north america, europe, APAC & RoW) - global forecast to 2030.
- [23] Naoki Nitta, Feixiang Wu, Jung Tae Lee, and Gleb Yushin. Li-ion battery materials: present and future. *Materials Today*, 18(5):252–264, June 2015. ISSN 1369-7021. doi: 10.1016/j.mattod.2014.10.040.
- [24] Beta Writer. Anode Materials, SEI, Carbon, Graphite, Conductivity, Graphene, Reversible, Formation. In Beta Writer, editor, *Lithium-Ion Batteries: A Machine-Generated Summary of Current Research*, pages 1–71. Springer International Publishing, Cham, 2019. ISBN 978-3-030-16800-1. doi: 10.1007/978-3-030-16800-1_1.
- [25] David Schneider. Silicon anodes will give lithiumion batteries a boost. *IEEE Spectrum*, 56(1):48–49, January 2019. ISSN 1939-9340. doi: 10.1109/MSPEC.2019.8594797.
- [26] Wangda Li, Evan M. Erickson, and Arumugam Manthiram. High-nickel layered oxide cathodes for lithium-based automotive batteries. *Nature Energy*, 5(1):26–34, January 2020. ISSN 2058-7546. doi: 10.1038/s41560-019-0513-0.
- [27] Maxwell D. Radin, Sunny Hy, Mahsa Sina, Chengcheng Fang, Haodong Liu, Julija Vinckeviciute, Minghao Zhang, M. Stanley Whittingham, Y. Shirley Meng, and Anton Van der Ven. Narrowing the Gap between Theoretical and Practical Capacities in Li-Ion Layered Oxide Cathode Materials. *Advanced Energy Materials*, 7(20):1602888, 2017. ISSN 1614-6840. doi: 10.1002/aenm.201602888.

- 1105 [28] Francesco Nobili and Roberto Marassi. Fundamental principles of battery electrochemistry. In *Encyclopedia of Electrochemistry*, pages 1–36. John Wiley & Sons, Ltd. ISBN 978-3-527-61042-6. doi: 10.1002/9783527610426.bard110001.
- [29] Fabian I. Ezema, Chandrakant D. Lokhande, and Rajan Jose. *Chemically Deposited Nanocrystalline Metal Oxide Thin Films: Synthesis, Characterizations, and Applications*. Springer Nature, June 2021. ISBN 978-3-030-68462-4.
1110
- [30] Jie Xiao, Qiuyan Li, Yujing Bi, Mei Cai, Bruce Dunn, Tobias Glossmann, Jun Liu, Tetsuya Osaka, Ryuta Sugiura, Bingbin Wu, Jihui Yang, Ji-Guang Zhang, and M. Stanley Whittingham. Understanding and applying coulombic efficiency in lithium metal batteries. *Nature Energy*, 5(8):561–568, August 2020. ISSN 2058-7546. doi: 10.1038/s41560-020-0648-z.
- 1115 [31] Arumugam Manthiram. A reflection on lithium-ion battery cathode chemistry. *Nature Communications*, 11(1):1550, March 2020. ISSN 2041-1723. doi: 10.1038/s41467-020-15355-0.
- [32] Santosh K. Gupta, R. M. Kadam, R. Gupta, Manjulata Sahu, and V. Natarajan. Evidence for the stabilization of manganese ion as Mn (II) and Mn (IV) in α -Zn₂P₂O₇: Probed by
1120 EPR, luminescence and electrochemical studies. *Materials Chemistry and Physics*, 145(1):162–167, May 2014. ISSN 0254-0584. doi: 10.1016/j.matchemphys.2014.01.054.
- [33] M. Rosa Palacín. Recent advances in rechargeable battery materials: a chemist’s perspective. *Chemical Society Reviews*, 38(9):2565–2575, August 2009. ISSN 1460-4744. doi: 10.1039/B820555H.
- 1125 [34] Zhi Chang, Yu Qiao, Han Deng, Huijun Yang, Ping He, and Haoshen Zhou. A stable high-voltage lithium-ion battery realized by an in-built water scavenger. *Energy & Environmental Science*, 13(4):1197–1204, April 2020. ISSN 1754-5706. doi: 10.1039/D0EE00060D.
- [35] Ragupathy Pitchai, Velmurugan Thavasi, Subodh G. Mhaisalkar, and Seeram Ramakrishna. Nanostructured cathode materials: a key for better performance in Li-ion batteries. *Journal of Materials Chemistry*, 21(30):11040–11051, July 2011. ISSN 1364-5501. doi: 1130 10.1039/C1JM10857C.
- [36] Jing Fu, Zachary Paul Cano, Moon Gyu Park, Aiping Yu, Michael Fowler, and Zhongwei Chen. Electrically Rechargeable Zinc-Air Batteries: Progress, Challenges, and Perspectives. *Advanced Materials*, 29(7):1604685, 2017. ISSN 1521-4095. doi: 10.1002/adma. 1135 201604685.
- [37] Xiaopeng Han, Xiaopeng Li, Jai White, Cheng Zhong, Yida Deng, Wenbin Hu, and Tianyi Ma. Metal-Air Batteries: From Static to Flow System. *Advanced Energy Materials*, 8(27):1801396, 2018. ISSN 1614-6840. doi: 10.1002/aenm.201801396.

- [38] Jurgen Garche and Klaus Brandt. *Electrochemical Power Sources: Fundamentals, Systems, and Applications: Li-Battery Safety*. Elsevier, September 2018. ISBN 978-0-444-64008-6. 1140
- [39] Shujing Li, Hongtao Guo, Shuijian He, Haoqi Yang, Kunming Liu, Gaigai Duan, and Shao-hua Jiang. Advanced electrospun nanofibers as bifunctional electrocatalysts for flexible metal-air (O₂) batteries: Opportunities and challenges. *Materials & Design*, 214:110406, February 2022. ISSN 0264-1275. doi: 10.1016/j.matdes.2022.110406.
- [40] Wenhao Sun, Daniil A. Kitchaev, Denis Kramer, and Gerbrand Ceder. Non-equilibrium crystallization pathways of manganese oxides in aqueous solution. *Nature Communica-tions*, 10(1):573, February 2019. ISSN 2041-1723. doi: 10.1038/s41467-019-08494-6. 1145
- [41] Sunghak Park, Yoon Ho Lee, Seungwoo Choi, Hongmin Seo, Moo Young Lee, Mani Bal-amurugan, and Ki Tae Nam. Manganese oxide-based heterogeneous electrocatalysts for water oxidation. *Energy & Environmental Science*, 13(8):2310–2340, August 2020. ISSN 1754-5706. doi: 10.1039/D0EE00815J. 1150
- [42] Serge Rebouillat, Michael E G Lyons, Michael P Brandon, and Richard L Doyle. Paving the way to the integration of smart nanostructures: Part II: Nanostructured microdispersed hydrated metal oxides for electrochemical energy conversion and storage applications. 6:88. 1155
- [43] Fatin Saiha Omar, Arshid Numan, Shahid Bashir, Navaneethan Duraisamy, R. Vik-neswaran, Yueh-Lin Loo, K. Ramesh, and S. Ramesh. Enhancing rate capability of amor-phous nickel phosphate supercapattery electrode via composition with crystalline sil-ver phosphate. *Electrochimica Acta*, 273:216–228, May 2018. ISSN 0013-4686. doi: 10.1016/j.electacta.2018.03.136. 1160
- [44] I.N. Varakin A.B. Stepanov, and V.V. Menukhov. Capacitor with a double electrical layer, Feb 1997.
- [45] Bamidele Akinwolemiwa, Chuang Peng, and George Z. Chen. Redox Electrolytes in Su-percapacitors. *Journal of The Electrochemical Society*, 162(5):A5054, January 2015. ISSN 1945-7111. doi: 10.1149/2.0111505jes. 1165
- [46] Sho Makino, Yuto Shinohara, Takayuki Ban, Wataru Shimizu, Keita Takahashi, Nobuyuki Imanishi, and Wataru Sugimoto. 4 V class aqueous hybrid electrochemical capacitor with battery-like capacity. *RSC Advances*, 2(32):12144–12147, 2012. doi: 10.1039/C2RA22265E.
- [47] Xinliang Feng. *Nanocarbons for Advanced Energy Storage, Volume 1*. John Wiley & Sons, June 2015. ISBN 978-3-527-33665-4. 1170
- [48] Anthony J. Stevenson, Denys G. Gromadskyi, Di Hu, Junghoon Chae, Li Guan, Linpo Yu, and George Z. Chen. Supercapatteries with Hybrids of Redox Active Polymers and

- Nanostructured Carbons. In *Nanocarbons for Advanced Energy Storage*, volume 1, pages 179–210. Wiley, March 2015. ISBN 978-3-527-33665-4. doi: 10.1002/9783527680054.ch6.
- 1175 [49] Jun Liu. Addressing the Grand Challenges in Energy Storage. *Advanced Functional Materials*, 23(8):924–928, 2013. ISSN 1616-3028. doi: 10.1002/adfm.201203058.
- [50] Catherine Heymans, Sean B. Walker, Steven B. Young, and Michael Fowler. Economic analysis of second use electric vehicle batteries for residential energy storage and load-leveling. *Energy Policy*, 71:22–30, August 2014. ISSN 0301-4215. doi: 10.1016/j.enpol.
1180 2014.04.016.
- [51] George Z. Chen. Perception of Supercapacitor and Supercapattery. *ECS Meeting Abstracts*, MA2011-02(11):559, August 2011. ISSN 2151-2043. doi: 10.1149/MA2011-02/11/559.
- [52] Daniel M. Teffu, Morongwa E. Ramoroka, Mogwasha D. Makhafola, Katlego Makgopa, Thabiso C. Maponya, Ostar A. Seerane, Mpitloane J. Hato, Emmanuel I. Iwuoha, and
1185 Kwena D. Modibane. High-performance supercabattery based on reduced graphene oxide/metal organic framework nanocomposite decorated with palladium nanoparticles. *Electrochimica Acta*, 412:140136, April 2022. ISSN 0013-4686. doi: 10.1016/j.electacta.2022.140136.
- [53] Assumpta Chinwe Nwanya, Miranda M. Ndipingwi, Chinwe O. Ikpo, R. M. Obodo,
1190 Stephen C. Nwanya, Subelia Botha, Fabian I. Ezema, Emmanuel I. Iwuoha, and Malik Maaza. Zea mays lea silk extract mediated synthesis of nickel oxide nanoparticles as positive electrode material for asymmetric supercabattery. *Journal of Alloys and Compounds*, 822:153581, May 2020. ISSN 0925-8388. doi: 10.1016/j.jallcom.2019.153581.
- [54] W.R. Grove. LXXII. On a gaseous voltaic battery. *The London, Edinburgh, and Dublin
1195 Philosophical Magazine and Journal of Science*, 21(140):417–420, December 1842. ISSN 1941-5966. doi: 10.1080/14786444208621600.
- [55] Manish Kumar Singla, Parag Nijhawan, and Amandeep Singh Oberoi. Hydrogen fuel and fuel cell technology for cleaner future: a review. *Environmental Science and Pollution Research*, 28(13):15607–15626, April 2021. ISSN 1614-7499. doi: 10.1007/s11356-020-12231-8.
- 1200 [56] Thapar Institute of Engineering and Technology Patiala, India and Manish Kumar Singla. Trends so far in Hydrogen Fuel Cell Technology: State of the art. *International Journal of Advanced Trends in Computer Science and Engineering*, pages 1146–1155, August 2019. ISSN 22783091. doi: 10.30534/ijatcse/2019/23842019.
- [57] Nor Fatina Raduwan, Norazuwana Shaari, Siti Kartom Kamarudin, Mohd Shabudin Masdar, and Rozan Mohamad Yunus. An overview of nanomaterials in fuel cells: Synthesis method and application. 47(42):18468–18495. ISSN 0360-3199. doi: 10.1016/j.ijhydene.
1205 2022.03.035.

- [58] Mohammed Yousri Silaa, Mohamed Derbeli, Oscar Barambones, and Ali Cheknane. Design and Implementation of High Order Sliding Mode Control for PEMFC Power System. *Energies*, 13(17):4317, January 2020. ISSN 1996-1073. doi: 10.3390/en13174317.
- [59] Adam Mohd Izhan Noor Azam, Pua Mei Choon, Mohd Shahbudin Masdar, Azran Mohd Zainoodin, and T. Husaini. Performance and water transport behaviour in Polymer Electrolyte Membrane fuel cells. *International Journal of Hydrogen Energy*, 47(96):40803–40813, December 2022. ISSN 0360-3199. doi: 10.1016/j.ijhydene.2021.12.146.
- [60] Chao Wei, Reshma R. Rao, Jiayu Peng, Botao Huang, Ifan E. L. Stephens, Marcel Risch, Zhichuan J. Xu, and Yang Shao-Horn. Recommended Practices and Benchmark Activity for Hydrogen and Oxygen Electrocatalysis in Water Splitting and Fuel Cells. *Advanced Materials*, 31(31):1806296, 2019. ISSN 1521-4095. doi: 10.1002/adma.201806296.
- [61] Boying Zhang, Wenbo Wang, Linan Liang, Zhice Xu, Xiaoyun Li, and Shanlin Qiao. Prevailing conjugated porous polymers for electrochemical energy storage and conversion: Lithium-ion batteries, supercapacitors and water-splitting. *Coordination Chemistry Reviews*, 436:213782, June 2021. ISSN 0010-8545. doi: 10.1016/j.ccr.2021.213782.
- [62] Alfredo Ursua, Luis M. Gandia, and Pablo Sanchis. Hydrogen Production From Water Electrolysis: Current Status and Future Trends. *Proceedings of the IEEE*, 100(2):410–426, February 2012. ISSN 1558-2256. doi: 10.1109/JPROC.2011.2156750.
- [63] Zi-You Yu, Yu Duan, Xing-Yu Feng, Xingxing Yu, Min-Rui Gao, and Shu-Hong Yu. Clean and Affordable Hydrogen Fuel from Alkaline Water Splitting: Past, Recent Progress, and Future Prospects. *Advanced Materials*, 33(31):2007100, 2021. ISSN 1521-4095. doi: 10.1002/adma.202007100.
- [64] Kai Zeng and Dongke Zhang. Recent progress in alkaline water electrolysis for hydrogen production and applications. *Progress in Energy and Combustion Science*, 36(3):307–326, June 2010. ISSN 0360-1285. doi: 10.1016/j.peccs.2009.11.002.
- [65] Marcelo Carmo, David L. Fritz, Jürgen Mergel, and Detlef Stolten. A comprehensive review on PEM water electrolysis. *International Journal of Hydrogen Energy*, 38(12):4901–4934, April 2013. ISSN 0360-3199. doi: 10.1016/j.ijhydene.2013.01.151.
- [66] Ting Yuan, Hyongki Lee, Hahn Chul Jung, Abureli Aierken, Edward Beighley, Douglas E. Alsdorf, Raphael M. Tshimanga, and Donghwan Kim. Absolute water storages in the Congo River floodplains from integration of InSAR and satellite radar altimetry. *Remote Sensing of Environment*, 201:57–72, November 2017. ISSN 0034-4257. doi: 10.1016/j.rse.2017.09.003.
- [67] Hydrogen from renewable power: Technology outlook for the energy transition.

- [68] Jumeng Wei, Min Zhou, Anchun Long, Yanming Xue, Hanbin Liao, Chao Wei, and Zhichuan J. Xu. Heterostructured Electrocatalysts for Hydrogen Evolution Reaction Under Alkaline Conditions. *Nano-Micro Letters*, 10(4):75, November 2018. ISSN 2150-5551. doi: 10.1007/s40820-018-0229-x.
- [69] Carlos G. Morales-Guio, Lucas-Alexandre Stern, and Xile Hu. Nanostructured hydrotreating catalysts for electrochemical hydrogen evolution. *Chemical Society Reviews*, 43(18):6555–6569, August 2014. ISSN 1460-4744. doi: 10.1039/C3CS60468C.
- [70] Yao Zheng, Yan Jiao, Mietek Jaroniec, and Shi Zhang Qiao. Advancing the Electrochemistry of the Hydrogen-Evolution Reaction through Combining Experiment and Theory. *Angewandte Chemie International Edition*, 54(1):52–65, 2015. ISSN 1521-3773. doi: 10.1002/anie.201407031.
- [71] J. K. Nørskov, T. Bligaard, A. Logadottir, J. R. Kitchin, J. G. Chen, S. Pandalov, and U. Stimming. Trends in the Exchange Current for Hydrogen Evolution. *Journal of The Electrochemical Society*, 152(3):J23, January 2005. ISSN 1945-7111. doi: 10.1149/1.1856988.
- [72] Jing Zhu, Liangsheng Hu, Pengxiang Zhao, Lawrence Yoon Suk Lee, and Kwok-Yin Wong. Recent advances in electrocatalytic hydrogen evolution using nanoparticles. 120(2):851–918. ISSN 0009-2665. doi: 10.1021/acs.chemrev.9b00248.
- [73] Egill Skúlason, Vladimir Tripkovic, Mårten E. Björketun, Sigrídur Gudmundsdóttir, Gustav Karlberg, Jan Rossmeisl, Thomas Bligaard, Hannes Jónsson, and Jens K. Nørskov. Modeling the Electrochemical Hydrogen Oxidation and Evolution Reactions on the Basis of Density Functional Theory Calculations. *The Journal of Physical Chemistry C*, 114(42):18182–18197, October 2010. ISSN 1932-7447. doi: 10.1021/jp1048887.
- [74] Nicolas Dubouis and Alexis Grimaud. The hydrogen evolution reaction: from material to interfacial descriptors. 10(40):9165–9181. ISSN 2041-6539. doi: 10.1039/C9SC03831K.
- [75] Zonghua Pu, Tingting Liu, Ibrahim Saana Amiin, Ruilin Cheng, Pengyan Wang, Chengtian Zhang, Pengxia Ji, Weihua Hu, Jian Liu, and Shichun Mu. Transition-Metal Phosphides: Activity Origin, Energy-Related Electrocatalysis Applications, and Synthetic Strategies. *Advanced Functional Materials*, 30(45):2004009, 2020. ISSN 1616-3028. doi: 10.1002/adfm.202004009.
- [76] Huanyu Jin, Chunxian Guo, Xin Liu, Jinlong Liu, Anthony Vasileff, Yan Jiao, Yao Zheng, and Shi-Zhang Qiao. Emerging Two-Dimensional Nanomaterials for Electrocatalysis. *Chemical Reviews*, 118(13):6337–6408, July 2018. ISSN 0009-2665. doi: 10.1021/acs.chemrev.7b00689.

- 1275 [77] Fengmei Wang, Tofik Ahmed Shifa, Xueying Zhan, Yun Huang, Kaili Liu, Zhongzhou Cheng, Chao Jiang, and Jun He. Recent advances in transition-metal dichalcogenide based nanomaterials for water splitting. *7*(47):19764–19788. ISSN 2040-3372. doi: 10.1039/C5NR06718A.
- [78] Zhenhua Yan, Huanhuan Liu, Zhimeng Hao, Meng Yu, Xiang Chen, and Jun Chen. Electrodeposition of (hydro)oxides for an oxygen evolution electrode. *Chemical Science*, *11*(39):10614–10625, 2020. doi: 10.1039/D0SC01532F.
- 1280 [79] Isabela C. Man, Hai-Yan Su, Federico Calle-Vallejo, Heine A. Hansen, José I. Martínez, Nilay G. Inoglu, John Kitchin, Thomas F. Jaramillo, Jens K. Nørskov, and Jan Rossmeisl. Universality in Oxygen Evolution Electrocatalysis on Oxide Surfaces. *ChemCatChem*, *3*(7):1159–1165, 2011. ISSN 1867-3899. doi: 10.1002/cctc.201000397.
- 1285 [80] Yuanyuan Cong, Baolian Yi, and Yujiang Song. Hydrogen oxidation reaction in alkaline media: From mechanism to recent electrocatalysts. *44*:288–303. ISSN 2211-2855. doi: 10.1016/j.nanoen.2017.12.008.
- [81] Ze-Cheng Yao, Tang Tang, Zhe Jiang, Lu Wang, Jin-Song Hu, and Li-Jun Wan. Electrocatalytic hydrogen oxidation in alkaline media: From mechanistic insights to catalyst design. *16*(4):5153–5183. ISSN 1936-0851. doi: 10.1021/acsnano.2c00641.
- 1290 [82] Xiaoyu Tian, Pengcheng Zhao, and Wenchao Sheng. Hydrogen evolution and oxidation: Mechanistic studies and material advances. *31*(31):1808066. ISSN 1521-4095. doi: 10.1002/adma.201808066.
- [83] Wei Xia, Asif Mahmood, Zibin Liang, Ruqiang Zou, and Shaojun Guo. Earth-Abundant Nanomaterials for Oxygen Reduction. *Angewandte Chemie International Edition*, *55*(8):2650–2676, 2016. ISSN 1521-3773. doi: 10.1002/anie.201504830.
- 1295 [84] J. K. Nørskov, J. Rossmeisl, A. Logadottir, L. Lindqvist, J. R. Kitchin, T. Bligaard, and H. Jónsson. Origin of the Overpotential for Oxygen Reduction at a Fuel-Cell Cathode. *The Journal of Physical Chemistry B*, *108*(46):17886–17892, November 2004. ISSN 1520-6106. doi: 10.1021/jp047349j.
- 1300

CHAPTER 2

MANGANESE OXIDE FOR OXYGEN REDUCTION REACTION

Contents

| | | |
|------------|---|-----|
| 2.1 | Elaboration of the catalyst: Carbon film to powder Manganese oxide | 66 |
| 2.2 | Spectroscopic investigation | 70 |
| 2.3 | Electrochemical investigation | 87 |
| 2.3.1 | Investigation of manganese oxide with rotating ring-disk electrode RRDE | 87 |
| 2.3.2 | Oxygen reduction reaction mechanism analysis | 94 |
| 2.3.3 | Micro-kinetic studies | 100 |
| 2.4 | Conclusion | 106 |
| References | | 108 |

Manganese oxide belongs to the family of Transition metal oxides (TMOs). This chemical family has been highly studied during the past decade due to its catalytic activity toward the oxygen reduction reaction (ORR) in alkaline media. We can use this material as the catalyst for the cathode to the fuel cell or the metal-air battery.^[1-3]

One of the reasons we chose manganese oxide as our catalyst is that it has a variety of manganese-based oxides among various transition metals. We can have MnO, Mn₂O₃, Mn₃O₄, and MnO₂, which are highly studied for their catalytic properties. They are used as electrode materials for their high theoretical capacity, and their cost value is very cheap compared to classic catalysts like ruthenium oxide and platinum.^[4] The manganese oxide powder or nanoparticles can be obtained after thermal treatment of fiber prepared by electrospinning. Electrospinning allowed us to prepare new materials. We will look closer at it in the chapter. The thermal treatment is an important parameter because it greatly impacts the properties of the obtained nanomaterials. In this chapter, we will investigate various ranges of temperature. Thanks to the spectroscopic investigation, we will analyze the relationships between the

electrocatalytic concerning ORR in alkaline medium and nanomaterials' morphology which depends upon the thermal treatment.

2.1 Elaboration of the catalyst: Carbon film to powder Manganese oxide

1335

In the following part, we focus on every step of the conception of the catalyst. The final form of our catalyst is a powder composed of manganese oxide that we identified as bixbyite $\alpha\text{-Mn}_2\text{O}_3$ thanks to spectroscopic investigations. We look closer in the chapter to prove it. To make our catalyst, we have following step. To make our powder will use the electrospinning step to make nanofiber and treat it thermally. We will see in the section below a quick introduction to the electrospinning technique, and we will look at the synthesis of our powder and the different steps used to produce it.

1340

Electrospinning is an electrohydrodynamic process. Thanks to this technique, we can transform the solution (the precursor solution) into fiber thanks to an electric field applied. Figure 2.1; illustrates the electrospinning step up. The electrospinning step up is composed of a high-voltage power supply, a syringe pump, a spinneret, and a conductive collector. The voltage delivered can be direct current (DC) or alternating current (AC).

1345

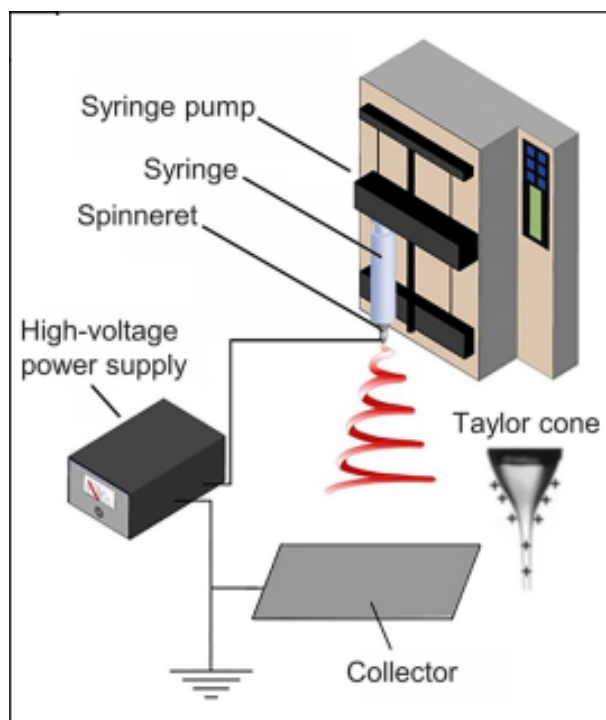


Figure 2.1 – Electrospinning setup^[5]

We can divide the electrospinning process into four-step listed below :

The first step is pumping the precursor solution to the spinneret to obtain a liquid drop. To the electric field, one has a surface tension between the drop and the collector, and that deforms the drop. This high electric field distorts the liquid drop leading to the formation Taylor cone or cone-shaped jet. After the drop deformation and the Taylor cone's apparition, we have a charged jet ejected by the Taylor cone. The second step is the elongation of the charged jet to a straight line by the influence of the electric field. The third step is thinning of the jet due to the electric field and induces an electrical bending instability. And the fourth and last step is the collection of the jet to solid fiber on the grounded collector.^[5] Few parameters can be investigated to influence the fiber made by electrospinning. We can play on the precursor solution to control the film made or during the electrospinning.

In the below table, we can see the processing parameters involved in electrospinning^[6]:

| Solution properties (Precursor solution) | Processing conditions (In the step) | Ambient conditions (In the step) |
|--|---|---|
| Viscosity Polymer concentration Molecular weight of polymer Electrical conductivity | Applied voltage Distance from needle to the collector Volume feed rate Needle diameter | Temperature Humidity Atmospheric pressure |

Table 2.1 – Processing parameters involved in electrospinning

To prepare our fiber, we investigate the parameters of the precursor solution by changing the polymer concentration. After that, we optimize the processing conditions by changing the applied voltage, distance from the needle to the collector, and volume feed rate.

Now, we look at the different steps to prepare our catalytic powder. The first step is the preparation of the precursor : 20% w.t of manganese (II) acetate tetrahydrate ($C_4H_6MnO_4 \cdot 4H_2O$) was mixed with a polymer solution (20% w.t) of Polyvinylpyrrolidone (PVP, MW-3500) and ethanol. The solution is stirred for 24 h at room temperature to give a homogenous solution.

The second step is the elaboration of nanofiber by using electrospinning. The solution is stirred for 24 h at room temperature to give a homogenous solution. The solution prepared is the precursor solution used for the electrospinning. The solution is loaded onto a 5m mL syringe with an 18-gauge metallic needle. We applied an electric field of 9 kV and a flow rate of 1 mL/H. The distance between the grounded collector plate is kept at 12 cm. In Figure 2.2, we have the photo of the electrospun film made. Figure 2.3 shows SEM image of the prepared nanofiber film. We can see that we have various sizes of fiber. We have the smallest fiber, around 248 nm; the largest is about 1.90 μm .



Figure 2.2 – Photo of the film made

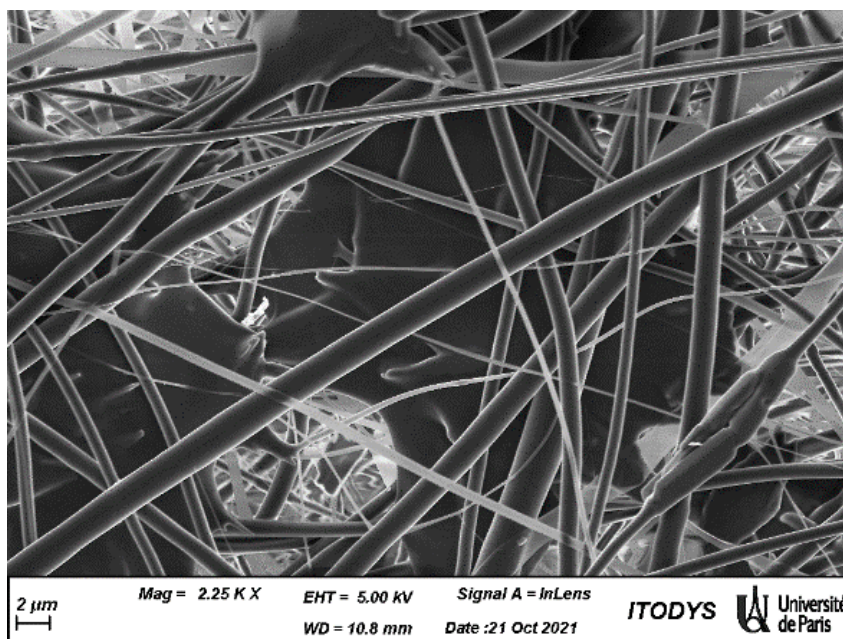


Figure 2.3 – SEM of the film

The third step is the calcination at a specific temperature shown in Table 2.2 for 2 h in air with a ramp of temperature at 5°C per min. We played on the parameters of the temperature and synthesized various powders. We have the table with the different temperatures explored.

| Powder made | Temperature applied during the calcination (°) |
|-------------|--|
| E500 | 500 |
| E600 | 600 |
| E700 | 700 |
| E800 | 800 |
| E900 | 900 |

Table 2.2 – Presentation of the different temperatures evaluated for thermic treatment during 2 H

1380 The name of the powder will include the temperature of the thermic treatment applied to
the fiber made by electrospinning. For example, E500 corresponds to powder treated at 500°C,
and “E” is for encre (how meaning ink in French). The four-step and last one is the crushing
of the powder obtained after calcination with mortar. This final step allows us to analyze the
catalyst powder in the following section.

1385 We obtained it and conducted spectroscopic investigations to find the manganese oxide pro-
duced.

2.2 Spectroscopic investigation

To characterize the obtained catalysts, we will combine various spectroscopy techniques: X-ray photoelectron spectroscopy (XPS), Raman spectroscopy, X-ray diffraction (XDR), and Scanning Electron Microscopy (SEM). All the investigations aim were conducted to find the nature of the manganese oxide nanoparticles.

The first technique used is X-ray photoelectron spectroscopy (XPS). The measurements were made with ThermoFisher Scientific K-Alpha⁺ fitted with a micro-focused, monochromatic Al K α ($h\nu = 1486.6$ eV).

Figure 2.4 shows five XPS spectra of Mn 2p. Each spectrum corresponds to a different powder made at a different temperature. All five spectra have the same response and behaviour. We observed two peaks at 641.3 and 653.0 eV and spin-orbit splitting around 11.7 eV. The values reported are typical of Mn₂O₃.^[7] The binding energy of Mn 2p_{3/2} is 641.4 eV and it is specific to Mn₂O₃ and MnO. Also, we are sure we do not have MnO because we do not see the satellite feature of MnO.

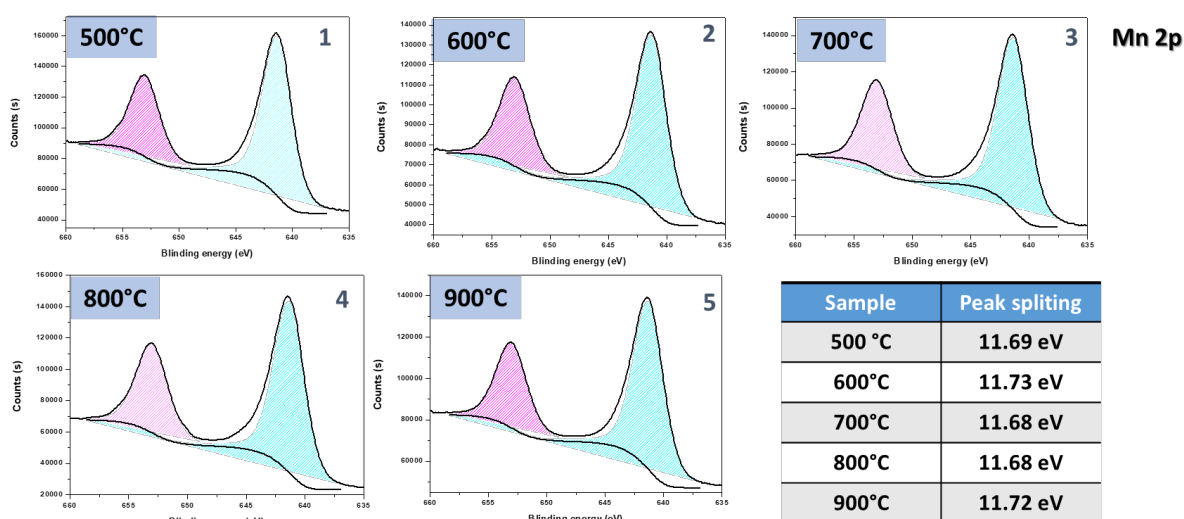


Figure 2.4 – Mn 2p XPS spectra for five manganese oxide powder synthesized with (1) powder made with the thermic treatment at 500° C, (2) 600° C, (3) 700° C, (4) 800° C and (5) 900° C

Figure 2.5 corresponds to all O 1s spectra for the five powders prepared at different temperatures. All samples have similar spectra with a peak at 529.5 eV attributed to the lattice oxygen (O_{latt}) bonding with Mn^[8]. The peak at 531.3 eV corresponds to the surface adsorbed oxygen species (O_{ads}).^[9] The presence of surface adsorbed oxygen species is related to the surface oxygen vacancy that can improve the catalytic activities for ORR. Based on XPS results, the nature of the prepared manganese oxide is Mn₂O₃.

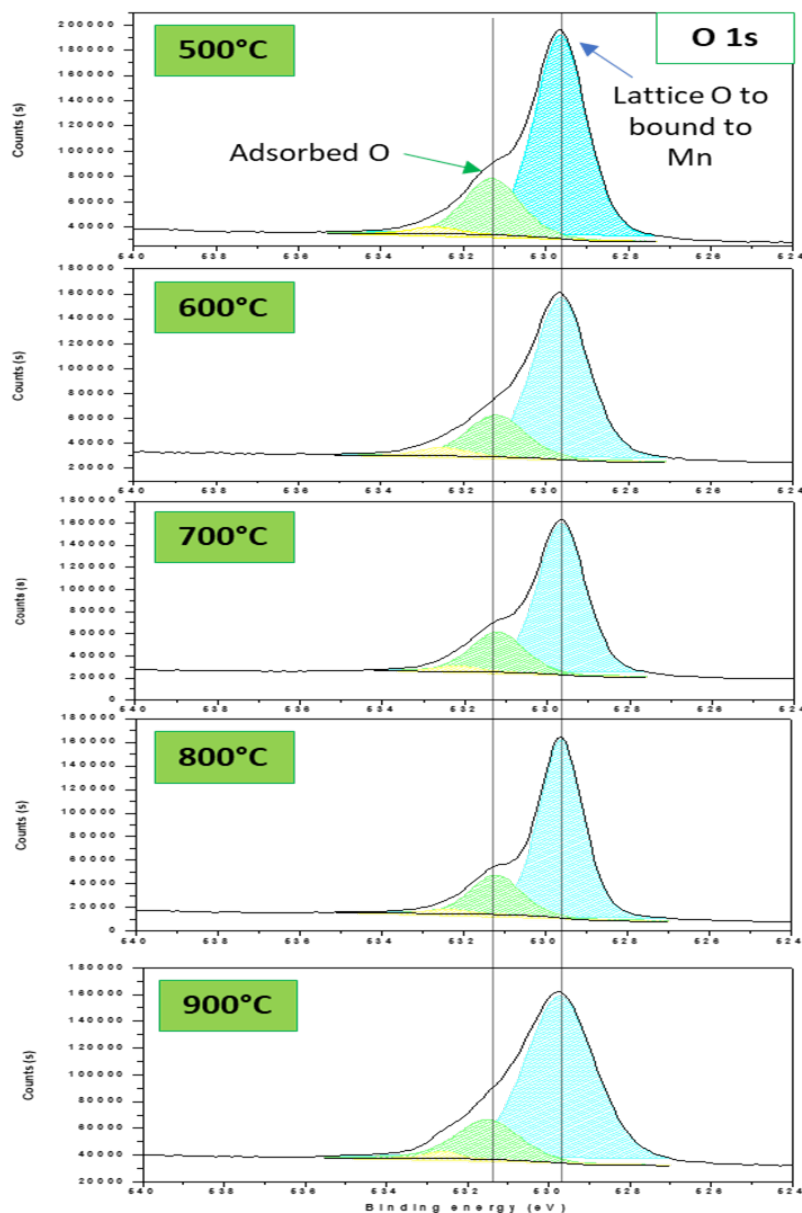


Figure 2.5 – O 1s XPS spectra for five manganese oxide powder synthesized

We used Horiba Jobin Yvon HR 800 Raman spectrometer with a 514 nm wavelength excitation to make the Raman spectroscopy. Figure 2.6 shows the Raman spectra for each powder made. We can see that the Raman active bands are found between 170 and 1000 cm^{-1} . This range of the active band is due to the Mn–O vibration modes of manganese oxides.^[10] We can find Raman bands at 312, 367, and 651 cm^{-1} correspond to the bending modes of Mn_2O_3 . The bending mode highlights the asymmetric stretch of Mn_2O_3 due to the $\text{Mn}^{(\text{III})}$ –O mode vibration group.^[11]

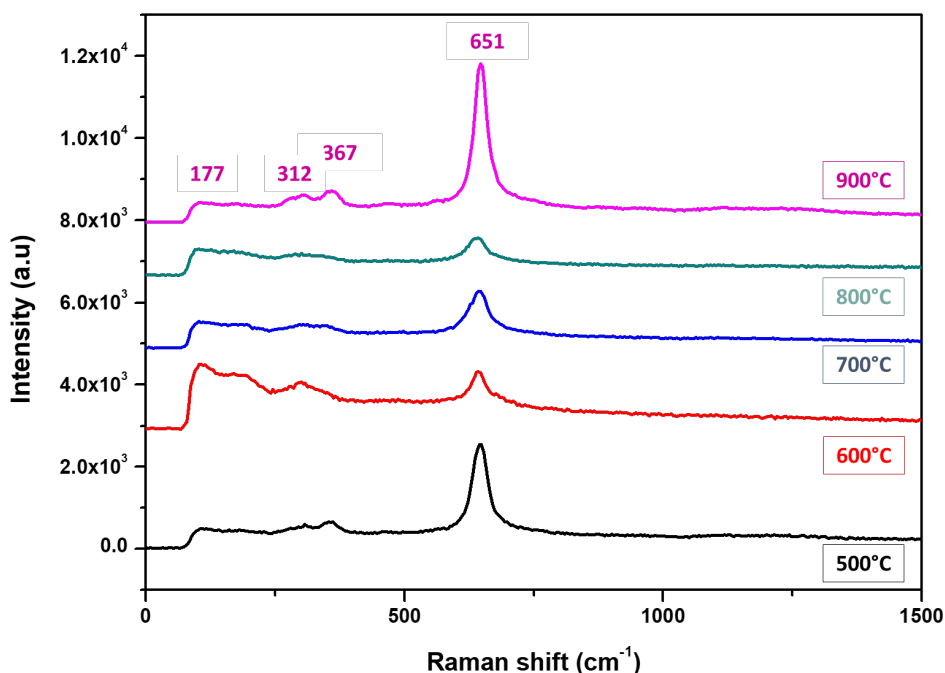


Figure 2.6 – Raman spectra for 500°C (black), 600°C (red), 700 °C (blue), 800°C (green) and 900°C (pink)

The scanning electron microscopy (SEM) images were obtained by MEB-FEG Zeiss (Zeiss SUPRA 40). Figures 2.7 and 2.8 show images obtained with scanning electron microscopy (SEM) of the powder prepared at 500°C (E500) and 900° C (E900). To prepare the sample for SEM imaging, we take the powder made at 500°C (E500) or 900° C (E900), dilute it in ethanol, and drop cast it in ITO (1 X 1 cm).

In figure 2.7, we can see that the nanoparticles are agglomerated. The forms of nanoparticles are in hybrid forms. In some particles, we can see between cubic and orthorhombic morphologies. The sizes of the particles are variable : the smallest particle is at 49 nm ,and the largest is at 81 nm.

In figure 2.8, we have SEM image of the powder prepared at 900°C. The morphology of the nanoparticles in figure 2.8 shows that we have an orthorhombic phase. Also, the sizes are variable: the smallest is around 175 nm, and the largest is around 237 nm.

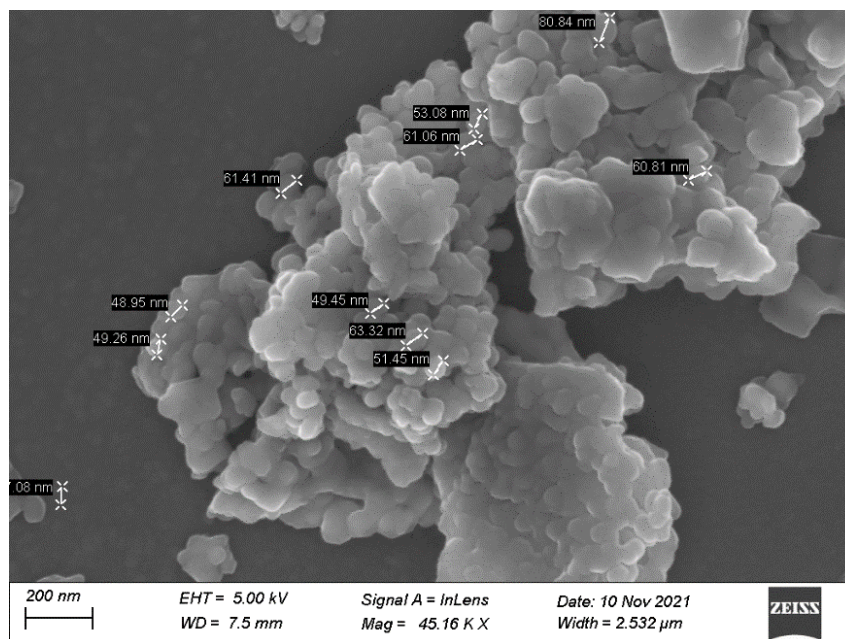


Figure 2.7 – SEM images of E500 deposited onto ITO

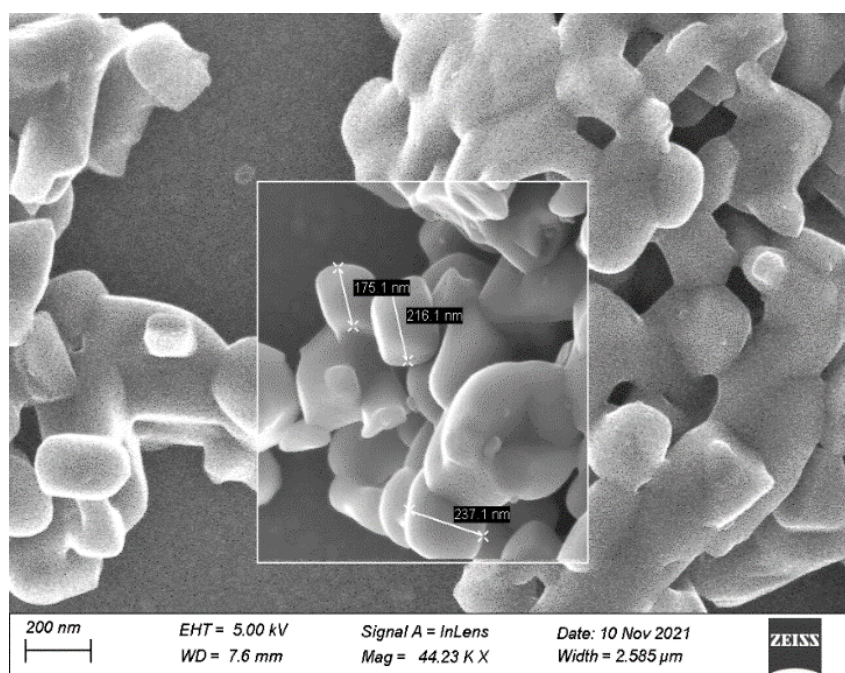


Figure 2.8 – SEM images of E900 deposited onto ITO

In the following part, we will investigate the influence of the phase on the α - Mn_2O_3 structure using XRD. We will also look at the influence of the structure when we look at the mechanism. This next section is a quick highlight on Jahn–Teller distortion. Indeed, Mn_2O_3 SEM images show can be in having different forms like cubic and orthorhombic. These differences in the structure can have an impact on the properties of the synthesized materials.

1430

In the first attendance before the use of the PXRD synchrotron.

Firstly, XRD analysis are carried out with Empyrean Panalytical. This step was crucial to have an idea of the nature of α - Mn_2O_3 . In Figure 2.9 shows XRD spectra.

As for the Raman spectra obtained before, we have the same behaviour for all the samples.

1435 We can see in figure 2.9, XRD was obtained. We can highlight the main characteristic diffraction peaks for 5 samples at 23.1° , 32.9° , 38.2° , and 55.1° , which correspond to the (211), (222), (400), and (440) planes of α - Mn_2O_3 cubic ((space group $Ia3[206]$, JCPDS card No. 00-041-1442).

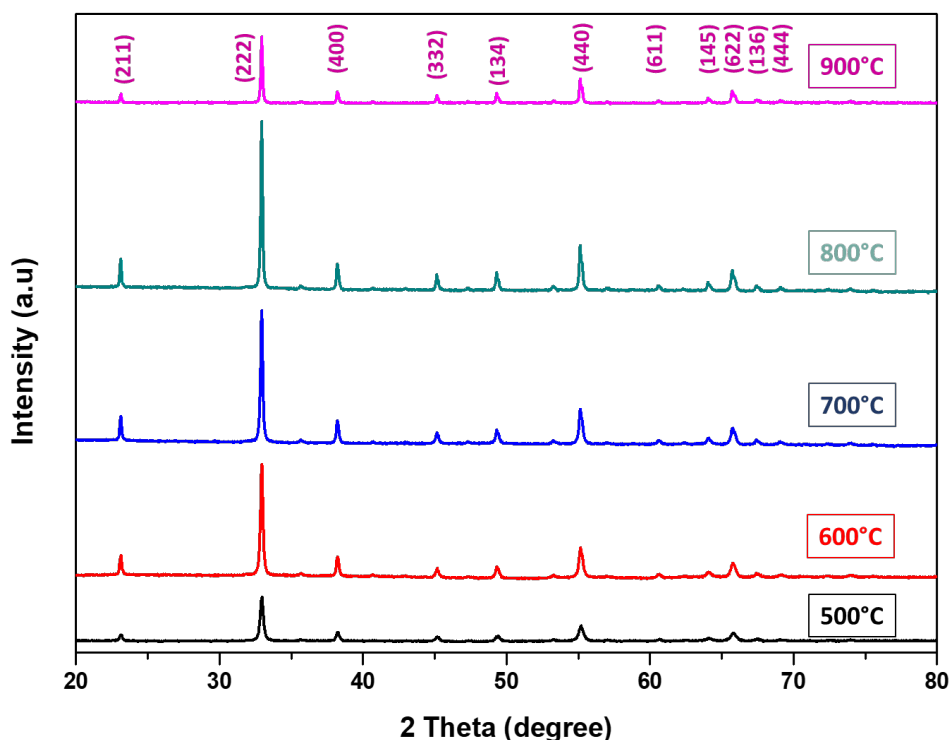


Figure 2.9 – X-ray diffraction patterns of α - Mn_2O_3 were obtained at different temperatures 500°C (black), 600°C (red), 700°C (blue), 800°C (green), and 900°C (pink)

Furthermore, the average crystallite sizes (L) of Mn_2O_3 were calculated according to Scherrer's equation as shown in equation (2.1):

$$1440 \quad L = \frac{K \cdot \lambda}{FWHM \cdot \cos \theta} \quad (2.1)$$

with K is the constant (0.9394), λ is the X-ray wavelength of Cu- $K\alpha$ (1.5148 Å), fill width at half maximum (FWHM) of the XRD peak in radian and θ is the angle of diffraction.

We have in table 2.3, the average crystallite sizes for each powder made at different temperatures.

| Powder sample | Average crystallite sizes (nm) |
|---------------|--------------------------------|
| 500°C | 45 |
| 600°C | 64 |
| 700°C | 87 |
| 800°C | 151 |
| 900°C | 204 |

Table 2.3 – Average crystallite sizes of the powder made at different temperature

We can see clearly that the temperature influences the size of the crystallite: the size increases as the temperature of the thermal treatment increases. Thanks to the X-ray investigation, we see that we have α -Mn₂O₃ cubic. However, they are nearly identical when we compare the patterns of α -Mn₂O₃ cubic and the α -Mn₂O₃ orthorhombic. We will see later that α -Mn₂O₃ cubic and α -Mn₂O₃ orthorhombic may induce a difference in the catalytic effect.

In order to improve the structure determination and the nature of manganese oxide, we perform spectroscopy measurements PXRD synchrotron (line CRISTAL at SOLEIL, Figure 2.10). The use of PXRD synchrotron allows having a clear answer to know if the synthesized Mn₂O₃ is cubic or orthorhombic.

One approach is to see if we have α -Mn₂O₃ cubic for the five samples we thought used the PXRD synchrotron.

To examine the powder with PXRD synchrotron, samples are put into capillaries (internal diameter of 0.3 mm) to decrease the risk associated with the nanoparticle and limit absorption. Through this introduction, we can improve the resolution of the measurement.

The PXRD data were obtained at the Soleil synchrotron, on the Cristal line, through two rapid access projects (proposals 20211694 and 20211727). (Saint-Aubin, France) .

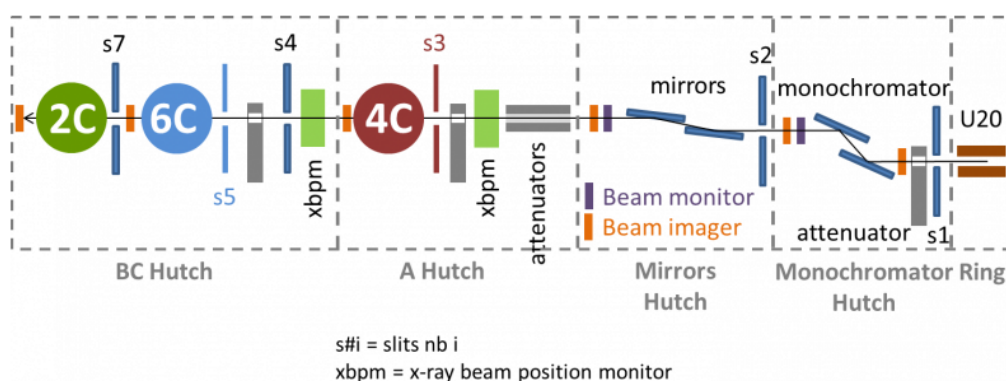


Figure 2.10 – CRISTAL synoptic^[12]

We used the Mythen 1D-detector installed on the 2-circles diffractometer to collect intense

signals in a reasonable time (30 min). We applied high energy (corresponding to the wavelength 0.72844 Å for the first session and 0.51362 for the second one).

1465 To identify the Mineral identification of the powder studied, we used the Highscore Plus 3.0 software with the help of the MAUD program (Material Analysis Using Diffraction). MAUD is an X-ray diffraction program is based mainly on the Rietveld refinement method^[13].

The Rietveld method can analyze the sample with by minimising of the difference between experimental and calculated XRD diagrams by a least-squares procedure. During the experi-
1470 ment, we must take count of the instrumental influence and absorption effects. We must have the same analytical conditions for each sample analyzed. For our case, we used a Lanthanum hexaboride (LaB₆) standard, certified by the National Institute of Standards and Technology (NIST).

In the following part, we are going to look at each powder made at different temperatures. To
1475 study it, we used the MAUD software with the theoretical cubic and orthorhombic phases of Mn₂O₃ to look at the similarity of our samples made. Thanks to that we can figure out the size and shape of the nanoparticles made and found the proportions if we have a mix of the two phases.

The first sample that we are going to focus on is the powder made at 500°C.

1480 In the case of 500°C, we look at figures 2.11 and 2.12 (given by the MAUD software) at the zoom at some show the nature of phases that we can see with a classic X-Ray.

In Figure 2.11 and Figure 2.12, we analyze deeply the spectra in the range of 12°, 16°, 16° and 20°, respectively.

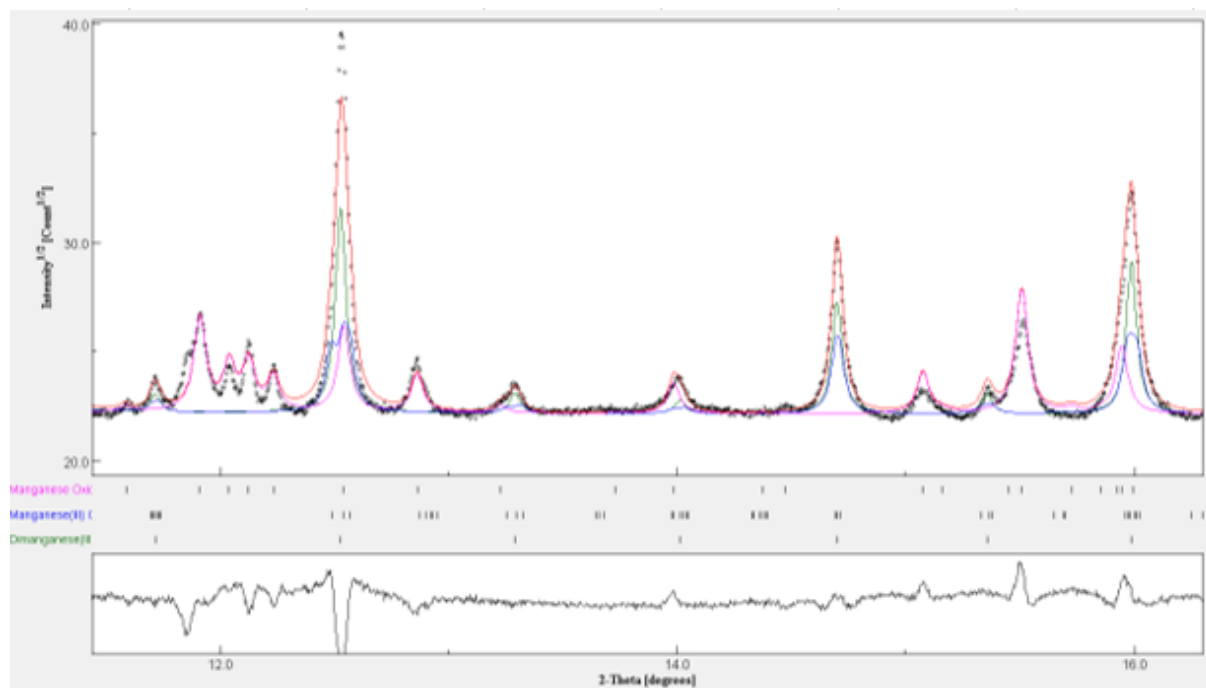


Figure 2.11 – PXDR patterns of α - Mn_2O_3 was obtained at 500°C around 12° and 16° with MAUD

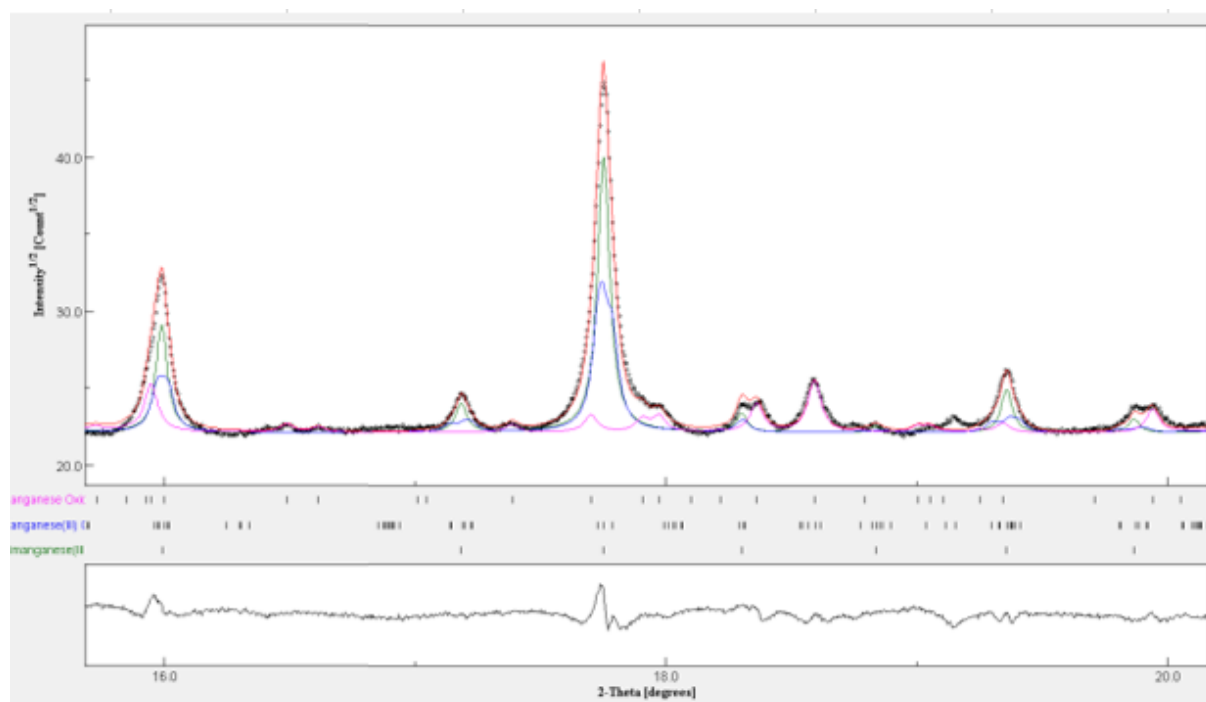


Figure 2.12 – PXDR patterns of α - Mn_2O_3 was obtained at 500°C around 16° and 20° with MAUD

In figures 2.11 and 2.12, we have in red the fitting of the PXDR patterns, in pink we have the signal corresponding to Mn_5O_8 , in blue and green correspond to α - Mn_2O_3 orthorhombic and α - Mn_2O_3 cubic. In table 2.4, we can find the portions of the compounds of our powder made at 500°C obtained with Cristal line.

| | | | |
|-----------------------------------|--------|----------------|----------|
| α - Mn_2O_3 orthorhombic | 30.3 % | sig | 0.468 |
| | | a | 9.387343 |
| | | b | 9.446818 |
| | | c | 9.408613 |
| | | L average (nm) | 43.8 |
| α - Mn_2O_3 cubic | 41.1 % | sig | 0.2270 |
| | | a | 9.415806 |
| | | L average (nm) | 46.2 |
| Mn_5O_8 | 28.6 % | L average (nm) | 38 |

Table 2.4 – Measured obtained with the Cristal line for the powder made at 500°C with a, b and c: lattice parameters; L: average crystallite sizes and sig or X^2 : Goodness of Fit

Thanks to the measurement and MAUD calculations, we can see that we have a trace of Mn_5O_8 (28,60%). Accordingly, we have the two phases in the sample. This information wasn't given in previous XRD investigations (classical XRD). We can see that we have the presence of the orthorhombic in the Pcab space group. This information wasn't found in the earlier study made by classic XRD. We have a higher part of cubic (41.1 %) than orthorhombic (30.3 %). We have a hybrid structure mix of both structures. It indicates that the measurements obtained with PXRD synchrotron improve the structure determination. If we look at the average crystallite sizes (L), we are around the same value that we obtain with the classic XDR. We found 45 nm, with the Cristal line we have 43.8 nm for the cubic one and 46.2 nm for the orthorhombic one.

In the second case study, we are going to look at the powder made at 600°C. We used the same method that we had seen before. Figures 2.13 and 2.14 are given by MAUD software.

In figures 2.13 and 2.14, we have in red the fitting of the PXDR patterns. For α - Mn_2O_3 orthorhombic and α - Mn_2O_3 cubic, the fitting is in blue and green respectively.

In table 2.5, we can find the portions of the compounds of our powder made at 600°C.

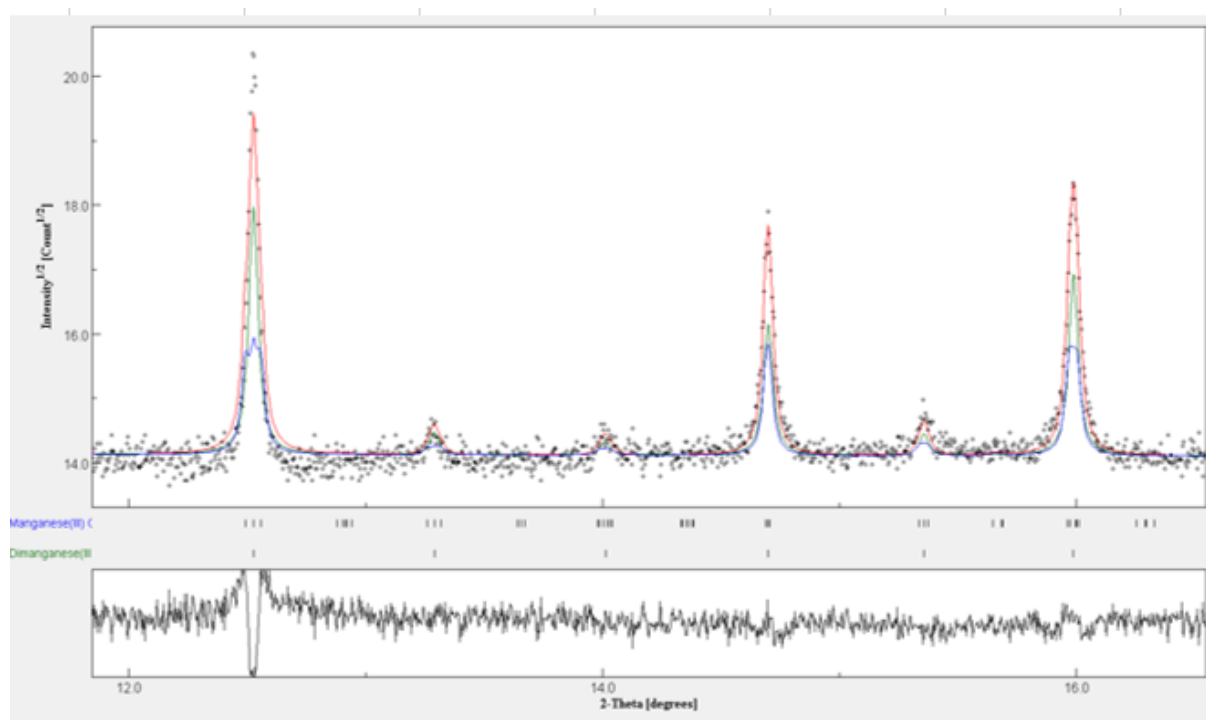


Figure 2.13 – PXDR patterns of α - Mn_2O_3 was obtained at 600°C around 12° and 16° with MAUD

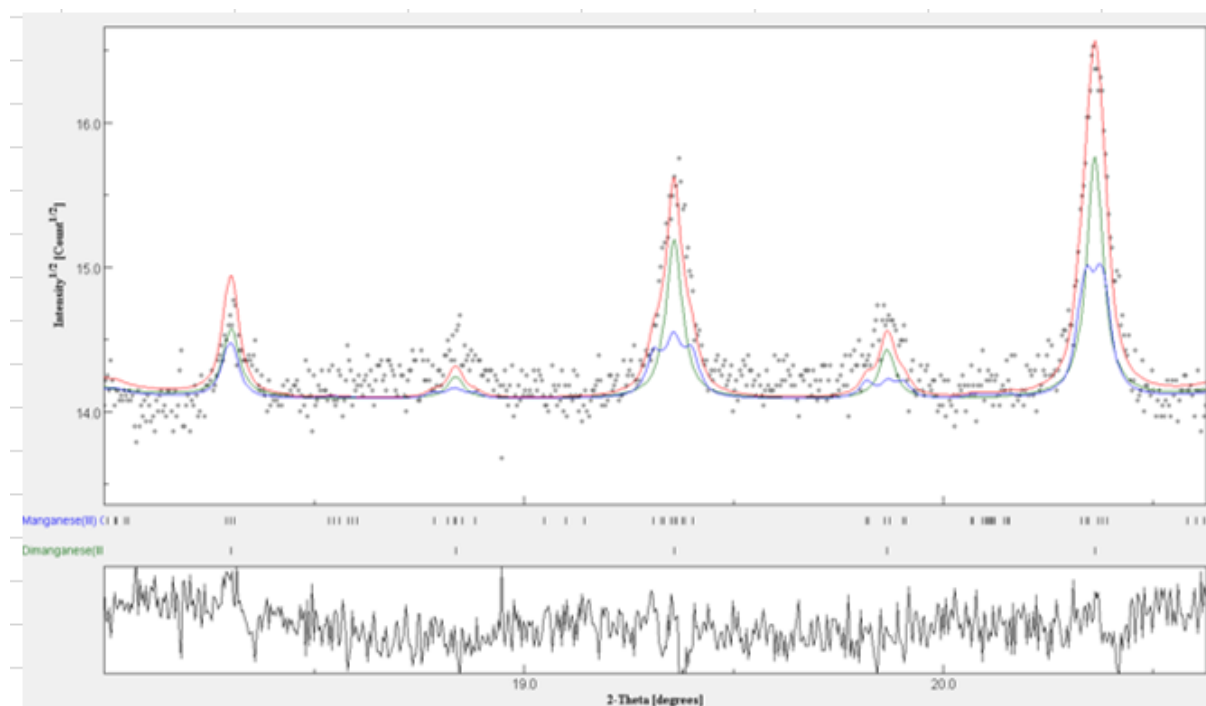


Figure 2.14 – PXDR patterns of α - Mn_2O_3 was obtained at 600°C around 19° and 20° with MAUD

Like in the case of 500°C, we have a mix of cubic (57.2 %) and orthorhombic (42.8 %).

| | | | |
|---|--------|----------------|----------|
| α -Mn ₂ O ₃ orthorhombic | 42.8 % | sig | 0.468 |
| | | a | 9.3930 |
| | | b | 9.4419 |
| | | c | 9.4160 |
| | | L average (nm) | 63.3 |
| α -Mn ₂ O ₃ cubic | 57.2 % | sig | 0.2270 |
| | | a | 9.415949 |
| | | L average (nm) | 52.3 |

Table 2.5 – Measured obtained with the Cristal line for the powder made at 600°C

1505 If we look at the average crystallite sizes (L) for the cubic phase is 52.3 and 63.3 nm for the orthorhombic phase. If we compare the results obtained with classic XDR, we have 64 nm. This value is closer to the orthorhombic.

The third case is about the powder made at 700°C. In figure 2.15, we look at around 12° and 16° and it is given by MAUD software. The red line corresponds to the fitting of the PXDR patterns. And finally, in blue and green, we have for α -Mn₂O₃ orthorhombic and α -Mn₂O₃ cubic fitting. Table 2.6, gives the parameters obtained by Cristal measured for the sample made at 700°C.

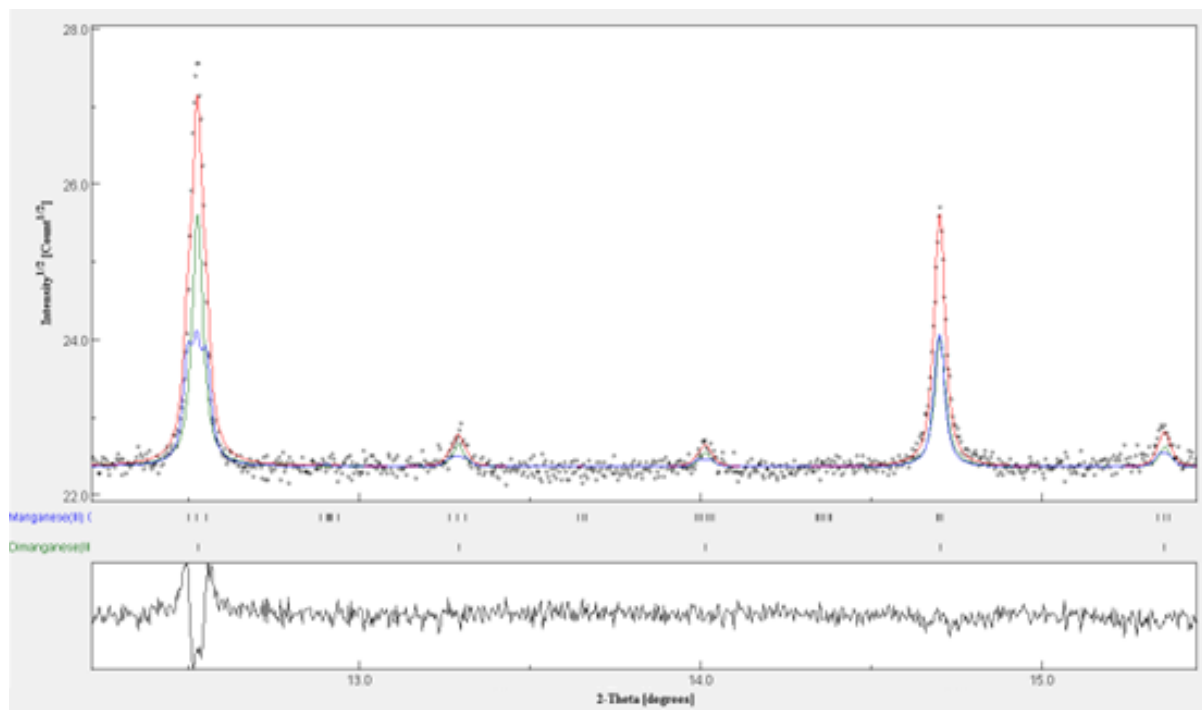


Figure 2.15 – PXDR patterns of α -Mn₂O₃ was obtained at 700°C around 12° and 16° with MAUD

| | | | |
|---|--------|----------------|----------|
| α -Mn ₂ O ₃ orthorhombic | 47.6 % | sig | 0.468 |
| | | a | 9.3952 |
| | | b | 9.4460 |
| | | c | 9.4161 |
| | | L average (nm) | 81.3 |
| α -Mn ₂ O ₃ cubic | 52.4 % | sig | 0.2270 |
| | | a | 9.414182 |
| | | L average (nm) | 67.04 |

Table 2.6 – Measured obtained with the Cristal line for the powder made at 700°C

When we look at the obtained parameters, we can see that the percentage of both phases are almost close even if we have a small advantage for the cubic phase. Like two previous studies, we have a hybrid between the two phases. The average crystallite sizes (L) are 81.3 and 67.04 nm for the orthorhombic phase and the cubic phase. The size obtained with the classic XRD is 87 nm. The value is closer to the orthorhombic than cubic. We can see that we observe the phase transition when we increase the temperature. We will look at the two last samples to see this hypothesis.

The fourth sample, that we are going to look at is the powder prepared at 800°C.

In Figure 2.16, we look at around 13° and 15°, and in figure 2.17, we are around 18° and 20°. Similar to the previous cases, the red line corresponds to the fitting of the PXRD patterns and α -Mn₂O₃ orthorhombic and α -Mn₂O₃ cubic fitting in blue and green, respectively.

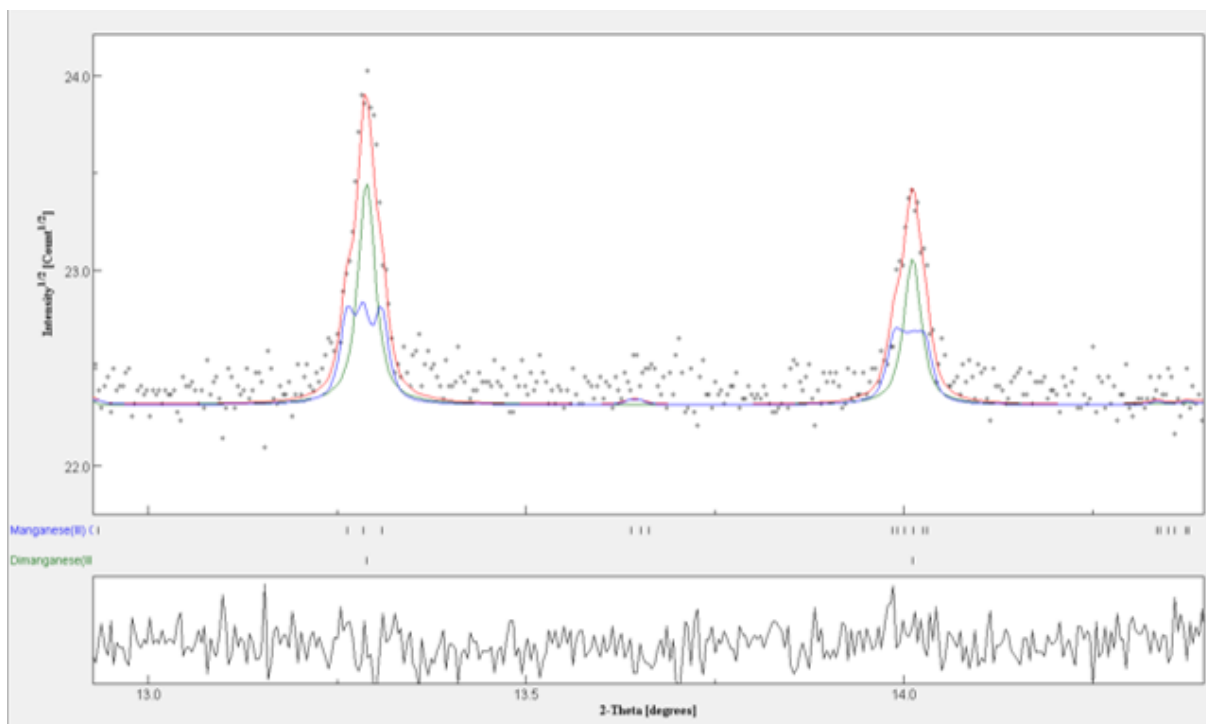


Figure 2.16 – PXDR patterns of α - Mn_2O_3 was obtained at 800°C around 13° and 15° with MAUD

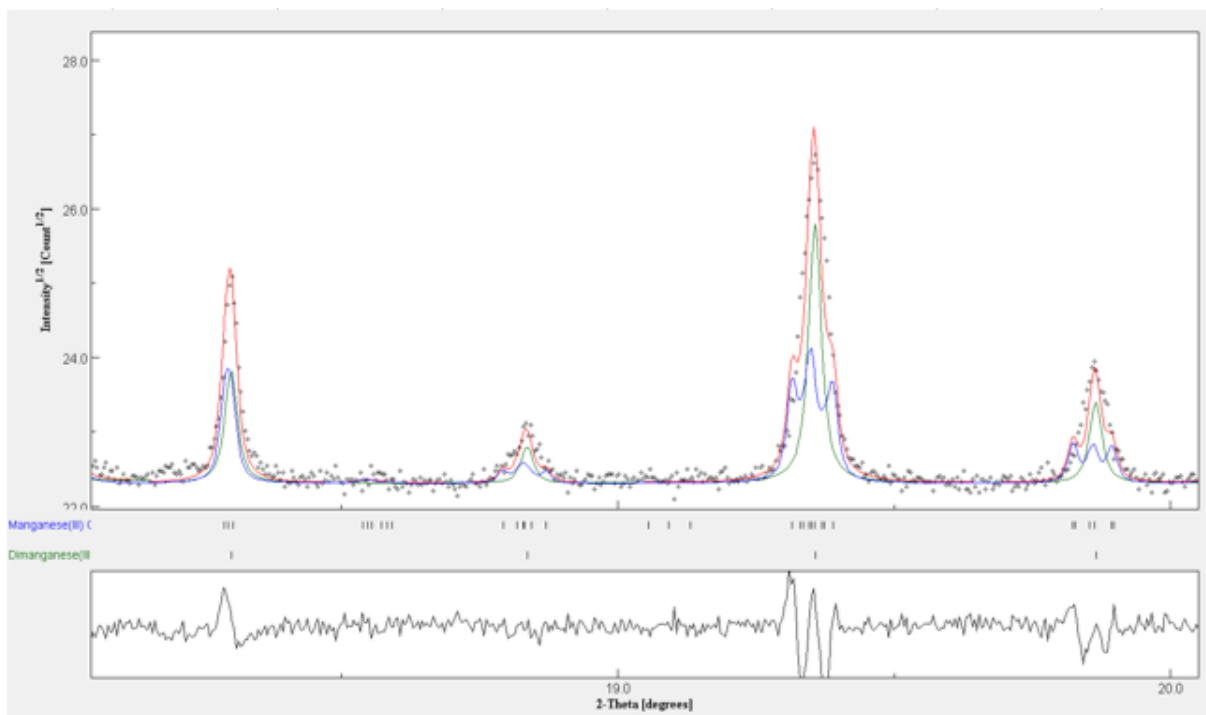


Figure 2.17 – PXDR patterns of α - Mn_2O_3 was obtained at 800°C around 18° and 20° with MAUD

In table 2.7, we have the different parameters given by our sample at 800°C.

| | | | |
|---|------|----------------|----------|
| α -Mn ₂ O ₃ orthorhombic | 50 % | sig | 0.468 |
| | | a | 9.3996 |
| | | b | 9.4383 |
| | | c | 9.4202 |
| | | L average (nm) | 134.9 |
| α -Mn ₂ O ₃ cubic | 50 % | sig | 0.4680 |
| | | a | 9.416624 |
| | | L average (nm) | 99.6 |

Table 2.7 – Measured obtained with the Cristal line for the powder made at 800°C

1525 We have a hybrid with the same amount of cubic and orthorhombic phases. The average
crystallite size (L) is larger for the orthorhombic phase 134.9 nm compared to the cubic 99.6
nm. When we look at table 2.3, we can see that the size is 151 nm which is close to the size of
the orthorhombic phase.

1530 In the last sample is prepared at 900°C. In Figures 2.18 and 2.19, we analyze the spectra around
17.4° and 18.2°, and around 22.4° and 23.2°. In both figures, the fitting of the PXDR patterns
and in blue and green indicated a perfect matching with orthorhombic α -Mn₂O₃.

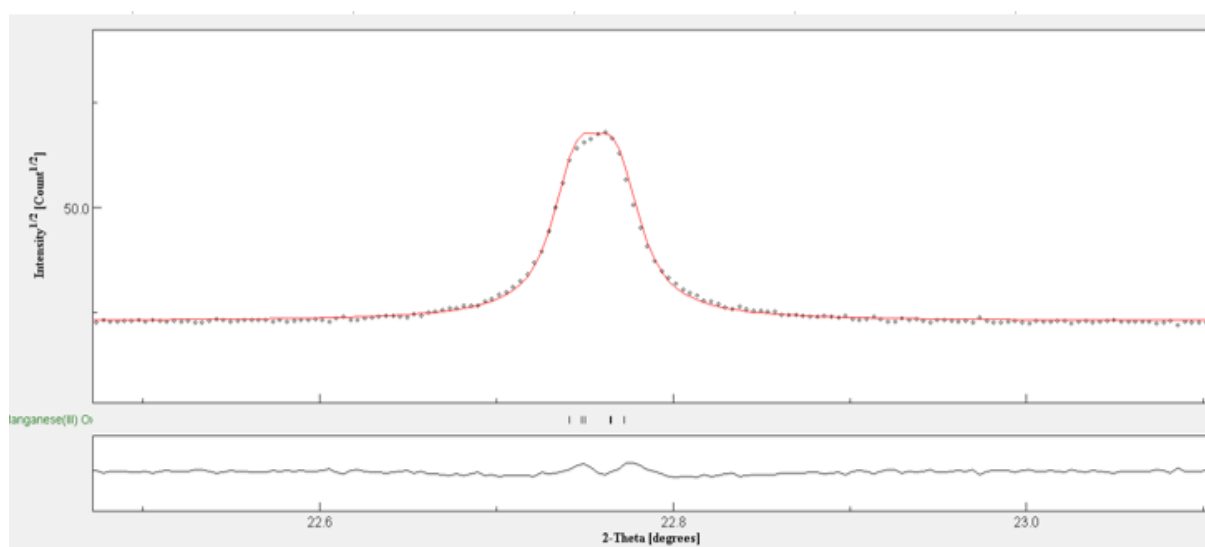


Figure 2.18 – PXDR patterns of α -Mn₂O₃ was obtained at 900°C around 17.4° and 18.2° with MAUD

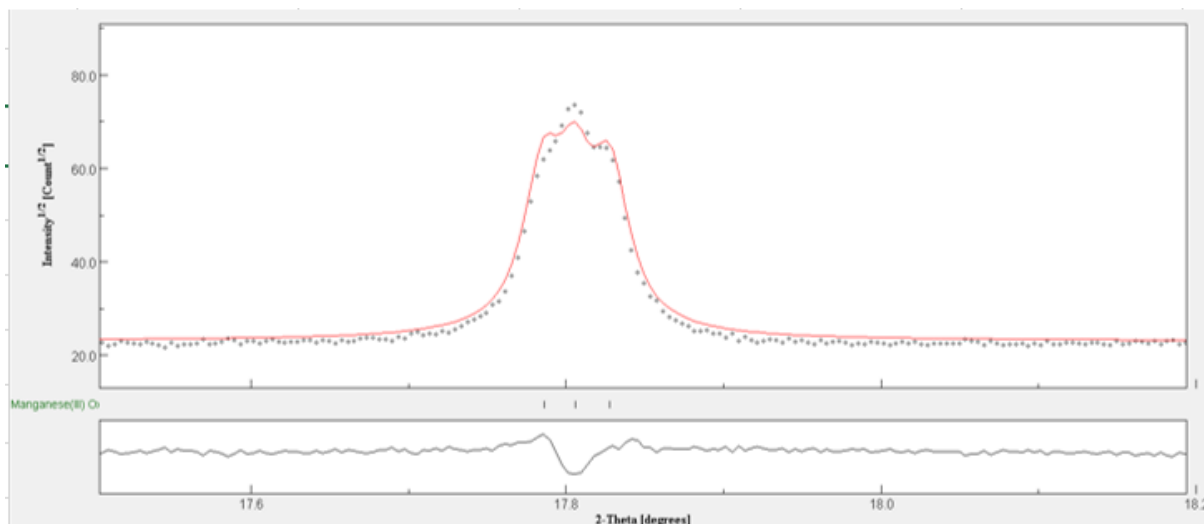


Figure 2.19 – PXDR patterns of α - Mn_2O_3 was obtained at 900°C around 22.4° and 23.2° with MAUD

The parameters for the powder prepared at 900°C are reported in Table 2.8.

| | | | |
|---|-------|----------------|--------|
| α - Mn_2O_3 orthorhombic | 100 % | sig | 1.5126 |
| | | a | 9.4040 |
| | | b | 9.4154 |
| | | c | 9.4258 |
| | | L average (nm) | 171.5 |

Table 2.8 – Measured obtained with the Cristal line for the powder made at 900°C

In table 2.8, we can clearly see that we have an orthorhombic phase with a Goodness of Fit (sig) at 1.5126. Closer to 1 is the goodness of fit ; better will be the fitting. The average crystallite size (L) is 171.5 nm and is agreement with the previous value found with the classic XRD (see table 2.3).

Thanks to the acces to the Soleil synchrotron, on the Cristal line, we were able to find the structure of the powder made at different temperatures. If we compare it with the first studied XRD, we can see have the same range for the average crystallite size (L) for the different powders analyses. And that observations locked the affirmations that the powder made with a higher temperature is larger. The complexity of finding the phases of Mn_2O_3 was highlighted with the use of a synchrotron. With the PXRD synchrotron investigations, we found the phases more complex than a simple α - Mn_2O_3 with cubic phase for all samples.

The first observation made was that we didn't have α - Mn_2O_3 with a cubic phase, but a hybrid phase composed of orthorhombic and cubic forms. Figure 2.20 regrouped all the parameters

obtained by the Cristal line for the powders made.

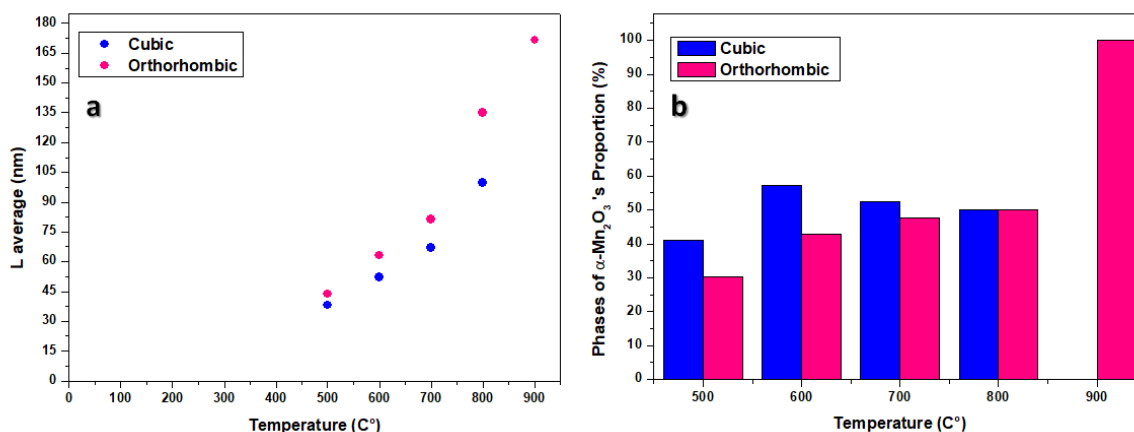


Figure 2.20 – (a) Evolution of the average crystallite sizes L (nm) as function of the temperature ($^{\circ}\text{C}$) (b) Evolution of the Phases of $\alpha\text{-Mn}_2\text{O}_3$'s Proportion (%) as function of the temperature ($^{\circ}\text{C}$)

We can see that in Figure 2.20, we increase the temperature for the powder, we are more likely to produce $\alpha\text{-Mn}_2\text{O}_3$ with an orthorhombic form and increase a hybrid phase composed of cubic and orthorhombic phases saw the other powders.

1550

Thanks to the XRD investigations seen previously, we can have $\alpha\text{-Mn}_2\text{O}_3$ with an orthorhombic phase or a cubic phase. (Figure 2.21)

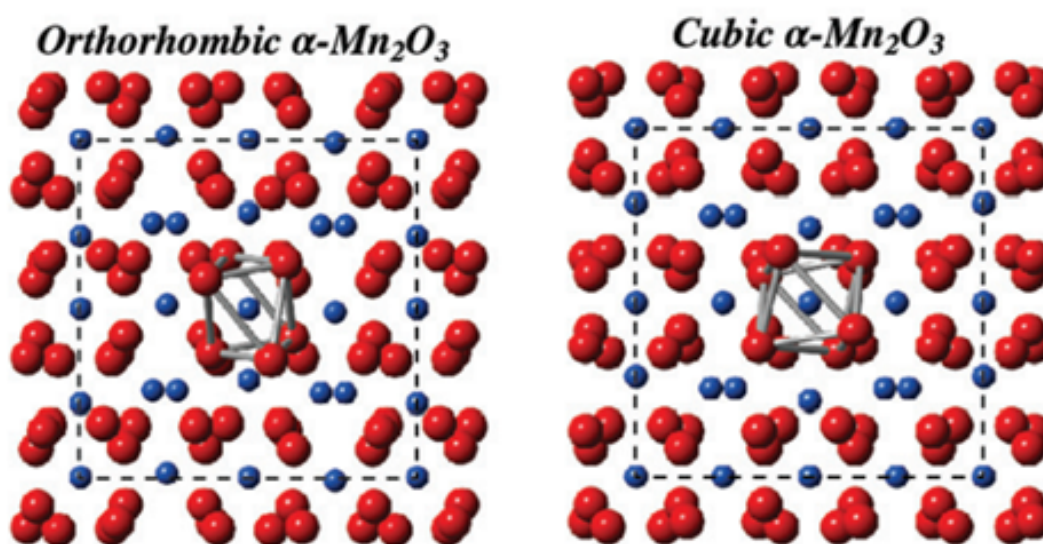


Figure 2.21 – Orthorhombic and cubic $\alpha\text{-Mn}_2\text{O}_3$ structures^[14]

The orthorhombic phase is well-known to be stable at room temperature with distortion. Geller^[15] studies showed transition of the orthorhombic phase to cubic around ~ 302 K. In recent studies, Henzie and al^[16] proved the suppression of Jahn–Teller distortions of α -Mn₂O₃ orthorhombic to cubic phase. Indeed, the orthorhombic exhibits high activity with respect to ORR. The crystalline structure of Bixbyite α -Mn₂O₃ is composed of five symmetry-inequivalent MnIII O₆ octahedra. They are connected thanks to corner- and edge-sharing as shown in Figure 2.22.

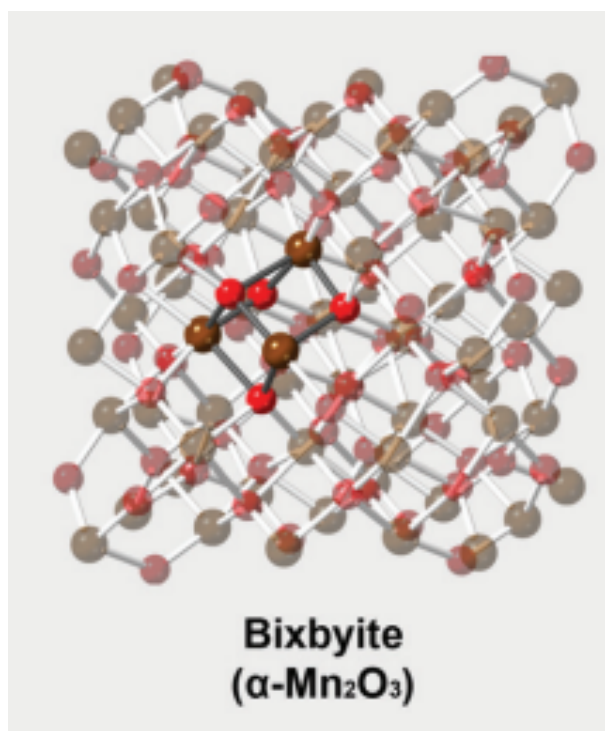


Figure 2.22 – Crystal structures of α -Mn₂O₃^[17] With Mn^(III) and O a brown and red sphere

Jaramillo and al.^[18] prepared thin films of nanostructured manganese oxide composed of Mn³⁺, which has a great catalytic activity through the OER and ORR in alkaline media. To understand the high catalytic activity for the Mn^{III} species, we must look at the electronic structure. There is a Jahn–Teller distortion for these manganese oxides with high spin electronic configuration of the Mn^{III} octahedron t_{2g}^3, e_g^1 .^[19] For the orthorhombic phase, there is a Jahn–Teller distortion. This distortion can be translated by the elongation of two long Mn–O bonds. These flexible Mn–O bonds will increase the formation of Mn–OH₂ species and improve the catalytic affinity.^[19]

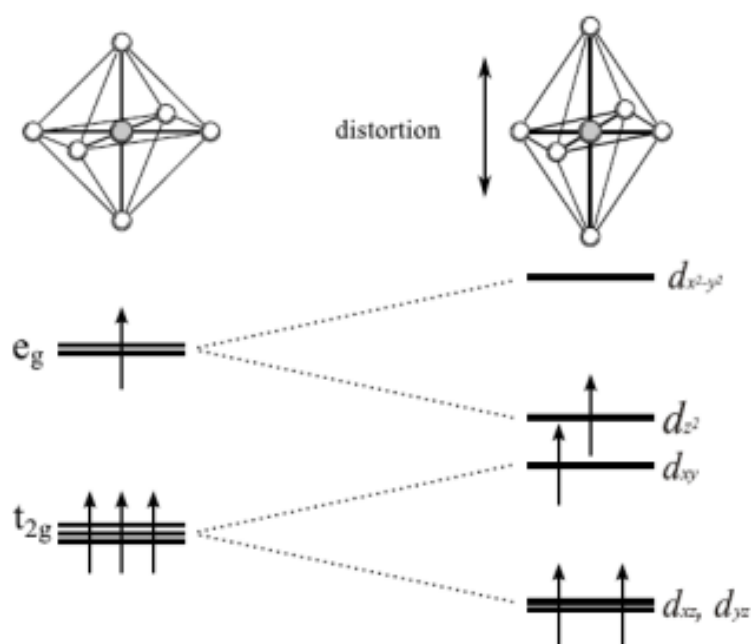


Figure 2.23 – Jahn-Teller distortion for $\text{Mn}^{(\text{III})}\text{O}_6$ octahedra^[20]

In the next section, we look at the electrochemical investigation lead by our powder made
 1570 and the mechanism link to the structure and the micro kinetics studies given by its.

The first step of the electrochemical investigation is the use of rotating ring disk electrode
 (RRDE) to be a first approach to understand the mechanism obtained by our powder made.

2.3 Electrochemical investigation

2.3.1 Investigation of manganese oxide with rotating ring-disk electrode RRDE

To study the oxygen reduction reaction (ORR), we used the rotating ring-disk electrode
 (RRDE) to find the number of electron exchanges, and the percentages of hydrogen peroxide
 produced HO_2^- . These informations will give us an idea of the ORR process that we will in-
 vestigate. The RRDE electrode comprises two electrodes: a platinum, which corresponds to
 1580 the ring electrode, and a glassy carbon, which corresponds to the disk electrode. The identi-
 fication of the species is given by the fact that the reaction products of the disk electrode will
 be diffused to the ring electrode and detected on it. If we look at the RRDE during ORR, we
 can see that RRDE can find the intermediate given during the reaction. We can show if we are
 producing HO_2^- (or H_2O_2 in acidic media). The oxygen will be reduced to HO_2^- (or H_2O_2) at
 1585 the disk. The species captured here is the intermediate or the H_2O . The species captured here
 will be oxidized at the ring electrode. To have this, we must apply a fixed potential for the

platinum ring (here 1.33 V/RHE).

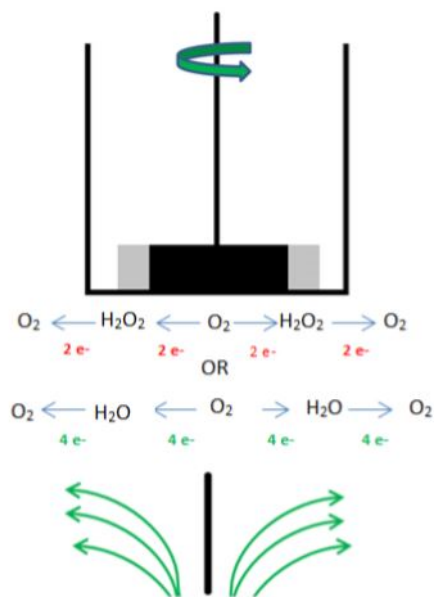


Figure 2.24 – Schema of Rotating ring-disk electrode

One parameter we have not with RDE but present in RRDE is the collection rate N . This parameter N corresponds to the ratio of the amount of the oxidized species at the ring with respect to species reduced at the disk. We will look closer at the powder made at 500°C.

To study it, we prepare a catalytic ink that will be deposited onto the electrode. The ink is composed of 10 mg of catalyst (here E500) and diluted in a solution of 25 μL Nafion[®] and 175 μL EtOH and sonication for 30 min. We drop cast 10 μL of the ink to the glassy carbon of the RRDE electrode. The final step is the drying step of the catalyst deposited and it gives the homogeneous film on the glassy carbon of RRDE.

And the blank is 500 μL of ethanol with of 25 μL of Nafion[®].

The reference of the electrode is E7R9 ThinGap Fixed-Disk RRDE tips with 320 μm gap composed with glassy carbon disk = 0.247 cm^2 , platinum ring = 0.187 cm^2 made by PINE. The measurements were performed in the three-electrode system with RRDE electrode as working electrode, a stainless-steel mesh, and saturated Ag/AgCl electrodes were used as counter electrodes and reference electrodes. The measurements were carried by CHI920C potentiostat (CH Instruments, Austin, Texas).

Figure 2.25 corresponds to the linear sweep voltammetry (LSV) recorded for ink catalyzed (with E500) and the blank. LVS was performed in 0.1 M KOH solution at 1600 rpm with 10 $\text{mV}\cdot\text{s}^{-1}$ as the scan rate under O_2 atmosphere.

The comparison between the two curves shows that we have selectivity for ORR electrocatalytic activity with the catalyst made. If we look closer at the curve form of ink with the catalyst, we can see that we have two reduction waves. The presence of these two reduction waves can highlight the process during the ORR. It can suggest that we have consecutive two-electron steps with the generation of HO_2^- as an intermediate. In our studies, we find two parameters that are important to evaluate the catalytic activity.

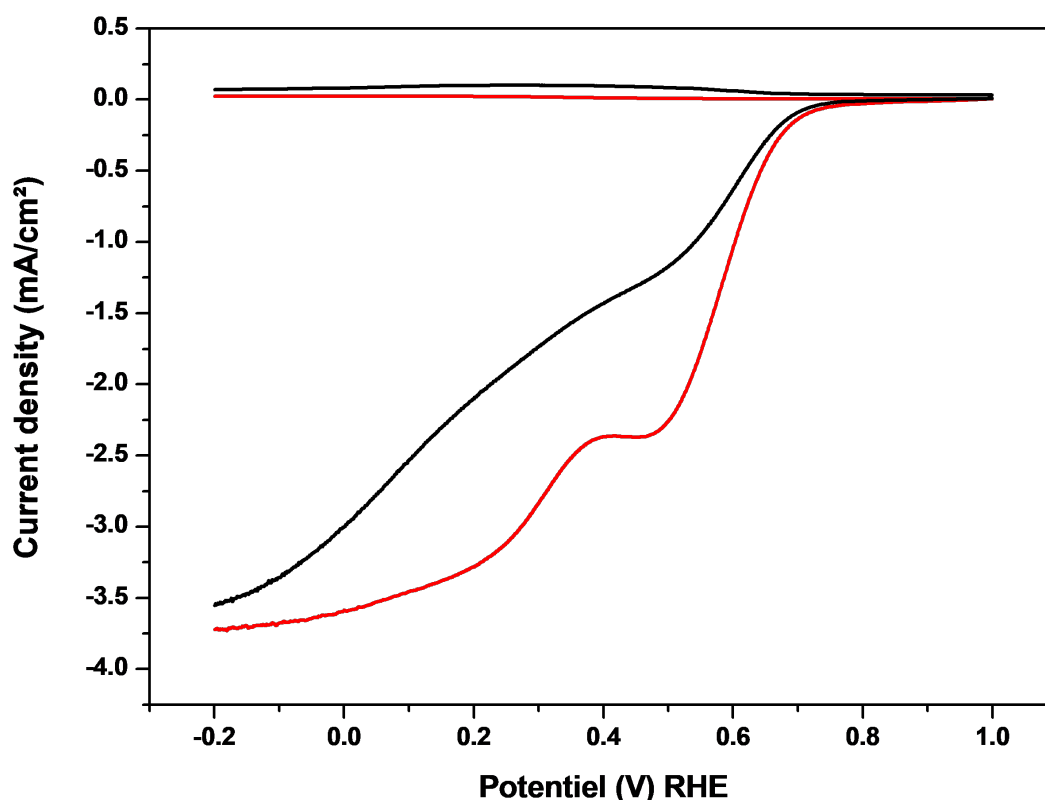


Figure 2.25 – LSV comparison of ORR polarization curves between the blank (black) and the catalytic ink E500 (red), in O_2 saturated 0.1 M KOH solution, using RRDE at rotation 1600 rpm with 10 mV/s scan rate

The first parameter here, onset potential E_{onset} corresponds to the thermodynamic barrier of the reaction, in our case, it is the oxygen reduction reaction. The determination of the onset potential E_{onset} , it found in two ways. The first way defines onset potential E_{onset} is the potential where the current starts to deviate from the baseline^[21]; here we define it at the potential corresponding to 0.1 mA/cm². The second way is to trace the intersection between tangents from the non-faradaic zone and faradaic zone^[22].

Herein, we choose to use the first way to find the onset potential. We obtained onset potential reduction around 0.712 V vs RHE for the catalytic ink and for the blank 0.694 V vs. RHE. The

value of E_{onset} of our catalyst being more positive highlights the selectivity toward ORR.

The second parameter, current density J_d can be used to analyze the kinetics of the reaction. It allows determining the number of electrons exchanged, or the percentage of HO_2^- produced.

Figure 2.26 shows, we have recorded LSV on RRDE at various rotation rates. We can see that we also observed the current presents two reduction current waves at the disk electrode. These waves are both attributed to two-electron reduction as the intermediaries to the reduction mechanism. Also, LSV shows that the limiting current is proportional to the square root of the rotation rate.

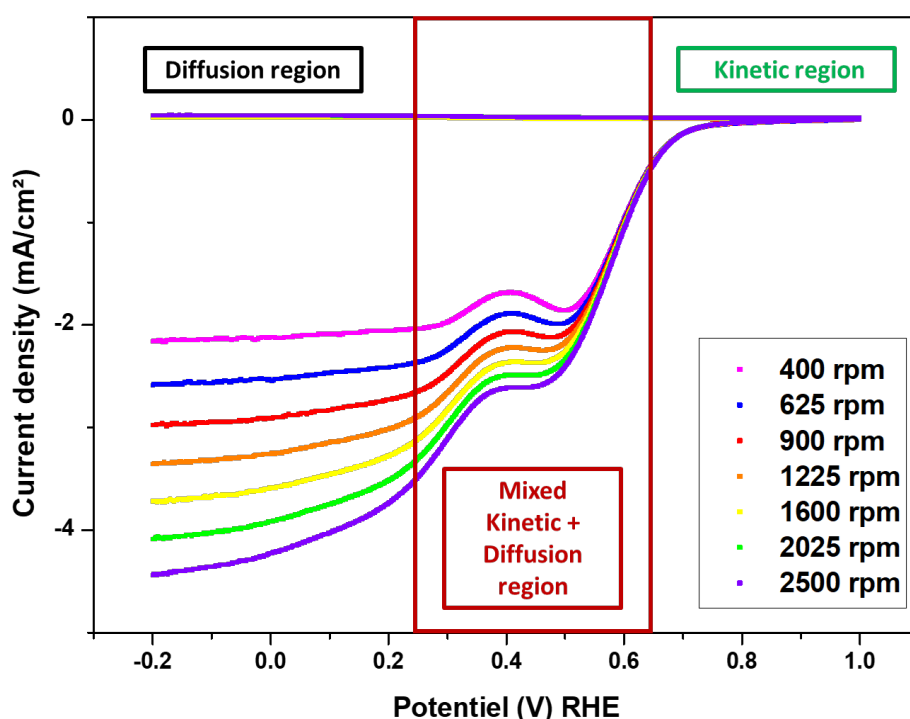


Figure 2.26 – ORR polarization curves in O_2 -saturated 0.1 M KOH solution using RRDE for powder made at 500°C in ink form

The use of the RRDE can give access to basic kinetic parameters controlling to understand the ORR how take place at the electrode and to find the efficacy of the catalyst studied.

If we look at figure 2.26, we can see that electrochemical reaction is controlled differently depending on the potential at which the electrode we are. We can divide the graph into three parts :

- (i) A region controlled by the kinetic phenomenon
- (ii) A mixed controlled region, by the mass transport controlled region
- (iii) A hybrid regime controlled by potential range limited by both phenomenons

The current density can be defined by the Koutecky-Levich equation^[23]:

$$\frac{1}{|J|} = \frac{1}{|J_{dif}|} + \frac{1}{|J_k|} \quad (2.2)$$

where J_{dif} corresponds to the density current controlled by the diffusion (Levich current) given by the following equation:

$$J_{dif} = 0.201 \cdot n F A D^{2/3} \nu^{-1/6} \omega^{1/2} C \quad (2.3)$$

With J_{dif} : density current controlled by diffusion (mA.cm⁻²)

n: the number of electrons exchanged

A: Surface area of the electrode (cm²)

F: Faraday constant (C.mol⁻¹)

D: Diffusion coefficient of O₂ (cm².s⁻¹)

ν : Dynamic viscosity of the electrolyte solution (cm².s⁻¹)

ω : Rotation speed of the electrode (rpm)

C₀: bulk concentration of O₂ (mol.cm⁻³)

In the literature, we can find 0.62 instead of 0.201, and it is because the rotation speed is given in rad.s⁻¹. J_k corresponds to the density current control under the kinetic region and expressed by the following equation:

$$J_k = n F A k C_0 \quad (2.4)$$

where k is the electron-transfer rate constant.

We can go back to the percentage H₂O₂ or HO₂⁻ (depending on the media studied) produced and the electron transfer number n. The electron transfer number n is determined by

$$n = \frac{4 \cdot |J_d|}{|J_d| + \frac{J_r}{N}} \quad (2.5)$$

and the percentage H₂O₂ or HO₂⁻% is given by :

$$H_2O_2 \text{ or } HO_2^- \% = \frac{200 \frac{J_r}{N}}{|J_d| + \frac{J_r}{N}} \quad (2.6)$$

Knowing the platinum ring collection rate N_c in RRDE that was determined previously by

$$N_c = \frac{J_r}{J_d} \quad (2.7)$$

We use equations (2.5) and (2.6) to determine the number of electrons exchanged and % HO₂⁻ in the window of potential studied for ORR. Figure 2.27 reports the evolution of electron transfer number (in black) and the percentage of HO₂⁻ produced (blue) as a function of the potential

window studied. This potential window corresponds to the mixed region to the diffusion region i.e 0.6 to -0.2 V vs RHE.

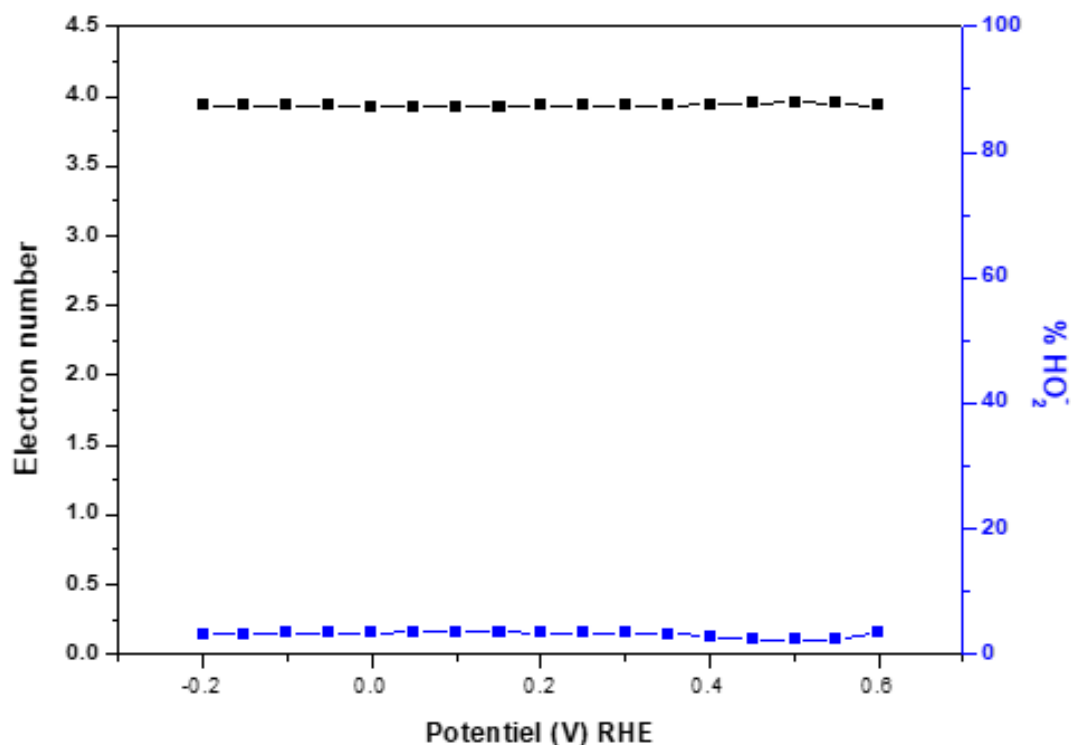


Figure 2.27 – Variation of the electron number and the % HO₂⁻ as function of Applied potential (V) RHE for the powder made at 500°C in ink form

One obtains an electron transfer number near 4 and low percentage production of HO₂⁻. These results indicate that E500 electrocatalyst exhibit high a selectivity of the production for hydroxyde. Previously, we reported in the bibliography part (first chapter) that there are various ORR electroreduction mechanisms leading to water : 4 electrons pathways, and 2+2 electrons pathways.

Before analyzing in detail, the ORR mechanism, we compare first the catalytic activity of the prepared catalysts. To this end, we use the same strategy as for E500. Figure 2.28 shows the electron number, and the percentage of produced HO₂⁻. In both two figure 2.28, we use the same colour code that we saw in the legends of each figure. All the five series studied was made the 3 times to look at the reproductivity. We take the average rate of each parameters studied to make the figure 2.28.

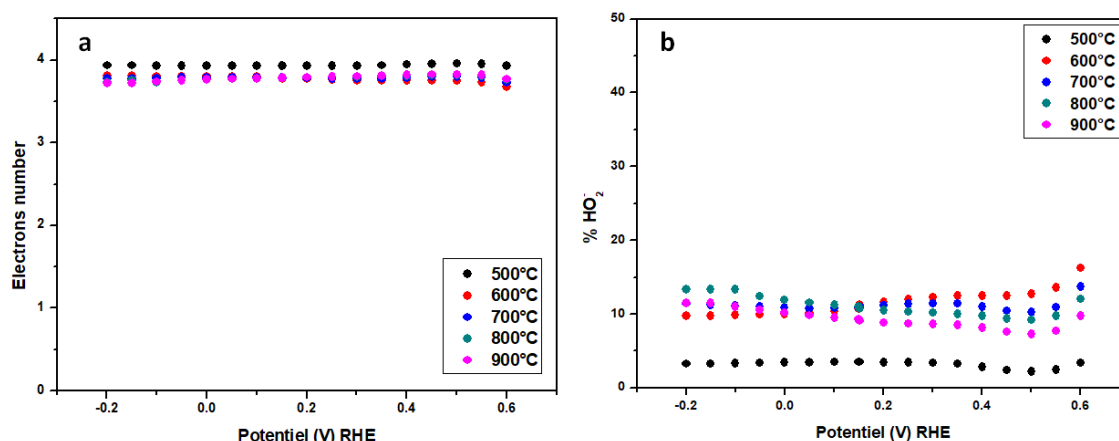


Figure 2.28 – (a) Evolution of electron number exchanged as function of applied potential E (V) RHE
 (b) Evolution of HO₂⁻ produced as a function of applied potential E (V) RHE

If we look at the Figure 2.28(a), we can see that we have an electron number near 4 and a HO₂⁻ production lower than 15 % for the five studied series.

These results indicated an excellent selectivity for ORR to the produce hydroxide (OH⁻). The best catalyst is the powder prepared at 500°C. If we look at the range of potential studied, we have a variation of production of HO₂⁻ of 3.39 to 3.24 %. Thanks to the XRD investigation, we found the average size of it and discovered that it is a smaller size synthesized compared to the other powder made.

Powder made at 500°C presents a better selectivity. We have the number of electron exchanged closer to 4 electrons.

Figure 2.28(b) illustrates the evolution of the production of HO₂⁻ as function of applied potential. This figure highlights that all the powders studied have low production of HO₂⁻. We see that we can divide the evolution into three parts, the first part corresponds to 0.6 to 0.35 V vs RHE, we are around the first wave of reduction (around 0.5 V vs RHE), and the second part corresponds to the middle range of potential between the two waves of reduction. This range of potential is the potential window between 0.35 to 0 V vs RHE. Furthermore, the last part is the potential range between 0 to -0.2 V vs RHE. Figure 2.28(b) highlights the number exchange as function of potential. We can see all the five series of powder studied; we have a production of HO₂⁻ under 20%.

In the following part, we will look at the ORR mechanisms, and analyse the relationships between the catalysts' structures and their catalytic proprieties.

2.3.2 Oxygen reduction reaction mechanism analysis

1700 In this following part, we will study the electrocatalytical activity of the series of Mn_2O_3 prepared at various temperature, and the corresponding ORR mechanism. Thanks to the electrochemical investigation, we show that all prepared Mn_2O_3 are able to reduce O_2 by 4 electrons. The 4 electrons pathway can be obtained by the reduction of the O_2 to HO^- as shown in Figure 2.29a or by the 2 + 2 electrons pathways (Figure 2.29c). In Figure 2.29, there are different colors to differentiate various species: in orange is the species on the catalyst surface, ones in
1705 purples and blues species are present in the solution. Figure 2.29b illustrate the 2 electrons pathways.^[24] Herein, we will focus on the two ways allowing 4 electrons reduction pathway, Figures 2.29a and 2.29c respectively.

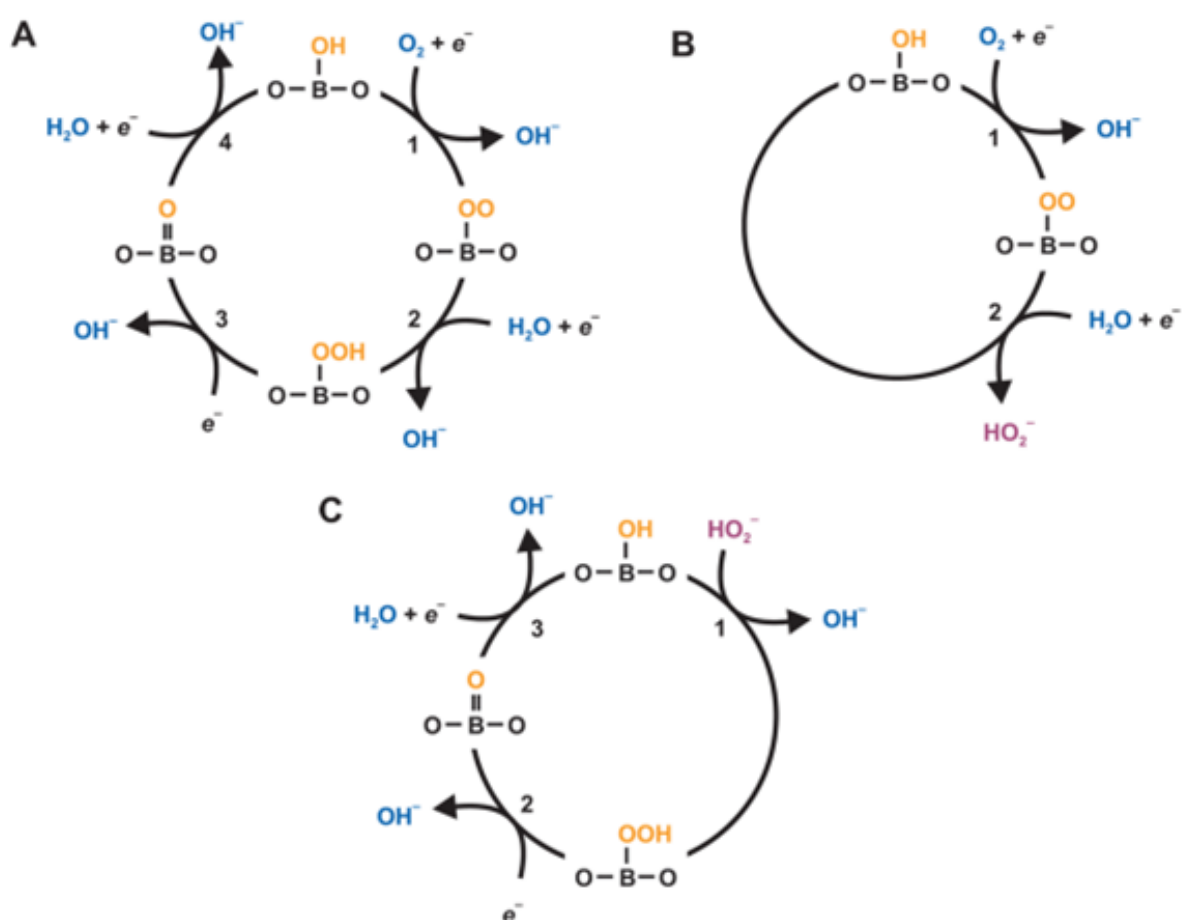


Figure 2.29 – Possible mechanisms for oxygen reduction reaction^[24]

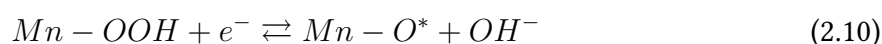
Let us first study the direct 4 electron pathways in Figure 2.29a. One has 4 steps to reduce of O₂ to HO⁻. The first step is the electron transfer associated to O₂ adsorption onto adsorbed OH species on the Mn (III) sites :(2.9)



The second step is the reduction of O_{2ad} into adsorbed HO_{2ad} (OOH⁻) given by equation (2.9) :

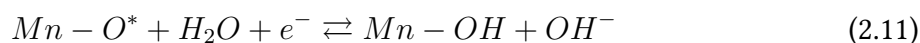


The third step is when HO⁻ group is replaced from the surface by Mn-O* and the formation of hydroxide. (2.10)



The fourth step corresponds to the protonation of O* to give Mn-OH. This reaction is possible thanks to the reconstruction of the initial hydroxyl-covered surface of the Mn (III) site here.

These reactions translate by the following equation (2.11) :



In the 4 electrons reduction mechanism described in Figure 2.29a, the first step is the kinetic limiting step for the metal oxides. During this step, the oxygen adsorption strength through the Mn(III) site is given by the electron filling of e_g orbital of the metal oxide and generally for the metal iron.^[25,26] We will see later in detail the role of the e_g orbital.

In Figures 2.29b and 2.29c, the 2-electron reduction and 2 + 2 electrons reduction steps. In both cases, one has the reduction of O₂ to hydroperoxide HOO⁻. If we look at 2 + 2 electrons pathway, there is also two electrons reduction of the reabsorbed hydroperoxide to hydroxide by a superoxo O₂⁻ intermediate. Furthermore, the peroxide disproportionation reaction can occur.

On key element giving the catalytic effect during ORR is the presence of Mn³⁺ with some Mn⁴⁺. These two ions increase the catalytic effect, and the number of transferred electrons.^[17] We can also look at the structure of α-Mn₂O₃ to understand how it plays a critical role in the catalytic effect. In all the powders made, we have the presence of α-Mn₂O₃ orthorhombic. If we look closer at the geometry of Mn^{III} octahedra for α-Mn₂O₃ orthorhombic, we can see that we have five symmetry-inequivalent of Mn^{III}O₆ sites. Three sites present in the geometry have different Mn-O bond lengths. The length difference in these three sites is due to the distortion of the D_{4h} symmetry with two long and four short bonds. For two other sites, all Mn-O bond lengths are the same, which translates to the presence of trigonal antiprismatic D_{3d} symmetry. Figure 2.30 shows that the surface of Mn^{III}O₆ takes place in a three-fold axis and gives the D_{3d} symmetry created by the three oxo bridges. The d-orbital electronic configuration is given by e_g¹. The three fixed oxo bridges with the same length of Mn-O bonds created trigonal ligand

field which limits the Jahn–Teller distortion.^[17]

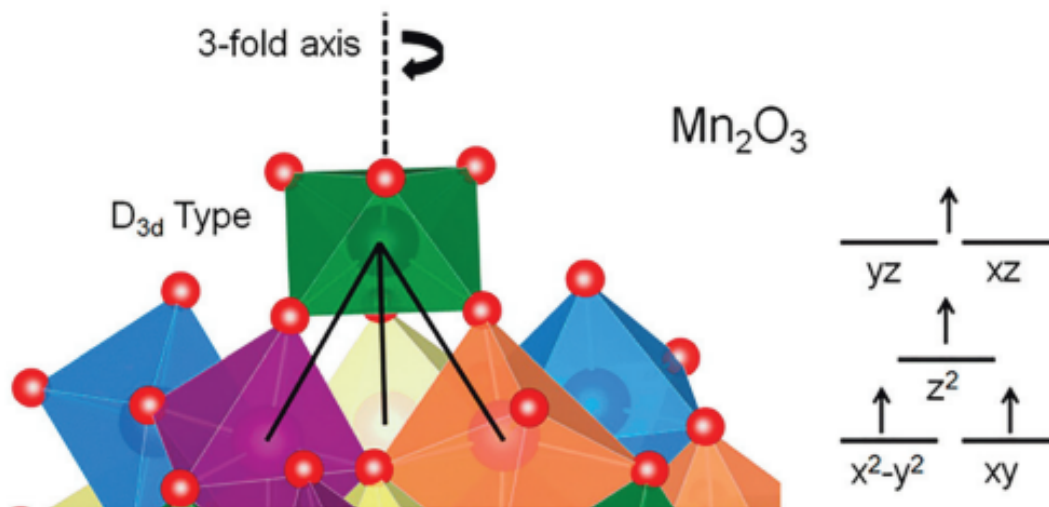


Figure 2.30 – Representation of crystal structure and d-orbital electronic configuration of Mn_2O_3 ^[17]

The other structure of Mn_2O_3 is a cubic phase which is found in the powder prepared at 500,600,700 and 800°C. We will compare the electrocatalytic activity with respect to ORR of the cubic phase and the orthorhombic. In the recent decade, it has been reported that the morphology of the manganese oxide can influence electrocatalytic activity. To explain that, we have to look at the type of planes exposed to the surface and check the structural defect that will improve the reactivity.^[14,27–29] Henzie et al.^[16] carried out density functional theory (DFT) calculations to analyse the properties of the orthorhombic and the cubic Mn_2O_3 . They showed that the orthorhombic phase has a bandgap semiconductor and cubic phase has a bandgap semi-metal.

The cubic phase has this propriety due to the mixing and overlap of the Mn_{3d} and O_{2p} orbitals. This study underlined the impact of the phase on the affinity for ORR.

Indeed, $\alpha\text{-Mn}_2\text{O}_3$ cubic exhibit higher activity for OER, and ORR than the commercial $\alpha\text{-Mn}_2\text{O}_3$ powder. In the same study, authors found that the selectivity through ORR is improved due to the phase transition occurring in Mn_2O_3 from orthorhombic to cubic phase.^[16] In a recent study, Wang et al.^[30] studied the performance of $\alpha\text{-Mn}_2\text{O}_3$ cubic for the ORR and highlighted a high electrocatalytical activity of the cubic phase for ORR.

Liu et al.^[31] also showed the importance of face exposure in their studies. They looked at three types of Mn_3O_4 , one composed of nanoparticles, nanorods (exposure of (101)), and nanoflake (exposure of (001)). The higher affinity through ORR was nanoflake exposed (001) because the formation of *OOH thermodynamically was easier on the face (001).

Wang et al.^[30]'s focused on the influence of facets of the cubic $\alpha\text{-Mn}_2\text{O}_3$ of the ORR/OER. They revealed that the exposure of (100) facet increased the catalytic activity compared to the other

types of Mn_2O_3 . This behaviour can be explained by the low-coordinated on surface oxygen sites.

These oxygen vacancy sites allow transferring more electrons (increase of electron transfer number), and improve adsorption energies for oxygen species intermediate. Accordingly, the ORR follow mainly 4 electrons pathway. Wang et al.^[30]'s investigations on the impact of the facet depending on the ORR, found that the $\alpha\text{-Mn}_2\text{O}_3$ cubic that they studied had lattice fringe spacing of 0.23 nm. They showed that this lattice fringe spacing corresponds to the (400) plane of cubic Mn_2O_3 . This plane is parallel to the (100) plane. This observation highlighted that the (100) plane is the main exposed plane of $\alpha\text{-Mn}_2\text{O}_3$ cubic with the higher concentrations of low-coordinated surface oxygen sites. This information can explain the influence of the facet type on the electrocatalytic response of oxygen.

The surfaces O atoms will be easier flexible on (100) facet and (100) had lower oxygen vacancy formation energy. Thanks to (100) facets proprieties, the oxygen can interact with more (100) facets. The presence of the oxygen vacancy will help charge transfer and improve the adsorption energies for intermediates. This improvement leads to a better selectivity and catalytic property for OER or ORR.^[32,33]

Thanks to the structural phases of $\alpha\text{-Mn}_2\text{O}_3$ that can be orthorhombic or cubic, we had an information on the impact of these two on trough the ORR activity. However, we looked at all the samples of powder made, and the one that presents a high catalytic power is the one made at 500°C. For this one, we found the presence of Mn_5O_8 and we see if it had an impact on the ORR activity.

The $\alpha\text{-Mn}_2\text{O}_3$ powder prepared at 500°C contains two phases (cubic and orthorhombic) and both structures played a role in the catalytic effect in ORR. We also found the presence of Mn_5O_8 that can impact the ORR catalytic due to the structure that induces interaction between the electronic structure and absorbed oxygen. Mn_5O_8 crystallizes in a monoclinic structure with a mixed valanced of Mn^{2+} and Mn^{4+} as $\text{Mn}_2^{2+}\text{Mn}_3^{4+}$.^[34] As seen before, the coexistence of the manganese in the two forms, Mn^{3+} and Mn^{4+} will improve the cleavage of O–O bonds and accelerate the reduction of O_2 to OH^- . Mn^{3+} has the high spin d^4 configuration $t_2^3e_g^1$.^[35] In the case of Mn_5O_8 , we gave a truncated octahedral environment, where the antibonding orbitals of Mn^{3+} overlap with the top-absorbed O species as shown in Figure 2.31. This phenomenon will have an impact on the bonding strength of O_2 onto Mn^{3+} , and improves the activity through the ORR activity by accelerating the reduction of O_2 .^[24]

Figure 2.31 represent the lattice structure of Mn_5O_8 and the adsorption of the O_2 on the surface of Mn_5O_8 .^[36]

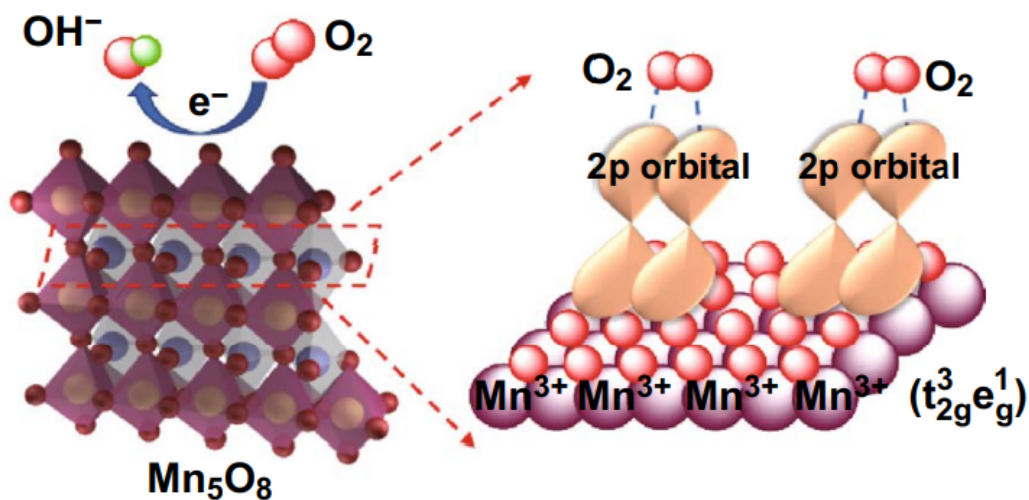


Figure 2.31 – Representation of lattice structure of Mn_5O_8 [36]

1805 The other model proposed for ORR with Mn_2O_3 electrocatalyst by Savinova et al. [27] is also very interesting as shown Figure 2.32. Their studies demonstrated the importance of $\text{Mn}^{\text{III}}/\text{Mn}^{\text{IV}}$ transition in the ORR.

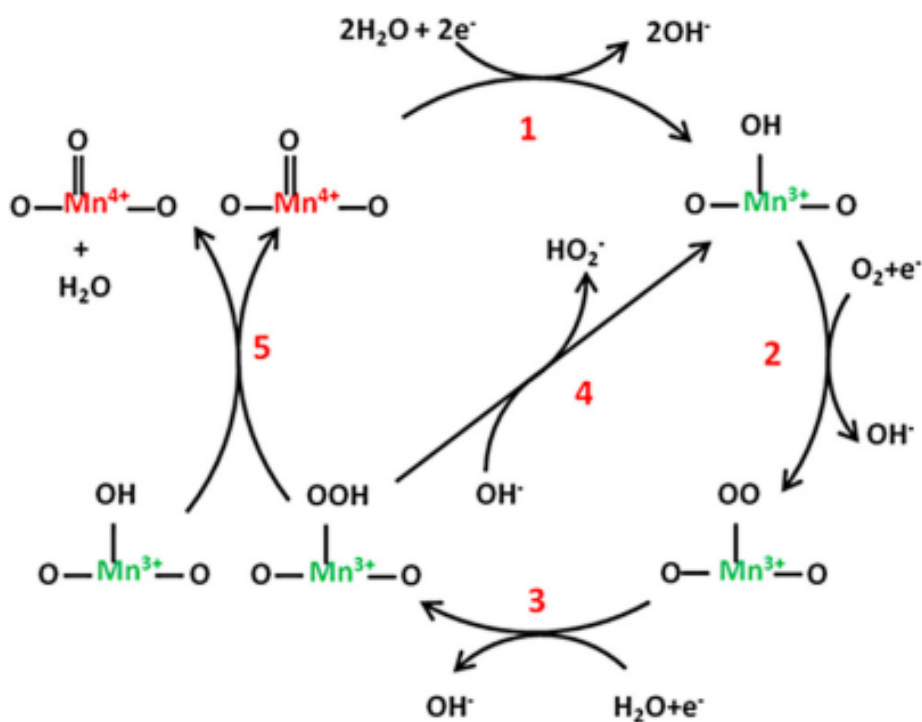


Figure 2.32 – Oxygen reduction reaction mechanism for Mn oxides [27]

The main difference between this mechanism and the previous one is the role of Mn^{4+} and Mn^{3+} , which we will define in each step.^[1,27] The first step is the transition of $Mn^{(IV)} / Mn^{(III)}$.
 1810 During this step, O adsorbed and OH adsorbed species are coordinated to each Mn ion : Mn^{4+} and Mn^{3+} . Equation (2.12) translates this first step:



The second step involves the O_2 adsorption and desorption that occurs during the electron transfer of $Mn^{(III)}$ surface cations



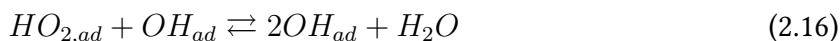
The third step is the reduction of $O_{2,ad}$ to $HO_{2,ad}$:



The fourth step is the desorption/adsorption of HO_2^- :



1820 And the last step O–O is going to break. And it is highlighted by the equation (2.16):



In their studies and the microkinetic modelling, they demonstrated that the differences in the ORR kinetics of the Mn_2O_3 are due to different formal potential values, and also the structure-dependent rate constants of the reaction steps (corresponding to the step 2, step 3,
 1825 and step 5) in the mechanism proposed in Figure 2.32. In 2018's, Nikitina et al.^[37] did quantum chemical calculations to analyse this phenomenon. They showed the influence of surface structure-dependent adsorbate with the activation barrier of O–O bond-breaking leading to the adsorbed hydrogen peroxide (this step corresponds to the fifth step). In the same studies, they proved that the shorter the distance between the Mn cations allowed to strength the interaction of adsorbed OH and OOH and also the interaction between O and OH. This increase in the interactions decreases the activation barrier of the bond-breaking step. It leads
 1830 to a fast O–O bond breaking for Mn_2O_3 electrocatalyst favouring the four-electron transfer mechanism, and lower the amount of detected H_2O_2 or HO_2^- by the ring of RRDE.

Based on LSV recorded during ORR investigation, we can suppose that our nanomaterials prepared at different temperatures follow this mechanism and that can explain the LSV recorded
 1835 during ORR investigation. To look more in details, we are going to focus on the microkinetic study in the next part.

2.3.3 Micro-kinetic studies

Herein, we will do first the micro-kinetic studies of the powder prepared at 500°C, and we
 1840 compare with the other powders prepared at different temperatures in the following. This
 part aims to determine the Tafel slope, to calculate the value of $(n' + \alpha_{RDS})$, to identify rate
 determining step, and the number of electrons n' transferred prior to the rate determining
 step. In order to access to these parameters, we go back to the IUPAC definitions^[38,39] of the
 transfer coefficients, α obtained from the analysis of experimental current (I) – voltage (E)
 1845 data. For a reduction reaction, transfer coefficients α is given by equation (2.17) :

$$\alpha = -\frac{RT}{F} \frac{d \ln I}{dE} \quad (2.17)$$

With T : temperature (K)

R : the Gas constant ($J.K^{-1}.mol^{-1}$)

and F : Faraday constant ($C.mol^{-1}$)

1850 The definition of α given by IUPAC is related to the value of the experimental data E - I curve
 and haven't a presumed theoretical model of the electron transfer event. Using this approach,
 the values obtained are based on experimental practice and can be in contradiction with classic
 methods used in the literature.^[40] For example, if we look at the overall number of electrons
 transferred n , we need to know the inference of this quantity which may not be measurable.
 1855 These two parameters can be measured, and we depend only on the voltammetric timescale
 conducted.

In our case, ORR had multi-step f reduction process. When we have this type of processes; we
 can adopt Butler-Volmer formalism given by this following equation (2.18)^[41]:



1860 The corresponding Tafel slope is (2.19):

$$\frac{d \ln I}{dE} = -\frac{RT}{F} (n' + \alpha_{RDS}) \quad (2.19)$$

Where α_{RDS} is the transfer coefficient and n' is the number of electrons transferred prior to
 the rate determining step.^[42]

We look at the equation (2.17) and (2.19), we can see that the current rises exponentially as a
 1865 function of the applied potential. During the reduction reaction, the concentration of A (ini-
 tial specie) decreases at the electrode surface leading to a lower exponential relationship. The
 decreasing of A concentration will also lead to an apparent potential dependency of the trans-
 fer coefficient if no correction mass transport effects is performed^[42]. To solve the problem
 linked to the concentration depletion of A during the analysis; it is recommended the limited
 1870 the analysis at 30 % of the peak or limiting current.^[43]

In the case of the RRDE which is an uniformly accessible to the electrode, one has the revised equation with the mass transport correction for an irreversible process (like in our case)

$$\ln\left[\frac{1}{I} - \frac{1}{I_{lim}}\right] = -(n' + \alpha_{RDS})\frac{FE}{RT} + constant. \quad (2.20)$$

1875

where I_{lim} correspond to the transport-limited current.

Thanks to the equation (2.20), if we trace the plot of $\ln\left[\frac{1}{I} - \frac{1}{I_{lim}}\right]$ vs E then the slope is $-(n' + \alpha_{RDS})\frac{FE}{RT}$. Then, we can calculate the value of $(n' + \alpha_{RDS})$. To simplify the expression of the equation (2.20), we introduced the kinetic current I_k defined as the expression of kinetic

1880 current I_k is given by this following equation :

$$I_k = \frac{(I_{lim} \times I)}{(I_{lim} - I)} \quad (2.21)$$

Combining equations (2.20) and (2.21), we can plot $-\ln(I_k)$ or $\ln |I_k|$ vs E and determine $(n' + \alpha_{RDS})$.

1885

Figure 2.33 shows typical ORR polarization curves in O_2 -saturated 0.1 M KOH solution using RRDE. In order to analyze these polarization curves, To conduct this investigation, we separate two zones:

(i) Zone K-L 1 where the electrochemical response is controlled by the charge transfer kinetic,

1890

(ii) One K-L 2 where the current is diffusion controlled

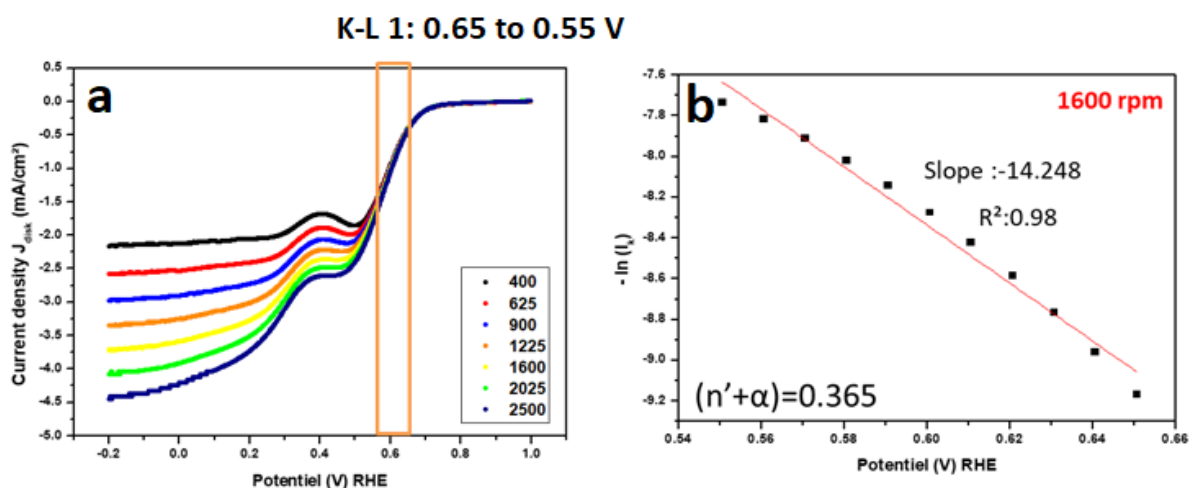


Figure 2.33 – (a) ORR polarization curves in O_2 -saturated 0.1 M KOH solution using RRDE for powder made at 500°C in ink form
(b) Linear Tafel plot for powder made at 500°C in ink form (K-L 1 zone)

Focus on the K-L 1 :

Firstly, we will analyze the first zone of K-L 1 for the powder prepared at 500°C . The K-L 1 zone corresponds to potential window between 0.65 and 0.55 V vs RHE before the first wave of reduction. For each series powder prepared at different temperatures, we analyse three series to verify the reproducibility of the results. The micro-kinetic investigations are carried out from the I-E curves recorded at 1600 rpm.

Figure 2.33.(a) reported the ORR polarization curves obtained with various rotating rates for the powder prepared at 500°C . One obtains a linear Tafel plot from LSV recorded at 1600 rpm with a slope of -14.249 mV/dec and a correlation coefficient R^2 of 0.98. Using equations (2.20) and (2.21), the value of the slope allows determining the value of $(n' + \alpha_{RDS})$ corresponding to the transfer coefficient. One has a transfer coefficient of 0.365. We use the same methodology for the other powder prepared at various temperature. We remind that the size of the nanoparticles increases with the temperature as reported in Table 2.3.

| Powder sample | Average crystallite sizes (nm) |
|---------------------|--------------------------------|
| 500°C | 45 |
| 600°C | 64 |
| 700°C | 87 |
| 800°C | 151 |
| 900°C | 204 |

Table 2.3 - Average crystallite sizes of the powder made at different temperature

The variation of the transfer coefficient as a function of the nanoparticles' size is shown in Figure 2.34. Also, the electron number and the fraction of produced HO_2^- in the zone K-L 1

is shown in Figure 2.35. For the other powder made, we conduct the same studied to obtain the value of transfer coefficient of each series studies. We will compare each value obtained at look at the correlation with the size, transfer coefficient obtains by the Tafel plot, and the number of electrons exchanged calculated thanks to the equation (2.5) for K-L 1 zone. We look at the correlation of the size of the powder and the transfer coefficient. We trace the evolution of the average value transfer coefficient as function of the average size of the powder obtained for all the studied series. We can see that the powder made at 500°C had the smaller size than the other synthesised powder series and had a lower value for the transfer coefficient. We will see if it results can be also correlate with the number of electrons exchanged and percentage of HO_2^- in this K-L 1 zone studied.

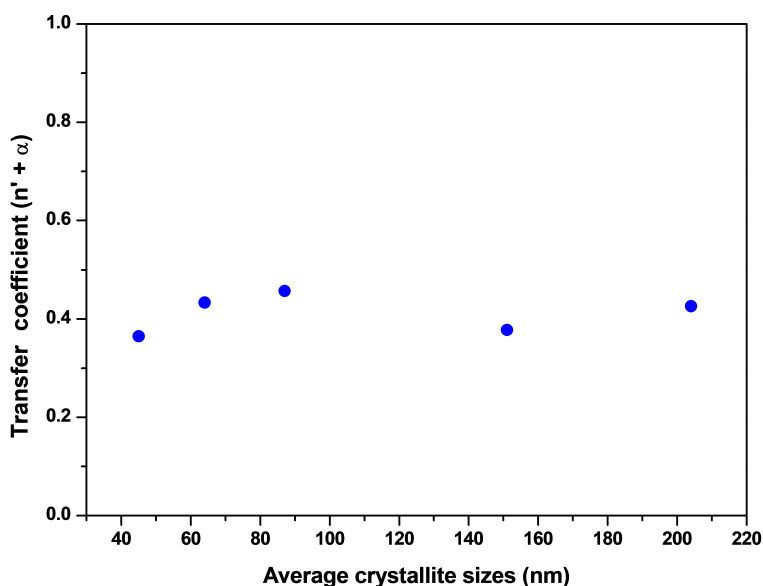


Figure 2.34 – Evolution of the transfer coefficient ($n' + \alpha$) as function of the size of powder made at different temperatures (nm)

Figures 2.34 and 2.35 highlight that the powder prepared at 500°C is more efficiency for ORR: the electron number is close to 4 and percentage of HO_2^- is the lowest. When the size increases, one observes a decrease of the electron number, and in the same time the percentage of HO_2^- is higher (in the range between 20% and 30%). These results indicate that the size of the crystallite plays a role in the electrocatalytic performance for ORR. And the figure 2.35 demonstrate that we have a quicker catalysis to ORR for the powder made at 500° C.

In the next part, we will look at the second zone K-L 2 where we follow the same methodology used for K-L 1 zone. We begin to investigate the powder prepared at 500°C. We will look at the investigation made.

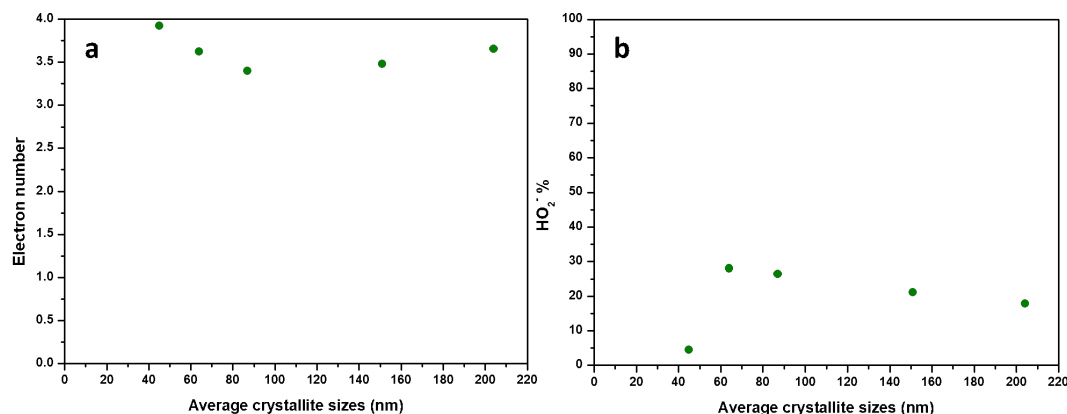


Figure 2.35 – Evolution of (a) electron number exchanged and (b) % HO_2^- in K-L 1 zone as function of the size of powder made at different temperatures (nm)

Focus on the K-L 2 :

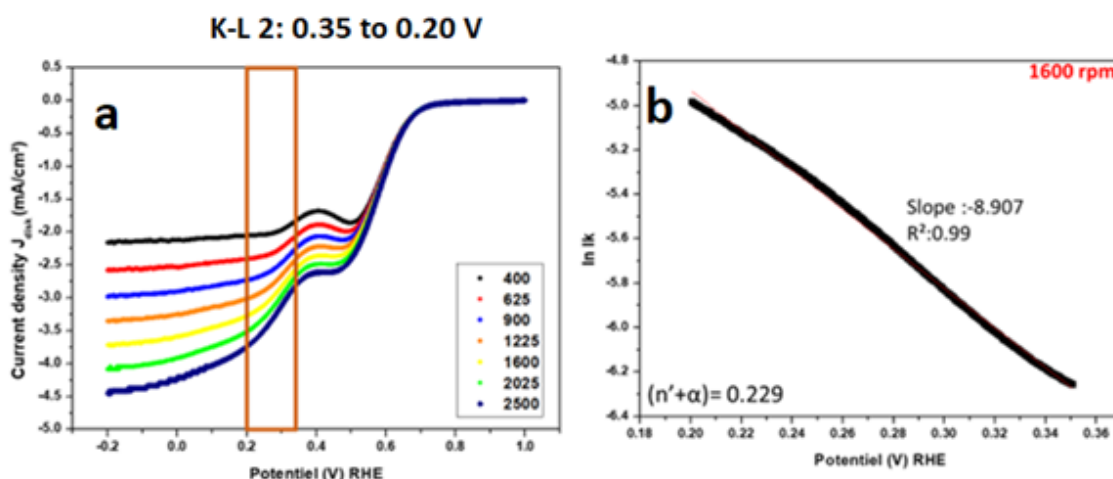


Figure 2.36 – (a) ORR polarization curves in O_2^- saturated 0.1 M KOH solution using RRDE for powder made at 500°C in ink form (b) Linear Tafel plot for powder made at 500°C in ink form (K-L 2 zone)

Figure 2.36.(a) reported the ORR polarization curves obtained with various rotating rates for the powder prepared at 500°C. Also, one obtains a linear Tafel plot from LSV recorded at 1600 rpm. Figure 2.36.(b) give a straight line with a slope value of -8.907 mV/dec and with a correlation coefficient of determination R^2 of 0.99. Thanks to the slope value, one obtain a transfer coefficient $(n' + \alpha_{RDS})$ of 0.229.

In Figure 2.37, we shown the variation of the size of the nanoparticles and the transfer coefficient in the K-L 2 zone. In all case, the electron number is near 4, and the HO_2^- percentage is lower than 15%. One can remark that the nanoparticle prepared at 500°C gives the lower

HO_2^- percentage (Figure 2.38.(b)). Comparing to K-L 1 zone, lower values of transfer coefficient are obtained in K-L 2 zone. The value around 0.2 and 0.1 for all the series made.

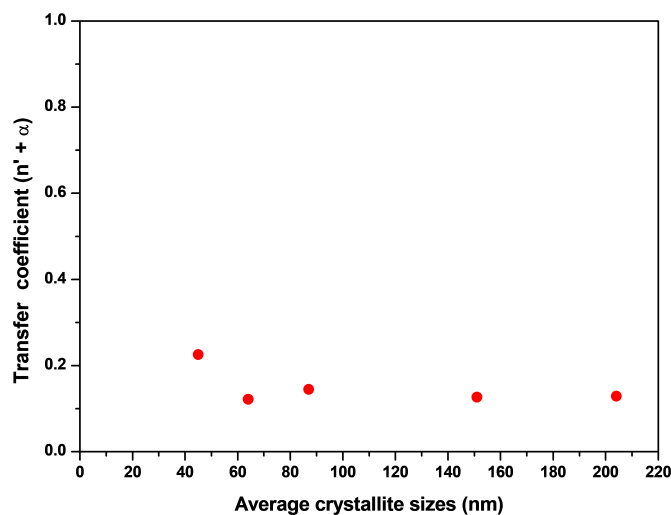


Figure 2.37 – Evolution of the transfer coefficient (K-L 2 zone) as function of the size of powder made at different temperatures (nm)

Figure 2.38 indicates that all of the prepared nanoparticles are able to reduce O_2 to HO^- i.e. the electron number is near 4 in the both K-L-1 and K-L 2 zones. However, the sample prepared at 500°C is the best nanoparticle for ORR because it produces the lower amount of HO_2^- . In the K-L 2, one has a high selectivity of 4 electrons ways but the analysis of the zone K-L 1 indicates a mechanism in which HO_2^- is also produced during ORR. This point described the mechanism proposed by Savinova et al. [27]

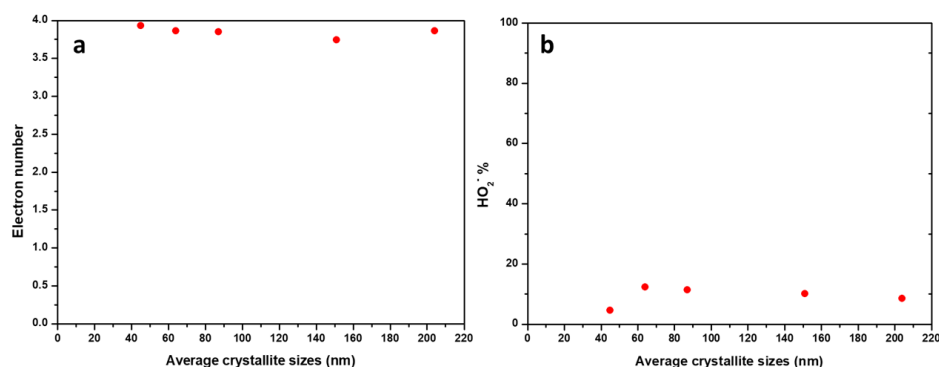


Figure 2.38 – Evolution of (a) electron number exchanged and (b) % HO_2^- in K-L 2 zone as function of the size of powder made at different temperatures (nm)

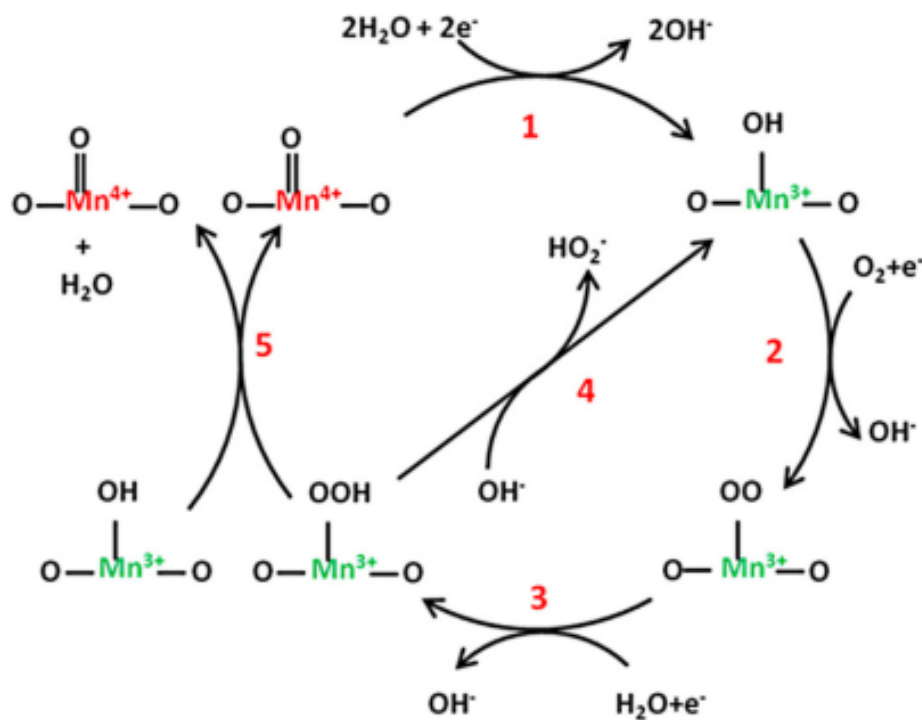


Figure 2.33 - Oxygen reduction reaction mechanism for Mn oxides Ryabova et al.^[27]

1945

2.4 Conclusion

In this chapter, we have prepared a series of manganese oxide nanoparticles. To prepare these nanoparticles, we use electrospinning to obtain a film of polymer doped with manganese. After that, these films are submitted to thermal treatment at different temperatures. We combine various spectroscopy techniques to analyse the structure and to determine the chemical composition. We have identified the nature of the oxide; the majority of the synthesized powder was $\alpha\text{-Mn}_2\text{O}_3$. The one prepared powder at 500°C presents a small fraction of Mn_5O_8 . This information was highlighted by the use of the Synchrotron to identify the nature of the $\alpha\text{-Mn}_2\text{O}_3$. $\alpha\text{-Mn}_2\text{O}_3$ can be cubic or orthorhombic. This subtle nuance has a great influence on the catalytic properties of the $\alpha\text{-Mn}_2\text{O}_3$ studied. The electrochemical properties of each series of powder are analysed by means of RRDE. RRDE was useful to understand the possible pathway take by catalyst through ORR in alkaline media. During this investigation, we saw that the powder prepared at 500°C present an excellent selectivity towards the 4 electron pathway, with an electron number exchanged close to 4 electrons and a production of the HO_2^- lower than 5% in the investigated potential window. The other nanoparticles have also a good catalytic property. These remarkable properties can be due to the fact that we have Mn_5O_8 and

1960

more cubic form of α - Mn_2O_3 . To understand the mechanism, the micro-kinetic study is carried out in the two zones to determine the transfer coefficient (Figure 2.39), the electron number and percentage of HO_2^- (Figure 2.40).

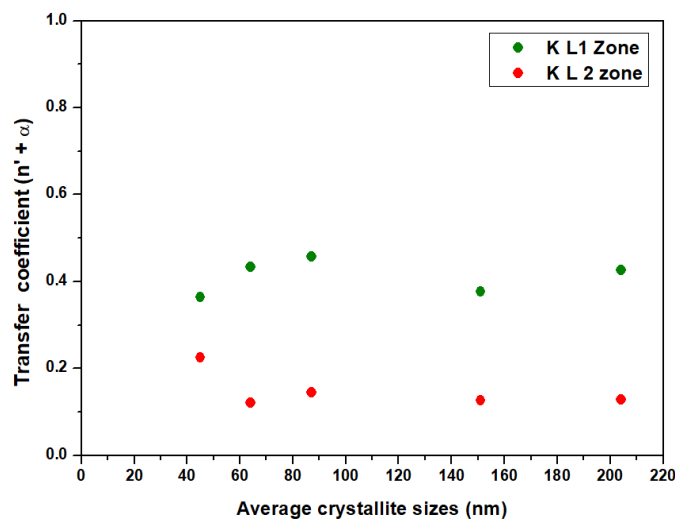


Figure 2.39 – Evolution of the transfer coefficient for K-L 1 (green) and K-L 2 (red) as function the size of powder made at different temperatures (nm)

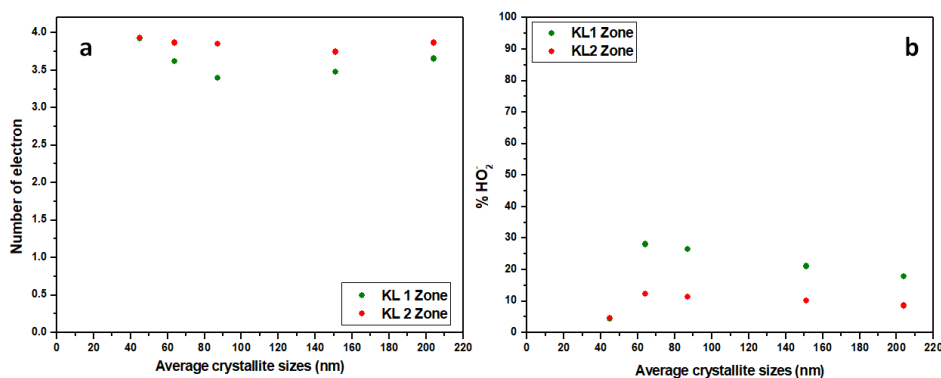


Figure 2.40 – Evolution of (a) electron number exchanged and (b) HO_2^- % for K-L 1 and K-L 2 as function of the size of powder made at different temperatures (nm)

Figures 2.39 and 2.40 show that we have clear difference between the two zone studies. For K-L 1, one has a higher value for the transfer coefficient than that observes in K-L 2. We can see that correlation with the electron number exchanged and the percentage of HO_2^- for these two zones.

The size plays an important role. The smallest nanoparticle which is prepared at 500°C exhibits the best performance for 4 electron ORR. In the future, we look at the stability of the catalyst made, and we need to do the turnover frequency (TOF) for each powder made.

And we can compare our results with Zhong group recent studies^[44] who investigated on manganese-based oxides. We will focus on the onset potential. The onset potential is the potential at which the current density exceeds 0.1 mA/cm². When we compare our catalyst, we have an onset potential of 0.712 V to their catalyst 0.95 V. We didn't have the best catalyst but we have a promising result.

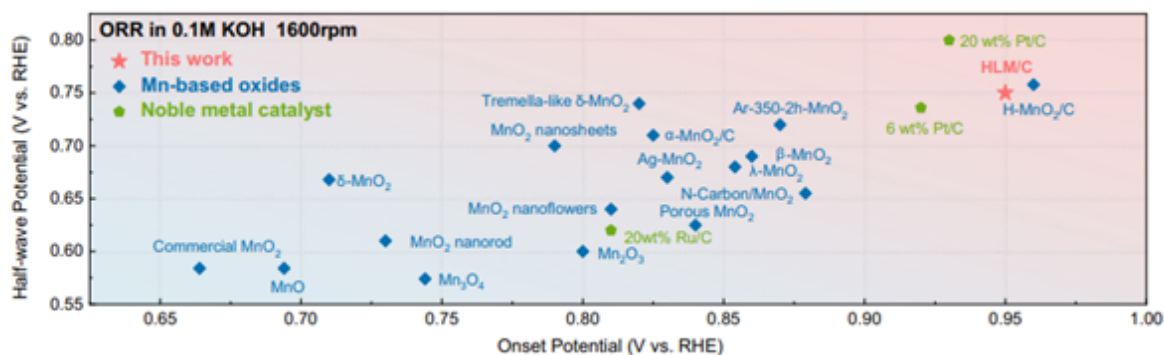


Figure 2.41 – Comparison Mn-based oxides and noble metal catalysts for ORR^[44]

1980

The other track that we want to improve is the understanding of the phase transition of α -Mn₂O₃. Like we seen, the nature of α -Mn₂O₃ can have an impact on the catalytic proprieties. To look closer, we have to make intrinsic measured to follow the ORR. This part, we be look by the following internship of PhD student how will take the project. In the next chapter, we are going to look at the electrode nickel oxide. It will be studied in 3 ways:

1985

- Firstly as a catalyst for hydrogen evolution reaction
- Secondly as a catalyst for oxygen evolution reaction
- And finally as electrode how plays the anodic part in a supercabattery made.

REFERENCES

1990

1995

2000

2005

2010

2015

2020

- [1] Anna S. Ryabova, Sergey Ya. Istomin, Kirill A. Dosaev, Antoine Bonnefont, Joke Hadermann, Natalya A. Arkharova, Anton S. Orekhov, Robert Paria Sena, Viktoriia A. Saveleva, Gwénaëlle Kéranguéven, Evgeny V. Antipov, Elena R. Savinova, and Galina A. Tsirlina. Mn₂O₃ oxide with bixbyite structure for the electrochemical oxygen reduction reaction in alkaline media: Highly active if properly manipulated. *Electrochimica Acta*, 367:137378, January 2021. ISSN 0013-4686. doi: 10.1016/j.electacta.2020.137378.
- [2] Vladimir Neburchilov, Haijiang Wang, Jonathan J. Martin, and Wei Qu. A review on air cathodes for zinc–air fuel cells. *Journal of Power Sources*, 195(5):1271–1291, March 2010. ISSN 0378-7753. doi: 10.1016/j.jpowsour.2009.08.100.
- [3] Hannah Osgood, Surya V. Devaguptapu, Hui Xu, Jaephil Cho, and Gang Wu. Transition metal (Fe, Co, Ni, and Mn) oxides for oxygen reduction and evolution bifunctional catalysts in alkaline media. *Nano Today*, 11(5):601–625, October 2016. ISSN 1748-0132. doi: 10.1016/j.nantod.2016.09.001.
- [4] Hanaa M. Abuzeid, Ahmed M. Hashem, Maximilian Kaus, Michael Knapp, Sylvio Indris, Helmut Ehrenberg, Alain Mauger, and Christian M. Julien. Electrochemical performance of nanosized MnO₂ synthesized by redox route using biological reducing agents. *Journal of Alloys and Compounds*, 746:227–237, May 2018. ISSN 0925-8388. doi: 10.1016/j.jallcom.2018.02.260.
- [5] Jiajia Xue, Jingwei Xie, Wenying Liu, and Younan Xia. Electrospun Nanofibers: New Concepts, Materials, and Applications. *Accounts of Chemical Research*, 50(8):1976–1987, August 2017. ISSN 0001-4842. doi: 10.1021/acs.accounts.7b00218.
- [6] Jiajia Xue, Tong Wu, Yunqian Dai, and Younan Xia. Electrospinning and Electrospun Nanofibers: Methods, Materials, and Applications. *Chemical Reviews*, 119(8):5298–5415, April 2019. ISSN 0009-2665. doi: 10.1021/acs.chemrev.8b00593.
- [7] S-H. Tan, R. Inai, M. Kotaki, and S. Ramakrishna. Systematic parameter study for ultra-fine fiber fabrication via electrospinning process. *Polymer*, 46(16):6128–6134. ISSN 0032-3861. doi: 10.1016/j.polymer.2005.05.068.
- [8] Shao-Zhuan Huang, Jun Jin, Yi Cai, Yu Li, Zhao Deng, Jun-Yang Zeng, Jing Liu, Chao Wang, Tawfique Hasan, and Bao-Lian Su. Three-Dimensional (3D) Bicontinuous Hierarchically Porous Mn₂O₃ Single Crystals for High Performance Lithium-Ion Batteries. *Scientific Reports*, 5(1):14686, October 2015. ISSN 2045-2322. doi: 10.1038/srep14686.

- [9] Junkai Wang, Rui Gao, Dong Zhou, Zhongjun Chen, Zhonghua Wu, Gerhard Schumacher, Zhongbo Hu, and Xiangfeng Liu. Boosting the Electrocatalytic Activity of Co₃O₄ Nanosheets for a Li-O₂ Battery through Modulating Inner Oxygen Vacancy and Exterior Co³⁺/Co²⁺ Ratio. *ACS Catalysis*, 7(10):6533–6541, October 2017. doi: 10.1021/acscatal.7b02313.
- [10] Fangyi Cheng, Jian Shen, Bo Peng, Yuede Pan, Zhanliang Tao, and Jun Chen. Rapid room-temperature synthesis of nanocrystalline spinels as oxygen reduction and evolution electrocatalysts. *Nature Chemistry*, 3(1):79–84, January 2011. ISSN 1755-4349. doi: 10.1038/nchem.931.
- [11] Observation of the Reversible Phase-Transformation of α -Mn₂O₃ Nanocrystals during the Catalytic Combustion of Methane by in Situ Raman Spectroscopy. 111. ISSN 1932-7447.
- [12] CRISTAL | centre de rayonnement synchrotron français.
- [13] Luca Lutterotti, S. Matthies, and Hans-Rudolf Wenk. MAUD (material analysis using diffraction): a user friendly Java program for Rietveld texture analysis and more. In *Proceeding of the twelfth international conference on textures of materials (ICOTOM-12)*, volume 1, page 1599. NRC Research Press Ottawa, Canada, 1999.
- [14] Maryam Jahan, Satoshi Tominaka, and Joel Henzie. Phase pure α -Mn₂O₃ prisms and their bifunctional electrocatalytic activity in oxygen evolution and reduction reactions. *Dalton Transactions*, 45(46):18494–18501, November 2016. ISSN 1477-9234. doi: 10.1039/C6DT03158G.
- [15] S. Geller. Structure of α -Mn₂O₃, (Mn_{0.983}Fe_{0.017})₂O₃ and (Mn_{0.37}Fe_{0.63})₂O₃ and relation to magnetic ordering. *Acta Crystallographica Section B: Structural Crystallography and Crystal Chemistry*, 27(4):821–828, April 1971. ISSN 0567-7408. doi: 10.1107/S0567740871002966.
- [16] Junais Habeeb Mokkath, Maryam Jahan, Masahiko Tanaka, Satoshi Tominaka, and Joel Henzie. Temperature-dependent electronic structure of bixbyite α -Mn₂O₃ and the importance of a subtle structural change on oxygen electrocatalysis. *Science and Technology of Advanced Materials*, 22(1):141–149, December 2021. ISSN 1468-6996. doi: 10.1080/14686996.2020.1868949.
- [17] Sunghak Park, Yoon Ho Lee, Seungwoo Choi, Hongmin Seo, Moo Young Lee, Mani Balamurugan, and Ki Tae Nam. Manganese oxide-based heterogeneous electrocatalysts for water oxidation. *Energy & Environmental Science*, 13(8):2310–2340, August 2020. ISSN 1754-5706. doi: 10.1039/D0EE00815J.
- [18] Yelena Gorlin and Thomas F. Jaramillo. A Bifunctional Nonprecious Metal Catalyst for Oxygen Reduction and Water Oxidation. *Journal of the American Chemical Society*, 132(39):13612–13614, October 2010. ISSN 0002-7863. doi: 10.1021/ja104587v.
- [19] Paul F. Smith, Benjamin J. Deibert, Shivam Kaushik, Graeme Gardner, Shinjae Hwang, Hao Wang, Jafar F. Al-Sharab, Eric Garfunkel, Laura Fabris, Jing Li, and G. Charles Dismukes. Coordination Geometry and Oxidation State Requirements of Corner-Sharing MnO₆ Octahedra for Water Oxidation Catalysis: An Investigation of Manganite (γ -MnOOH). *ACS Catalysis*, 6(3):2089–2099, March 2016. doi: 10.1021/acscatal.6b00099.

- [20] S.Blundell. *Magnetism in Condensed Matter*. Publisher : Oxford University Press, 2001.
- 2065 [21] Alexander J. R. Botz, Michaela Nebel, Rosalba A. Rincón, Edgar Ventosa, and Wolfgang Schuhmann. Onset potential determination at gas-evolving catalysts by means of constant-distance mode positioning of nanoelectrodes. *Electrochimica Acta*, 179:38–44, October 2015. ISSN 0013-4686. doi: 10.1016/j.electacta.2015.04.145.
- 2070 [22] Guolong Lu, Haishen Yang, Youlong Zhu, Tyler Huggins, Zhiyong Jason Ren, Zhenning Liu, and Wei Zhang. Synthesis of a conjugated porous Co(II) porphyrinylene–ethynylene framework through alkyne metathesis and its catalytic activity study. *Journal of Materials Chemistry A*, 3(9):4954–4959, February 2015. ISSN 2050-7496. doi: 10.1039/C4TA06231K.
- [23] A.J.Bard L.R.Faulkner. *Electrochemical Methods: Fundamentals and Applications, 2nd edition*. Publisher: New York : Wiley, 2000.
- 2075 [24] Kelsey A. Stoerzinger, Marcel Risch, Binghong Han, and Yang Shao-Horn. Recent Insights into Manganese Oxides in Catalyzing Oxygen Reduction Kinetics. *ACS Catalysis*, 5(10): 6021–6031, October 2015. doi: 10.1021/acscatal.5b01444.
- 2080 [25] Jin Suntivich, Hubert A. Gasteiger, Naoaki Yabuuchi, Haruyuki Nakanishi, John B. Goodenough, and Yang Shao-Horn. Design principles for oxygen-reduction activity on perovskite oxide catalysts for fuel cells and metal–air batteries. *Nature Chemistry*, 3(7):546–550, July 2011. ISSN 1755-4349. doi: 10.1038/nchem.1069.
- [26] Yasuharu Yokoi and Hiroshi Uchida. Catalytic activity of perovskite-type oxide catalysts for direct decomposition of NO: Correlation between cluster model calculations and temperature-programmed desorption experiments. *Catalysis Today*, 42(1):167–174, June 1998. ISSN 0920-5861. doi: 10.1016/S0920-5861(98)00087-X.
- 2085 [27] Anna S. Ryabova, Filipp S. Napolskiy, Tiphaine Poux, Sergey Ya. Istomin, Antoine Bonfont, Denis M. Antipin, Alexander Ye. Baranchikov, Eduard E. Levin, Artem M. Abakumov, Gwénaëlle Kéranguéven, Evgeny V. Antipov, Galina A. Tsirlina, and Elena R. Savinova. Rationalizing the Influence of the Mn(IV)/Mn(III) Red-Ox Transition on the Electrocatalytic Activity of Manganese Oxides in the Oxygen Reduction Reaction. *Electrochimica Acta*, 187:161–172, January 2016. ISSN 0013-4686. doi: 10.1016/j.electacta.2015.11.012.
- 2090 [28] Yuan Fang, Yonghui Wang, Fen Wang, and Jianfeng Zhu. 3D structured Mn₂O₃ synthesized using tween surfactant: influence on the morphology and oxygen reduction catalytic performance. *CrystEngComm*, 21(3):420–429, January 2019. ISSN 1466-8033. doi: 10.1039/C8CE01358F.
- 2095 [29] J. Venkata Swetha, Haridas Parse, Bhalchandra Kakade, and A. Geetha. Morphology dependent facile synthesis of manganese oxide nanostructures for oxygen reduction reaction. *Solid State Ionics*, 328:1–7, December 2018. ISSN 0167-2738. doi: 10.1016/j.ssi.2018.11.002.
- 2100 [30] Ying Wang, Tianjun Hu, Yan Chen, Hongjie Yuan, and Yanting Qiao. Crystal facet-dependent activity of α -Mn₂O₃ for oxygen reduction and oxygen evolution reactions. *International Journal of Hydrogen Energy*, 45(43):22744–22751, September 2020. ISSN 0360-3199. doi: 10.1016/j.ijhydene.2020.06.085.

- [31] Jing Liu, Luhua Jiang, Tianran Zhang, Jutao Jin, Lizhi Yuan, and Gongquan Sun. Activating Mn₃O₄ by Morphology Tailoring for Oxygen Reduction Reaction. *Electrochimica Acta*, 205:38–44, July 2016. ISSN 0013-4686. doi: 10.1016/j.electacta.2016.04.103.
- [32] Rui Gao, Lei Liu, Zhongbo Hu, Peng Zhang, Xingzhong Cao, Baoyi Wang, and Xiangfeng Liu. The role of oxygen vacancies in improving the performance of CoO as a bifunctional cathode catalyst for rechargeable Li–O₂ batteries. *Journal of Materials Chemistry A*, 3(34): 17598–17605, August 2015. ISSN 2050-7496. doi: 10.1039/C5TA03885E.
- [33] Dafeng Yan, Yunxiao Li, Jia Huo, Ru Chen, Liming Dai, and Shuangyin Wang. Defect Chemistry of Nonprecious-Metal Electrocatalysts for Oxygen Reactions. *Advanced Materials*, 29(48):1606459, 2017. ISSN 1521-4095. doi: 10.1002/adma.201606459.
- [34] Susana G. Sanf elix. Manganese Oxide Nanoparticles: Synthesis and Magnetic Properties. *researchgate*, January 2008. doi: 10.13140/RG.2.2.10513.35684.
- [35] Nobuyuki Sakai, Yasuo Ebina, Kazunori Takada, and Takayoshi Sasaki. Photocurrent Generation from Semiconducting Manganese Oxide Nanosheets in Response to Visible Light. *The Journal of Physical Chemistry B*, 109(19):9651–9655, May 2005. ISSN 1520-6106. doi: 10.1021/jp0500485.
- [36] Han Tian, Liming Zeng, Yifan Huang, Zhonghua Ma, Ge Meng, Lingxin Peng, Chang Chen, Xiangzhi Cui, and Jianlin Shi. In Situ Electrochemical Mn(III)/Mn(IV) Generation of Mn(II)O Electrocatalysts for High-Performance Oxygen Reduction. *Nano-Micro Letters*, 12(1):161, August 2020. ISSN 2150-5551. doi: 10.1007/s40820-020-00500-7.
- [37] Victoria A. Nikitina, Aleksandr A. Kurilovich, Antoine Bonfont, Anna S. Ryabova, Renat R. Nazmutdinov, Elena R. Savinova, and Galina A. Tsirlina. ORR on Simple Manganese Oxides: Molecular-Level Factors Determining Reaction Mechanisms and Electrocatalytic Activity. *Journal of The Electrochemical Society*, 165(15):J3199, October 2018. ISSN 1945-7111. doi: 10.1149/2.0261815jes.
- [38] Rolando Guidelli, Richard G. Compton, Juan M. Feliu, Eliezer Gileadi, Jacek Lipkowski, Wolfgang Schmickler, and Sergio Trasatti. Definition of the transfer coefficient in electrochemistry (IUPAC Recommendations 2014). *Pure and Applied Chemistry*, 86(2):259–262, February 2014. ISSN 1365-3075. doi: 10.1515/pac-2014-5025.
- [39] Rolando Guidelli, Richard G. Compton, Juan M. Feliu, Eliezer Gileadi, Jacek Lipkowski, Wolfgang Schmickler, and Sergio Trasatti. Defining the transfer coefficient in electrochemistry: An assessment (IUPAC Technical Report). *Pure and Applied Chemistry*, 86(2): 245–258, February 2014. ISSN 1365-3075. doi: 10.1515/pac-2014-5026.
- [40] A.J. Bard L.R. Faulkner. *Electrochemical Methods: Fundamentals and Applications, 1st edition*. Publisher : New York : Wiley, 1980.
- [41] J. a. V. Butler. Studies in heterogeneous equilibria. Part II.—The kinetic interpretation of the nernst theory of electromotive force. *Transactions of the Faraday Society*, 19(March): 729–733, January 1924. ISSN 0014-7672. doi: 10.1039/TF9241900729.
- [42] H. Chen R.G. Compton. *Journal of Electroanalytical Chemistry*, volume 880. Publisher : Elsevier, 2021.

- 2145 [43] Danlei Li, Chuhong Lin, Christopher Batchelor-McAuley, Lifu Chen, and Richard G. Compton. Tafel analysis in practice. *Journal of Electroanalytical Chemistry*, 826:117–124, October 2018. ISSN 1572-6657. doi: 10.1016/j.jelechem.2018.08.018.
- 2150 [44] Xuepeng Zhong, M’hamed Oubla, Xiao Wang, Yangyang Huang, Huiyan Zeng, Shaofei Wang, Kun Liu, Jian Zhou, Lunhua He, Haihong Zhong, Nicolas Alonso-Vante, Chin-Wei Wang, Wen-Bin Wu, Hong-Ji Lin, Chien-Te Chen, Zhiwei Hu, Yunhui Huang, and Jiwei Ma. Boosting oxygen reduction activity and enhancing stability through structural transformation of layered lithium manganese oxide. *Nature Communications*, 12(1):3136, May 2021. ISSN 2041-1723. doi: 10.1038/s41467-021-23430-3.

CHAPTER 3

NIOX SYSTEM, HYBRID MATERIALS. : CATALYST FOR HER

2155

Contents

| | | |
|------|--|------------|
| | 3.1 General properties: Nickel oxide | 116 |
| | 3.1.1 Mechanism and catalyst for hydrogen evolution reaction | 116 |
| 2160 | 3.1.2 Synthesis of the self-standing NiOx electrodes | 120 |
| | 3.1.3 Spectroscopic investigation | 120 |
| | 3.2 Electrochemical investigation | 125 |
| | 3.2.1 Mechanism of hydrogen evolution reaction for Nickel oxide and influence of KOH concentration | 125 |
| 2165 | a) Electrochemical active surface area and the uncompensated resistance | 125 |
| | b) Hydrogen evolution reaction response | 127 |
| | c) Tafel slope and mechanism investigation | 129 |
| | 3.2.2 Electrochemical impedance spectroscopy (EIS) | 131 |
| | 3.3 Conclusion: Correlation between LSV and EIS | 140 |
| 2170 | References | 141 |

In this chapter and the following chapters (Chapter 4 and Chapter 5), we will study a tridimensional self-supported nickel oxide $\text{Ni}(\text{OH})_x$ doped with iron and phosphorus electrocatalyst. This study is a part of an international collaboration with Prof. Cho from Korean Advanced Institute of Science and Technology (KAIST, South Korea). The main attraction point for this kind of electrode is that it can be viewed as a trifunctional material. This nickel foam electrode can be used as a catalyst for the hydrogen evolution reaction (HER) and the oxygen evolution reaction (OER) in alkaline media. These reactions (HER and OER) are the key elements of the electrochemical water-splitting, which is an interesting process for hydrogen production. The aim to developing the water splitting studies is to find a sustainable production of hydrogen through the development of renewable energy resources and to replace the use of the fossil energies that impact the planet.^[1] Indeed, nickel foam doped with non-noble metal is interesting for water splitting.^[2-7] This is because nickel foam can be used as the substrate exhibiting conductivity and presents a good activity for the HER and OER.^[7]

2185

In the first part of this chapter, we will briefly present the mechanism of HER. After that, we will perform spectroscopy investigations (XPS, EDS, SEM) to identify the elements present in the electrode studied. Finally, we will focus on the HER response of the electrode in alkaline media at different concentrations.

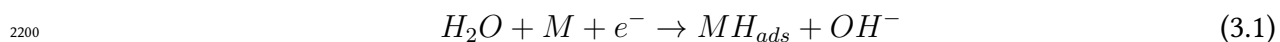
3.1 General properties: Nickel oxide

3.1.1 Mechanism and catalyst for hydrogen evolution reaction

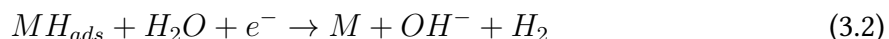
In this first part, we will look at the HER mechanism and the use of Nickel-based compounds through the HER. Hydrogen evolution reaction (HER) can be divided into three-step acidic and alkaline media.

We will see the mechanism that takes place in alkaline media for HER.

We have the Volmer reaction corresponding to electrochemical hydrogen adsorption given by equation (3.1) :



The Volmer reaction is followed by the Heyrovsky reaction corresponding to the electrochemical desorption step. (3.2) :



The Volmer reactions can be followed by the Tafel reaction, also given by equation (3.3):

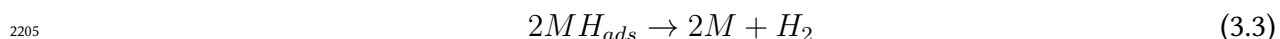


Figure 3.1. (right side) shows the HER mechanism in alkaline media.

We can also look at the mechanism for the HER in acidic media.

We have the Volmer reaction given by equation (3.4):



The Heyrovsky reaction for acidic media is given by equation (3.5) :



Moreover, the Volmer reaction is the same in both media: (3.6) :



Figure 3.1. (left side) will find the HER mechanism in acidic media.

2215

The nature of the electrode materials will play a part in the activity of HER thanks to the electronic structure of the electrode.

2220

We can link the three pathways to the Tafel slopes given by Butler–Volmer conduct to find the determinate step limiting. Depending on the value of the Tafel slope, we can find the mechanism followed. (We saw this in detail in the first chapter) if we have a slope at 29 mV. dec^{-1} , we are going to have the Tafel mechanism. Furthermore, if the slope is at 38 or 116 mV. dec^{-1} , it is the Heyrovsky mechanism or Volmer mechanism. 3.1.

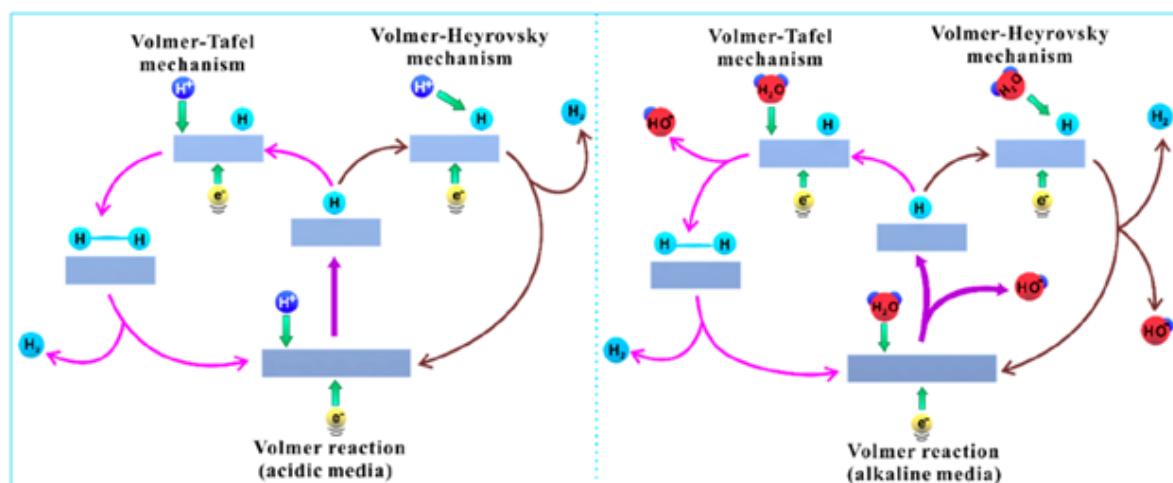


Figure 3.1 – Mechanism of hydrogen evolution reaction in acidic (left) and alkaline (right) solutions^[8]

2225

Nørskov et al.^[9] demonstrated that the rate-determining step in the case of HER is the adsorption energy of hydrogen ($\Delta G_{H_{ads}}$). To have an excellent catalyst through the HER, the bonding strength between the adsorbed hydrogen atom and the catalyst has to be good.

2230

Li et al.^[10] highlighted that in alkaline media, there is an additional energy barrier due to the water molecule's dissociation which leads to a lower rate of HER. Even if hydrogen adsorption and dissociation are two consecutive steps, they are in competition. When we look closer at the bonding strength between the catalyst species and the hydrogen atom, we will not effectively adsorb hydrogen proton intermediates if the bond is too weak. On the other hand, if the bonding is too strong, the generated hydrogen will be challenging to desorb from the catalyst's surface. To have a suitable catalyst for HER, the catalyst must balance the adsorption and desorption steps and optimize the bonding strength through the hydrogen atom.^[11] To find the best catalyst, let us look at the Volcano plot made by Sheng et al.^[12]. We can find the volcano plot in figure 3.2. Figure 3.2 illustrated the volcano plot of various metals in alkaline conditions of HER. With the help of the volcano plot, we can see which metal is a suitable catalyst through HER activity. We look at figure 3.2, which illustrates the behaviour of various metals in alkaline

2235

conditions for HER. If the position of the metal is close to the apex of the volcano plot, the metal presents the best balance for the adsorption and desorption of hydrogen, leading to the best catalyst. One observes that the best catalysts are the platinum Pt and the palladium Pd. In our case, nickel Ni presents a lower adsorption free energy of hydrogen and can be selected as a suitable candidate for HER. To improve the catalytic property of nickel concerning HER, we can dope Ni with heteroatoms such as iron, phosphor, and alloying.

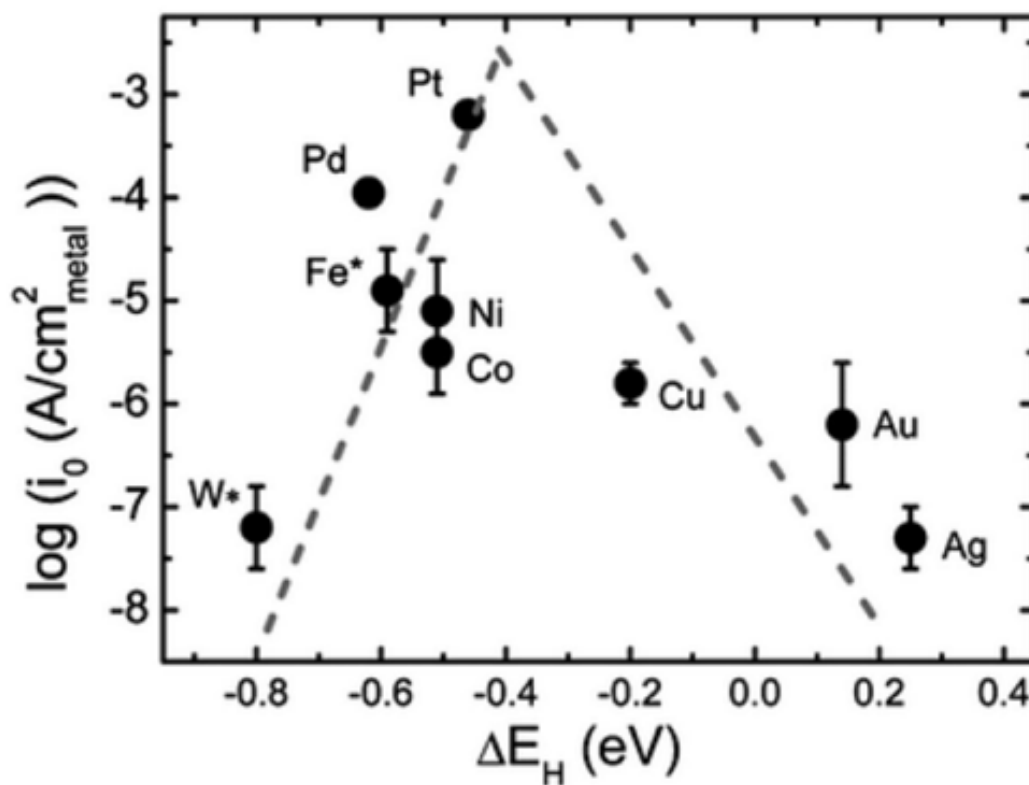


Figure 3.2 – Volcano plot for hydrogen evolution reaction in the alkaline medium for various metals^[12]

In the past decade, transition metals (TMs) became an alternative to the use of precious catalyst for HER thanks to their cheap cost, their abundance, and their good stability in the alkaline solution.^[13] For the water-splitting, various studies were performed to find excellent catalysts in alkaline media though composed of sulfides (a-MoS₂, Ni₃S₂, etc.)^[14,15], selenides (CoNiSe₂, CoSe/MoSe₂, etc.)^[16,17], perovskites^[18], phosphides^[19,20], and nitride^[21,22]. Herein, we used a nickel oxide foam (NiOx), a possible candidate as a bifunctional catalyst for water spitting. This criterion is due to the optimal active site on the nickel surface for the absorption of protons and hydride. The adsorption is good for the O site present in NiOx, allowing the bonding with the reaction intermediates in water splitting.^[8] Furthermore, the doping of NiOx with phosphides/phosphates phosphate P atom has a significant role in optimising the electronic structure of the catalyst material.

To turn the electronic structure of the catalyst, we can dope it with heteroatoms. We can use metal elements (like Ce, V, Cr, Mn, Fe, Co, Ni, Cu, Zn, W, Mo, etc.) and non-metal elements (such as N, O, P, S, Se, Te, F, etc.). The aim of doping with heteroatom is to modify lattice periodicity, which is responsible for the change of local electronic structure.^[23]

The doping of heteroatoms on the catalytic materials will be different for the HER and OER.

We will look at the dopant effect on HER. The doping with P atom into metal crystal lattices will impact the metal's conductivity, corrosion resistance, and electron structure. The catalyst will exhibit a metallic character if it presents a metal-rich phosphide. If we have a semiconductive feature of the metal, it is due to restricted electron delocalization of the P-P bond.^[24] Concerning the influence of Fe doping under the reduction environment of HER is also investigated. In the case studies by He and al.^[25], on the F-doped doped Ni₃S₂ nanosheet array electrode (F-Ni₃S₂/NF). In this study, they prove the substitution of S by F how present a stronger electronegativity influences the catalytic response. This stronger electronegativity will have an impact and conduct to the redistribution of electrons on Ni sites, which is further proved by the DFT calculations.^[25]

In our case, we can suppose this following hypothesis on the dopping effetct. The electronegative property of the P atom allows capturing of positively charged protons in water and increases the catalytic hydrogen evolution rate. The other transition metal used to improve the catalyst is iron Fe. When we co-doped the NiOx system with Fe, we can change P's electronic structure and optimise the H atom's adsorption energy.^[26]

| Material | Overpotential at 10 mA.cm ⁻² (mV) | Tafel slope (mV.dec ⁻¹) | Reference |
|---|---|--|--------------------------------|
| CoFe@NiFe-200/NF | 240 | 88.88 | Wang et al. ^[27] |
| NiFe/NiCo ₂ O ₄ /NF | 105 | 88 | Wang et al. ^[27] |
| Ni(OH) ₂ /NF | 250 | | Tang et al. ^[28] |
| Nickel foam | 255 | 129 | Tang et al. ^[28] |
| NiFeS/NF | 180 | | Zhang et al. ^[29] |
| Fe-doped NiSe / Ni foam | 163 | 71.4 | Zou et al. ^[30] |
| CoSe@NiFe-LDH/NF | 98 | 89 | Wang et al. ^[27] |
| NiCoP-C(TPA)/NF | 78 | | Zhang et al. ^[31] |
| Ni ₂ P/NF | 65 | 50 | Huang et al. ^[32] |
| NiFe-P/NF | 87 | 48 | Xing et al. ^[2] |
| CoFe-P/NF | 45 | 35.4 | Wang et al. ^[27] |
| O-NiMoP ₂ /NF | 31 | 62.1 | Zhang et al. ^[33] |
| Ni _{2(1-x)} Mo _{2x} P/NF | 72 | 46.4 | Yu et al. ^[34] |
| FeP/Ni ₂ P/NF | 14 | 24.2 | Yu et al. ^[35] |
| Ni ₁₁ (HPO ₃) ₈ (OH) ₆ /NF | 42 | 102 | Menezes et al. ^[36] |
| Ni _{1.85} Fe _{0.15} P NSAS/NF | 106 | 89.7 | Wang et al. ^[37] |
| Ni ₂ P/Ni/NF | 98 | 72 | You et al. ^[38] |
| Ni ₂ P/NF | 220 | - | Stern et al. ^[39] |

Table 3.1 – Comparison of hydrogen evolution reaction electrochemical activity parameters for selected materials in alkaline (1M KOH) for Nickel foam (NF) with Iron and Phosphor doped^[40]

3.1.2 Synthesis of the self-standing NiOx electrodes

The NiOx foam electrodes were prepared by Pr. Cho's team.^[41] Electrodeposition is used to synthesize the electrodes using a two-electrode system consisting of copper and pure nickel foam as the cathode and anode, respectively. We have no access to the detailed experimental protocol due to the confidentiality of the composition of the electrode. However, we can analyze their structure deeply by combining various spectroscopy techniques.

3.1.3 Spectroscopic investigation

In this following part, we combine various spectroscopy techniques to investigate the composition of the NiOx foam electrodes: X-ray photoelectron spectroscopy (XPS), scanning electron microscopy (SEM), and energy dispersive spectroscopy (EDS).

Firstly, we use X-ray photoelectron spectroscopy (XPS). The measurements on the nickel oxide foam were carried out with ThermoFisher Scientific K-Alpha⁺ fitted with a micro-focused,

monochromatic Al K α ($h\nu = 1486.6$ eV).

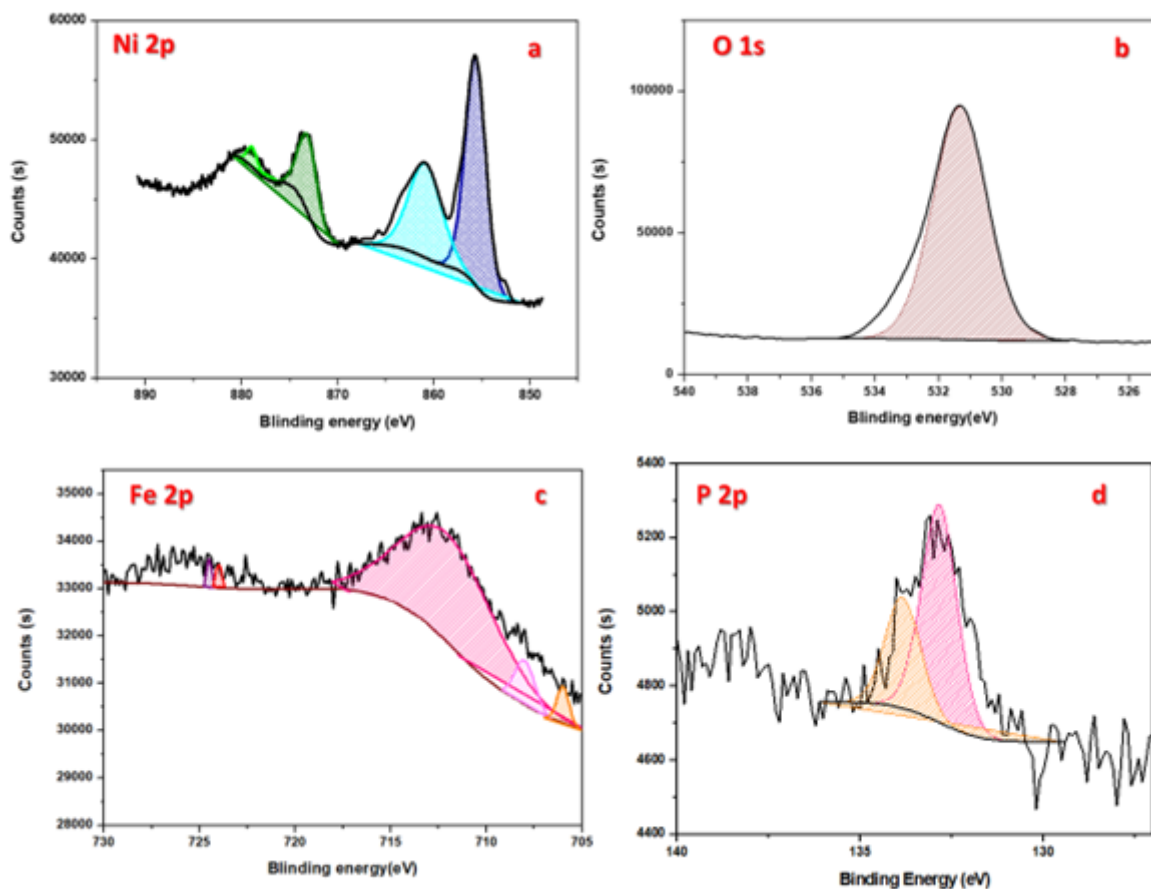


Figure 3.3 – XPS spectra of (a) Ni 2p, (b) O 1s, (c) Fe 2p and (d) P 2p of NiO foam electrode

In figure 3.3, we have all the XPS spectra obtained. Figure 3.3 is composed with the spectra of Ni 2p (3.3.a), O 1s (3.3.b), Fe 2p (3.3.c) and P 2p (3.3.d).

2290 Figure 3.3.a is the spectrum of Ni 2p. We observed two peaks at 855.7 and 873.4 eV (in dark blue and dark green), which correspond to Ni²⁺ 2p_{3/2} and Ni²⁺ 2p_{1/2}. Moreover, we can also find the two satellite peaks located at 861.5 and 879.4 eV (in light blue and light green) accordingly to Ni²⁺.^[42,43]

2295 Figure 3.3.b reports the spectrum of O 1s, with one observed peak at 530.5 eV corresponding to P–O compounds.^[44]

Figure 3.3.c shows the spectrum of Fe 2p with several peaks located at 706, 709.1, 712.3, 723, and 724.6 eV. These peaks can be attributed to Fe 2p_{3/2} and Fe 2p_{1/2}. The peak obtained can be correlated to the XPS spectra of a few species, such as metallic Fe, FeO, and Fe₂O₃.

2300 The peak observed at 706 eV (in orange) is Fe⁰ 2p_{3/2}, and the two peaks at 709.1 and 723 eV (in light pink and red) are assigned to the Fe 2p_{3/2} and Fe 2p_{1/2} of FeO. The two other peaks at 712.3 and 724.6 eV (in pink and purple) correspond to Fe 2p_{3/2} and Fe 2p_{1/2} of Fe₂O₃.^[7]

For the last spectrum (figure 3.3.d), the peak corresponding to metal phosphate is at 133 eV. We can identify the P 2p_{3/2} and P 2p_{1/2} at 133 and 133.8 eV (in pink and orange) with binding energy of $\Delta=0.80$ eV.

2305

The second part of the investigation used scanning electron microscopy (SEM) and energy dispersive spectroscopy (EDS) to look at the morphology and composition of the nickel oxide foam studied.

The scanning electron microscopy (SEM) was obtained with MEB-FEG Zeiss (Zeiss SUPRA 40).

2310

The SEM images are shown in figure 3.4. These images were obtained after the electrochemical investigation. Figure 3.4a shows the macroscopic 3D skeleton of Ni foam, and Figure 3.4b we have the SEM image of one zone zoomed of the skeleton observed in Figure 3.4a. The surface of the Ni foam is rough and presents some particles on it. One observes white dots and agglomeration on the skeleton. We zoomed one of the edges of the skeleton to look at the morphology of the particles (Figure 3.4b), and we show a dispersion of the nanostructured particles in a heterogeneous way. The average size of the particles is around 784.65 nm.

2315

To obtain a deep analysis of the composition of the nanostructured particles, we use EDS. We can see the presence of phosphorus and oxygen elements. Also, the potassium trace found is due to the use of potassium hydroxide KOH as the electrolyte during the electrochemical investigation. (Figure 3.5)

2320

The other track for the element identification was the elemental mappings in the one edge of the studied nickel foam (Figure 3.6). One can remark the dispersion of P and Fe elements as dopants on the studied Nickel oxide foam. SEM and EDS investigations allow us the element identification and confirm the results obtained by XPS.

2325

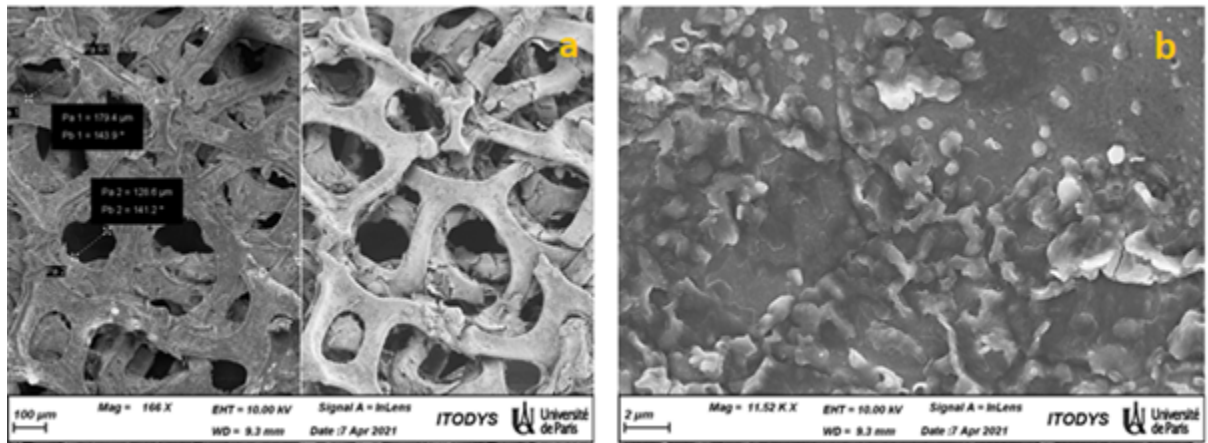


Figure 3.4 – SEM image of NiOx/Ni

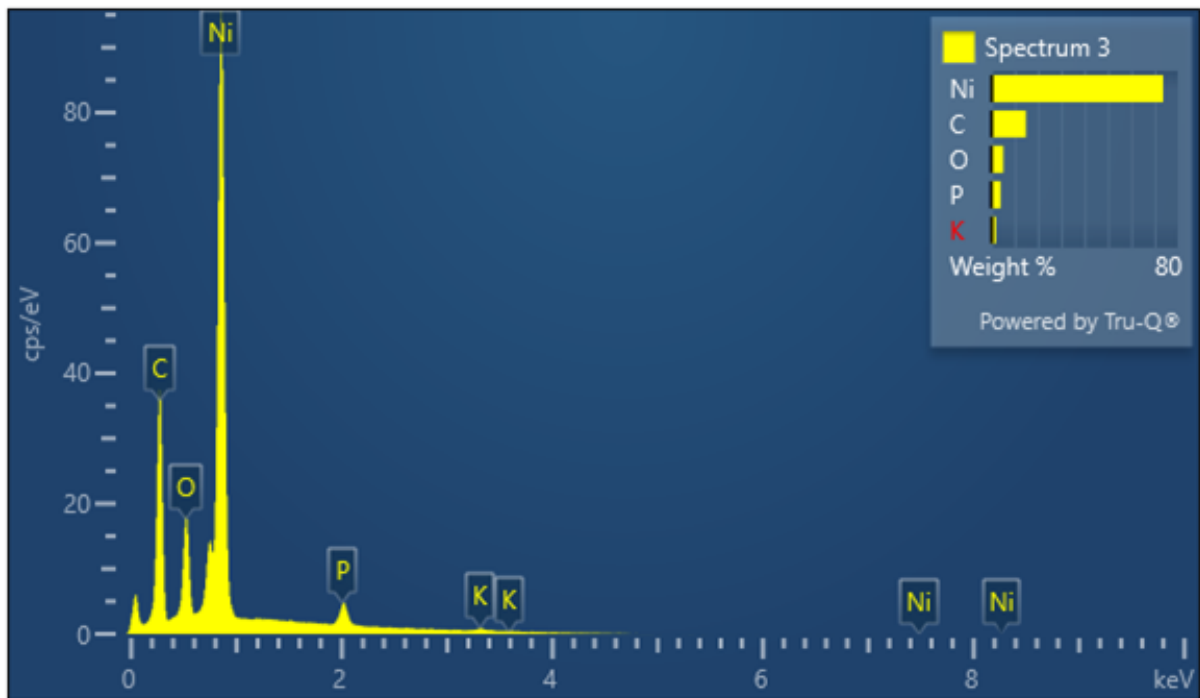


Figure 3.5 – EDS of the NiOx/Ni

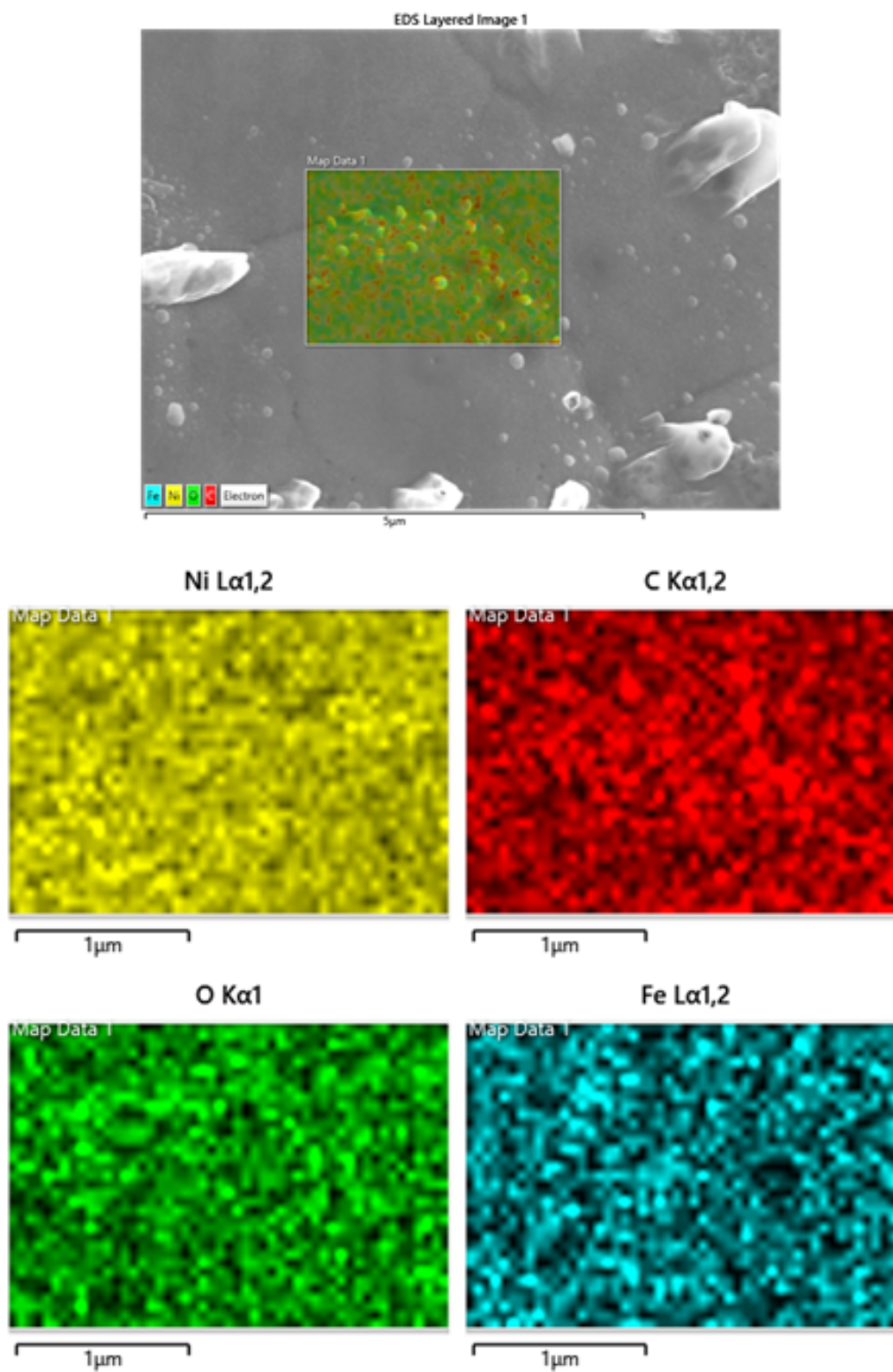


Figure 3.6 – Elemental mappings of the edge of NiOx

3.2 Electrochemical investigation

This section will look at the electrochemical investigation through HER by the doped NiOx electrode. HER was investigated in alkaline media at different potassium hydroxide KOH concentrations: 0.5; 0.75; 1 and 1.5 mol/L. To simplify the analysis of the results, we first present the results obtained at 1 mol/L KOH. After that, we investigate the influence of KOH concentration for HER. We can divide the electrochemical investigation into three parts:

1. In the first part, we are going to investigate the following parameters:
 - (i) the electrochemical active surface area (ECSA) from the capacitance (F) measurements,
 - (ii) Electrochemical impedance spectroscopy (EIS) to determine the uncompensated resistance R (Ω),
 - (iii) linear sweep voltammetry (LSV) to evaluate the catalytic performance and notice the various overpotentials at different current density (mA/cm^2) and
 - (iv) the Tafel slope which is linked to the HER mechanism.
2. In the second part of the electrochemical investigation, we will focus on electrochemical impedance spectroscopy (EIS) to determine the following parameters: (i) the Charge transfer resistance $R_2 = R_{ct}$,
- (ii) the polarization resistance R_p and (iii) the resistance R'_θ .
3. Moreover, in the last part, we will correlate the results obtained from the Tafel slope investigation and the EIS.

3.2.1 Mechanism of hydrogen evolution reaction for Nickel oxide and influence of KOH concentration

For the electrochemical investigation, the measurement was performed with a three-electrode system with Bio-Logic Potentiostat/Galvanostat using EC-Lab software (Bio-Logic Science Instruments, Seyssinet-Pariset, France) at room temperature under an oxygen-statured atmosphere. We converted all the data on the potential vs. RHE according to:

$$E_{RHE} = E_{Ag/AgCl} + E_{Ag/AgCl}^0 + 0.059 \times pH \text{ with } E_{Ag/AgCl}^0 = 0.197V \quad (3.7)$$

a) Electrochemical active surface area and the uncompensated resistance

To determine the electrochemical active surface area (ECSA), we will focus on the non-Faradaic charging zone. We recorded a series of cyclic voltammetry CV at different scan rates (5, 10, 25, 50, 75, and 100 $\text{mV}\cdot\text{s}^{-1}$). Thanks to all the data obtained with the CVs recorded, we can determine the capacitive current I_c of the electrode at each scan rate, as shown in Figure 3.7. The plot ΔI_c as a function of the scan rate ν gives a straight-line with a slope S where :

$$\Delta I_c = I_{anodic} - I_{cathodic} \quad (3.8)$$

Knowing the slope, the double-layer capacitance value C_{dl} can be calculated from the following equation (3.9) :

$$C_{dl} (F) = \frac{\Delta I_c}{2S\nu} \quad (3.9)$$

Based on the published value of the specific double-layer capacitance value C_{dl} of $300 \mu\text{F}/\text{cm}^2$ for nickel oxide electrode^[45] , we can determine the ECSA from^[46] :

$$ECSA(\text{cm}^2) = \frac{C_{dl}(\mu\text{F})}{c(\frac{\mu\text{F}}{\text{cm}^2})} \quad (3.10)$$

One obtains a double-layer capacitance C_{dl} (F) of 6.56×10^{-3} F and ECSA of 21.85 cm^2 .

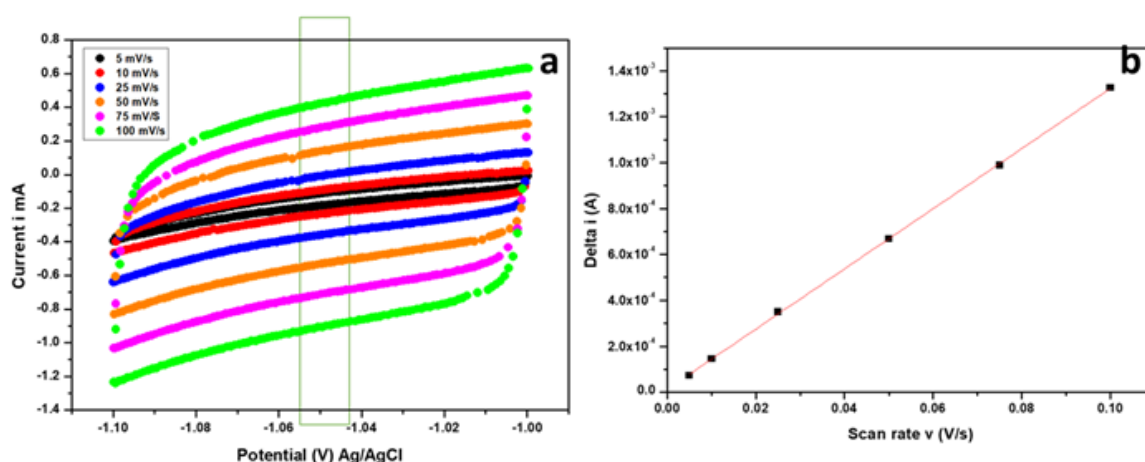


Figure 3.7 – (a) Cyclic voltammogram of modified NiOx recorded at various scan rates (b) Evolution of the charging current (A) as a function of the scan rate ($\text{V}\cdot\text{s}^{-1}$)

Electrochemical Impedance Spectroscopy (EIS) is used to determine the uncompensated resistance R , which should be considered during the electrochemical investigation. EIS is conducted by collecting the impedance spectrum from 20 kHz to 1 Hz. To find the R , we have to trace the inverse of the impedance's real part as function of the frequency inverse. The EIS measurements obtain the real part and the frequency. With the linear fitting, we can go back to the intercept value. The inverse of the intercept value is R (Figure 3.8). This uncompensated resistance R , herein 1.297Ω , is used to correct the voltammogram.

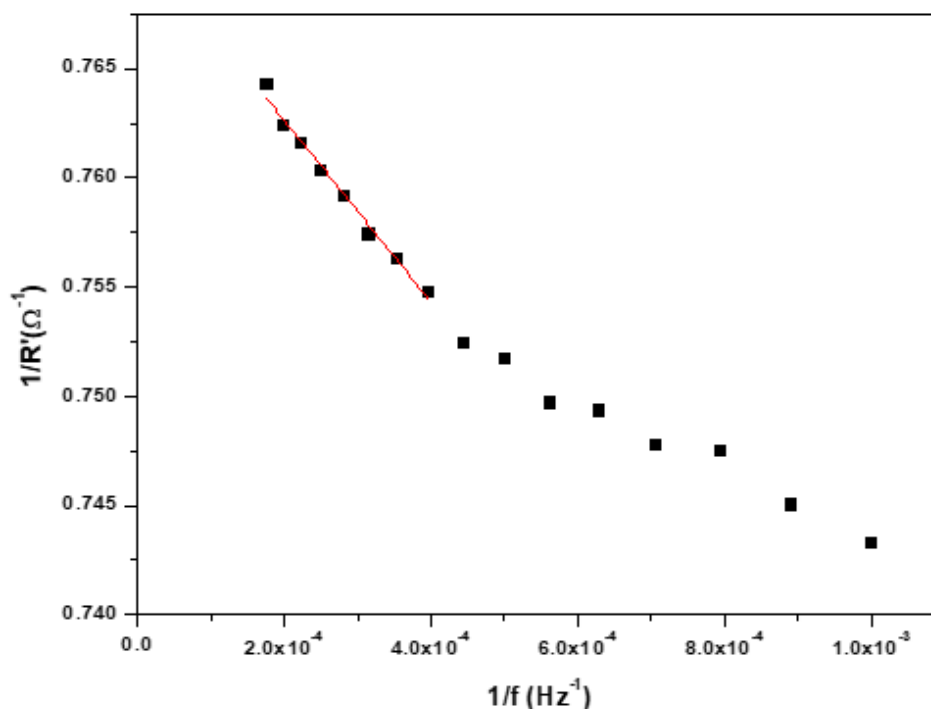


Figure 3.8 – Evolution of the inverse of the real part as a function the inverse of frequency

b) Hydrogen evolution reaction response

In this following part, we will look at the linear sweep voltammetry given by the potential corrected and the overpotential at different current densities for HER response. In the literature, to check the catalytic activity, it is common to compare the overpotential at -10 mA/cm^2 . For the catalyst based on nickel foam, we can also compare the value at different values of current density like -20 , -50 or -100 mA/cm^2 ^[47]. In the case of an ideal catalyst, we will have a higher current density at lower overpotential.

For our studies, we look at three values of current density to look at the overpotential. The current density range selected for the overpotential is -10 , -20 and -50 mA/cm^2 . Figure 3.9 shows the LSV for HER in 1M KOH recorded at 2 mV/s . The current density was calculated according to the geometric surface of $1 \text{ cm} \times 1 \text{ cm}$.

The values of the overpotential at the different current densities are: $\eta_{(10)} = 200.89 \text{ mV}$ at 10 mA/cm^2 , $\eta_{(20)} = 231.09 \text{ mV}$ at 20 mA/cm^2 and $\eta_{(50)} = 253.06 \text{ mV}$ at 50 mA/cm^2 .

The results are reproducible. Compared to the table (3.1), the NiOx catalyst we studied exhibits good catalytic activity. Now, we investigate HER with LSV studies at different concentrations of KOH.

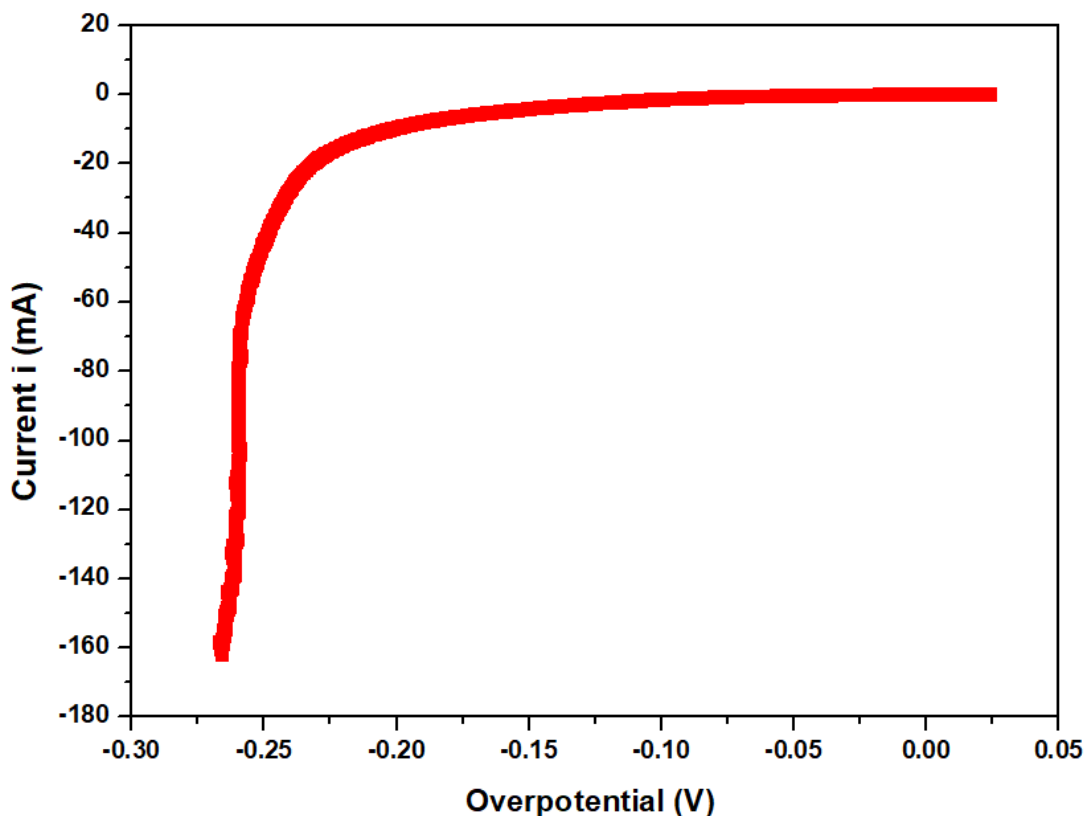


Figure 3.9 – Linear sweep voltammetry (LSV) of modified NiOx recorded at $\nu = 2$ mV/s in 1 M KOH

Figure 3.10 reports the overpotentials at different density currents as function of the KOH concentrations. One observes that the overpotential depends upon the KOH concentration. We can see an increase of the overpotentials with KOH concentration until 1 M followed by a decrease of the overpotentials for 1.5 M KOH. We can see that the lowest overpotentials are obtained with 0.5 M KOH. One explanation possible for these results is the influence of the cation electrolyte, which can impact the HER kinetic. Recent studies by M. Koper's group^[48] reported the influence of the cation on the HER kinetics in alkaline media. Moreover, they highlighted that at pH 12 when they increased the cation concentration, it is conducted by a small positive effect on the activity of HER to the highlighter concentrations studied. However, when they conducted the studies at pH 13, the increase of the cation concentrations provokes an inhibitive effect on HER activity. We can suppose that we can have this type of reaction for our studies conducted on NiOx electrode, which explains the results obtained. To look more in detail at the HER kinetics, we will investigate the Tafel slope and its mechanism in the next section.

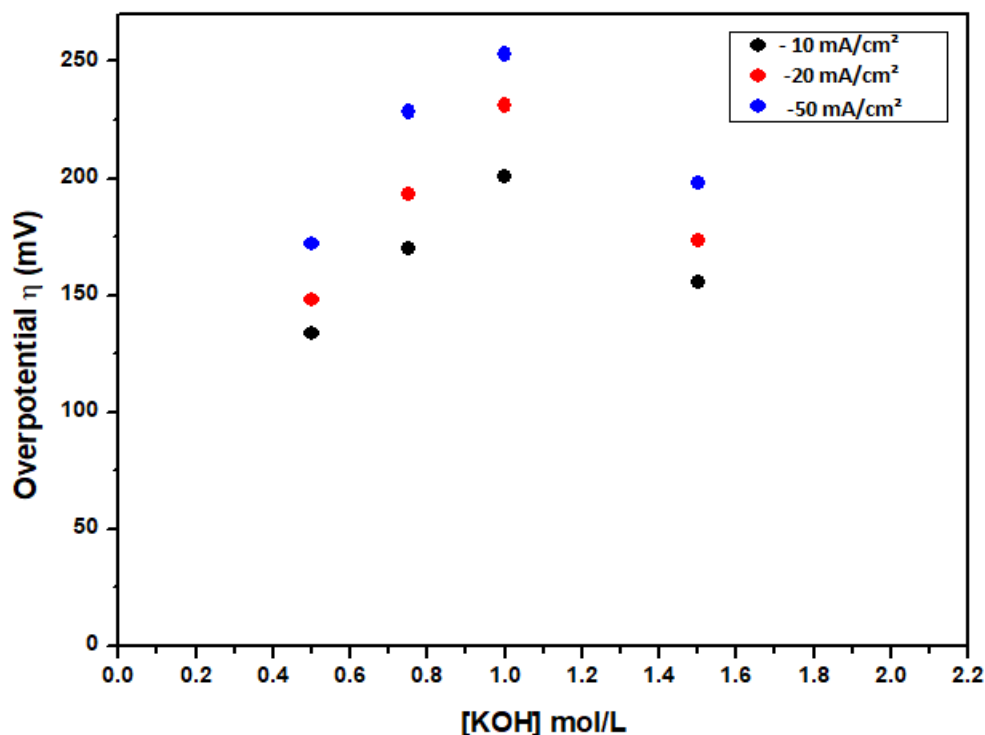


Figure 3.10 – Evolution of overpotentials (mV) at various density current as function of the KOH concentration (mol/L)

c) Tafel slope and mechanism investigation

In the last section of the first electrochemical investigation, we will look at the mechanism thanks to the Tafel slope obtained thanks to the LSV of HER seen in the previous section.

We all made a recap on the different mechanisms possible, and the Tafel slope liked it in the first section on the generalities on NiOx. We focus on the slope values obtained for the electrode tested at 1 M KOH and will compare them with the other values obtained for the studies made at different concentrations of KOH, as seen in the previous part.

To begin the study made 1 M, we used the LSV for HER recorded and presented in figure 3.9. When we look at figure 3.9, we can see that we can divided LSV into two parts. The first one is when the current density decreases slowly at the begging of LSV. Furthermore, the second one is when the current density decreases quickly at the end of LSV. We exclude the values at the end of the LSV. The bubbles were too strong and could impact the result obtained, which cannot represent the electrode behaviour at this range of potential.

In figure 3.11, we can find the LSV for HER with the two-part divided. In the black, we have the response at low overpotential, and in the red, the one at large overpotential.(Figure 3.11a). The figure 3.11b, we traced the Tafel slopes for the two-zones studied.

To trace the Tafel plot, we used the Tafel expression given by the following equation^[49] :

$$\eta = a + b \log j \quad (3.11)$$

with η : overpotential, j : current density, a : intercept associated with the exchange current density j_0 , and b : Tafel slope

The Tafel slope corresponds to the rate of change of the current density j with overpotential η .

Thanks to figure 3.11b, we can see that we have a difference of behaviour through the HER mechanism. For the value of the Tafel slope obtained for the low overpotential, we have 106 mV/dec; for the large overpotential, we have 53 mV/dec.

Two HER mechanisms are possible Volmer-Heyrovsky or Volmer-Tafel. The value obtained for the Tafel slope will indicate the rate-determining step (RDS) such as The Volmer, Heyrovsky, and Tafel steps, which are 120 mV/dec, 40 mV/dec, and 30 mV/dec, respectively. The results highlight that the Volmer–Heyrovsky step is RDS in the low overpotential zone, and in the large overpotential zone, the Volmer-Tafel is RDS.

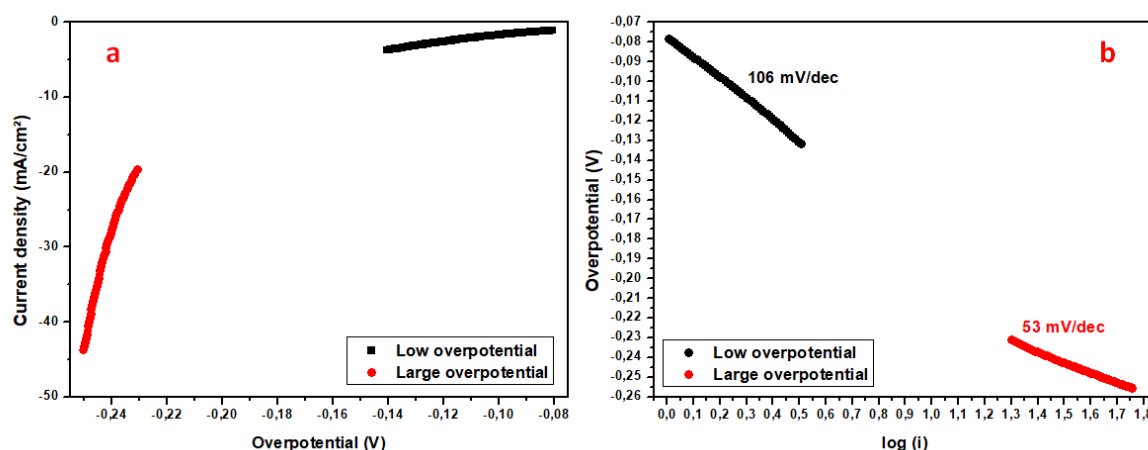


Figure 3.11 – (a) Linear sweep voltammetry (LSV) of modified NiOx recorded at $\nu = 2$ mV/s in 1 M KOH and (b) Tafel slope of 3.11a

In figure 3.12, we compare the Tafel slope in the two-zones delimited at different concentrations of an electrolyte, as we did for the overpotential studies. We can see that we have the same behaviours seen in the study made at 1 M. For the low overpotential zone, the Volmer–Heyrovsky step is RDS, and for the large overpotential zone, the Volmer-Tafel is RDS. The differences of the RDS in the two zones can be explained by doping with P. Electrode is composed of Ni-P; it is favourable water dissociation of Ni-P that will enhance the adsorption of H into adsorption sites of the Ni–P surface. It can explain the selectivity for Volmer–Tafel in the large overpotential zone.^[41] We will look at the EIS investigations conducted.

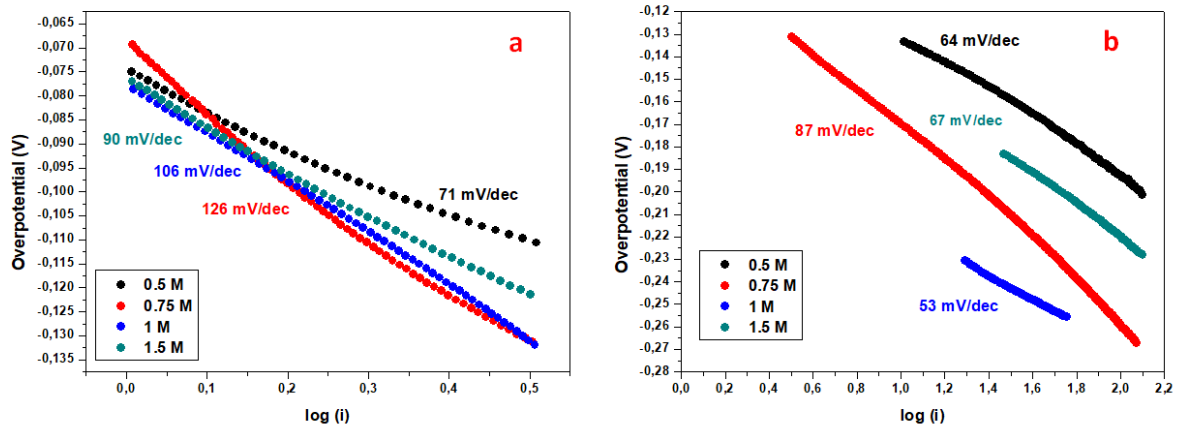


Figure 3.12 – (a) Evolution of the Tafel slope for low overpotential, (b) and large overpotential for different KOH concentration

3.2.2 Electrochemical impedance spectroscopy (EIS)

Electrochemical impedance spectroscopy (EIS) is a powerful tool for analyzing electrochemical kinetics. We perform EIS at different potentials in 1M KOH in this regard. Figure 3.13 shows EIS results obtained at different potentials. Nyquist plot show arcs which exhibit inductive loop at low frequency.

2445

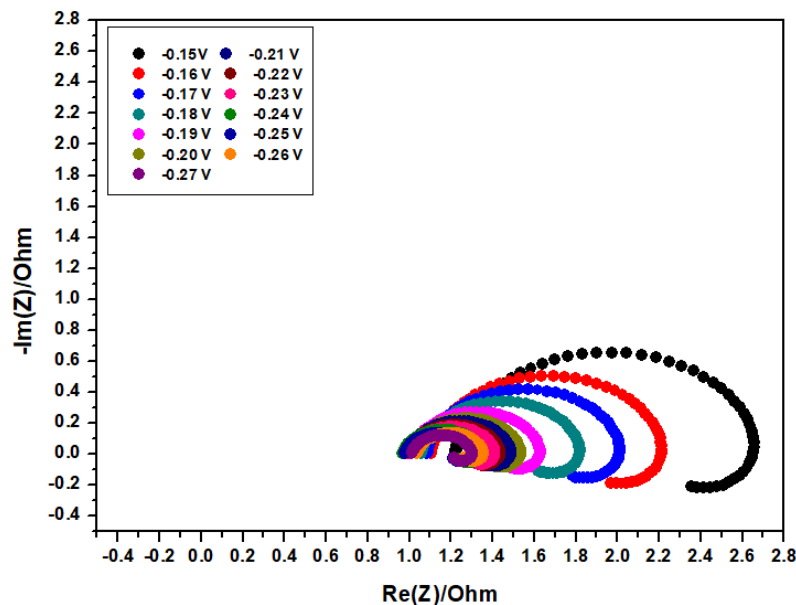


Figure 3.13 – Nyquist plot for NiOx at different potential (1M KOH)

The evolution of these shapes through the polarization point of the electrochemical system allows analyzing the mechanism that takes place on the electrode.^[50]

In the case of two-electron transfer steps, the mechanism proposed can involve an intermediate species adsorbed onto the surface of the electrode and one (or more) species of the electrolytes used. This mechanism proposed for HER corresponds to the Volmer-Heyrovsky mechanism, given in the following equations :



For this type of mechanism, Armstrong and Henderson^[51] highlighted that the transport of the electroactive species in the electrolyte is not limit the kinetics of the reaction. In this case, the impedance diagrams present an inductive arc in the low frequency (LF) region. Impedance analysis of the hydrogen production on the nickel electrode was also deeply performed by Diard's group^[52]. They showed two capacitive arcs: one high-frequency (HF) capacitive arc and one low-frequency (LF) inductive arc.

To analyze EIS data, we use the equivalent circuit shown in 3.14. This equivalent circuit contains the following elements: R_s (solution resistance), CPE (double layer capacitance described by a constant phase element), R_{ct} (charge transfer resistance), R'_θ (resistance of the electrical circuit), and L'_θ (inductance).

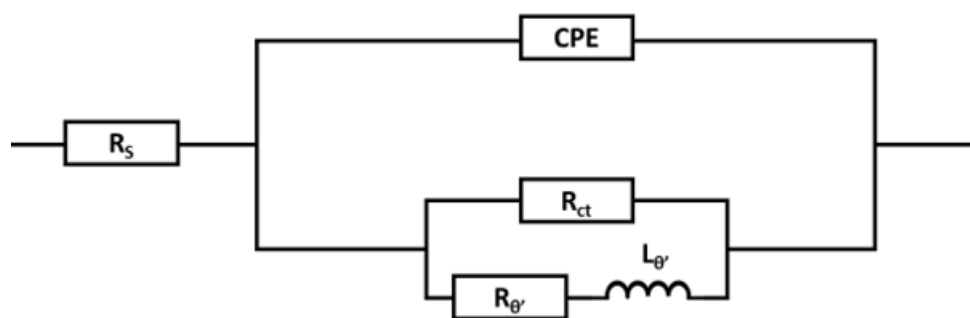


Figure 3.14 – Equivalent circuit for analyzing EIS responses during HER with NiOx electrode^[53]

Let us now describe this equivalent circuit regarding the electrochemical mechanism related to HER. For Volmer- Heyrovsky mechanism, one can write these following equations (3.14):

$$i(t) = i_1(t) + i_2(t) \text{ and } F.\Gamma.\frac{d\theta(t)}{dt} = i_2(t) - i_1(t) \quad (3.14)$$

where i is the density of the total faradaic current, i_1 and i_2 are the density of the partial currents of the two steps of the mechanism, θ is the surface coverage of the electrode by the adsorbate, F is Faraday constant, Γ is the number of electroadsorption sites per unit area of the

electrode surface.

Supposing that the reaction is kinetically controlled, one can link the densities of the partial current i_k with the electrode surface coverage θ and potential E as :

$$i_k(t) = i_k[\theta(t), E(t)] \text{ with } k = 1, 2 \quad (3.15)$$

2475 Under steady-state conditions, one has $\frac{d\theta(t)}{dt} = 0$ and one obtains

$$i_1(\theta, E) = i_2(\theta, E) \quad (3.16)$$

The above partial current densities i_k depend upon θ and E under steady-state conditions as

$$i_{k\theta} = \left(\frac{\partial i_k}{\partial \theta}\right)_E \text{ and } i_{kE} = \left(\frac{\partial i_k}{\partial E}\right)_\theta \text{ with } k = 1, 2 \quad (3.17)$$

Epelboin and Keddam^[54] expressed the faradaic impedance Z_f by this equation (3.18) as

$$2480 \quad Z_f(\omega) = [i_{1E} + i_{2E} + \frac{(i_{2E} - i_E)(i_{1\theta} + i_{2\theta})}{(i_{1\theta} - i_{2\theta} + j\omega FI)}]^{-1} \quad (3.18)$$

With $j = (-1)^{1/2}$

ω : the angular frequency ($\omega = 2\pi f$)

$i_{1\theta}$ and $i_{2\theta}$: the values of the partial derivatives of the current densities i_1 and i_2

indicate i_{1E} and i_{2E} : the values of the partial derivatives of the current densities i_1 and i_2

2485 linked to the variables θ and E .

Thanks to these partial derivatives of the current densities, it is possible to express the charge transfer resistance R_{ct} and the electrode polarization resistance R_p . In this context, the charge transfer resistance R_{ct} is the high frequency (HF) limits of the faradaic impedance:

$$R_{ct} = \lim_{f \rightarrow +\infty} Z_f = (i_{1E} + i_{2E})^{-1} \quad (3.19)$$

2490 and the electrode polarization resistance R_p is the low frequency (LF) limits of the faradaic impedance:

$$R_p = \lim_{f \rightarrow +\infty} Z_f = [i_{1E} + i_{2E} + \frac{(i_{2E} - i_E)(i_{1\theta} + i_{2\theta})}{(i_{1\theta} - i_{2\theta})}]^{-1} \quad (3.20)$$

With the expression of the charge transfer resistance R_{ct} and the electrode polarization resistance R_p , we can redefine the faradaic impedance $Z_f(\omega)$ given the equation (3.18) by the following equation (3.21):

$$2495 \quad Z_f(\omega) = R_{ct} + Z_\theta(\omega) = R_{ct} + \left[\frac{R_\theta}{(1 + j\omega\tau)}\right] \text{ where } R_\theta = R_{ct} - R_p \quad (3.21)$$

τ corresponds to the time constant and can be defined as the inverse of the characteristic angular frequency ω_c . This time constant is given by the following equation (3.22) :

$$\tau = \omega_c^{-1} = \frac{F\Gamma(i_{1E} + i_{2E})}{[2(i_{1\theta}i_{2E} - i_{2\theta}i_{1E})]} \quad (3.22)$$

2500 The concentration impedance Z_θ ((3.21)) corresponds to the impedance of an electrical circuit composed of a resistance R_θ and a capacitance C_θ connected in parallel. The resistance R_θ and the capacitance C_θ are linked to another time constant τ' :

$$\tau' = R_\theta C_\theta \quad (3.23)$$

By combining equations (3.21) and (3.22), one can express R_θ and C_θ by the following equations (3.24) and (3.25):

$$R_\theta = \frac{(i_{1E} - i_{2E})(i_{1\theta} + i_{2\theta})}{[2(i_{1E} + i_{2E})(i_{1\theta}i_{2E} - i_{2\theta}i_{1E})]} \quad (3.24)$$

$$C_\theta = \frac{F\Gamma(i_{1E} + i_{2E})^2}{[(i_{1E} - i_{2E})(i_{1\theta} + i_{2\theta})]} \quad (3.25)$$

Thanks to the faradaic impedance, we can introduce a new parameter, faradaic admittance Y_f , which is the inverse of Z_f (3.26).

$$Y_f = Z_f^{-1} \quad (3.26)$$

The faradaic admittance Y_f corresponds to the sum of the charge transfer conductance R_{ct}^{-1} and the concentration admittance Y_θ of the adsorbate. The expression of Y_f is given by (3.27):

$$Y_f(\omega) = R_{ct}^{-1} + Y_\theta(\omega) = R_{ct}^{-1} + \left[\frac{(R'_\theta)^{-1}}{(1 + \tau'p)} \right] \quad (3.27)$$

2515 With

$$R'_\theta = -\frac{R_{ct}(R_{ct} + R_\theta)}{R_\theta} \quad (3.28)$$

$$\tau' = \frac{L'_\theta}{R'_\theta} \quad \text{and} \quad L'_\theta = -R_{ct}^2 C_\theta \quad (3.29)$$

2520 To express the total impedance Z , we must consider the double layer capacitance C_{dl} which is linked in parallel with the faradaic impedance. Accordingly, the total impedance Z is given by (3.30) :

$$Z(\omega) = \frac{Z_f(\omega)}{[1 + j\omega C_{dl} Z_f(\omega)]} \quad (3.30)$$

Now, we will focus on the EIS results. For clarity, EIS results are separated into two zones depending on the overpotential values: the first zone corresponds to the low overpotential (Figure 3.15 b, and the second one to the large overpotential (Figure 3.15c).

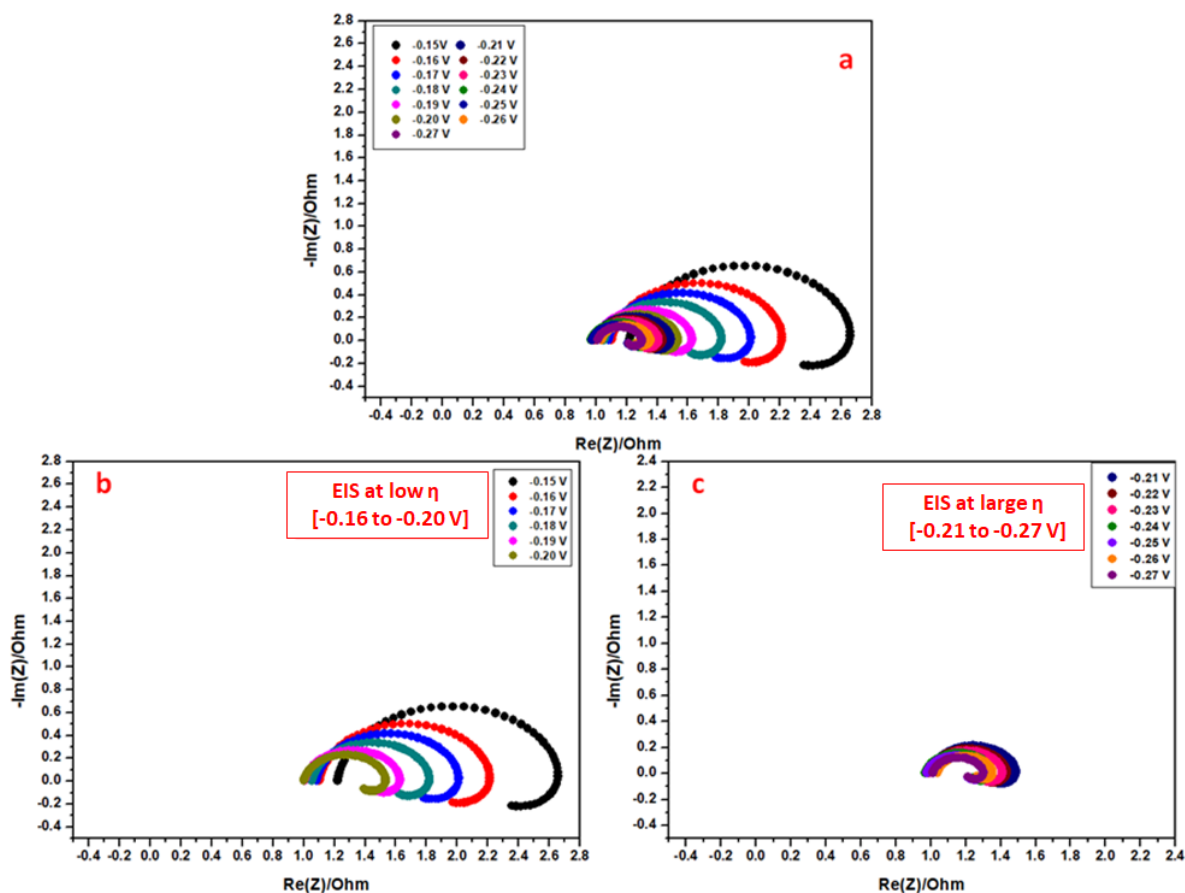


Figure 3.15 – (a) Nyquist plot for NiOx at 1 M KOH. (b) Nyquist plot at Low overpotential zone. (c) Nyquist plot for NiOx at large overpotential zone

One observes that the equivalent circuit described in Figure 3.14 fits well with the experimental data. Figure 3.16 shows two typical Nyquist plots with the fitting corresponding to the electrical circuit proposed (Figure 3.14). In figure 3.16a, we have the measurement and the fitting for one measurement obtained in the low overpotential zone (at -0.17 V), and in Figure 3.16b, we have one made in large overpotential (at -0.23 V).

Figures 3.17 shows that the Bode plot is similar to the experimental measurement obtained thanks to the fitting. Figure 3.17a and 3.17b correspond to the experimental measurement and the fitting for -0.17 V (in the low overpotential zone). For 3.17c and 3.17d correspond to the experimental measurement and the fitting for -0.23 V (in the large overpotential zone).

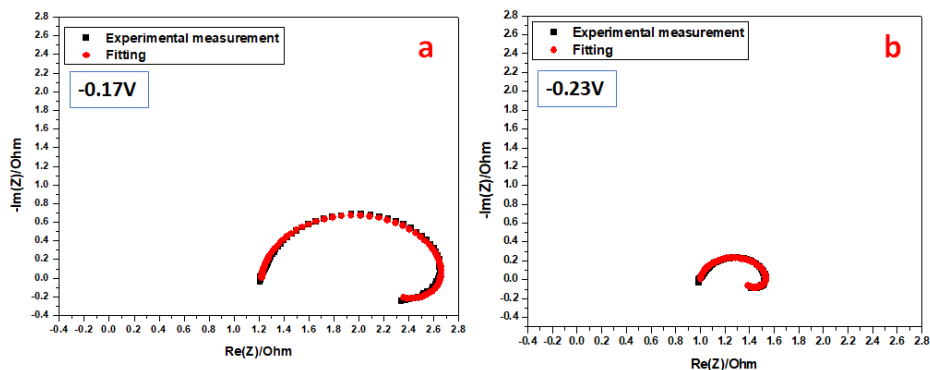


Figure 3.16 – (a) Nyquist plot for NiOx at 1 KOH M (low overpotential zone) (b) Nyquist plot for NiOx at 1 KOH M (large overpotential zone)

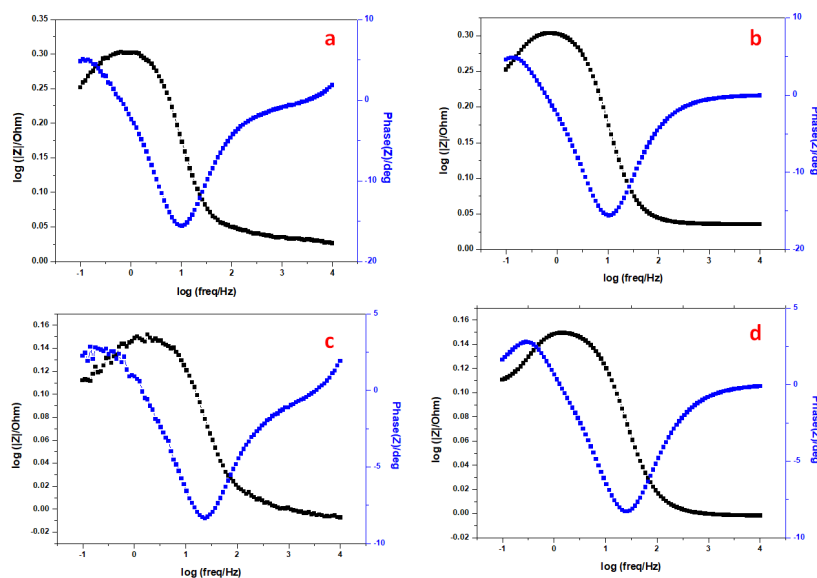


Figure 3.17 – (a) Experimental recorded Bode plot for -0.17 V (b) Fitting for -0.17 V (low overpotential zone) (c) Experimental recorded Bode plot for -0.23 V (b) Fitting for -0.23 V (large overpotential zone)

Let us first look at the charge transfer resistance R_{ct} , which is associated with high frequency (HF) limits of the faradaic impedance.^[55] R_{ct} is associated with the interface charge-transfer process of the electrode. When we look at the size of the diameter of the semicircles in the two defined zones (low and large overpotential), we can see a notable difference in the sizes. The decrease in semicircle size corresponds to a lower value of R_{ct} , which means a faster reaction rate.^[7] Now, we can study the variation of the charge-transfer resistance R_{ct} as function of the potential (Figure 3.18). In Figure 3.18, we can see the values of R_{ct} obtained in the low overpotential zone (black dots) and those obtained in the large overpotential zone (red dots). We can see the different responses corresponding to the two zones.

2540

2545

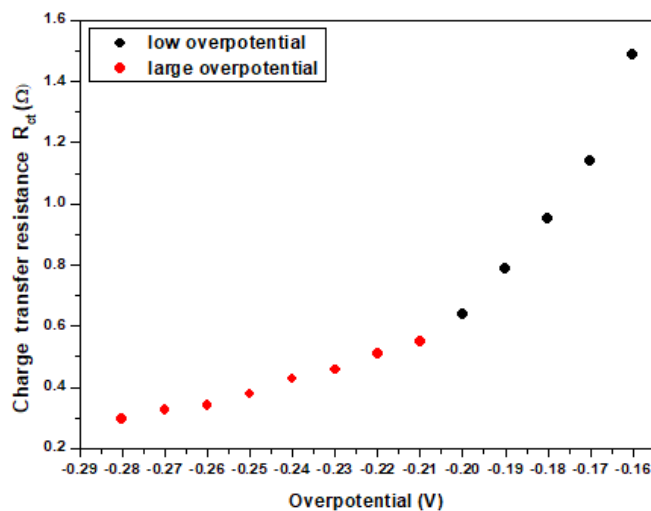


Figure 3.18 – Evolution of the Charge transfer resistance R_{ct} (Ω) as function of the overpotential η (V)

The second parameter that we analyze is the electrode polarization resistance R_p . R_p is the resistance linked to low frequency (LF) limits of the faradaic impedance (Figure 3.19). We can also divide the variation of R_p as a function of the overpotential into two parts, as in the case of R_{ct} shown in Figure 3.18.

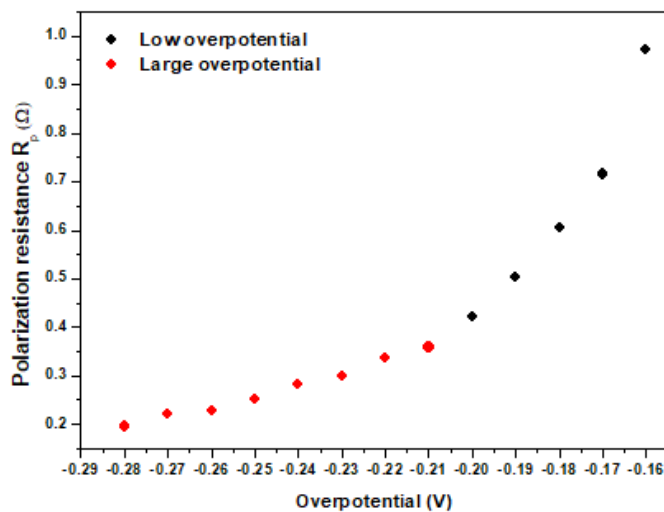


Figure 3.19 – Evolution of the polarization resistance R_p (Ω) as function of the overpotential η (V)

2550 From the values of R_{ct} and R_p , we can calculate a third parameter R'_θ . which is the resistance of the electrical circuit by combining, Equations (3.21) and (3.28) :

$$R_\theta = R_{ct} - R_p \quad (3.21)$$

$$R'_\theta = -\frac{R_{ct}(R_{ct} + R_\theta)}{R_\theta} \quad (3.28)$$

Figure 3.20 reports the variation of R'_θ as a function of the potential which also exhibits two zones.

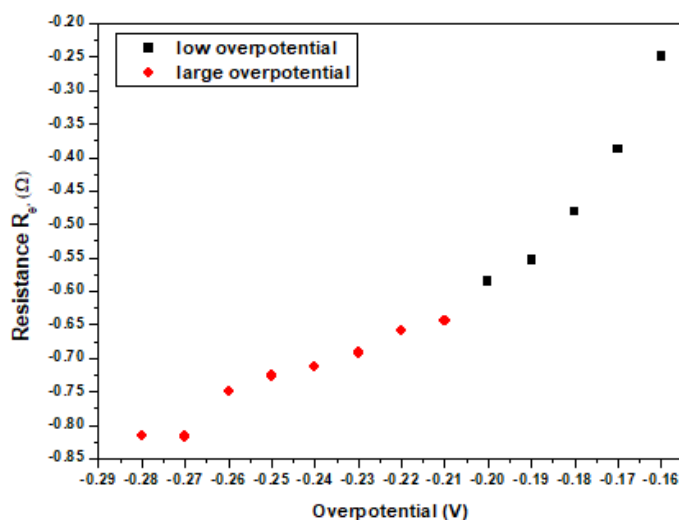


Figure 3.20 – Evolution of the electrical circuit resistance R'_θ (Ω) as function of the overpotential η (V)

2555

At this stage, it is interesting to find the relationship between each resistance and the other. One must remind that the resistances limited at high frequency (HF) (charge transfer resistance R_{ct}) and limited at low frequency (LF) (polarization resistance R_p) are linked to the resistance of the electrical circuit R'_θ .

2560

We write back the equations for the resistances cited :

$$R_{ct} = \lim_{f \rightarrow +\infty} Z_f = (i_{1E} + i_{2E})^{-1} \quad (3.19)$$

$$R_p = \lim_{f \rightarrow +\infty} Z_f = [i_{1E} + i_{2E} + \frac{(i_{2E} - i_{1E})(i_{1\theta} + i_{2\theta})}{(i_{1\theta} - i_{2\theta})}]^{-1} \quad (3.20)$$

And

$$R'_\theta = -\frac{R_{ct}(R_{ct} + R_\theta)}{R_\theta} \quad (3.28)$$

2565

We observe a correlation that is related to the validity of the chosen equivalent circuit. As shown in Figure 3.21 a, we find a linear correlation between charge transfer resistance R_{ct} and the polarization resistance R_p . Figures 3.21b and 3.21c show the evolution of the resistance of the electrical circuit R'_θ as function of polarization resistance R_p and the evolution of the resistance of the electrical circuit R'_θ as function of polarization resistance R_p , respectively. One can remark in Figures 3.21b and 3.21c the presence of two zones that have different slope values. We observe a linear correlation.

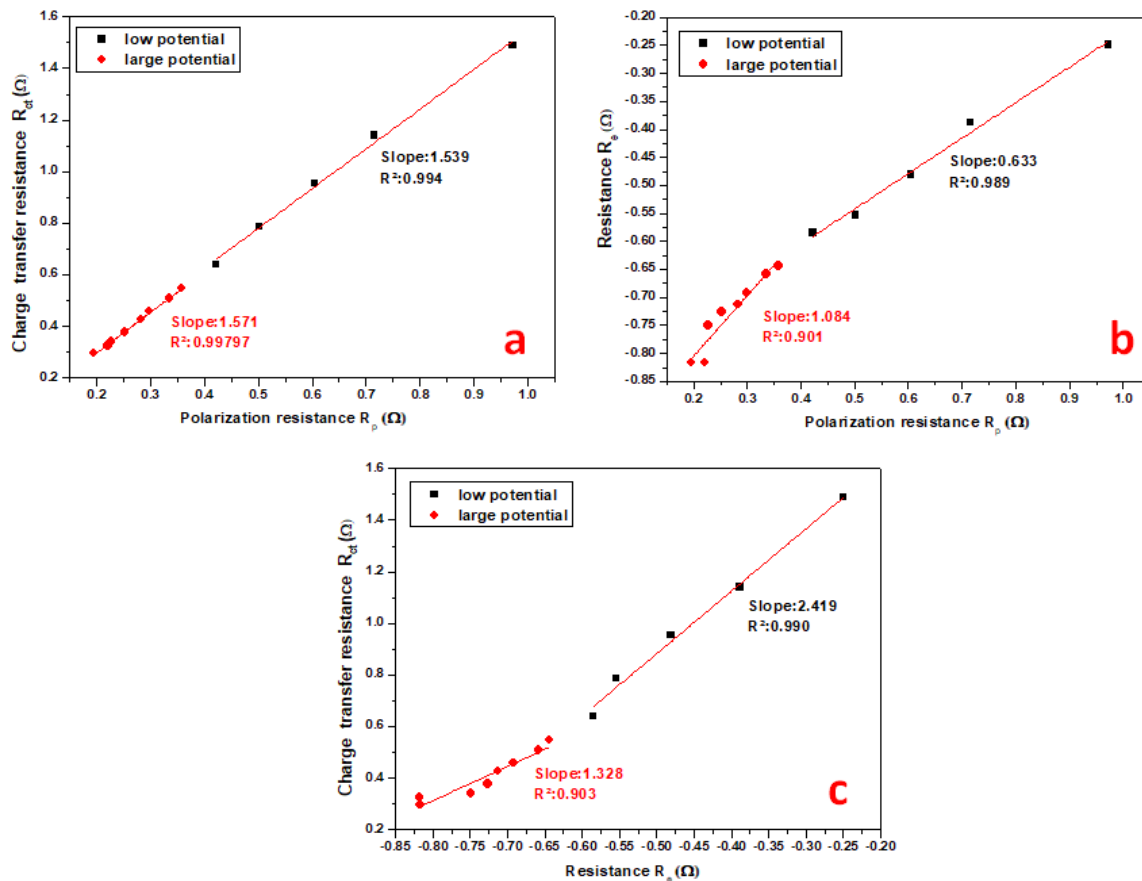


Figure 3.21 – (a) Evolution of the charge transfer resistance R_{ct} (Ω) as function the polarization resistance R_p (Ω), (b) Evolution of the electrical circuit resistance R'_θ (Ω) as function the polarization resistance R_p (Ω) and (c) Evolution of the charge transfer resistance R_{ct} (Ω) as function the electrical circuit resistance R'_θ (Ω)

3.3 Conclusion: Correlation between LSV and EIS

It is interesting to compare the information from the experimental results obtained with different techniques. Here, we assume that the kinetic is irreversible and the current follows the Butler Volmer equation:

$$j = j_0 \left(-e^{-\frac{\alpha n F \eta}{RT}} \right) \quad (3.31)$$

With j is the current density (A/cm^2), j_0 is the exchange current density (A/cm^2), α is the cathodic charge transfer coefficient, and η is the overpotential (V). F , R and T are Faraday constant, universal gas constant, and temperature, respectively.

To this end, we rewrite the resistances obtained from EIS experiments in terms of conductance which is just the inverse of the resistance. Figure 3.22 reports $\ln(i)$ vs η (from LSV experiments), $\ln(1/R_{ct})$ vs η , and $\ln(1/R_p)$ vs η .

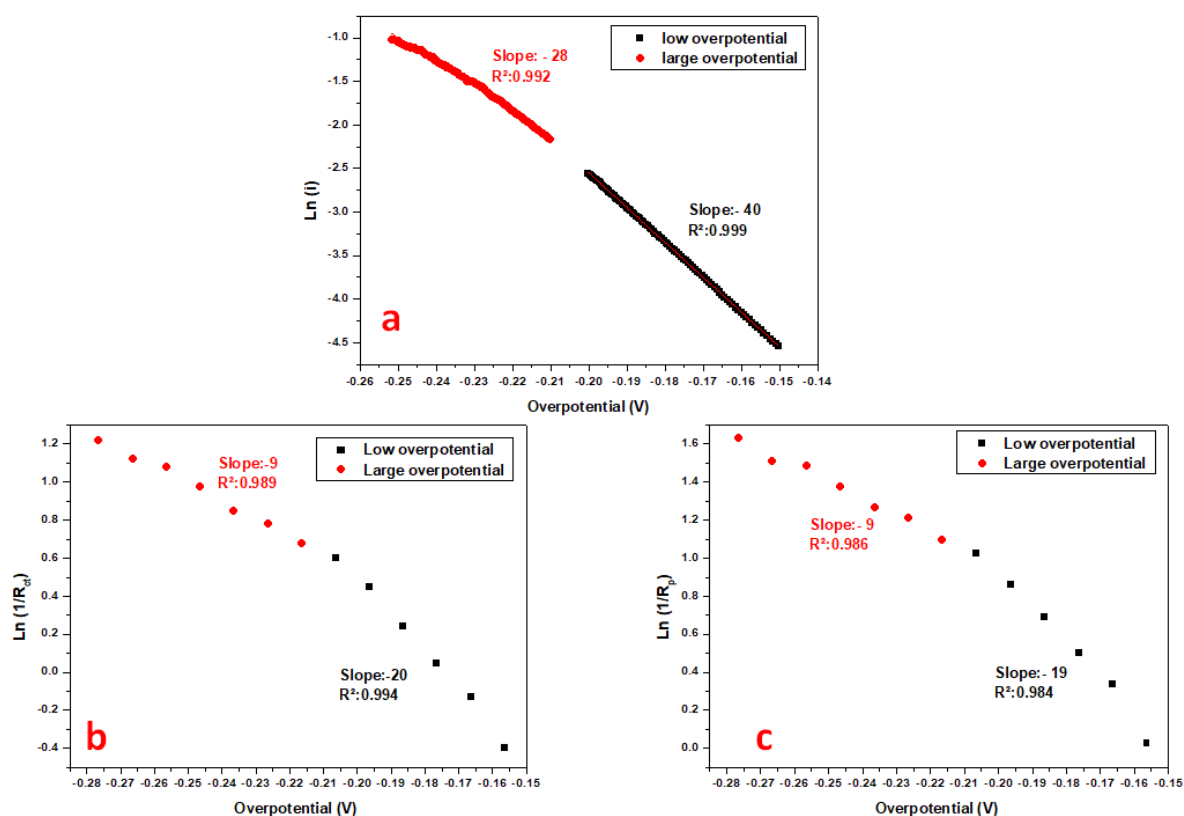


Figure 3.22 – (a) Evolution of $\ln(i/A.cm^{-2})$ as function of the overpotential (V), (b) Evolution of $\ln(1/R_{ct})$ as function of the overpotential (V), (c) Evolution of $\ln(1/R_p)$ as function of the overpotential (V)

One observes the same behaviour. The potential dependence of the current and the conductance exhibits two zones. It indicates that LSV and EIS results are well correlated and give similar electrochemical information regarding mechanism pathways.

In this chapter 3, we have studied doped nickel oxide electrode material by combining different spectroscopy techniques and its electrochemical behaviour to HER. The electrode material exhibits nanostructure. We have shown that a doped nickel oxide electrode has good electrocatalytic activity. The electrochemical response depended upon the potential, and we have defined two zones: one in low overpotential and the other in large overpotential. Thanks to the Tafel plot from LSV experiments, we showed that HER follows The Volmer–Heyrovsky mechanism at low overpotential and The Volmer-Tafel mechanism in a large overpotential zone. We have also performed EIS measurements in which we have determined the main electrochemical parameters (charge transfer resistance R_{ct} , electrode polarization resistance R_p , and the resistance of the electrical circuit $R'\theta$). The relationship between LSV and EIS results was studied and summarized in Table 3.2 where we calculate various ratios. The first ratio corresponds to the ratio of the slopes of $\ln(1/R_{ct})$ vs E and $\ln(j)$ vs E. The second ratio is the ratio of the slopes of $\ln(1/p)$ vs E and $\ln(j)$ vs E. Table 3.2, shows that there are two zones, and the same value of the ratio is obtained for each zone. This result underlines the coherency of the electrochemical investigations.

| Ratio of slopes $\ln(1/R_{ct})$ vs E and $\ln(j)$ vs E | Ratio of slopes $\ln(1/R_p)$ vs E and $\ln(i)$ vs E |
|--|---|
| Low overpotential zone: 0.32 | Low overpotential zone: 0.32 |
| Large overpotential zone:0.50 | Large overpotential zone:0.48 |

Table 3.2 – Table of the Ratio of slopes for the evolution’s curves studied in figure 3.22

In this next chapter, we are going to look NiOx through OER.

REFERENCES

- 2605 [1] Ya Yan, Bao Yu Xia, Bin Zhao, and Xin Wang. A review on noble-metal-free bifunctional heterogeneous catalysts for overall electrochemical water splitting. *Journal of Materials Chemistry A*, 4(45):17587–17603, 2016. doi: 10.1039/C6TA08075H.
- [2] Junheng Xing, Hui Li, Mark Ming-Cheng Cheng, Scott M. Geyer, and K. Y. Simon Ng. Electro-synthesis of 3D porous hierarchical Ni–Fe phosphate film/Ni foam as a high-
2610 efficiency bifunctional electrocatalyst for overall water splitting. *Journal of Materials Chemistry A*, 4(36):13866–13873, September 2016. doi: 10.1039/C6TA05952J.
- [3] Wei Zhang, Daohao Li, Longzhou Zhang, Xilin She, and Dongjiang Yang. NiFe-based nanostructures on nickel foam as highly efficiently electrocatalysts for oxygen and hydrogen evolution reactions. *Journal of Energy Chemistry*, 39:39–53, December 2019. doi:
2615 10.1016/j.jechem.2019.01.017.
- [4] Junzhi Li, Guodong Wei, Yukun Zhu, Yunlong Xi, Xuexue Pan, Yuan Ji, Igor V. Zatovsky, and Wei Han. Hierarchical NiCoP nanocone arrays supported on Ni foam as an efficient and stable bifunctional electrocatalyst for overall water splitting. *Journal of Materials Chemistry A*, 5(28):14828–14837, July 2017. doi: 10.1039/C7TA03947F.
- 2620 [5] Bo Zhang, Chunhui Xiao, Sanmu Xie, Jin Liang, Xu Chen, and Yuhai Tang. Iron–Nickel Nitride Nanostructures in Situ Grown on Surface-Redox-Etching Nickel Foam: Efficient and Ultrasustainable Electrocatalysts for Overall Water Splitting. *Chemistry of Materials*, 28(19):6934–6941, October 2016. doi: 10.1021/acs.chemmater.6b02610.
- 2625 [6] Zhao Li, Wenhan Niu, Le Zhou, and Yang Yang. Phosphorus and Aluminum Codoped Porous NiO Nanosheets as Highly Efficient Electrocatalysts for Overall Water Splitting. *ACS Energy Letters*, 3(4):892–898, April 2018. doi: 10.1021/acsenerylett.8b00174.
- [7] Xiaoyan Hu, Xuemei Tian, Ying-Wu Lin, and Zhonghua Wang. Nickel foam and stainless steel mesh as electrocatalysts for hydrogen evolution reaction, oxygen evolution reaction

- and overall water splitting in alkaline media. *RSC Advances*, 9(54):31563–31571, 2019. doi: 10.1039/C9RA07258F.
- 2630
- [8] Jing Zhu, Liangsheng Hu, Pengxiang Zhao, Lawrence Yoon Suk Lee, and Kwok-Yin Wong. Recent Advances in Electrocatalytic Hydrogen Evolution Using Nanoparticles. *Chemical Reviews*, 120(2):851–918, January 2020. doi: 10.1021/acs.chemrev.9b00248.
- [9] J. K. Nørskov, T. Bligaard, A. Logadottir, J. R. Kitchin, J. G. Chen, S. Pandalov, and U. Stimming. Trends in the Exchange Current for Hydrogen Evolution. *Journal of The Electrochemical Society*, 152(3):J23, January 2005. doi: 10.1149/1.1856988.
- 2635
- [10] Zhe Li, Yi Feng, Yu-Lin Liang, Chuan-Qi Cheng, Cun-Ku Dong, Hui Liu, and Xi-Wen Du. Stable Rhodium (IV) Oxide for Alkaline Hydrogen Evolution Reaction. *Advanced Materials*, 32(25):1908521, 2020. doi: 10.1002/adma.201908521.
- [11] Md Delowar Hossain, Zhenjing Liu, Minghao Zhuang, Xingxu Yan, Gui-Liang Xu, Chaitanya Avinash Gadre, Abhishek Tyagi, Irfan Haider Abidi, Cheng-Jun Sun, Hoilun Wong, Alexander Guda, Yufeng Hao, Xiaoqing Pan, Khalil Amine, and Zhengtang Luo. Rational Design of Graphene-Supported Single Atom Catalysts for Hydrogen Evolution Reaction. *Advanced Energy Materials*, 9(10):1803689, 2019. doi: 10.1002/aenm.201803689.
- 2640
- [12] Wenchao Sheng, MyatNoeZin Myint, Jingguang G. Chen, and Yushan Yan. Correlating the hydrogen evolution reaction activity in alkaline electrolytes with the hydrogen binding energy on monometallic surfaces. *Energy & Environmental Science*, 6(5):1509–1512, April 2013. doi: 10.1039/C3EE00045A.
- 2645
- [13] Shiwei Song, Jianbing Zang, Shuyu Zhou, Hongwei Gao, Xueqing Tian, Yungang Yuan, Wei Li, and Yanhui Wang. Self-supported amorphous nickel-iron phosphorus oxides hollow spheres on Ni-Fe foam for highly efficient overall water splitting. *Electrochimica Acta*, 392:138996, October 2021. doi: 10.1016/j.electacta.2021.138996.
- 2650
- [14] Yanna Guo, Teahoon Park, Jin Woo Yi, Joel Henzie, Jeonghun Kim, Zhongli Wang, Bo Jiang, Yoshio Bando, Yoshiyuki Sugahara, Jing Tang, and Yusuke Yamauchi. Nanoarchitectonics for Transition-Metal-Sulfide-Based Electrocatalysts for Water Splitting. *Advanced Materials*, 31(17):1807134, 2019. doi: 10.1002/adma.201807134.
- 2655
- [15] Shiwei Song, Yanhui Wang, Wei Li, Pengfei Tian, Shuyu Zhou, Hongwei Gao, Xueqing Tian, and Jianbing Zang. Amorphous MoS₂ coated Ni₃S₂ nanosheets as bifunctional electrocatalysts for high-efficiency overall water splitting. *Electrochimica Acta*, 332:135454, February 2020. doi: 10.1016/j.electacta.2019.135454.
- 2660
- [16] Yaqing Yang, Wenbiao Zhang, Yongle Xiao, Zhangping Shi, Xiaoming Cao, Yi Tang, and Qingsheng Gao. CoNiSe₂ heteronanorods decorated with layered-double-hydroxides for

- efficient hydrogen evolution. *Applied Catalysis B: Environmental*, 242:132–139, March 2019. doi: 10.1016/j.apcatb.2018.09.082.
- 2665 [17] Menglei Yuan, Sobia Dipazir, Meng Wang, Yu Sun, Denglei Gao, Yiling Bai, Min Zhang, Peilong Lu, Hongyan He, Xiangyang Zhu, Shuwei Li, Zhanjun Liu, Zhaopeng Luo, and Guangjin Zhang. Polyoxometalate-assisted formation of CoSe/MoSe₂ heterostructures with enhanced oxygen evolution activity. *Journal of Materials Chemistry A*, 7(7):3317–3326, February 2019. doi: 10.1039/C8TA11976G.
- 2670 [18] Yanguang Li, Ming Gong, Yongye Liang, Ju Feng, Ji-Eun Kim, Hailiang Wang, Guosong Hong, Bo Zhang, and Hongjie Dai. Advanced zinc-air batteries based on high-performance hybrid electrocatalysts. *Nature Communications*, 4(1):1805, May 2013. doi: 10.1038/ncomms2812.
- [19] Xiaolong Zhang, Jinsong Hu, Xiaofei Cheng, Kojo Aboagye Nartey, and Lei Zhang. Double metal–organic frameworks derived Fe–Co–Ni phosphides nanosheets as high-performance electrocatalyst for alkaline electrochemical water splitting. *Electrochimica Acta*, 367:137536, January 2021. doi: 10.1016/j.electacta.2020.137536.
- 2675 [20] Jin-Xian Feng, Si-Yao Tong, Ye-Xiang Tong, and Gao-Ren Li. Pt-like Hydrogen Evolution Electrocatalysis on PANI/CoP Hybrid Nanowires by Weakening the Shackles of Hydrogen Ions on the Surfaces of Catalysts. *Journal of the American Chemical Society*, 140(15):5118–5126, April 2018. doi: 10.1021/jacs.7b12968.
- 2680 [21] Yi Gong, Linan Wang, Hailang Xiong, Mingfei Shao, Lidong Xu, Ao Xie, Shuxian Zhuang, Yang Tang, Xiaojin Yang, Yongmei Chen, and Pingyu Wan. 3D self-supported Ni nanoparticle@N-doped carbon nanotubes anchored on NiMoN pillars for the hydrogen evolution reaction with high activity and anti-oxidation ability. *Journal of Materials Chemistry A*, 7(22):13671–13678, June 2019. doi: 10.1039/C9TA03473K.
- 2685 [22] Peng Zhou, Danning Xing, Yuanyuan Liu, Zeyan Wang, Peng Wang, Zhaoke Zheng, Xiaoyan Qin, Xiaoyang Zhang, Ying Dai, and Baibiao Huang. Accelerated electrocatalytic hydrogen evolution on non-noble metal containing trinickel nitride by introduction of vanadium nitride. *Journal of Materials Chemistry A*, 7(10):5513–5521, March 2019. doi: 10.1039/C8TA12043A.
- 2690 [23] Shasha Li, Enze Li, Xiaowei An, Xiaogang Hao, Zhongqing Jiang, and Guoqing Guan. Transition metal-based catalysts for electrochemical water splitting at high current density: Current status and perspectives. *Nanoscale*, 13(30):12788–12817, August 2021. ISSN 2040-3372. doi: 10.1039/D1NR02592A.
- 2695 [24] Zi-You Yu, Yu Duan, Xing-Yu Feng, Xingxing Yu, Min-Rui Gao, and Shu-Hong Yu. Clean and Affordable Hydrogen Fuel from Alkaline Water Splitting: Past, Recent Progress, and

- Future Prospects. *Advanced Materials*, 33(31):2007100, 2021. ISSN 1521-4095. doi: 10.1002/adma.202007100.
- 2700 [25] Wenjun He, Lili Han, Qiuyan Hao, Xuerong Zheng, Ying Li, Jun Zhang, Caichi Liu, Hui Liu, and Huolin L. Xin. Fluorine-Anion-Modulated Electron Structure of Nickel Sulfide Nanosheet Arrays for Alkaline Hydrogen Evolution. *ACS Energy Letters*, 4(12):2905–2912, December 2019. doi: 10.1021/acsenergylett.9b02316.
- 2705 [26] Donghong Duan, Desheng Guo, Jie Gao, Shibin Liu, and Yunfang Wang. Electrodeposition of cobalt-iron bimetal phosphide on Ni foam as a bifunctional electrocatalyst for efficient overall water splitting. *Journal of Colloid and Interface Science*, 622:250–260, September 2022. doi: 10.1016/j.jcis.2022.04.127.
- 2710 [27] Kaihang Wang, Yingying Si, Zunhang Lv, Tianpeng Yu, Xin Liu, Guixue Wang, Guangwen Xie, and Luhua Jiang. Efficient and stable Ni–Co–Fe–P nanosheet arrays on Ni foam for alkaline and neutral hydrogen evolution. *International Journal of Hydrogen Energy*, 45(4):2504–2512, January 2020. doi: 10.1016/j.ijhydene.2019.11.154.
- 2715 [28] Chun Tang, Ningyan Cheng, Zonghua Pu, Wei Xing, and Xuping Sun. NiSe Nanowire Film Supported on Nickel Foam: An Efficient and Stable 3D Bifunctional Electrode for Full Water Splitting. *Angewandte Chemie*, 127(32):9483–9487, 2015. doi: 10.1002/ange.201503407.
- [29] Ling Zhang, Ibrahim Saana Amiin, Xiang Ren, Zhiang Liu, Gu Du, Abdullah M. Asiri, Baozhan Zheng, and Xuping Sun. Surface Modification of a NiS₂ Nanoarray with Ni(OH)₂ toward Superior Water Reduction Electrocatalysis in Alkaline Media. *Inorganic Chemistry*, 56(22):13651–13654, November 2017. doi: 10.1021/acs.inorgchem.7b02466.
- 2720 [30] Zexian Zou, Xiangyu Wang, Jiansong Huang, Zhengcui Wu, and Feng Gao. An Fe-doped nickel selenide nanorod/nanosheet hierarchical array for efficient overall water splitting. *Journal of Materials Chemistry A*, 7(5):2233–2241, January 2019. doi: 10.1039/C8TA11072G.
- 2725 [31] Long Zhang, Yuyang Qi, Lan Sun, Guanjun Chen, Luxue Wang, Mingshuo Zhang, Dejun Zeng, Yongnan Chen, Xingang Wang, Kewei Xu, and Fei Ma. Facile route of nitrogen doping in nickel cobalt phosphide for highly efficient hydrogen evolution in both acid and alkaline electrolytes. *Applied Surface Science*, 512:145715, May 2020. doi: 10.1016/j.apsusc.2020.145715.
- 2730 [32] Can Huang, Ting Ouyang, Ying Zou, Nan Li, and Zhao-Qing Liu. Ultrathin NiCo₂P_x nanosheets strongly coupled with CNTs as efficient and robust electrocatalysts for overall water splitting. *Journal of Materials Chemistry A*, 6(17):7420–7427, May 2018. doi: 10.1039/C7TA11364A.

- [33] Ling Zhang, Xingyue Wang, Xingqun Zheng, Lishan Peng, JingJun Shen, Rui Xiang, Zihua Deng, Li Li, Hongmei Chen, and Zidong Wei. Oxygen-Incorporated NiMoP₂ Nanowire Arrays for Enhanced Hydrogen Evolution Activity in Alkaline Solution. *ACS Applied Energy Materials*, 1(10):5482–5489, October 2018. doi: 10.1021/acsaem.8b01044. 2735
- [34] Luo Yu, Ishwar Kumar Mishra, Yunlong Xie, Haiqing Zhou, Jingying Sun, Jianqing Zhou, Yizhou Ni, Dan Luo, Fang Yu, Ying Yu, Shuo Chen, and Zhifeng Ren. Ternary Ni₂(1-x)Mo₂xP nanowire arrays toward efficient and stable hydrogen evolution electrocatalysis under large-current-density. *Nano Energy*, 53:492–500, November 2018. doi: 10.1016/j.nanoen.2018.08.025. 2740
- [35] Fang Yu, Haiqing Zhou, Yufeng Huang, Jingying Sun, Fan Qin, Jiming Bao, William A. Goddard, Shuo Chen, and Zhifeng Ren. High-performance bifunctional porous non-noble metal phosphide catalyst for overall water splitting. *Nature Communications*, 9(1):2551, June 2018. doi: 10.1038/s41467-018-04746-z. 2745
- [36] Prashanth W. Menezes, Chakadola Panda, Stefan Loos, Florian Bunschei-Bruns, Carsten Walter, Michael Schwarze, Xiaohui Deng, Holger Dau, and Matthias Driess. A structurally versatile nickel phosphite acting as a robust bifunctional electrocatalyst for overall water splitting. *Energy & Environmental Science*, 11(5):1287–1298, May 2018. doi: 10.1039/C7EE03619A. 2750
- [37] Pengyan Wang, Zonghua Pu, Yanhui Li, Lin Wu, Zhengkai Tu, Min Jiang, Zongkui Kou, Ibrahim Saana Amiin, and Shichun Mu. Iron-Doped Nickel Phosphide Nanosheet Arrays: An Efficient Bifunctional Electrocatalyst for Water Splitting. *ACS Applied Materials & Interfaces*, 9(31):26001–26007, August 2017. doi: 10.1021/acsaami.7b06305.
- [38] Bo You, Nan Jiang, Meili Sheng, Margaret Winona Bhushan, and Yujie Sun. Hierarchically Porous Urchin-Like Ni₂P Superstructures Supported on Nickel Foam as Efficient Bifunctional Electrocatalysts for Overall Water Splitting. *ACS Catalysis*, 6(2):714–721, February 2016. doi: 10.1021/acscatal.5b02193. 2755
- [39] Lucas-Alexandre Stern, Ligang Feng, Fang Song, and Xile Hu. Ni₂P as a Janus catalyst for water splitting: the oxygen evolution activity of Ni₂P nanoparticles. *Energy & Environmental Science*, 8(8):2347–2351, July 2015. doi: 10.1039/C5EE01155H. 2760
- [40] Martin Ďurovič, Jaromír Hnát, and Karel Bouzek. Electrocatalysts for the hydrogen evolution reaction in alkaline and neutral media. A comparative review. *Journal of Power Sources*, 493:229708, May 2021. doi: 10.1016/j.jpowsour.2021.229708.

- 2765 [41] DongHoon Song, Doosun Hong, YongKeun Kwon, HyoWon Kim, Jaewook Shin, Hyuck Mo Lee, and EunAe Cho. Highly porous Ni–P electrode synthesized by an ultra-fast electrodeposition process for efficient overall water electrolysis. *Journal of Materials Chemistry A*, 8(24):12069–12079, June 2020. doi: 10.1039/D0TA03739G.
- [42] K. K. Lian, D. W. Kirk, and S. J. Thorpe. Investigation of a “Two-State” Tafel Phenomenon for the Oxygen Evolution Reaction on an Amorphous Ni-Co Alloy. *Journal of The Electrochemical Society*, 142(11):3704, November 1995.
2770
- [43] A. N. Mansour. Characterization of NiO by XPS. *Surface Science Spectra*, 3(3):231–238, July 1994. doi: 10.1116/1.1247751.
- [44] A. A. Mirghni, M. J. Madito, K. O. Oyedotun, T. M. Masikhwa, N. M. Ndiaye, Sekhar J. Ray, and N. Manyala. A high energy density asymmetric supercapacitor utilizing a nickel phosphate/graphene foam composite as the cathode and carbonized iron cations adsorbed onto polyaniline as the anode. *RSC Advances*, 8(21):11608–11621, March 2018. doi: 10.1039/C7RA12028A.
2775
- [45] Amanda C. Garcia, Thomas Touzalin, Celine Nieuwland, Nickson Perini, and Marc T. M. Koper. Enhancement of Oxygen Evolution Activity of Nickel Oxyhydroxide by Electrolyte Alkali Cations. *Angewandte Chemie International Edition*, 58(37):12999–13003, 2019. doi: 10.1002/anie.201905501.
2780
- [46] Emily Cossar, Mohamed S. E. Houache, Zhihao Zhang, and Elena A. Baranova. Comparison of electrochemical active surface area methods for various nickel nanostructures. *Journal of Electroanalytical Chemistry*, 870:114246, August 2020. doi: 10.1016/j.jelechem.2020.114246.
2785
- [47] Damien Voiry, Manish Chhowalla, Yury Gogotsi, Nicholas A. Kotov, Yan Li, Reginald M. Penner, Raymond E. Schaak, and Paul S. Weiss. Best Practices for Reporting Electrocatalytic Performance of Nanomaterials. *ACS Nano*, 12(10):9635–9638, October 2018. doi: 10.1021/acsnano.8b07700.
2790
- [48] Akansha Goyal and Marc T. M. Koper. The Interrelated Effect of Cations and Electrolyte pH on the Hydrogen Evolution Reaction on Gold Electrodes in Alkaline Media. *Angewandte Chemie International Edition*, 60(24):13452–13462, 2021. doi: 10.1002/anie.202102803.
- 2795 [49] D. S. P. Cardoso, S. Eugénio, T. M. Silva, D. M. F. Santos, C. a. C. Sequeira, and M. F. Montemor. Hydrogen evolution on nanostructured Ni–Cu foams. *RSC Advances*, 5(54):43456–43461, May 2015. doi: 10.1039/C5RA06517H.

- [50] J. P. Diard, B. Le Gorrec, and C. Montella. Calculation, simulation and interpretation of electrochemical impedances: Part 3. Conditions for observation of low frequency inductive diagrams for a two-step electron transfer reaction with an adsorbed intermediate species. *Journal of Electroanalytical Chemistry*, 326(1):13–36, May 1992. doi: 10.1016/0022-0728(92)80500-4.
- [51] R. D. Armstrong and M. Henderson. Impedance plane display of a reaction with an adsorbed intermediate. *Journal of Electroanalytical Chemistry and Interfacial Electrochemistry*, 39(1):81–90, September 1972. doi: 10.1016/S0022-0728(72)80477-7.
- [52] J. P. Diard, B. LeGorrec, and S. Maximovitch. Etude de l'activation du degagement d'hydrogene sur electrode d'oxyde de nickel par spectroscopie d'impedance. *Electrochimica Acta*, 35(6):1099–1108, June 1990. doi: 10.1016/0013-4686(90)90049-6.
- [53] Andrzej Lasia. Mechanism and kinetics of the hydrogen evolution reaction. *International Journal of Hydrogen Energy*, 44(36):19484–19518, July 2019. doi: 10.1016/j.ijhydene.2019.05.183.
- [54] Israel Epelboin and Michel Keddam. Faradaic Impedances: Diffusion Impedance and Reaction Impedance. *Journal of The Electrochemical Society*, 117(8):1052, August 1970. doi: 10.1149/1.2407718.
- [55] Bin Wang, Cheng Tang, Hao-Fan Wang, Xiao Chen, Rui Cao, and Qiang Zhang. A Nano-sized CoNi Hydroxide@Hydroxysulfide Core–Shell Heterostructure for Enhanced Oxygen Evolution. *Advanced Materials*, 31(4):1805658, 2019. doi: 10.1002/adma.201805658.

CHAPTER 4

NIOX SYSTEM, HYBRID MATERIALS : CATALYST FOR

OER

2820

Contents

| | | |
|------|--|------------|
| | 4.1 Mechanism and catalyst for Oxygen evolution reaction (OER) | 151 |
| | 4.2 Experimental section | 154 |
| 2825 | 4.3 Oxygen evolution reaction response | 155 |
| | 4.3.1 Oxygen evolution reaction mechanism and influence of KOH concentration | 156 |
| | 4.3.2 Tafel slope and mechanism investigation | 158 |
| | 4.3.3 EIS study | 162 |
| | 4.3.4 Correlation between LSV and EIS | 166 |
| 2830 | 4.4 Conclusion Water splitting | 167 |
| | References | 169 |

2835 4.1 Mechanism and catalyst for Oxygen evolution reaction (OER)

In the last decades, studies around hydrogen and oxygen have taken a prominent place. These two elements are the key point to finding alternatives to fossil energy and developing more systems that respect environmental issues.^[1] One field of research is developing a system to obtain high-purity hydrogen through electrochemical water splitting. The water splitting is composed of two half-reactions, oxygen evolution reaction (OER) and hydrogen evolution reaction (HER).^[2,3] For water-splitting, the primary limiting step is OER. OER is more complicated to deal with due to the complexity of the reaction, such as the multistep proton-coupled electron transfer process.^[4] In previous chapter 3, the catalytic effect of our NiOx electrode

2840

2845 through HER. The following part will look at the OER catalyst through the doped NiOx electrode.

We will divide chapter 4 into four parts. For the first part, we will introduce the mechanism and the different catalysts for OER. The second time, we will look at the electrochemical investigation, which includes two aspects :

- 2850 (i) LSV analysis of the mechanism of OER and the influence of KOH concentration
 (ii) EIS investigations

All of these electrochemical investigations are performed in alkaline media. The third part will analyse of the correlation between LSV and EIS investigations. In the last part, we will be the water-splitting applications of doped NiOx electrodes.

2855 One of the main problems for the OER is the complexity of the mechanism and the kinetic multistep.^[5] To understand the mechanisms and kinetics for OER, the use of the Tafel slope plays an important role. The value of the Tafel slope can indicate the mechanism through the rate-determining step (RDS) and the electron transfer coefficient (α).^[6] In alkaline media like the one we studied; the global equilibrium is given by equation (4.1) :



We have seen in chapter 1 that OER can have a variety of mechanisms. We look at simplified OER mechanism pathways in alkaline media for our studies, illustrated in Figure 4.1.

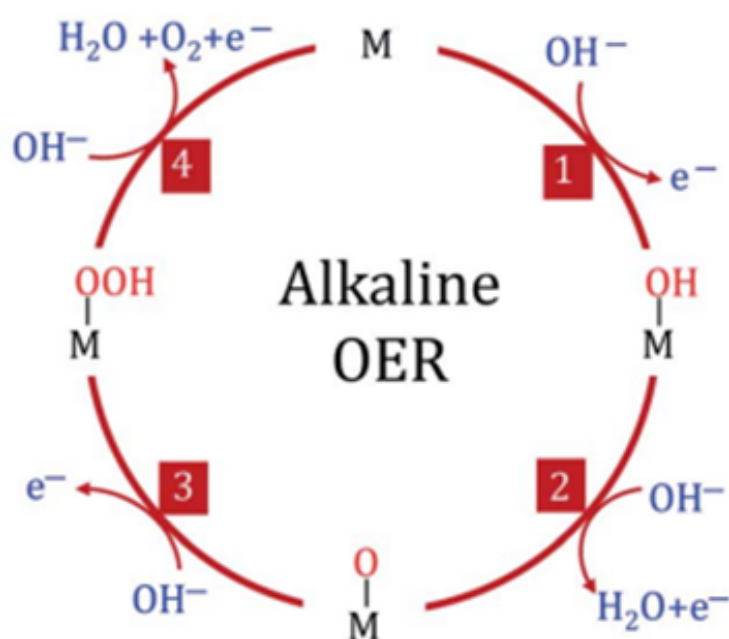
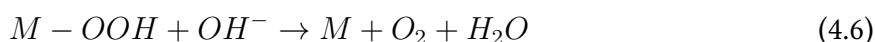
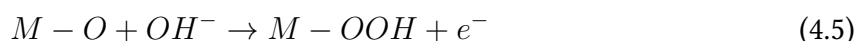


Figure 4.1 – Simplified Oxygen evolution reaction mechanisms pathways in alkaline media^[7]

Based on Figure 4.1, there are the following possible mechanisms for the OER:



The reaction described in equation (4.3) can evolve in two possible pathways:



The intermediates species denote with * such as OH*, OOH*, and O*.

We can see that we can have two pathways. In the first pathway, we combine two O* to give O₂. On the other hand, the second possible pathway is the formation of the OOH* intermediate. In both pathways, we can see that the bonding with the other intermediates is significant interaction (M–OH, M–O, and M–OOH).

To find the best catalyst, the theoretical approaches such as Density Functional Theory (DFT) calculations can be used to determine the OER overpotential (η) and adsorption energy. In the literature, the work of Nørskov et al.^[8] was focused on the OER kinetics for metal (hydro)oxide surfaces. The difference in the adsorption energy between two intermediates ($\Delta G_{O^*} - \Delta G_{OH^*}$) can be used as a descriptor to compare various catalysts. Figure 4.2 shows a volcano plot based on this descriptor.

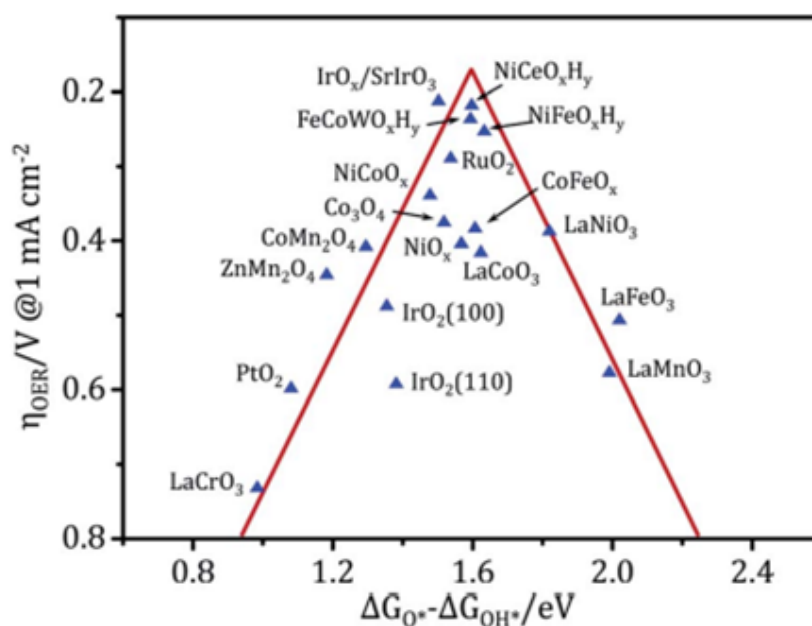


Figure 4.2 – Volcano plot for Oxygen evolution reaction^[7]

The critical properties of a suitable catalyst for the OER are a low overpotential and a low Tafel slope. The best catalysts for OER are iridium dioxide (IrO₂) and ruthenium dioxide (RuO₂)^[9,10]. However, these two catalysts are too expensive for a large-scale application (like industry). Then, one can use alternative catalysts such as nickel-based catalysts. In this regard, recent works are studying the catalytic activity of Ni-based materials through OER by the combination of Nickel with oxides^[11,12], hydroxide^[13,14], sulfides^[15,16], and nitrides^[17,18] in alkaline solution. To increase the OER activity, one can introduce some dopants such as Fe. The incorporation of Fe will enhance not only the electrical conductivity but also the physical structure.^[19] To overview nickel-based catalysts for OER, we report in Table 4.1 selected Iron and Phosphor doped nickel foam (NF).

| Material | Overpotential at 10 mA.cm ⁻² (mV) | Tafel slope (mV.dec ⁻¹) | Reference |
|---|--|-------------------------------------|--------------------------------|
| HP Ni-P on foam | 279 | 44.0 | Song et al. ^[20] |
| Ni ₁₁ (HPO ₃) ₈ (OH) ₆ /NF | 245 | 102 | Menezes et al. ^[21] |
| Ni ₂ P/NF | - | 84.6 | Wang et al. ^[22] |
| Ni _{1.85} Fe _{0.15} P NSAS/NF | - | 96 | Wang et al. ^[23] |
| Ni ₂ P/Ni/NF | 200 | - | You et al. ^[24] |
| Ni ₂ P/NF | 290 | 47 | Stern et al. ^[25] |
| NiFe foam | 320 | 56 | Liang et al. ^[26] |
| NiFe-OH/NiFeP/ NF | 199 | 39 | Liang et al. ^[27] |

Table 4.1 – Comparison of Oxygen evolution reaction electrochemical activity parameters for selected materials in alkaline (1M KOH) for Nickel foam (NF) with Iron and Phosphor doped^[20]

4.2 Experimental section

The experimental setup and approach are similar to the previous chapter. For all the electrochemical investigation parts, the measurements are made with a three-electrode system with Bio-Logic Potentiostat/Galvanostat, which was paired with the EC-Lab software (Bio-Logic Science Instruments, Seyssinet-Pariset, France) at room temperature under oxygen-saturated atmosphere. The three-electrode system is composed of an Ag/AgCl electrode, steel mesh, and NiOx electrode as the reference, counter, and working electrodes, respectively. We converted all the data on the potential vs RHE according to :

$$E_{RHE} = E_{Ag/AgCl} + E_{Ag/AgCl}^0 + 0.059 \times pH \text{ with } E_{Ag/AgCl}^0 = 0.197V \quad (4.7)$$

To calculate the electrical active surface area (ECSA), we perform a series of cyclic voltammetry CV at different scan rates (5, 10, 25, 50, 75, and 100 mV/s) in the potential range corresponding to the non-faradaic zone of the NiOx. The capacitive current I_c (at a potential selected, here 0.05 V vs RHE) and the specific charge density of $300 \mu\text{F}/\text{cm}^2$ ^[28] allow us to determine the ECSA. One has an ECSA of 4.09 cm^2 . The electrolyte resistance R_s is determined from EIS measurement, and the corrected potential is obtained according to^[29]:

$$E_{cor} = E_{app} - iR_s \quad (4.8)$$

4.3 Oxygen evolution reaction response

Firstly we analyze the electrochemical responses of NiOx electrode in 1 M KOH saturated in oxygen. The presence of phase transition during redox reaction is well-known for the NiOx electrode. Figure 4.3 reports the CV of the electrode NiOx showing the oxidation and reduction peaks. The oxidation peak corresponds to the oxidation of NiO into NiOOH (Ni^{2+} to Ni^{3+}). The reduction peak is linked to the reduction of NiOOH into NiO (Ni^{3+} to Ni^{2+}).

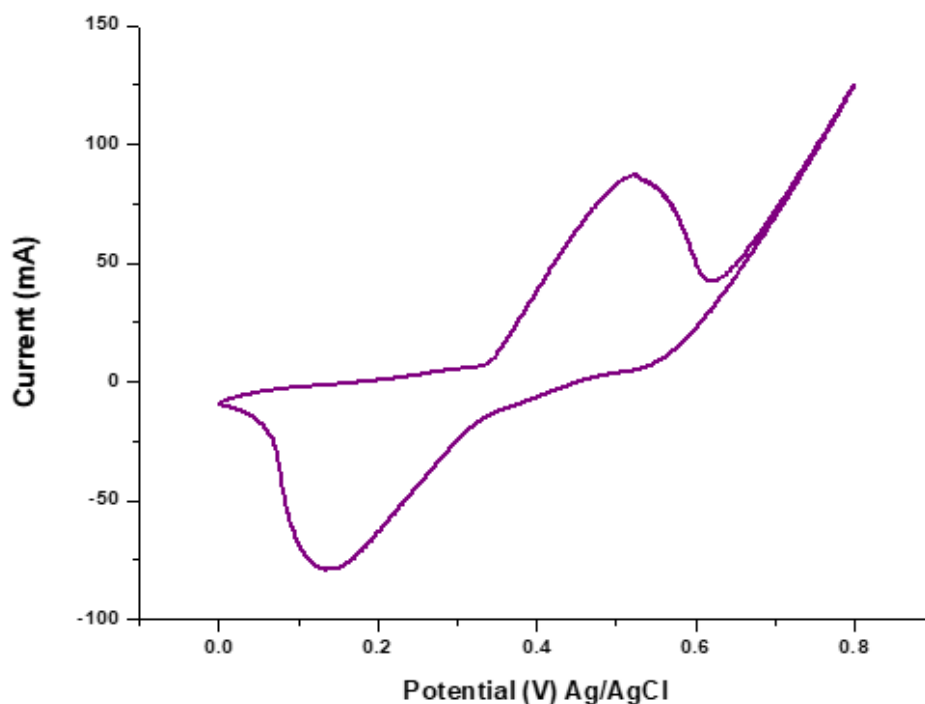


Figure 4.3 – Cyclic voltammogram of modified NiO recorded at $\nu = 100 \text{ mV/s}$ in 1 M KOH

2915 To highlight the phase transition process, we conducted a series of CV measurements
 around the value of the oxidation peak. We can see a loop which is a feature of the phase
 transition. This transition involves two ternary phases $\text{Ni}(\text{OH})_2$ and NiOOH . Between the two
 phases, we have the insertion reaction. We have seen those two forms of hydroxide nickel
 that participated in the phase transition are the α -phase $\text{Ni}(\text{OH})_2$ and β -phase $\text{Ni}(\text{OH})_2$. The
 2920 α -phase $\text{Ni}(\text{OH})_2$ is unstable in alkaline media and can be translated by a rapid transition to
 the β -phase more stable in alkaline media. We can find the Bode diagram of nickel hydroxides
 in Figure 4.4.b.^[30]

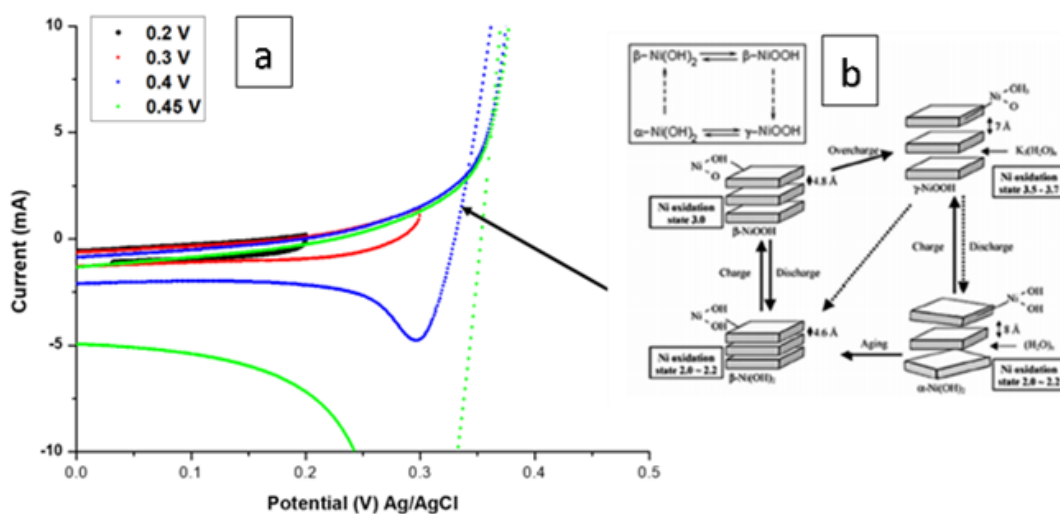


Figure 4.4 – (a) Cyclic voltammogram of modified NiO recorded at $\nu = 100$ mV/s in 1 M KOH saturated in oxygen (b) Bode diagram of nickel hydroxides

4.3.1 Oxygen evolution reaction mechanism and influence of KOH concentration

2925 To look at the OER activity, we use the linear sweep voltammetry to obtain figure 4.5. LSV
 studied here is the one recorded at 1 M KOH, and the electrochemical setup is still the same.
 We calculate the current density according to the geometric surface (1 cm x 1cm).
 For OER, the overpotential was calculated following this equation:

$$\eta = E_{cor} (V. vs RHE) - 1.23 \quad (4.9)$$

2930 To evaluate the OER performance of the NiOx electrode, we determine the overpotential
 obtained for various current densities (10, 20, 50, and 100 mA/cm²). The overpotentials for the
 selected current density indicate the good performance of NiOx for OER. Table 4.2 presents
 the different values of the overpotentials noted at these following current densities.

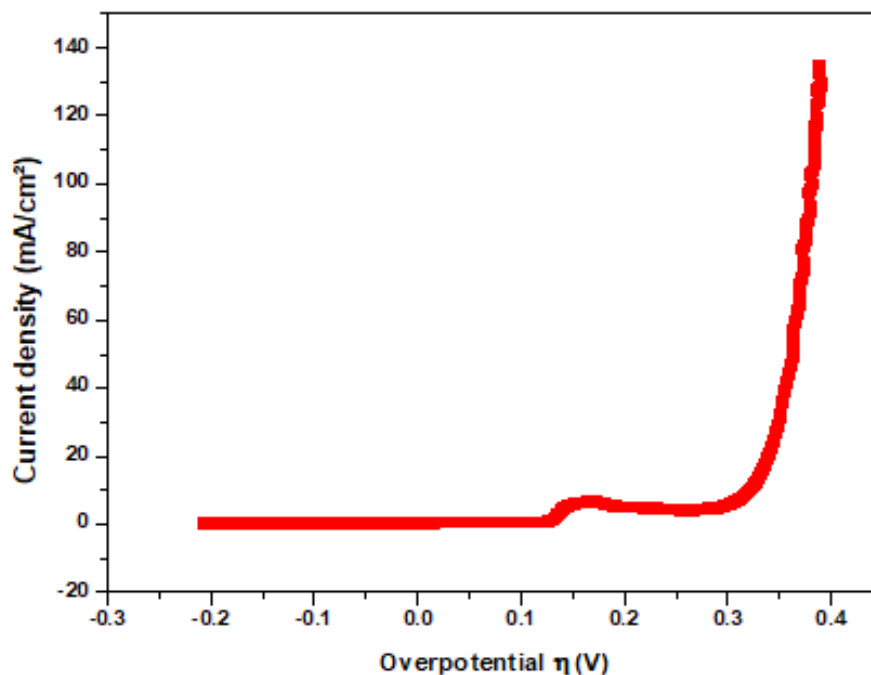


Figure 4.5 – Linear sweep voltammetry (LSV) of modified NiO for oxygen evolution reaction recorded at $\nu = 2$ mV/s in 1 M KOH saturated in O_2

| Current Density (mA/cm ²) | Overpotential η (V) |
|---------------------------------------|--------------------------|
| 10 | 0.32 |
| 20 | 0.34 |
| 50 | 0.36 |
| 100 | 0.38 |

Table 4.2 – Value of the overpotentials (V) for selected current density (mA/cm²)

We conduct the same LSV investigation through OER activity at different concentrations of KOH. We can find in Figure 4.6 the evolution of the overpotential notice at different density currents as a function of the electrolyte KOH concentrations. Thanks to Figure 4.6, we notice the influence of the concentration through the profile observed. We can see that the lower values of overpotential obtained in the selected current density are recorded in 1.5 M KOH. As seen in HER, we can suppose the difference in response can be linked to the cation of the electrolyte present and its influence on the OER kinetic.^[31]

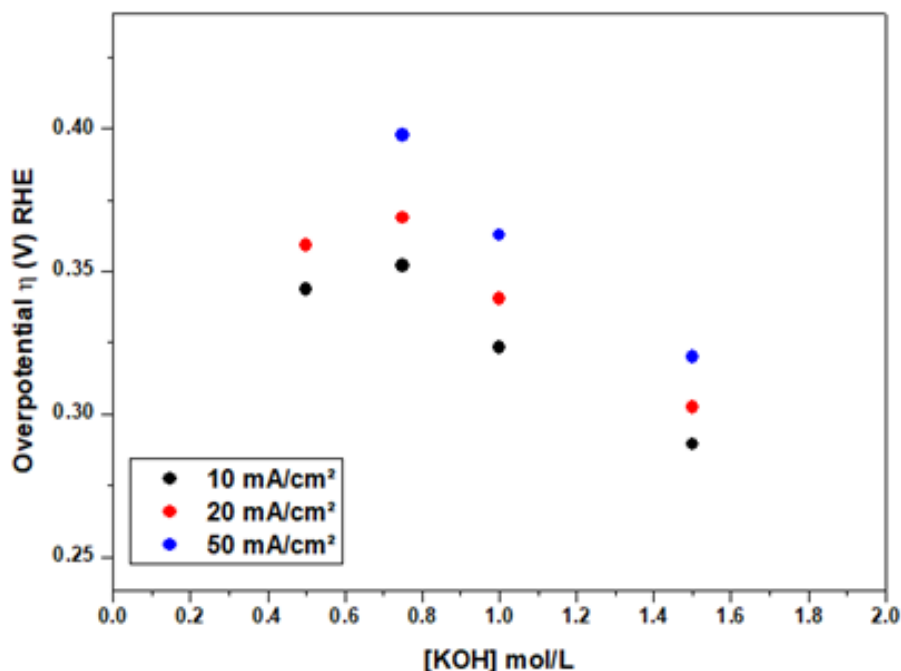


Figure 4.6 – Evolution of the overpotentials (V) at various density currents as function of the KOH concentration (mol/L)

4.3.2 Tafel slope and mechanism investigation

Tafel slope determined from LSV experiments is useful for studying the mechanism during the electrochemical reaction. For clarity, we separate the current density obtained by LSV into two parts: one is the low overpotential zone and the other is the large overpotential zone (Figure 4.7.(a)). The Tafel plot (Figure 4.7.(b)) can be expressed as:

$$\eta = a + b \log j \quad (4.10)$$

with η is the overpotential, j is the current density, a is the intercept associated with the exchange current density j_0 , and b is the Tafel slope.

We can see the two values of the Tafel slope in low and large overpotential are close, but the value for the large one is slightly higher. This value difference may be due to a change in the RDS or a variation of the potential impact adsorption of reaction intermediates.^[32,33] We can also suppose that the increasing slope can be due to decreasing ECSA, which is similar to increasing gas evolution in the large overpotential zone. Furthermore, the increase of the Tafel slope in the large overpotential zone may also be due to mass transfer limitations in this area.^[34]

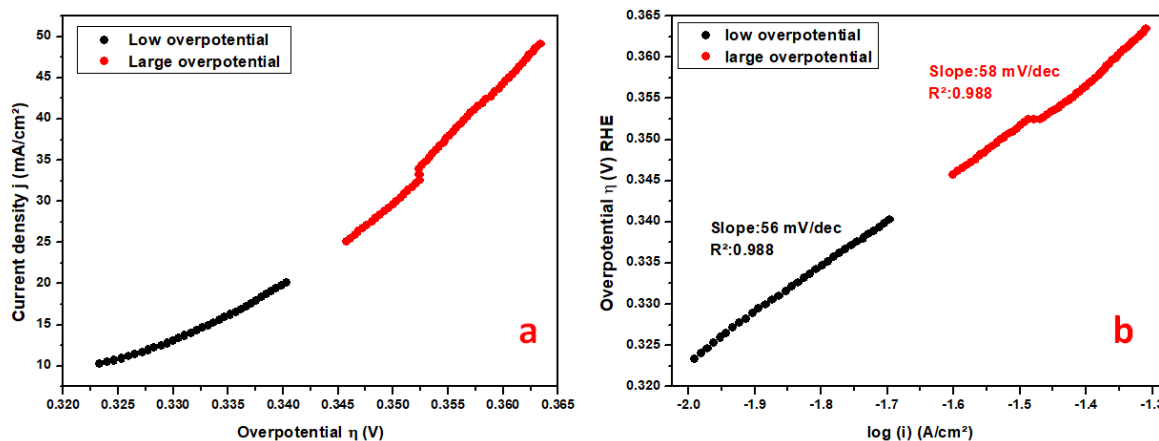


Figure 4.7 – a) Linear sweep voltammetry (LSV) of modified NiO recorded at $\nu = 2$ mV/s in 1 M KOH, (b) Tafel plot of the studies made with 1 M KOH

To understand this change in the value of the Tafel slope, we perform the same kind of measurements for various KOH concentrations. Figure 4.8 shows the different variations of the Tafel slope as function of the electrolyte concentration and indicates the difference between the studied overpotential zones.

2960

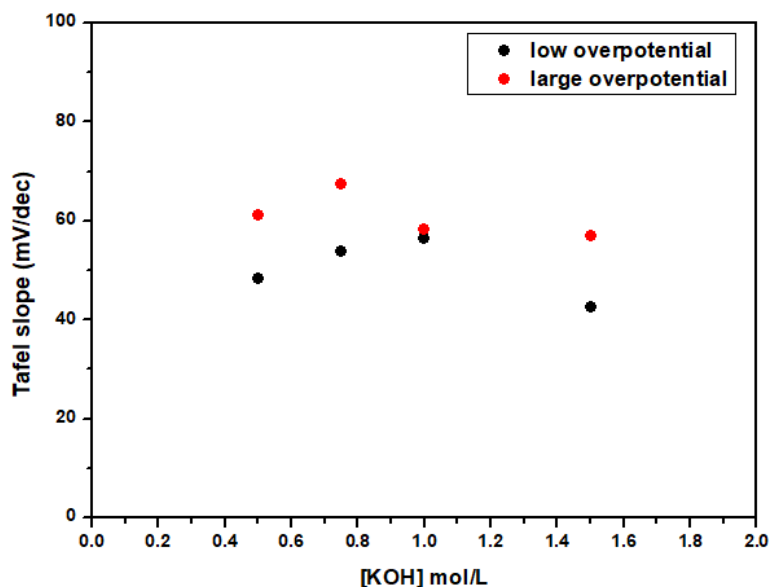


Figure 4.8 – Evolution of the Tafel slope for low overpotential and large overpotential for different KOH concentration

One can remind that a low Tafel slope indicates an efficient electrocatalytic performance.^[35] At this stage, it is of interest to analyze the parameters that determine the Tafel slope since it will give us information on the stoichiometry and succession of steps in the overall reaction through the transferred coefficient α_a :

$$\alpha_a = \frac{1}{b} \left(\frac{2.303RT}{F} \right) \text{ with } \left(\frac{2.303RT}{F} \right) = 0.059 \quad (4.11)$$

with b is the Tafel slope, R is the perfect gas coefficient $8,3145 \text{ J.mol}^{-1}.\text{K}^{-1}$, T is the temperature (here taken as 298 K), and F is the Faraday constant (96485 C.mol^{-1}).

Equation (4.11) indicates that the transfer coefficient is inversely proportional to the Tafel slope. Thus, a low value of the Tafel slope corresponds to a high value of the transfer coefficient. To analyze this relationship in terms of mechanism, let us go back to the definition of the transfer coefficient α_a :

$$\alpha_a = \frac{n_f}{\nu} + n_r \beta \quad (4.12)$$

with n_f is the number of electrons transferred before the RDS, ν is the stoichiometric number; n_r is the number of electrons transferred in each occurrence of the RDS, and β is the symmetrical of potential energy barrier (electrochemical Brønsted factor), which has a typical value around 0.5 (^[33,36]).

Accordingly, if the RDS steps are subsequent to the first electron transfer step, we will have β of 0.5, n_f and n_r of 1 each, α_a of 1.5, and Tafel slope around 40 mV/dec . In the case of RDS with n_r of 0 before a one-electron transfer step done twice ($\nu = 2$) and α_a of 0.5, we will have a Tafel slope around 120 mV/dec .^[34] Table 4.3 summarizes these two cases.

| Values of transfer coefficient | Tafel slope |
|---|-------------|
| $\beta = 0.5$ n_f and $n_r = 0.1$ each $\alpha_a = 1.5$ | 40 mV/dec |
| $n_r = 0$ $\nu = 2$ $\alpha_a = 0.5$ | 120 mV/dec |

Table 4.3 – Correlation between the values of transfer coefficient and the Tafel slope

2980

Then, the Tafel slope values for the most governing rate-determining steps (RDS) as^[34] :

1. if OH^- adsorption is the RDS, then the theoretical Tafel slope is 120 mV/dec
2. if O–H bond splitting is the RDS, then the theoretical Tafel slope is 30 mV/dec
3. if O_2 desorption is the RDS, then the theoretical Tafel slope is 20 mV/dec

2985

Figure 4.9 shows the values of the anodic transfer coefficient determined for various KOH concentrations for low and large overpotential.

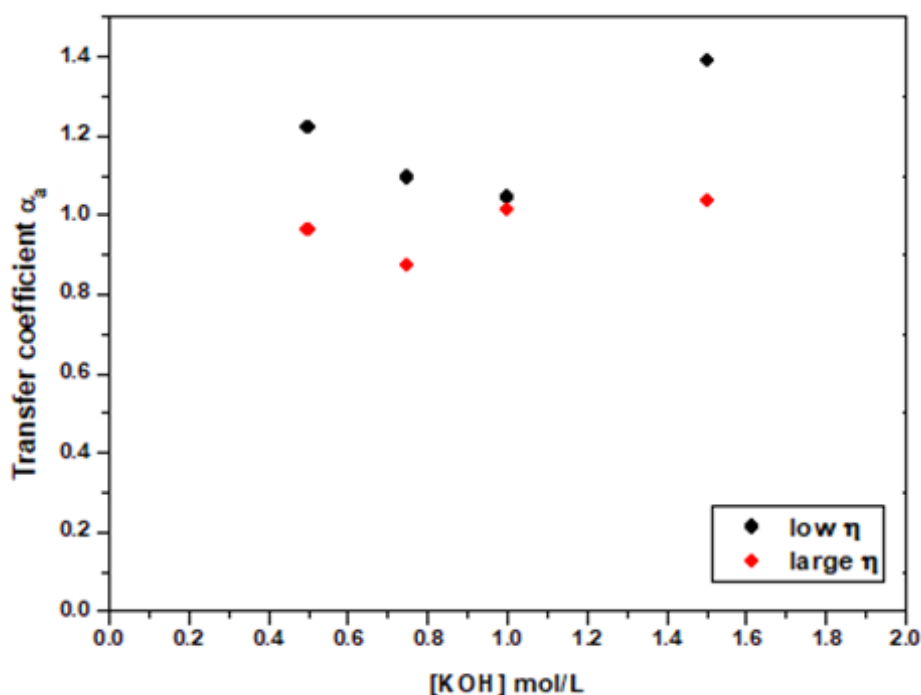


Figure 4.9 – Evolution of the transfer coefficient α_a for low overpotential and large overpotential for different KOH concentration

2990

In our case, based on the Tafel slope and the transfer coefficient values in the large and low overpotential zone, we can say that rate-determining steps involved mixed processes more likely involving OH^- adsorption and O–H bond splitting.^[37] Following the recent paper published by the Durrant group^[38], we can propose the following mechanism of the $\text{Ni}^{2+}/\text{Ni}^{3+}$ redox transition. We have the formation of oxyhydroxide when OH is bound to the Ni^{3+} site. When we increase the potential (> 1.5 V vs RHE beginning of the faradic current), we have OH groups that will be deprotonated to form $^*\text{O}$ species and increase in differential capacitance (due to adsorption). This event corresponds to the first step presented in Figure 4.10. The second step is when two oxo species are associated with forming molecular oxygen. The density of oxidized species can influence the reaction rate in this 2nd step. Furthermore, the last step involves OH^- ions from the solution, which will be adsorbed on a Ni site and bring back the active state of the catalyst. This mechanism can explain the OER process with NiOx electrode investigated here.

2995

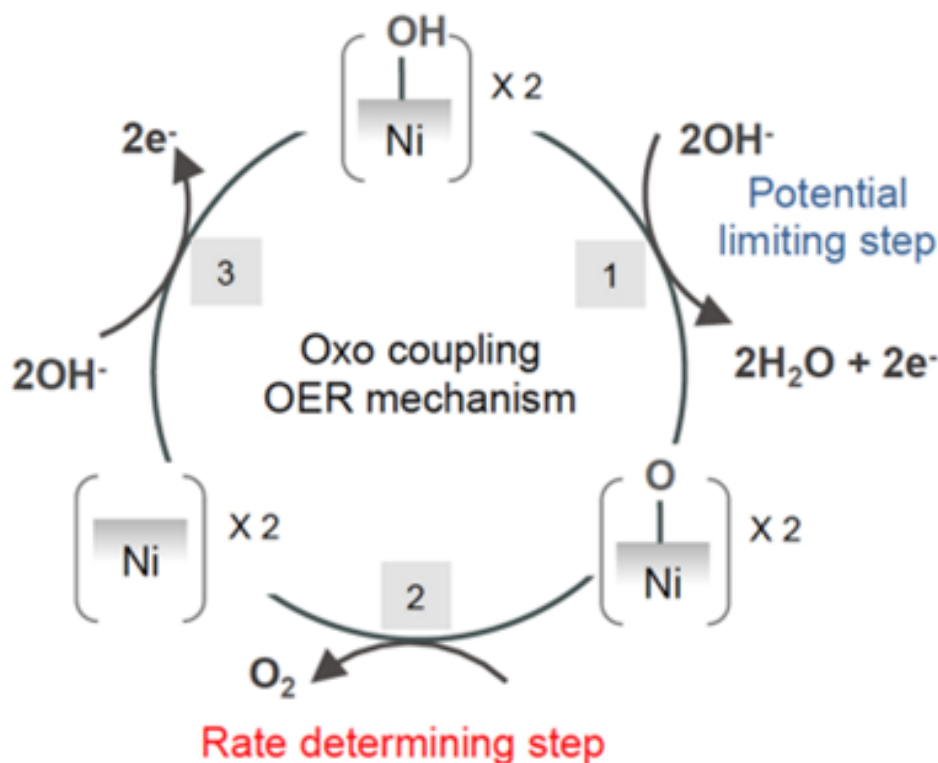


Figure 4.10 – Proposition of mechanism for oxygen evolution reaction involving two adjacent oxidized Ni sites^[38]

3000 4.3.3 EIS study

In the following section, EIS measurements are carried out to investigate the OER mechanism. Figure 4.11.(a) shows the experimental measurements obtained at different potentials. One observes a decrease in the semicircle arc when the potential increases. EIS data are analysed using Armstrong-Henderson equivalent circuit:^[39] with R_s as the uncompensated solution resistance, R_{ct} as the charge transfer resistance, R_a and C_a as the adsorption resistance and adsorption capacitance, and CPE as the constant phase element characterizing the double layer. Figure 4.11.(b) shows the fitting results with the equivalent circuit model. The potentials present in both figures are in Ag/AgCl reference. For the studies, we will convert to RHE and use the overpotential.

3005

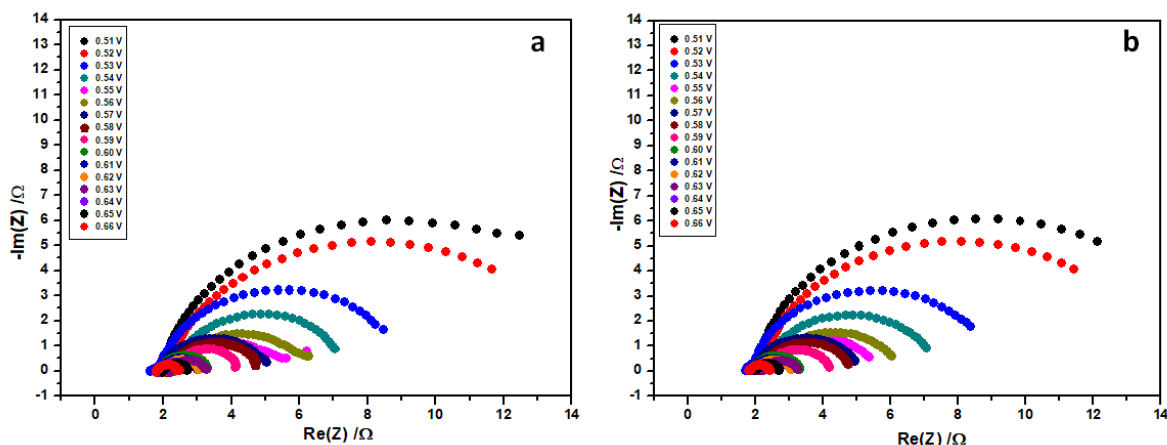


Figure 4.11 – (a) Nyquist plot for NiOx obtained with EIS measurement at 1 M KOH , (b) Nyquist plot for NiOx with fitting at 1 M KOH

3010 Hu^[40] and Cao^[41] demonstrated that the faradaic impedance Z_F for OER irreversible system is :

$$Z_F = R_{ct} + \frac{R_a}{(1 + j\omega R_a C_a)} \quad (4.13)$$

With R_{ct} : the charge transfer resistance, R_a and C_a are the resistance and capacitance associated with the relaxation of the surface coverage of an adsorbed intermediate in the OER mechanism.^[42,43]

3015 One can remark that Equation (4.13) corresponds to the faradaic impedance for the equivalent electrical circuit described in Figure 4.12.^[44]

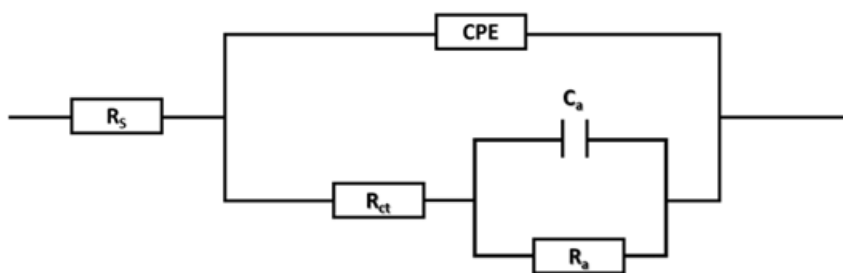


Figure 4.12 – Equivalent circuit for analyzing EIS responses during OER with NiO_x electrode

3020 Firstly, we investigate the charge transfer resistance R_{ct} . Figure 4.13 shows the variation of the charge transfer resistance R_{ct} as function of the overpotential for both zones studied. We observe a decrease of R_{ct} , indicating an increase in the electron transfer kinetics. Harrington and Conway^[39] demonstrated that the inversed R_{ct} gives us the sum of reciprocal resistances of each charge transfer step in OER.

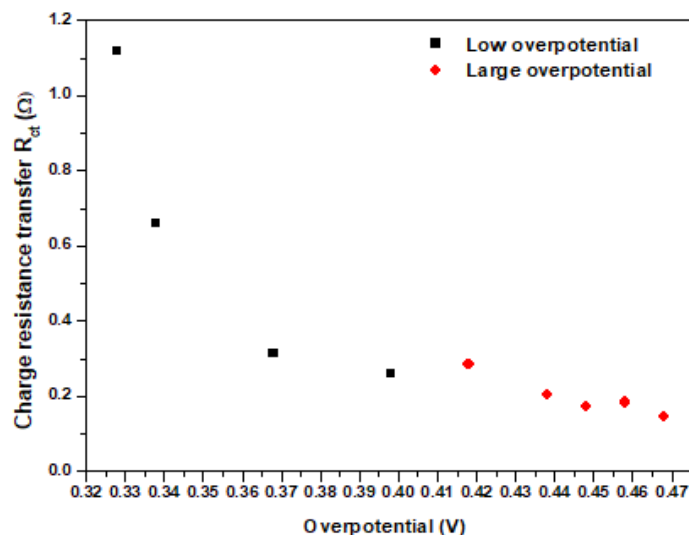


Figure 4.13 – Evolution of the Charge transfer resistance R_{ct} (Ω) as function of the overpotential (V)

The variation of adsorption resistance R_a as a function of the overpotential is reported in Figure 4.14. R_a is linked to the rate of surface intermediates formation, which is more favourable by increasing the overpotential. Figure 4.15 shows the variation of the adsorption resistance C_a as a function of the overpotential. C_a is linked to the surface concentration of charged intermediates during the OER. As shown in figure 4.15, there is not a notable variation of C_a . [45]

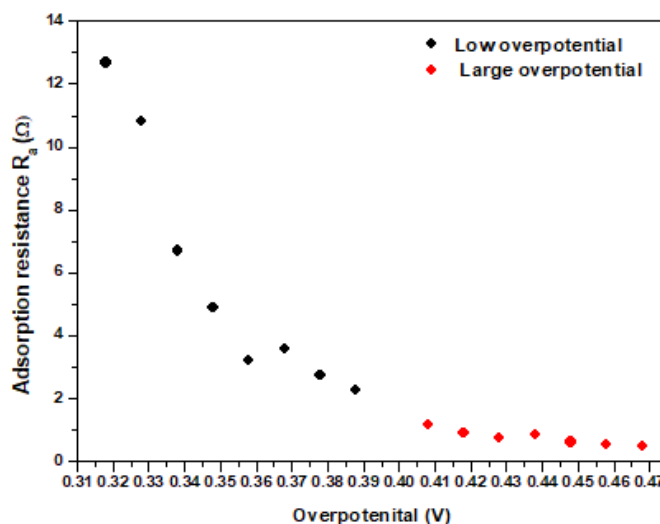


Figure 4.14 – Evolution of the adsorption resistance R_a (Ω) as function of the overpotential (V)

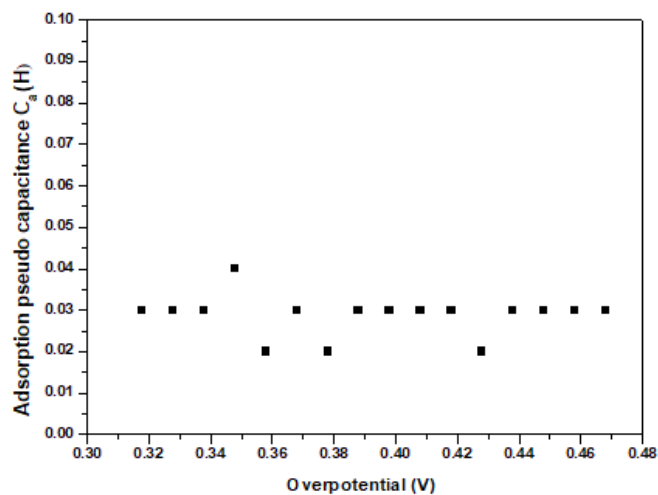


Figure 4.15 – Evolution of the adsorption capacitance C_a (H) as function of the overpotential (V)

Based on the successive reactions involved in OER, it is interesting to find the relationship between R_{ct} and R_a . As shown in Figure 4.16, we find a linear correlation. However, the slopes are different for the low and large overpotentials.

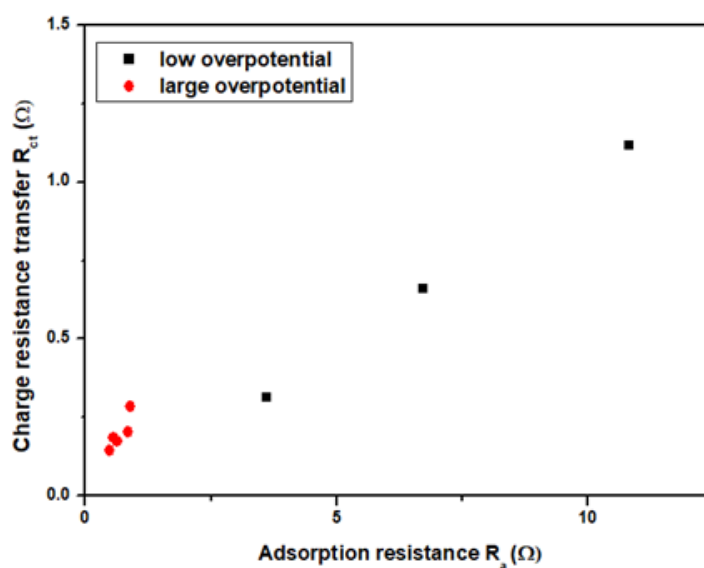


Figure 4.16 – Evolution of the charge transfer resistance R_{ct} (Ω) as function of the adsorption resistance R_a (Ω)

4.3.4 Correlation between LSV and EIS

In this last part, we will look at the correlation we can have by combining the LSV results and the EIS responses as we have done in the previous Chapter (Chapter 3). In Figure 4.17.(a), we plot $\ln j$ (A/cm^2) as a function of the overpotential (V). According to the Butler-Volmer equation, the difference observed in the two overpotential zones is related to the change of the charge transfer coefficient that reflects the mechanism. In Figure 4.17.(b), we plot the natural logarithm of the inverse of R_{ct} as a function of the overpotential (V). The inverse of R_{ct} is equal to the conductance (S). This figure shows us the response of conductance. We can see an increase of the conductance in both cases: a high increase in the low overpotential zone and a minor increase in the large overpotential. In Figure 4.17.(c), we have the evolution of $\ln(1/R_a)$ as a function of the overpotential (V), which shows the same behaviour as with $\ln(1/R_{ct})$ vs E in Figure 4.17.(b). These results indicate clearly that the OER mechanism is potential dependent.

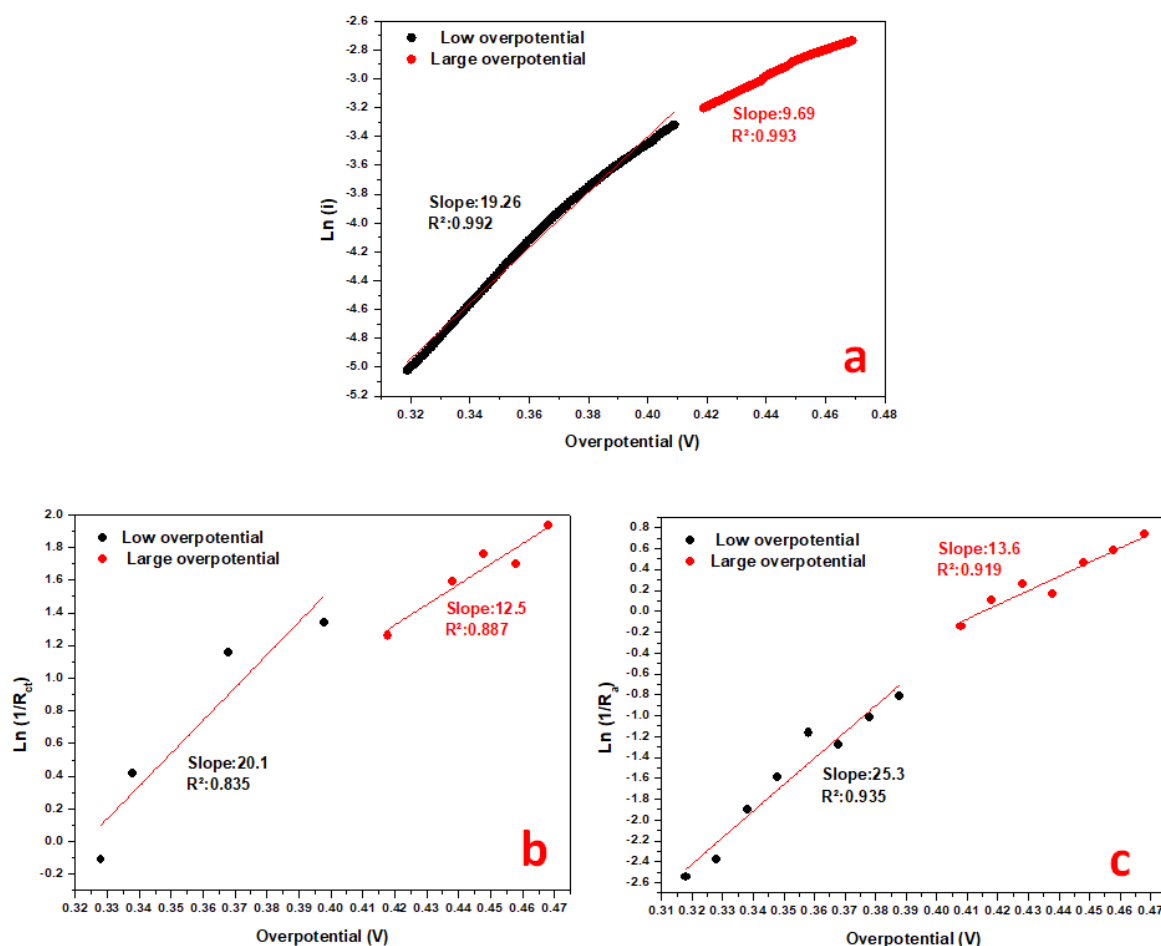


Figure 4.17 – a) Evolution of $\ln i$ (A/cm^2) as function of the overpotential (V), (b) Evolution of $\ln(1/R_{ct})$ as function of the overpotential (V), (c) Evolution of $\ln(1/R_a)$ as function of the overpotential (V)

4.4 Conclusion Water splitting

In this chapter 4, we focus on the catalyst of our NiOx electrode through OER. LSV investigation, we see that we have a suitable catalyst for OER. The Tafel slope analysis suggests that the rate-determining steps are more likely to involve OH⁻ adsorption and O–H bond splitting. We analysed the charge transfer resistance R_{ct} , adsorption resistance R_a , and adsorption capacitance C_a with the EIS study. We analyzed the correlation between LSV and EIS.

| Ratio of slopes $\ln(1/R_{ct})$ vs E and $\ln(j)$ vs E | Ratio of slopes $\ln(1/R_a)$ vs E and $\ln(i)$ vs E |
|--|---|
| Low overpotential zone: 1.04 | Low overpotential zone: 1.31 |
| Large overpotential zone: 1.29 | Large overpotential zone: 1.40 |

Table 4.4 – Table of the Ratio of slopes for the evolution's curves studied in figure 4.17

To conclude this Chapter 4 with Chapter 3, we wanted to correlate the catalytic effect of the NiOx electrode through HER and OER. To this end, we carry out overall water splitting in a two-electrode system using NiOx for anode and cathode. In Figure 4.18, we can see the LSV polarization curve obtained for water splitting.

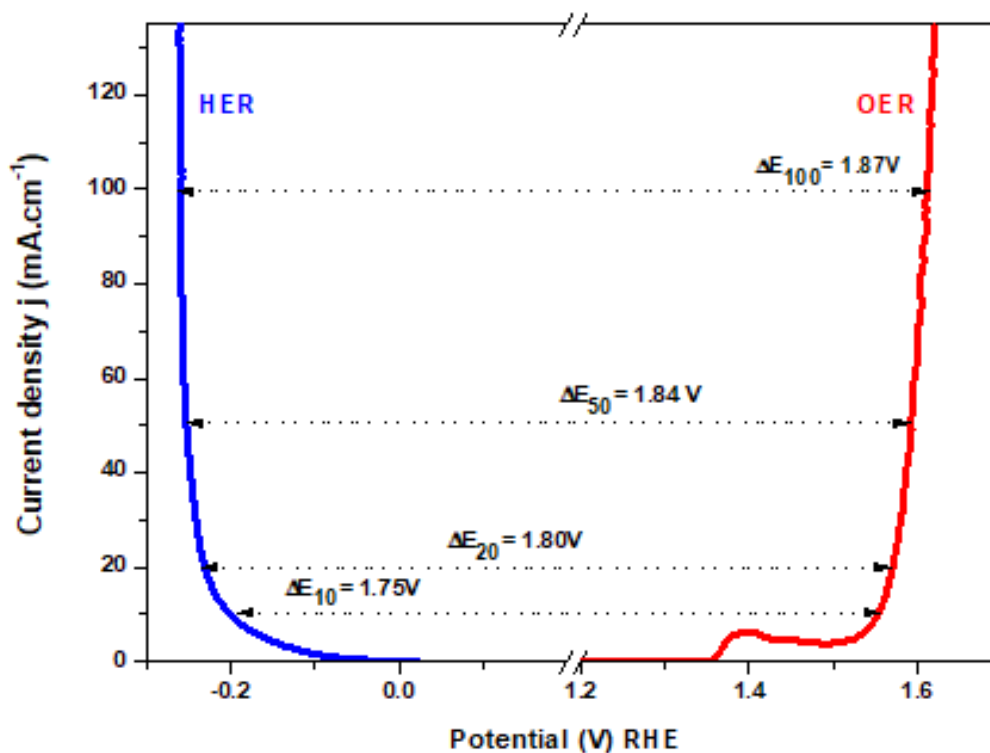


Figure 4.18 – Polarization curves in a two-electrode system with NiOx (+)||NiOx (-) in 1M KOH

3055 To emphasize the performance of dual P/Fe doped nickel oxide electrodes for water splitting, we determine the potential difference corresponding to 10, 20, 50, and 100 mA/cm² between HER and OER. We can see the potential difference for each current density seen in table 4.5.

| Current Density (mA/cm ²) | Potential difference (V vs RHE) |
|---------------------------------------|---------------------------------|
| 10 | 1.75 |
| 20 | 1.80 |
| 50 | 1.84 |
| 100 | 1.87 |

Table 4.5 – Table of the potential difference Δ_E (V vs RHE)

To finish this conclusion, we will evaluate the energy efficiency of water electrolysis. Before that, we have to introduce the thermoneutral voltage for water splitting. Its value is 1.48V and corresponds to the free reaction enthalpy for the water dissociation process at 25°C, 1 bar. The water electrolysis reaction has an enthalpy of 285.83 kJ/mol (25°C, 1 bar) with the Gibbs free energy change of $\Delta G = 237.1$ kJ/mol and the heat energy $\Delta TS = 48.7$ kJ/mol.

3065 During the electrolysis, the cell voltage is always higher than the theoretical voltage ($E_{0cell} = 1.23$ V), and the difference will be because of the heat exchange. The thermoneutral potential is 1.48 V. The thermoneutral potential is used as the standard of 100% efficiency.^[46,47]

To calculate the energy efficiency of water electrolysis, we divide 1.48 V by the practical cell voltage of our system (E_{cell}) that we give us approximately give the energy efficiency:

$$\varepsilon \approx \frac{1.48V}{E_{cell}} \times 100\% \quad (4.14)$$

When we calculate it and give the energy efficiency, we have more than 75% efficiency in our cell.

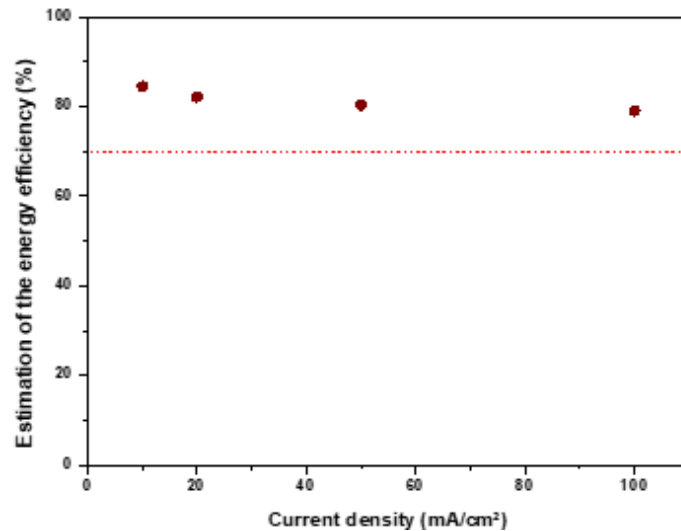


Figure 4.19 – Evaluation of the energy efficiency based on thermoneutral potential

3075

Finally, we can compare our system to different alkaline water electrolyzers thanks to Figure 4.20^[48]. We can see that we have a cell voltage of 1.75 V at 10 mA/cm². And we notice that we have a cell voltage of 1.87 V at 100 mA/cm². Comparing these results with the one in Figure 4.20, we can see a promising result.

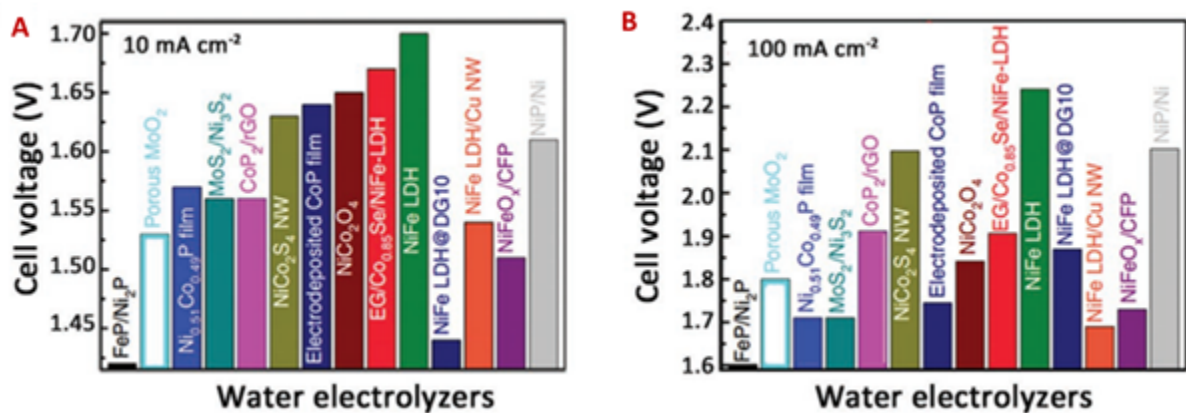


Figure 4.20 – Comparisons of cell voltages (A) at 10 mA/cm² and (B) 100 mA/cm² among different alkaline water electrolyzers^[48]

3080

These optimistic results can open an avenue for non-noble catalysts for water splitting by optimising the electrode nanostructure and/or the dopant (iron or phosphorus) concentration.

REFERENCES

- 3085 [1] Zhixuan Han, Xinyuan Liang, Shirong Wang, Lijing Zhou, and Zhen Zhao. One-step synthesis of Ni-Mo-S/MoO_x composite self-supported on Ni foam for efficient electrocatalytic hydrogen evolution. *Materials Letters*, 246:63–66, July 2019. doi: 10.1016/j.matlet.2019.03.027.
- 3090 [2] Mengqi Yao, Baolong Sun, Ni Wang, Wencheng Hu, and Sridhar Komarneni. Self-generated N-doped anodized stainless steel mesh for an efficient and stable overall water splitting electrocatalyst. *Applied Surface Science*, 480:655–664, June 2019. doi: 10.1016/j.apsusc.2019.03.036.
- [3] Shuaipeng Wang, Li Xu, and Weixin Lu. Synergistic effect: Hierarchical Ni₃S₂@Co(OH)₂ heterostructure as efficient bifunctional electrocatalyst for overall water splitting. *Applied Surface Science*, 457:156–163, November 2018. doi: 10.1016/j.apsusc.2018.06.253.
- 3095 [4] Yan Jiao, Yao Zheng, Mietek Jaroniec, and Shi Zhang Qiao. Design of electrocatalysts for oxygen- and hydrogen-involving energy conversion reactions. *Chemical Society Reviews*, 44(8):2060–2086, April 2015. doi: 10.1039/C4CS00470A.
- 3100 [5] Zonghua Pu, Tingting Liu, Ibrahim Saana Amiin, Ruilin Cheng, Pengyan Wang, Chengtian Zhang, Pengxia Ji, Weihua Hu, Jian Liu, and Shichun Mu. Transition-Metal Phosphides: Activity Origin, Energy-Related Electrocatalysis Applications, and Synthetic Strategies. *Advanced Functional Materials*, 30(45):2004009, 2020. doi: 10.1002/adfm.202004009.
- [6] Huanyu Jin, Chunxian Guo, Xin Liu, Jinlong Liu, Anthony Vasileff, Yan Jiao, Yao Zheng, and Shi-Zhang Qiao. Emerging Two-Dimensional Nanomaterials for Electrocatalysis. *Chemical Reviews*, 118(13):6337–6408, July 2018. doi: 10.1021/acs.chemrev.7b00689.
- 3105 [7] Zhenhua Yan, Huanhuan Liu, Zhimeng Hao, Meng Yu, Xiang Chen, and Jun Chen. Electrodeposition of (hydro)oxides for an oxygen evolution electrode. *Chemical Science*, 11(39):10614–10625, October 2020. doi: 10.1039/D0SC01532F.
- 3110 [8] Isabela C. Man, Hai-Yan Su, Federico Calle-Vallejo, Heine A. Hansen, José I. Martínez, Nilay G. Inoglu, John Kitchin, Thomas F. Jaramillo, Jens K. Nørskov, and Jan Rossmeisl. Universality in Oxygen Evolution Electrocatalysis on Oxide Surfaces. *ChemCatChem*, 3(7):1159–1165, 2011. doi: 10.1002/cctc.201000397.

- [9] Youngmin Lee, Jin Suntivich, Kevin J. May, Erin E. Perry, and Yang Shao-Horn. Synthesis and Activities of Rutile IrO₂ and RuO₂ Nanoparticles for Oxygen Evolution in Acid and Alkaline Solutions. *The Journal of Physical Chemistry Letters*, 3(3):399–404, February 2012. doi: 10.1021/jz2016507.
- [10] Charles C. L. McCrory, Suho Jung, Jonas C. Peters, and Thomas F. Jaramillo. Benchmarking Heterogeneous Electrocatalysts for the Oxygen Evolution Reaction. *Journal of the American Chemical Society*, 135(45):16977–16987, November 2013. doi: 10.1021/ja407115p.
- [11] Ksenia Fominykh, Johann M. Feckl, Johannes Sicklinger, Markus Döblinger, Sebastian Böcklein, Jürgen Ziegler, Laurence Peter, Jiri Rathousky, Ernst-Wilhelm Scheidt, Thomas Bein, and Dina Fattakhova-Rohlfing. Ultrasmall Dispersible Crystalline Nickel Oxide Nanoparticles as High-Performance Catalysts for Electrochemical Water Splitting. *Advanced Functional Materials*, 24(21):3123–3129, 2014. doi: 10.1002/adfm.201303600.
- [12] Lucas-Alexandre Stern and Xile Hu. Enhanced oxygen evolution activity by NiOx and Ni(OH)₂ nanoparticles. *Faraday Discussions*, 176(0):363–379, March 2015. doi: 10.1039/C4FD00120F.
- [13] Sheng Chen, Jingjing Duan, Mietek Jaroniec, and Shi Zhang Qiao. Three-Dimensional N-Doped Graphene Hydrogel/NiCo Double Hydroxide Electrocatalysts for Highly Efficient Oxygen Evolution. *Angewandte Chemie*, 125(51):13812–13815, 2013. doi: 10.1002/ange.201306166.
- [14] Minrui Gao, Wenchao Sheng, Zhongbin Zhuang, Qianrong Fang, Shuang Gu, Jun Jiang, and Yushan Yan. Efficient Water Oxidation Using Nanostructured α -Nickel-Hydroxide as an Electrocatalyst. *Journal of the American Chemical Society*, 136(19):7077–7084, May 2014. doi: 10.1021/ja502128j.
- [15] Weijia Zhou, Xue-Jun Wu, Xiehong Cao, Xiao Huang, Chaoliang Tan, Jian Tian, Hong Liu, Jiyang Wang, and Hua Zhang. Ni₃S₂ nanorods/Ni foam composite electrode with low overpotential for electrocatalytic oxygen evolution. *Energy & Environmental Science*, 6(10):2921–2924, September 2013. doi: 10.1039/C3EE41572D.
- [16] Chun Tang, Zonghua Pu, Qian Liu, Abdullah M. Asiri, Yonglan Luo, and Xuping Sun. Ni₃S₂ nanosheets array supported on Ni foam: A novel efficient three-dimensional hydrogen-evolving electrocatalyst in both neutral and basic solutions. *International Journal of Hydrogen Energy*, 40(14):4727–4732, April 2015. doi: 10.1016/j.ijhydene.2015.02.038.
- [17] Kun Xu, Pengzuo Chen, Xiuling Li, Yun Tong, Hui Ding, Xiaojun Wu, Wangsheng Chu, Zhenmeng Peng, Changzheng Wu, and Yi Xie. Metallic Nickel Nitride Nanosheets Realizing Enhanced Electrochemical Water Oxidation. *Journal of the American Chemical Society*, 137(12):4119–4125, April 2015. doi: 10.1021/ja5119495.
- [18] Menny Shalom, Debora Ressnig, Xiaofei Yang, Guylhaine Clavel, Tim Patrick Fellingner, and Markus Antonietti. Nickel nitride as an efficient electrocatalyst for water splitting. *Journal of Materials Chemistry A*, 3(15):8171–8177, 2015. doi: 10.1039/C5TA00078E.
- [19] Lena Trotochaud, Samantha L. Young, James K. Ranney, and Shannon W. Boettcher. Nickel–Iron Oxyhydroxide Oxygen-Evolution Electrocatalysts: The Role of Intentional

- and Incidental Iron Incorporation. *Journal of the American Chemical Society*, 136(18): 6744–6753, May 2014. doi: 10.1021/ja502379c.
- 3155 [20] DongHoon Song, Doosun Hong, YongKeun Kwon, HyoWon Kim, Jaewook Shin, Hyuck Mo Lee, and EunAe Cho. Highly porous Ni–P electrode synthesized by an ultra-fast electrodeposition process for efficient overall water electrolysis. *Journal of Materials Chemistry A*, 8(24):12069–12079, June 2020. doi: 10.1039/D0TA03739G.
- 3160 [21] Prashanth W. Menezes, Chakadola Panda, Stefan Loos, Florian Bunschei-Bruns, Carsten Walter, Michael Schwarze, Xiaohui Deng, Holger Dau, and Matthias Driess. A structurally versatile nickel phosphite acting as a robust bifunctional electrocatalyst for overall water splitting. *Energy & Environmental Science*, 11(5):1287–1298, May 2018. doi: 10.1039/C7EE03619A.
- 3165 [22] Xu-Dong Wang, Yang Cao, Yuan Teng, Hong-Yan Chen, Yang-Fan Xu, and Dai-Bin Kuang. Large-Area Synthesis of a Ni₂P Honeycomb Electrode for Highly Efficient Water Splitting. *ACS Applied Materials & Interfaces*, 9(38):32812–32819, September 2017. doi: 10.1021/acsami.7b10893.
- 3170 [23] Pengyan Wang, Zonghua Pu, Yanhui Li, Lin Wu, Zhengkai Tu, Min Jiang, Zongkui Kou, Ibrahim Saana Amiinu, and Shichun Mu. Iron-Doped Nickel Phosphide Nanosheet Arrays: An Efficient Bifunctional Electrocatalyst for Water Splitting. *ACS Applied Materials & Interfaces*, 9(31):26001–26007, August 2017. doi: 10.1021/acsami.7b06305.
- 3175 [24] Bo You, Nan Jiang, Meili Sheng, Margaret Winona Bhushan, and Yujie Sun. Hierarchically Porous Urchin-Like Ni₂P Superstructures Supported on Nickel Foam as Efficient Bifunctional Electrocatalysts for Overall Water Splitting. *ACS Catalysis*, 6(2):714–721, February 2016. doi: 10.1021/acscatal.5b02193.
- [25] Lucas-Alexandre Stern, Ligang Feng, Fang Song, and Xile Hu. Ni₂P as a Janus catalyst for water splitting: the oxygen evolution activity of Ni₂P nanoparticles. *Energy & Environmental Science*, 8(8):2347–2351, July 2015. doi: 10.1039/C5EE01155H.
- 3180 [26] Yanhui Liang, Qian Liu, Abdullah M. Asiri, Xuping Sun, and Yuquan He. Nickel–iron foam as a three-dimensional robust oxygen evolution electrode with high activity. *International Journal of Hydrogen Energy*, 40(39):13258–13263, October 2015. doi: 10.1016/j.ijhydene.2015.07.165.
- 3185 [27] Hanfeng Liang, Appala N. Gandhi, Chuan Xia, Mohamed N. Hedhili, Dalaver H. Anjum, Udo Schwingenschlögl, and Husam N. Alshareef. Amorphous NiFe–OH/NiFeP Electrocatalyst Fabricated at Low Temperature for Water Oxidation Applications. *ACS Energy Letters*, 2(5):1035–1042, May 2017. doi: 10.1021/acsenergylett.7b00206.
- 3190 [28] Amanda C. Garcia, Thomas Touzalin, Celine Nieuwland, Nickson Perini, and Marc T. M. Koper. Enhancement of Oxygen Evolution Activity of Nickel Oxyhydroxide by Electrolyte Alkali Cations. *Angewandte Chemie International Edition*, 58(37):12999–13003, 2019. doi: 10.1002/anie.201905501.
- [29] Yuan Li, Liangxing Jiang, Fangyang Liu, Jie Li, and Yexiang Liu. Novel phosphorus-doped PbO₂–MnO₂ bicontinuous electrodes for oxygen evolution reaction. *RSC Advances*, 4(46): 24020–24028, June 2014. doi: 10.1039/C4RA01831A.

- [30] M. E. G. Lyons, R. L. Doyle, I. Godwin, M. O'Brien, and L. Russell. Hydrous Nickel Oxide: Redox Switching and the Oxygen Evolution Reaction in Aqueous Alkaline Solution. *Journal of The Electrochemical Society*, 159(12):H932, October 2012. doi: 10.1149/2.078212jes.
- [31] Akansha Goyal and Marc T. M. Koper. The Interrelated Effect of Cations and Electrolyte pH on the Hydrogen Evolution Reaction on Gold Electrodes in Alkaline Media. *Angewandte Chemie International Edition*, 60(24):13452–13462, 2021. doi: 10.1002/anie.202102803.
- [32] A. Damjanovic, M. A. Genshaw, and J. O'm Bockris. The Mechanism of Oxygen Reduction at Platinum in Alkaline Solutions with Special Reference to H_2O_2 . *Journal of The Electrochemical Society*, 114(11):1107, November 1967. doi: 10.1149/1.2426425.
- [33] A. Damjanovic, A. Dey, and J. O'M. Bockris. Kinetics of oxygen evolution and dissolution on platinum electrodes. *Electrochimica Acta*, 11(7):791–814, July 1966. doi: 10.1016/0013-4686(66)87056-1.
- [34] Leila Negahdar, Feng Zeng, Stefan Palkovits, Cornelia Broicher, and Regina Palkovits. Mechanistic Aspects of the Electrocatalytic Oxygen Evolution Reaction over Ni-Co Oxides. *ChemElectroChem*, 6(22):5588–5595, 2019. doi: 10.1002/celec.201901265.
- [35] Abdul Qayoom Mugheri, Aneela Tahira, Umair Aftab, Adeel Liaquat Bhatti, Nusrat Naeem Memon, Jamil-ur-Rehman Memon, Muhammad Ishaque Abro, Aqeel Ahmed Shah, Magnus Willander, Ahmed Ali Hullio, and Zafar Hussain Ibupoto. Efficient trimetallic oxides NiCo₂O₄/CuO for the oxygen evolution reaction. *RSC Advances*, 9(72):42387–42394, December 2019. doi: 10.1039/C9RA09351F.
- [36] Rolando Guidelli, Richard G. Compton, Juan M. Feliu, Eliezer Gileadi, Jacek Lipkowski, Wolfgang Schmickler, and Sergio Trasatti. Defining the transfer coefficient in electrochemistry: An assessment (IUPAC Technical Report). *Pure and Applied Chemistry*, 86(2):245–258, February 2014. doi: 10.1515/pac-2014-5026.
- [37] Guangxing Zhang, Han Wang, Jinlong Yang, Qinghe Zhao, Luyi Yang, Hanting Tang, Chaokun Liu, Haibiao Chen, Yuan Lin, and Feng Pan. Temperature Effect on Co-Based Catalysts in Oxygen Evolution Reaction. *Inorganic Chemistry*, 57(5):2766–2772, March 2018. doi: 10.1021/acs.inorgchem.7b03168.
- [38] Reshma R. Rao, Sacha Corby, Alberto Bucci, Miguel García-Tecedor, Camilo A. Mesa, Jan Rossmeisl, Sixto Giménez, Julio Lloret-Fillol, Ifan E. L. Stephens, and James R. Durrant. Spectroelectrochemical Analysis of the Water Oxidation Mechanism on Doped Nickel Oxides. *Journal of the American Chemical Society*, 144(17):7622–7633, May 2022. doi: 10.1021/jacs.1c08152.
- [39] D. A. Harrington and B. E. Conway. ac Impedance of Faradaic reactions involving electroadsorbed intermediates—I. Kinetic theory. *Electrochimica Acta*, 32(12):1703–1712, December 1987. doi: 10.1016/0013-4686(87)80005-1.
- [40] Ji-Ming Hu, Jian-Qing Zhang, and Chu-Nan Cao. Oxygen evolution reaction on IrO₂-based DSA® type electrodes: kinetics analysis of Tafel lines and EIS. *International Journal of Hydrogen Energy*, 29(8):791–797, July 2004. doi: 10.1016/j.ijhydene.2003.09.007.

- 3235 [41] Chu-nan Cao. On the impedance plane displays for irreversible electrode reactions based on the stability conditions of the steady-state—I. One state variable besides electrode potential. *Electrochimica Acta*, 35(5):831–836, May 1990. doi: 10.1016/0013-4686(90)90077-D.
- 3240 [42] Lijun Bai, D. A. Harrington, and B. E. Conway. Behavior of overpotential–deposited species in Faradaic reactions—II. ac Impedance measurements on H₂ evolution kinetics at activated and unactivated Pt cathodes. *Electrochimica Acta*, 32(12):1713–1731, December 1987. doi: 10.1016/0013-4686(87)80006-3.
- [43] B. E. Conway and E. Gileadi. Kinetic theory of pseudo-capacitance and electrode reactions at appreciable surface coverage. *Transactions of the Faraday Society*, 58(0):2493–2509, January 1962. doi: 10.1039/TF9625802493.
- 3245 [44] R. D. Armstrong and M. Henderson. Impedance plane display of a reaction with an adsorbed intermediate. *Journal of Electroanalytical Chemistry and Interfacial Electrochemistry*, 39(1):81–90, September 1972. doi: 10.1016/S0022-0728(72)80477-7.
- 3250 [45] Richard L. Doyle and Michael E. G. Lyons. An electrochemical impedance study of the oxygen evolution reaction at hydrous iron oxide in base. *Physical Chemistry Chemical Physics*, 15(14):5224–5237, March 2013. doi: 10.1039/C3CP43464H.
- [46] Sengeni Anantharaj and Suguru Noda. Amorphous Catalysts and Electrochemical Water Splitting: An Untold Story of Harmony. *Small*, 16(2):1905779, 2020. ISSN 1613-6829. doi: 10.1002/smll.201905779.
- 3255 [47] Yue Qi, Qianxiao Zhang, Suci Meng, Di Li, Wenxian Wei, Deli Jiang, and Min Chen. Iron-doped nickel cobalt ternary phosphide hyperbranched hierarchical arrays for efficient overall water splitting. *Electrochimica Acta*, 334:135633, February 2020. ISSN 0013-4686. doi: 10.1016/j.electacta.2020.135633.
- 3260 [48] Fang Yu, Haiqing Zhou, Yufeng Huang, Jingying Sun, Fan Qin, Jiming Bao, William A. Goddard, Shuo Chen, and Zhifeng Ren. High-performance bifunctional porous non-noble metal phosphide catalyst for overall water splitting. *Nature Communications*, 9(1):2551, June 2018. ISSN 2041-1723. doi: 10.1038/s41467-018-04746-z.

CHAPTER 5

SUPERCABATTERY

Contents

| | | |
|------|---|------------|
| 3265 | 5.1 Introduction | 177 |
| | 5.2 Experimental section | 179 |
| | 5.2.1 Elaboration of the modified carbon cloth | 179 |
| | 5.2.2 Preconditioning of the electrodes | 180 |
| 3270 | 5.2.3 Supercabattery assembly | 181 |
| | 5.3 Electrochemical responses of the supercabattery | 181 |
| | 5.3.1 Supercabattery charging | 182 |
| | 5.3.2 Supercabattery discharging | 184 |
| | 5.3.3 Charging vs Discharging | 186 |
| 3275 | 5.3.4 Energy and Power of the supercabattery | 186 |
| | 5.3.5 Elastance and Conductance | 191 |
| | 5.3.6 Non-reciprocity of the charging/discharging processes | 194 |
| | 5.3.7 Modified Ragone plot | 195 |
| | 5.4 Conclusion | 196 |
| 3280 | References | 196 |

5.1 Introduction

3285 Increasing the demand for performed and eco-friendly energy devices is highly solicited in portable electronic devices and the development of hybrid electric vehicles. This need for new technologies aims to have high energy and power densities.^[1,2] In this regard, a hybrid device combining the battery and supercapacitor's behaviour is called the "Supercapattery". Within the family of supercapattery, we are mainly interested in supercabattery. The main 3290 advantage of a supercabattery has its high energy, power, and charging/discharging rate.^[3,4] These properties interests hybrid electric vehicles^[5]. Herein, we consider the supercabattery part of the battery-supercapacitor hybrid device (BSH). In Figure 5.1, we can find the different types of BSH with the different families of capacitive

and battery-like electrodes that we can use to elaboration of BSH. We can also see the variety of used electrolytes.^[6]

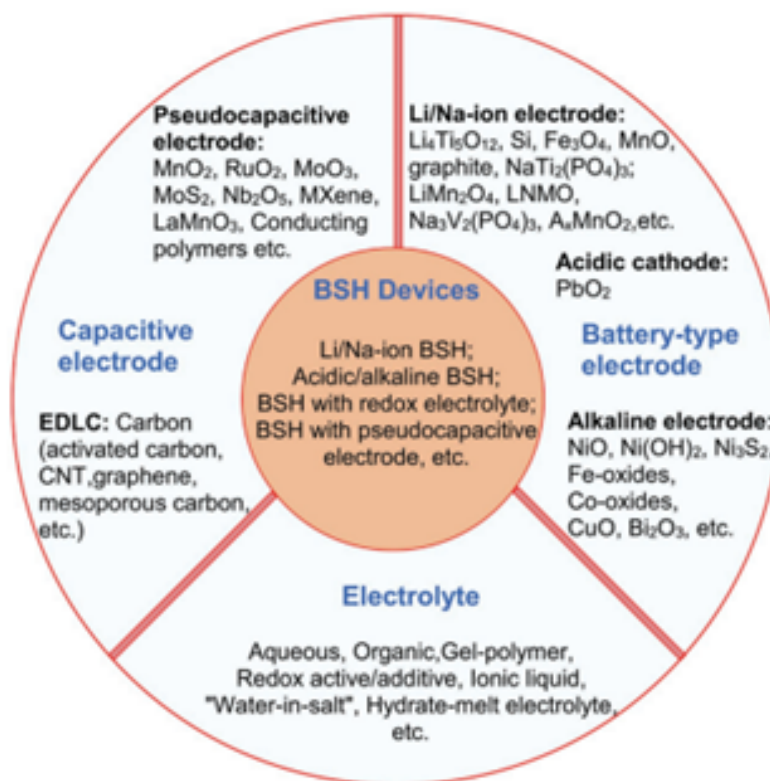


Figure 5.1 – Classification of the battery-supercapacitor hybrid device^[6]

3295

The key elements of the supercabattery are the nature of the electrodes. High power can be obtained with a double-layer capacitor (EDLC) and high-energy density for battery-type materials. The materials used for double-layer capacitors or capacitive (EDLC) electrodes are mainly carbon-based. For battery electrodes, redox-active metal oxides (MO) and metal-organic frameworks (MOFs) can be used.^[1] If we look closer at carbon-based materials, we can find such as carbon nanotubes, onion-like carbons, and graphene. These materials present high power density and long-life cycle characteristics to EDLC.^[7,8] Graphene and other forms like oxidized or reduced are widely known for the use of EDLC supercapacitors.^[9,10] For the battery-electrode, the redox-active materials such as metal oxides (ex: CuO, NiO, and Co₃O₄) present multiple redox states, higher theoretical capacitance, good electrical conductivity, and high ionic mobility. All the factors cited are highly recommended for electrode materials for supercabattery.^[5]

3300

3305

3310

One can see in Figure 5.2 the typical processes that took place in the BSH-like devices. At the battery-type electrode, one has bulk redox reactions. For the capacitive-type electrode, one has fast ionic exchange. Then, the electrons pass by the external circuit during the charging/discharging processes.^[6]

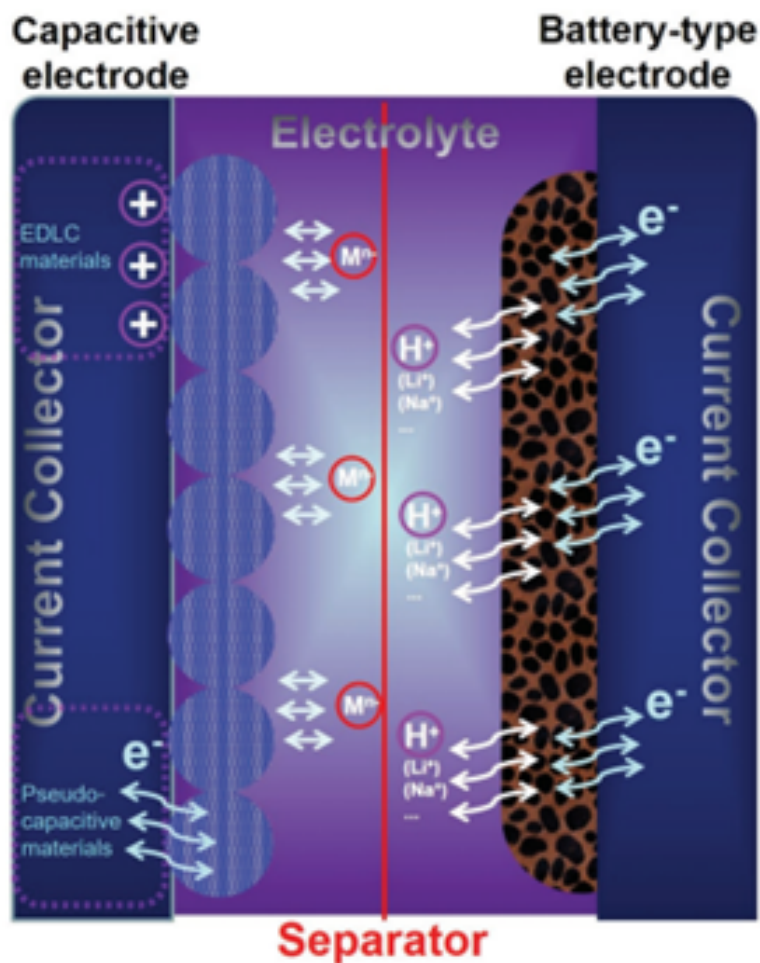


Figure 5.2 – Energy storage mechanism for the battery-supercapacitor hybrid device^[6]

Herein, we will prepare a supercabattery based on NiOx electrode and modified carbon cloth. We have grafted anthraquinone moiety from diazonium salt on the activated carbon cloth to improve the electrochemical responses. To consider the non-linearity of the electrical response and the irreversible nature of charging/discharging processes, we determine the electrical flux, the elastance, and the conductance during the charging/discharging processes at different currents and introduce a modified Ragone plot.

5.2 Experimental section

5.2.1 Elaboration of the modified carbon cloth

Firstly, the carbon cloth is pretreated to eliminate all the impurities. We cut 1x2 cm of the carbon cloth and put it for sonication for 20 min twice. The first sonication is in ethanol, and the second sonication takes place in water. After the sonication steps, the carbon cloth is dried in an oven at 60°C for 30 min.

The second step is activation of the carbon cloth, which involves four steps. The cleaned carbon cloth is submitted to thermal treatment at 400°C for 12 hours with a ramp of the temperature of 5°C/min. The following step is the electrochemical activation of the carbon cloth, during which the carbon cloth submitted a continuous series of cyclic voltammetry at a sweep rate = 50 mV/s during 100 cycles going from 0 V to $E_{\lambda} = 1.4$ V (vs Ag/AgCl) in 1 M NaSO₄ aqueous solution. After this oxidation step, the carbon cloth electrode is rinsed and dried by heating it in an oven for 30 min at 60°C. The modified carbon cloth electrode is prepared by electrografting an anthraquinone diazonium salt, 9,10-dioxo-9,10-dihydroanthracene-1-diazonium tetrafluoroborate (AQD), as shown in Figure 5.3.^[11,12] The electrografting of the AQD is carried out by cyclic voltammetry at a sweep rate $v = 1$ V/s using 25 cycles from 0.55 V to $E_{\lambda} = -1.5$ V (vs Ag/AgCl) in 2 mM of 9,10-Dioxo-9,10-dihydroanthracene-1-diazonium tetrafluoroborate (AQD) (Acros organics) and 0.1 M tetrabutylammonium tetrafluoroborate (Bu₄NBF₄) (Acros organics) in dry acetonitrile. After the electrografting, the modified electrode is rinsed in acetone, and sonication of 10 min in acetone is used to remove the excess of AQD that can be adsorbed onto carbon cloth.

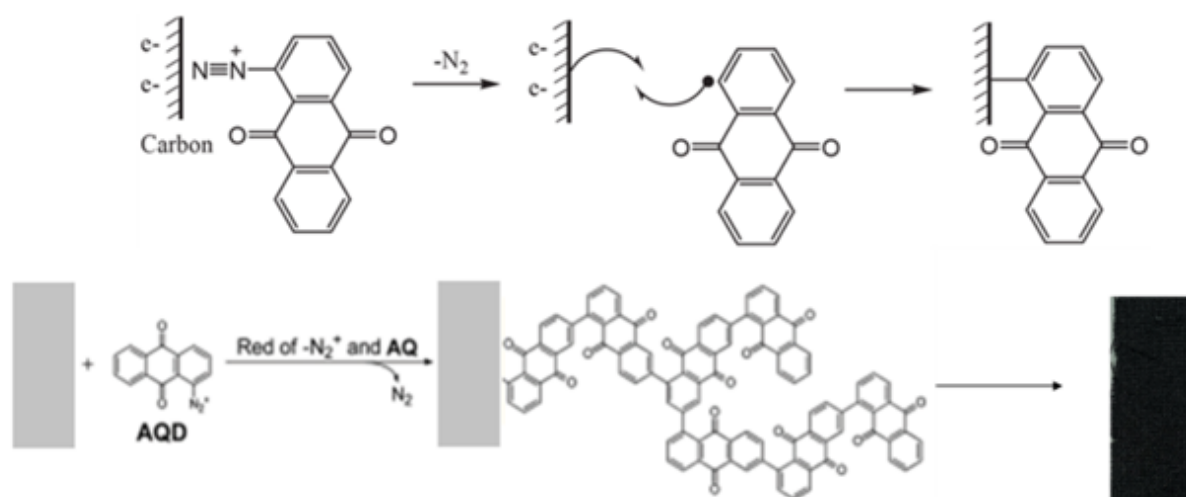


Figure 5.3 – Electrografting of AQD to Carbon cloth

5.2.2 Preconditioning of the electrodes

The nickel oxide is preconditioned as follows. The first step is a continuous 50 cycles of cyclic voltammetry at a sweep rate of 50 mV/s from 0 V to $E_{\lambda} = 0.8$ V (vs Ag/AgCl) in 1 M KOH (Sigma-Aldrich) aqueous solution with a three-electrode electrochemical setup with Biologic VMP3 (Bio-Logic SAS). The working electrode is the modified nickel oxide; the counter electrode is a steel sheet (1x2 cm), and the reference electrode is Ag/AgCl (Radiometer analytical XR300). The second step is a chronoamperometry at 0 V vs Ag/AgCl for 5 min under oxygen, made with the same electrochemical setup with Biologic VMP3. Finally, the nickel

oxide is dried under argon flux. The modified carbon cloth electrode is preconditioned using the same three-electrode electrochemical setup. The first step is its stabilization with 25 cycles of cyclic voltammetry at a sweep rate = 50 V/s from 0 V to $E_{\lambda} = -1.5$ V (vs Ag/AgCl) in 1 M KOH (Sigma-Aldrich) aqueous solution. Afterwards, the modified carbon cloth electrode submitted a chronoamperometry at 0 V vs Ag/AgCl for 5 min under oxygen. After that, the modified carbon cloth electrode is dried under argon flux.

5.2.3 Supercabattery assembly

The supercabattery developed is a two-electrode device containing nickel oxide (+) and modified carbon cloth (-). The electrolyte is an aqueous solution of 1 M KOH (Sigma-Aldrich). In Figure 5.4, we can see a photo of the supercabattery made.

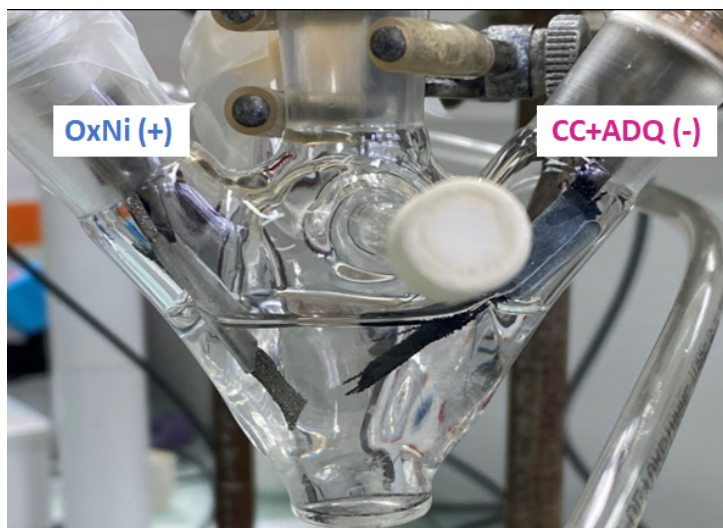


Figure 5.4 – Photo of the supercabattery made

5.3 Electrochemical responses of the supercabattery

The charging/discharging processes are analyzed within the following current range: 0.5; 0.6; 0.7; 0.8; 0.9; 1; 1.25 and 1.5 mA, as shown in Figure 5.5. One observes that:

- (i) the time variation of the voltage is non-linear
- (ii) the discharging process is not a mirror of the charging process, indicating an irreversible (in a thermodynamic sense)
- (iii) the charging (discharging time) depends upon the applied current.

For clarity, we analyze the charging separately and discharging processes.

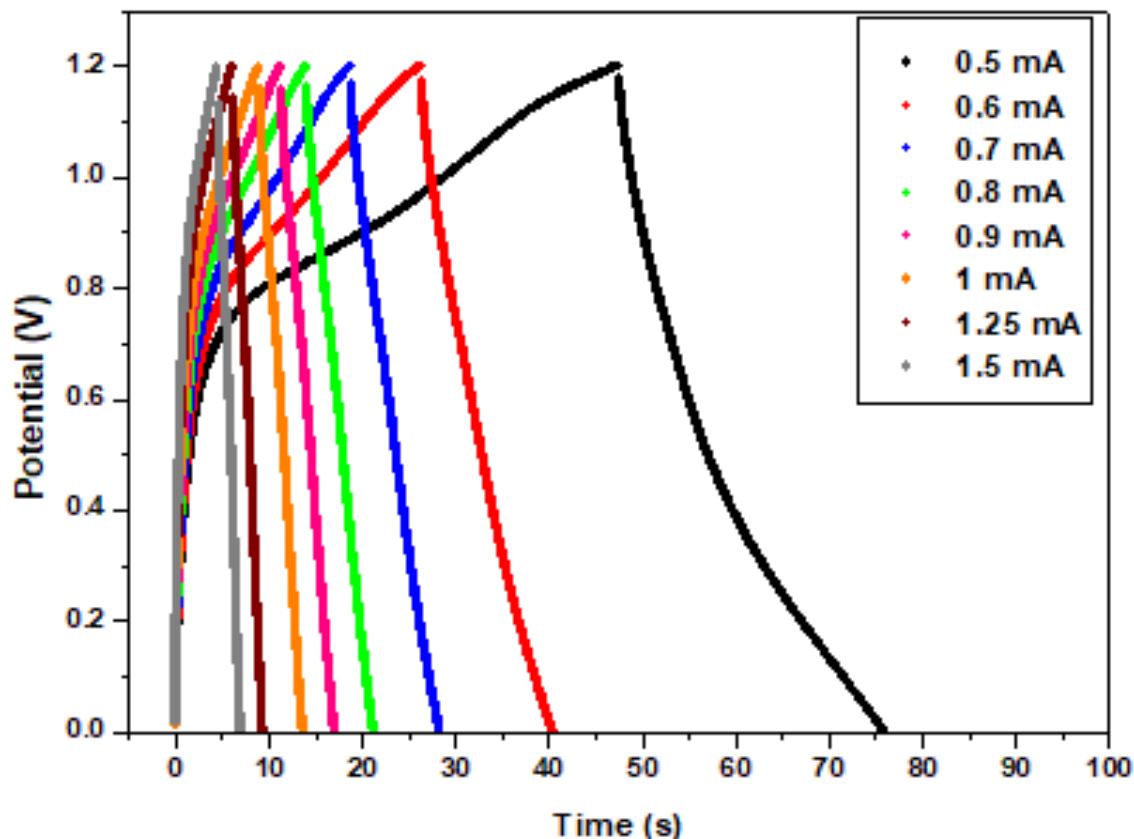


Figure 5.5 – Galvanostatic charge-discharge curves at different currents of NiO/CC-AQD supercabattery

5.3.1 Supercabattery charging

In Figure 5.6, we can see all of the galvanostatic charging curves (GCDs) recorded at different currents applied (Figure 5.6.(a)). The curves for the lowest current applied are in black for 0.5 mA and the highest one in grey for 1.5 mA in Figure 5.6.(b). We can see that all are non-linear and present two aspects: a fast linear increase of the voltage (typical of the supercapacitor) followed by a slower non-linear increase of the voltage through time. The shape of the curve is related to nature and the electrochemical behaviour of each electrode composing the supercabattery. The NiOx electrode provides battery behaviour, and the modified carbon cloth (CC/AQD) has pseudocapacitive properties. As expected, we can see that the current applied increases and the charging time decreases^[13].

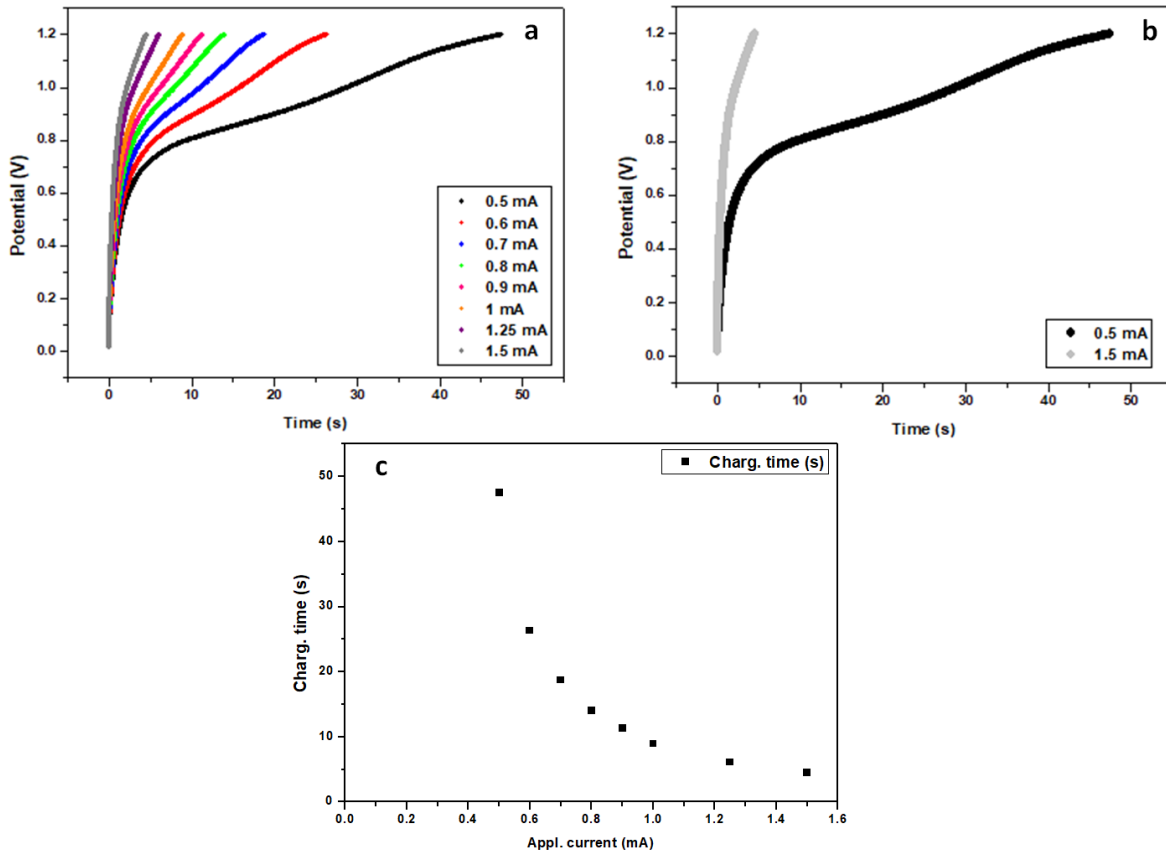


Figure 5.6 – (a) Galvanostatic discharge curves at different currents of NiO/CC-AQD superbattery, (b) Galvanostatic charge curves at 0.5 mA and 1.5 mA of NiO/CC-AQD superbattery, (c) Evolution of the charging time (s) as function of the applied current (mA)

3375 Since the time variation of the voltage is non-linear during the charging process, it is difficult to determine some typical parameters, such as capacitance. Thus, we use the electrical flux (V.s), which corresponds to the time integral of voltage defined as

$$\varphi = \int_0^t V dt \quad (5.1)$$

3380 The electrical flux depends upon the selected voltage window and the dynamics of the voltage change.

The variation of the electrical flux as a function of the applied current during the charging processes is shown in Figure 5.7.(a). Also, the mean voltage calculated from the electrical flux divided by the charging time is reported in Figure 5.7.(b). One can see that the electrical flux decreases as the applied current increases. However, the mean voltage during the charging is nearly constant.

3385

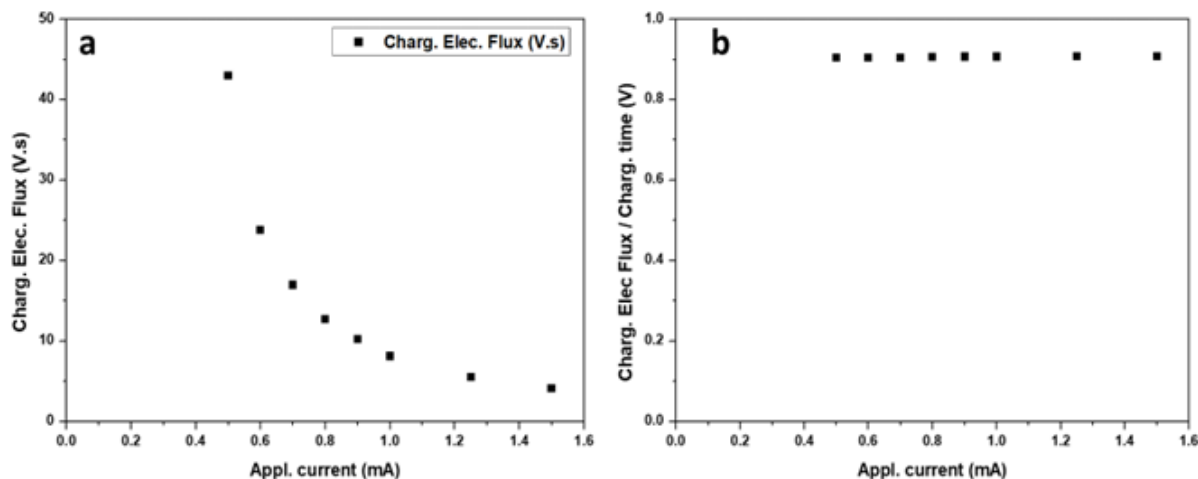


Figure 5.7 – (a) Evolution of the charging electrical flux (V.s) as function of the applied current (mA) , (b) Evolution of the charging electrical flux/charging time (V) as function of the applied current (mA)

5.3.2 Supercabattery discharging

We apply the same methodology used for the charging part. To facilitate the analysis of the figures, we use the absolute value of the current applied for the discharging part. We can see all the discharging GCDs recorded at different current ranges in Figure 5.8.(a). The time variation of the voltage is also non-linear exhibiting two aspects: a sharp linear decrease followed by a slighter decrease of the voltage with time. As seen for the charging part, this behaviour is due to the presence of the battery and pseudocapacitive electrodes composing the supercabattery. Figure 5.8.(b) emphasizes this behaviour by comparing the discharging curves at 0.5 mA and 1.5 mA. Also, we can see that the discharge time decreased when the applied current increased.

Figure 5.9.(a) reports the variation of the discharging electrical flux as function of the applied current. We can see that discharging electrical flux decreases when the applied current increases (in absolute value). The mean voltage calculated from the electrical flux divided by the charging time is reported in Figure 5.9.(b). One observes that the mean voltage during the discharging decreases when the applied current increases (in absolute value).

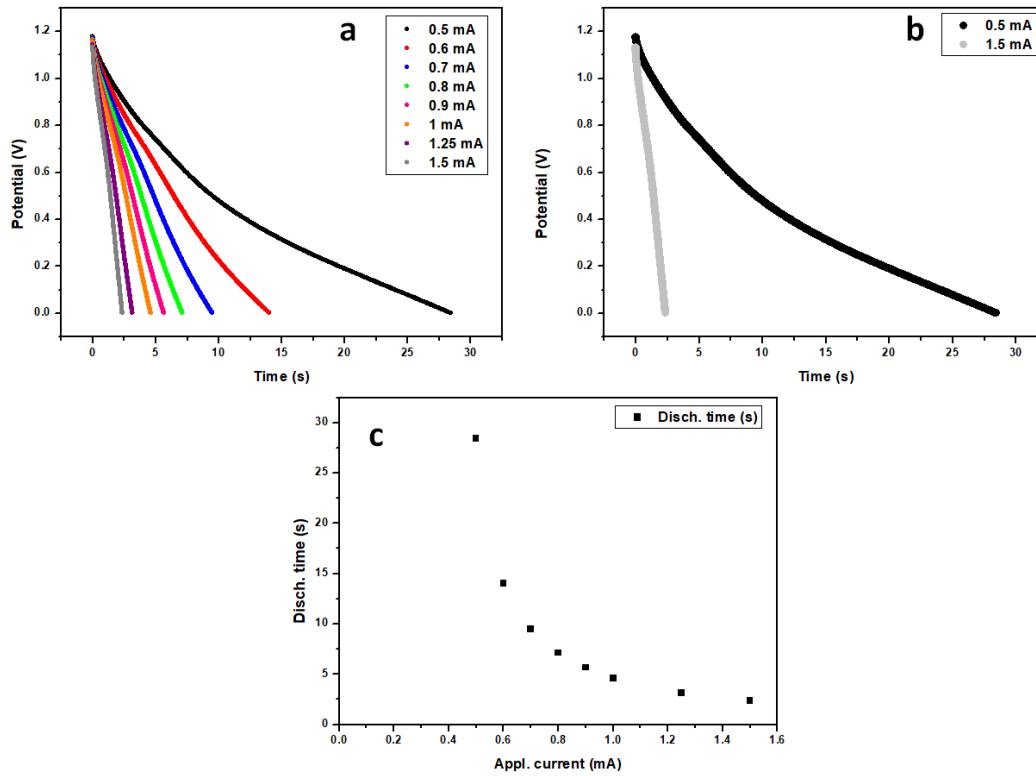


Figure 5.8 – (a) Galvanostatic discharge curves at different currents of NiO/CC-AQD superbattery , (b) Galvanostatic discharge curves at 0.5 mA and 1.5 mA of NiO/CC-AQD superbattery , (c) Evolution of the discharging time (s) as function of the applied current (mA)

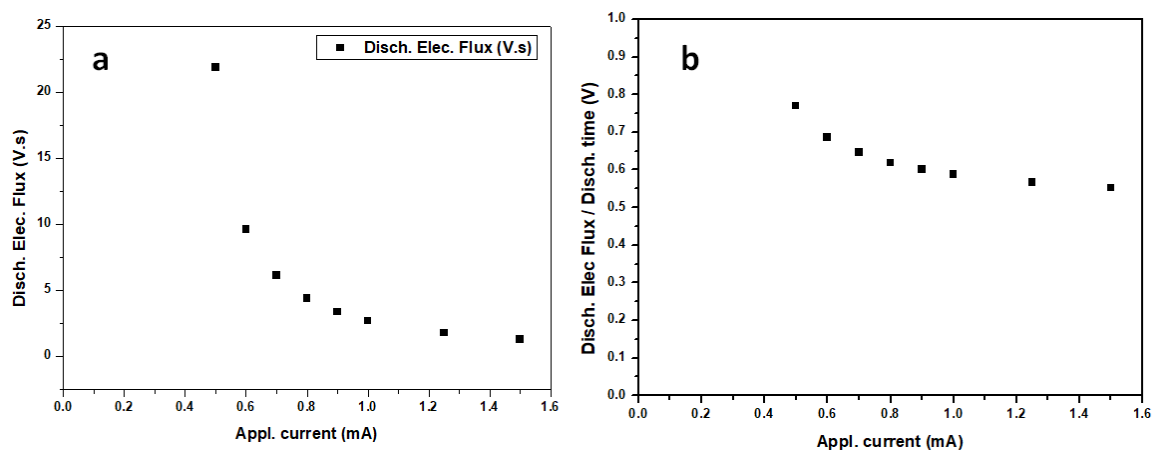


Figure 5.9 – (a) Evolution of the discharging electrical flux (V.s) as function of the applied current (mA) , (b) Evolution of the discharging electrical flux/discharging time (V) as function of the applied current (mA)

5.3.3 Charging vs Discharging

It is interesting to compare the charging and discharging processes at this stage. Comparing Figure 5.10.(a) and Figure 5.10.(b), one can see clearly that the mean voltages are not the same for the charging and discharging processes despite using the same voltage window.. It indicates the irreversible nature of the charging/discharging cycle. From a thermodynamic point of view, the charging pathway is not the same as the discharging one. One must remind that phase transition occurs during the redox process involving nickel oxide. The dynamic of this phase transition is highly controlled by the driving force applied to the electrode. This aspect may explain the irreversible nature of the charging/discharging cycle in a supercabattery based on nickel oxide and modified carbon cloth.

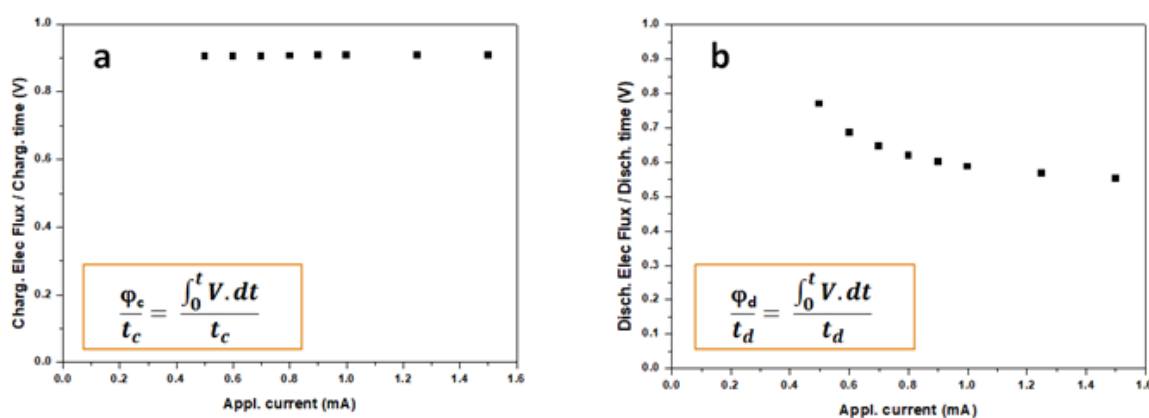


Figure 5.10 – (a) Evolution of the charging electrical flux/charging time (V) as function of the applied current (mA) , (b) Evolution of the discharging electrical flux/discharging time (V) as function of the applied current (mA)

5.3.4 Energy and Power of the supercabattery

The main goal in industrial and electrical vehicle applications is to increase electrical energy and power capabilities. In this section, we will determine: the energy, charge (capacity), and power. In the literature, the energy for hybrid and pseudo-capacitive devices was determined by the following equation^[14]:

$$E = \frac{1}{2}CV^2 \quad (5.2)$$

with C as the capacitance of the device (F), and V (in V) as the voltage.

However, this equation is only valid if the capacitance C is constant and does not vary with the voltage. In other words, a linear voltage variation as a function of the time should be observed during the charging/discharging processes. In Figure 5.11, we can see the equation (5.2) can

give an error in the estimation of the energy content for hybrid devices: an overestimate (Figure 5.11.(a)) and an underestimate (Figure 5.11.(b)) of the energy.

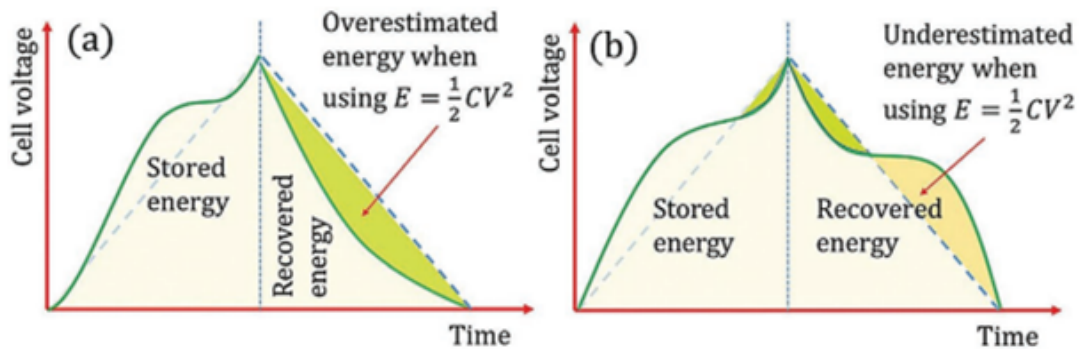


Figure 5.11 – GCDs of charge-discharge profiles of a hybrid supercapacitor with capacitive Faradaic charge storage (CFS) and non-capacitive Faradaic charge storage (NCFS) processes.^[15]

In our approach, we calculate the energy from the electrical flux. The energy density is given by :

$$E = I \int_0^t V \cdot dt = I \cdot \varphi \quad (5.3)$$

With this approach, the non-linearity of the curve did not modify the results and we did not need the capacitance. The total energy injected into the supercabattery during the charging part reflected the sum of the stored energy and dissipated energy (due to the Joule effect)^[14].

Herein, we neglect the dissipated energy, and we focus first on the stored energy. For clarity, we also separate the charging and discharging part. Then, during the charging part, the stored energy is given by

$$E_{stored} = \varphi_c \cdot I \quad (5.4)$$

with E_{stored} (J) as the stored energy, φ_c (V.s) is the electrical flux during the charging, and I (A) is the applied current for the charging.

Figure 5.12 shows the stored energy as function of the applied current. One observes that the stored energy decreases when the applied current increases.

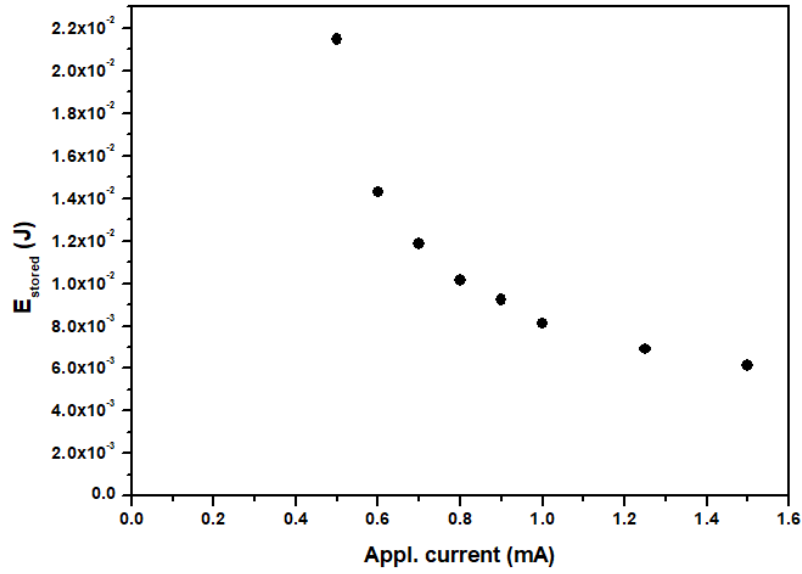


Figure 5.12 – Evolution of the stored energy (J) as function of the applied current (mA)

Now, we determine the stored charge (capacity) during the charging part. It is equal to

$$Q_{\text{stored}} = t_c \cdot I \quad (5.5)$$

3440 with Q_{stored} (C) as the stored charge, t_c (s) as the charging time, and I (A) as the applied current for the charging. Figure 5.13 reports the stored charge as function of the applied current. One observes that the stored charge decreases when the applied current decreases.

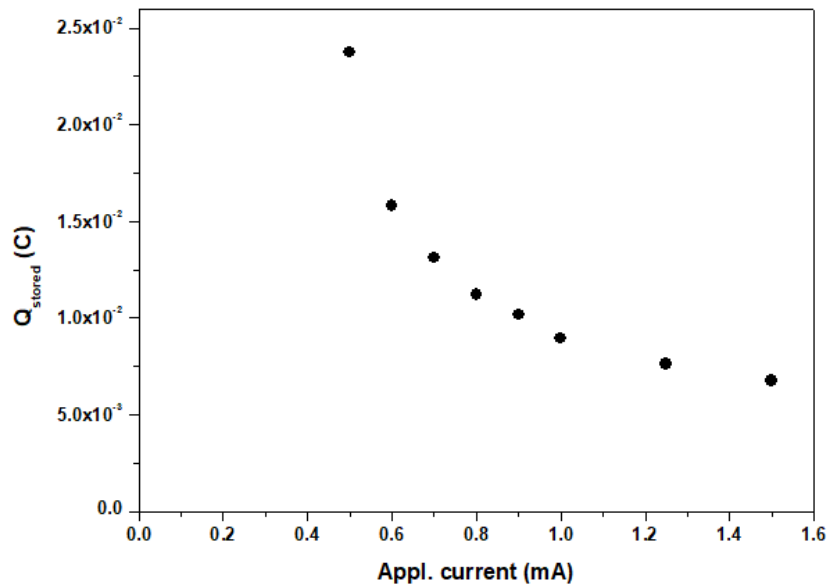


Figure 5.13 – Evolution of the stored charge (C) as function of the the applied current (mA)

By definition, the power density is the energy density E divided by the time t . Accordingly, one has for the charging part.

3445 The last parameter that we will look closer at is the power density. We can define the power density by the equation (5.6) followed^[16] :

$$P_{stored} = \frac{I \cdot \varphi_c}{t_c} \quad (5.6)$$

with P_{stored} (W) as the power, E (J) as the energy, φ (V.s) as the electrical flux, I (A) as the applied current, and t (s) as the time. Figure 5.14 shows the variation of the stored power as
3450 function of the applied current. We observed that the stored power increases linearly with the applied current.

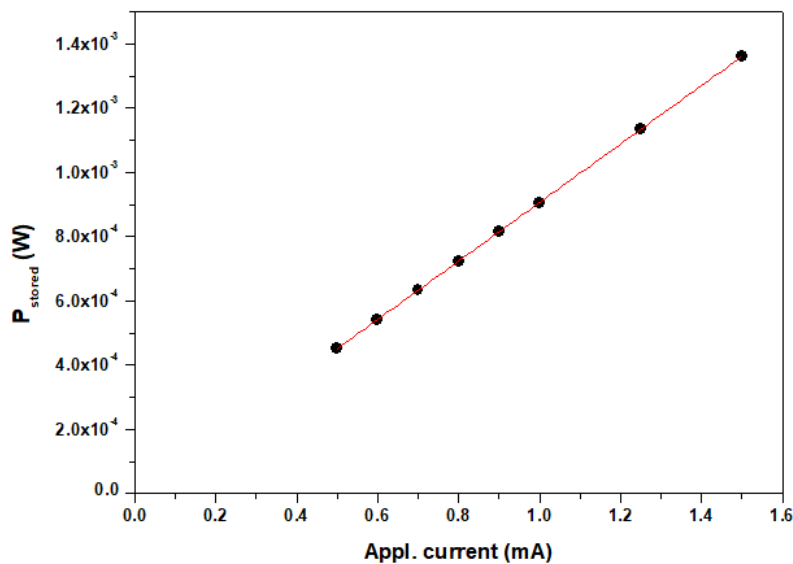


Figure 5.14 – Evolution of the stored power (W) as function of the applied current (mA)

We apply the same approach for the discharging process as for the charging part. To facilitate the analysis, we take the absolute value of the current applied. We define the total released energy related to the discharging part as the sum of the dissipated energy and useable energy^[14].
3455 Here, we also neglect the dissipated energy, and we focus first on the useable energy which is given by

$$E_{useable} = \varphi_d \cdot I \quad (5.7)$$

with $E_{useable}$ (J) as the useable energy, φ_d (V.s) as the electrical flux during the discharging, and
3460 I (A) as the applied current (in absolute value).

The useable charge $Q_{useable}$ and the useable $P_{useable}$ are given as follows.

$$Q_{useable} = t_d \cdot I \quad (5.8)$$

$$P_{useable} = \frac{I \cdot \varphi_d}{t_d} \quad (5.9)$$

3465

with t_d (s) as the discharging time, and I (A) as the applied current. Figure 5.15 shows the variation of the useable energy, the useable charge, and the useable power as function of the applied current. One observes that the useable energy and the useable charge decrease with the applied current. However, the useable power increases linearly with the applied current.

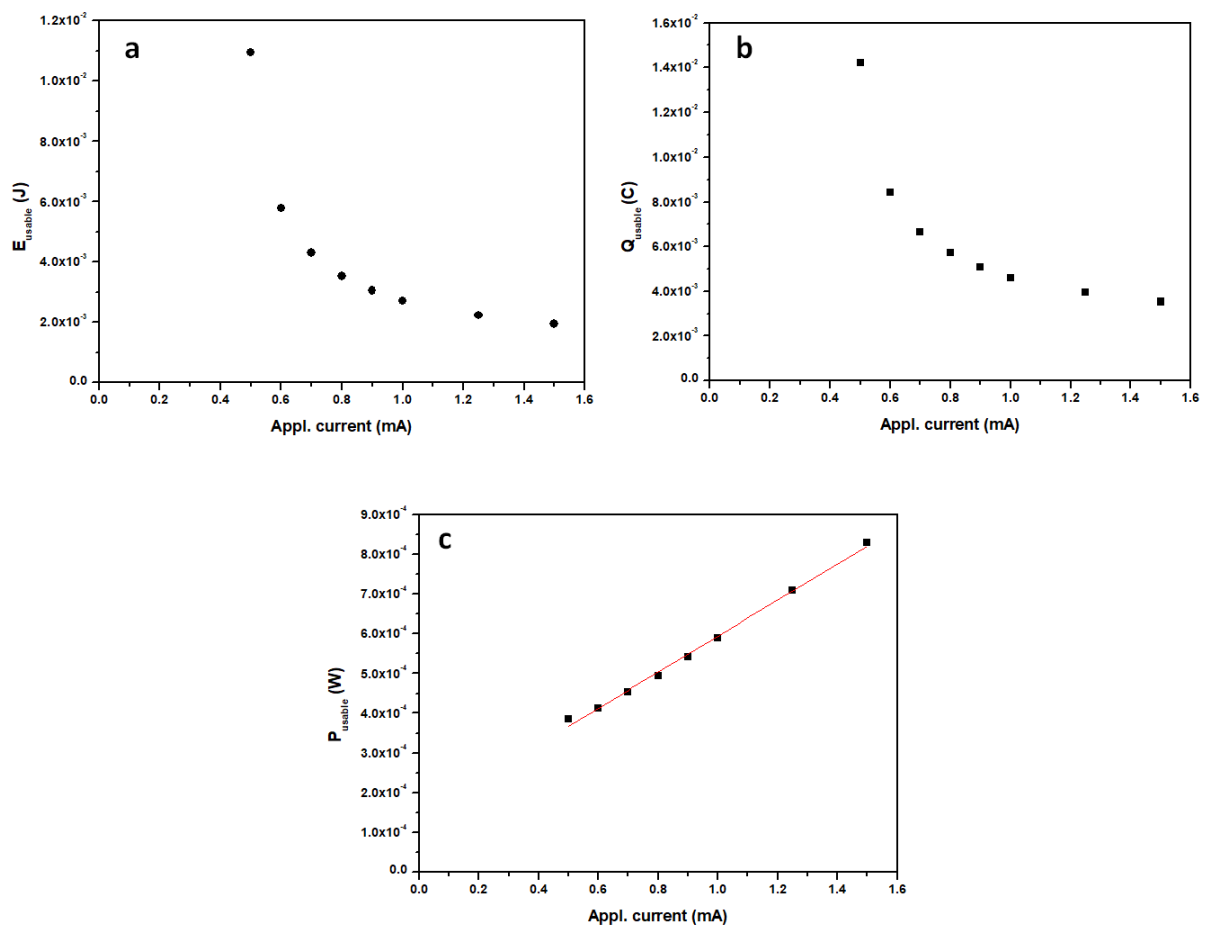


Figure 5.15 – (a) Evolution of the useable energy (J) as function of the applied current (mA) (b) Evolution of the useable charge (C) as function of the applied current (mA) (c) Evolution of the useable power (W) as function of the applied current (mA)

5.3.5 Elastance and Conductance

The term elastance S (in Farad^{-1}) is used through the analogue of a capacitor and mechanical spring. By definition, Elastance is the derivative of the voltage concerning the charge and it is the inverse of the capacitance as

$$S = \frac{dV}{dQ} \quad (5.10)$$

On the other hand, by definition the voltage (in volt) is the energy E (J) divided by the charge Q (C):

$$V = \frac{E}{Q} \quad (5.11)$$

According to these definitions, we can analyze the new relationship. By plotting the ratio (Useable energy/Stored charge) with a volt unit as function of the charge, we find a straight line (Figure 5.16) from which we can determine the elastance. One can remark that the elastance values depend upon the charge (stored or useable) used for the plot. Figure 5.16.(a), we have a first elastance of 10.73 F^{-1} that we label $(S_{\frac{E_u}{Q_s}})_{Q_s}$ with an intercept of 0.20 V . With the Figure 5.16.(b), we have a second elastance of 16.53 F^{-1} that we label $(S_{\frac{E_u}{Q_s}})_{Q_u}$ with an intercept of 0.23 V . One can the remark that the intercepts have similar values, an average value about 0.215 V . However, the fact that we do have not the same value of elastance is due to the difference between the stored charge and the useable charge. This behaviour is related to the irreversible nature of the charging/discharging processes.

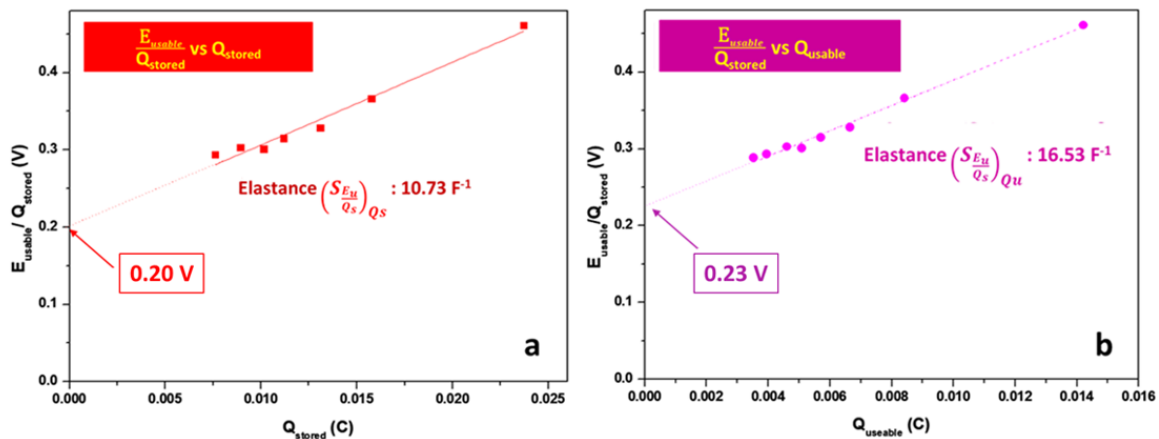


Figure 5.16 – (a) Evolution of the useable energy/stored charge (V) as function of the stored charge (C), (b) Evolution of the useable energy/stored charge (V) as function of the useable charge (C)

Furthermore, we find that another elastance obtained is through power. If we plot the ratio (Useable Power/Stored Charge) as a function of applied current, we have a straight line whose slope corresponds to an elastance. As shown in Figure 5.17, we obtain an elastance straight of 106.25 F^{-1} labelled $S_{\frac{P_u}{Q_s}}$ with an intersection with the x-axis at 0.37 mA corresponding to a current threshold labelled $I_{\frac{P_u}{Q}}$.

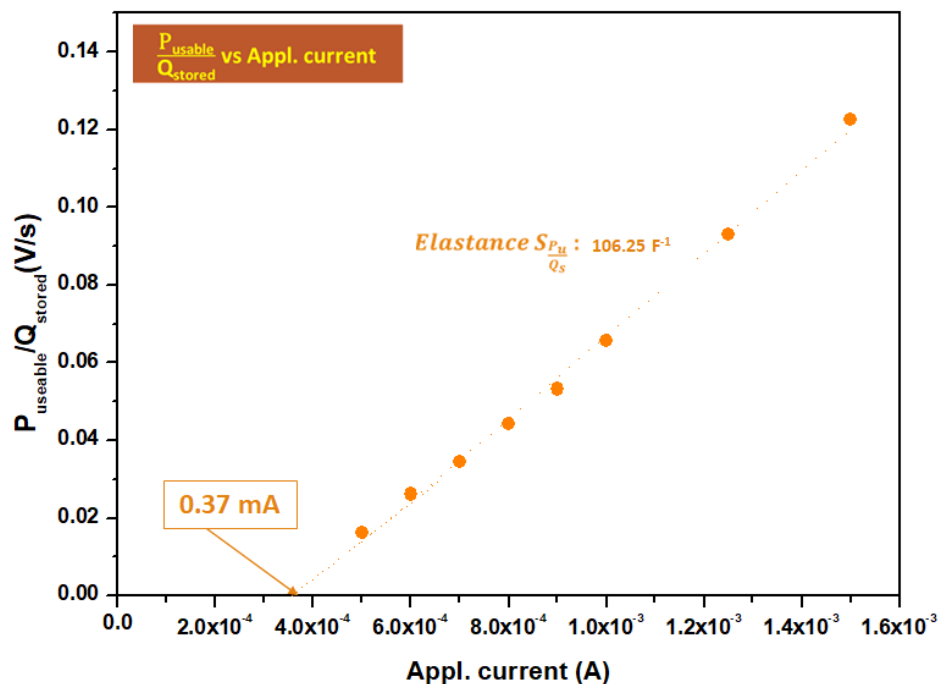


Figure 5.17 – Evolution of the useable power/stored charge (V/s) as function of applied current (A)

At this stage, we can summarize in Figure 5.18 the various elastance founded for the supercabattery: $(S_{\frac{E_u}{Q_s}})_{Q_s}$ and $(S_{\frac{E_u}{Q_s}})_{Q_u}$ are to the energy and $S_{\frac{P_u}{Q_s}}$ to the power.

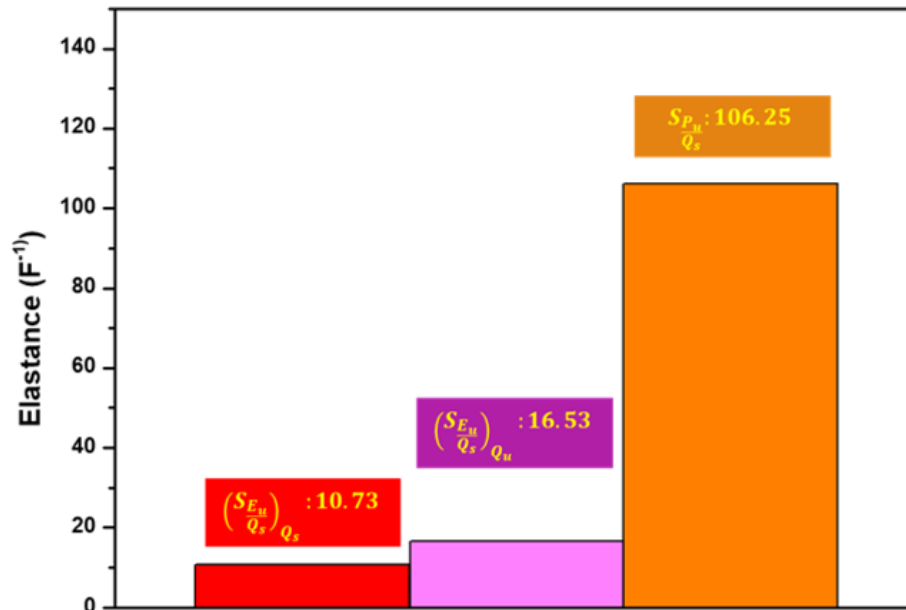


Figure 5.18 – Comparison of Elastance S

3495 Let us focus on the conductance G (in Ω^{-1} or Siemens). The conductance is the inverse of the resistance. This parameter is used to characterize the response dynamics of the system. The value of the conductance gives us an indication on the dispersion of the energy. The higher the conductance is, the lower the dissipated energy in an electrical system. The conductance G is given by

$$3500 \quad G = \frac{I}{V} \quad (5.12)$$

with I (A) as the current, and V (V) as the voltage. From Figures 5.16 and 5.17, it is possible to calculate a parameter that has the same role as a conductance. By combining the threshold potential $V_{\frac{E_u}{Q_u}}$ ($= 0.215$ V) from the plot (E/Q) vs Q (Figure 5.16) with the threshold current $I_{\frac{P_u}{Q}}$ ($= 0.37$ mA) from the plot (P/Q) vs I (Figure 5.17), one obtains a conductance of 1.72×10^{-3} S.

3505 It is of interest to link the elastance and the conductance on electrochemical energy storage properties. Low elastance indicates a high energy storage ability, and high conductance reflects a high power and low energy dissipation. In practice, the best electrochemical energy storage system should exhibit low elastance S and high conductance G . We think these parameters can help analyze and optimize the performance of a hybrid electrochemical energy storage device
3510 like a supercabattery.

5.3.6 Non-reciprocity of the charging/discharging processes

In this following part, we are going to investigate various efficiency metrics such as energy efficiency, coulombic efficiency, and power efficiency. We can define these efficiency metrics by :

$$\text{Energy Efficiency} : EE = \frac{E_{usable}}{E_{stored}} \quad (5.13)$$

$$\text{Coulombic Efficiency} : CE = \frac{Q_{usable}}{Q_{stored}} \quad (5.14)$$

$$\text{Power Efficiency} : PE = \frac{P_{usable}}{P_{stored}} \quad (5.15)$$

These three-efficiency metrics help us to quantify the dissipation processes inducing the entropy production. As shown in Figure 5.19, all efficiency metrics decreased with the applied current. These results indicate an irreversible process occurs during the charging/discharging processes.

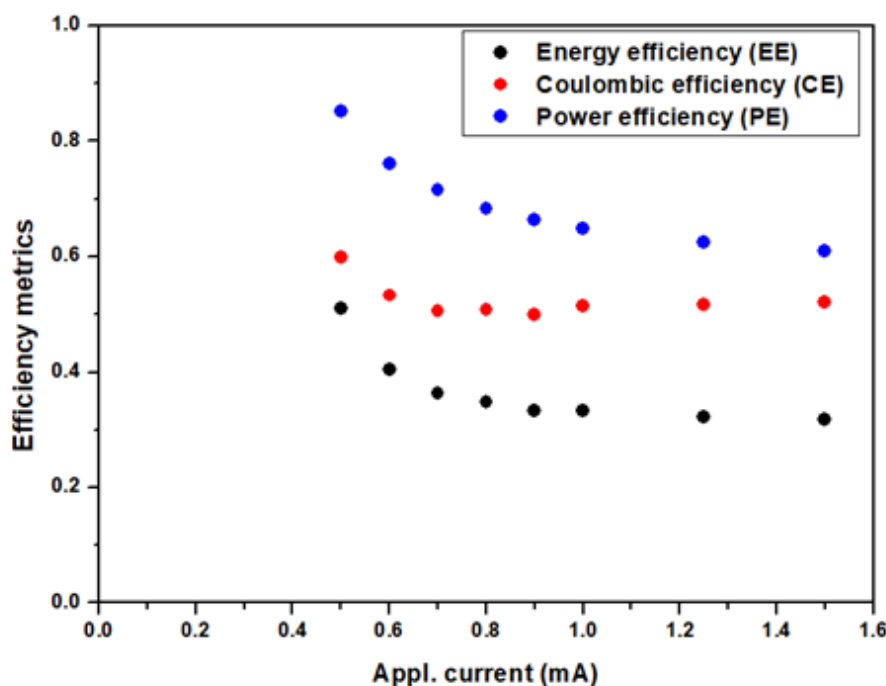


Figure 5.19 – Evolution of the efficiency metrics as function of the applied current (mA)

5.3.7 Modified Ragone plot

In this final part, we are going to introduce the modified Ragone plot. The Ragone plot is a pivotal element in comparing the performance of various energy storage such as a battery, supercapacitor, etc. The Ragone plot sees the evolution of specific energy as function of specific power. Both axes are on a logarithmic scale to compare various devices. It was used for the first time to compare the performance of batteries.^[17]

In Figure 5.20.(a), we show the classic Ragone plot. However, this plot's main drawback is that the influence of the voltage window is usually not considered. Herein, we introduce a modified Ragone plot that corresponds to (Useable energy/Stored charge) vs (Useable power/Stored charge). In the modified Ragone plot, we include the potential window through the electrical flux extension and the amount of the stored charge (during the charging or discharging process) to trace the plot. We can see a difference in the shape of these Ragone plots traced.

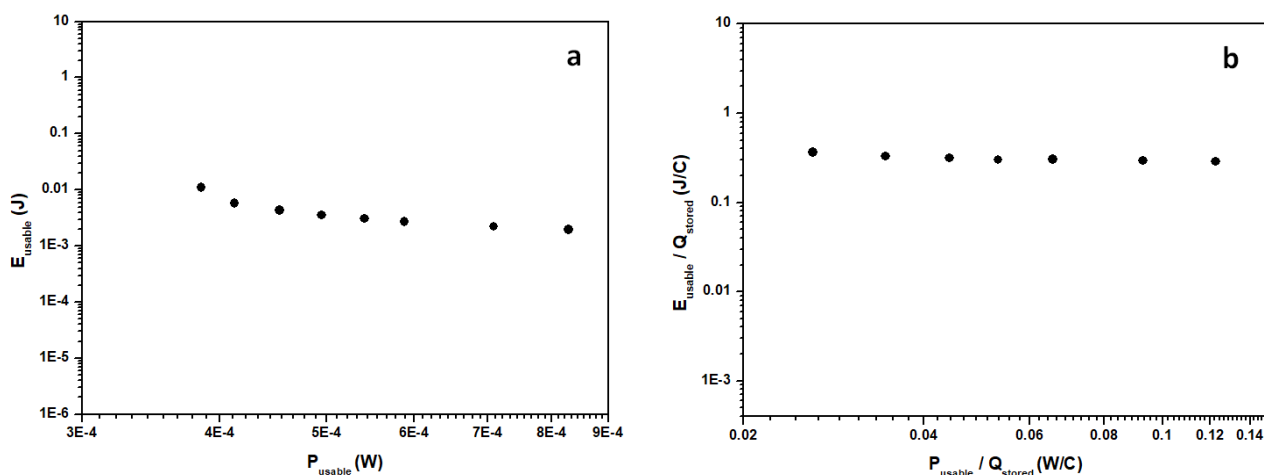


Figure 5.20 – (a) Ragone plot, (b) Modified Ragone plot

5.4 Conclusion

In this last chapter, we looked at elaborating a supercapattery using the NiOx electrode as the positive and battery electrode. Furthermore, for the pseudo-capacitive electrode, the modified activated carbon cloth is used for the negative electrode. We have investigated the charging/discharging curves. With the help of these curves, we determine the electrical flux φ plays a crucial role in analyzing the response of our studied system. Thanks to the electrical flux φ , we can determine the energy, charge, and power density. These three parameters are essential to evaluate the efficiency of the supercapattery. We introduced the elastance S and the conductance G , two critical parameters that are not well studied but can help to understand the investigated system's behaviour. Finally, we introduce a modified Ragone plot that considers the voltage window.

To increase the performance of the supercapattery, we can improve the positive electrode, NiOx, by changing its nanostructure. We currently investigate the response of supercapattery using another type of NiOx to improve energy density. We used carbon cloth with AQD as the negative electrode. We hope that the approach we have developed in this part will be helpful for the development of new electrochemical energy storage devices that exhibit high power and high energy.

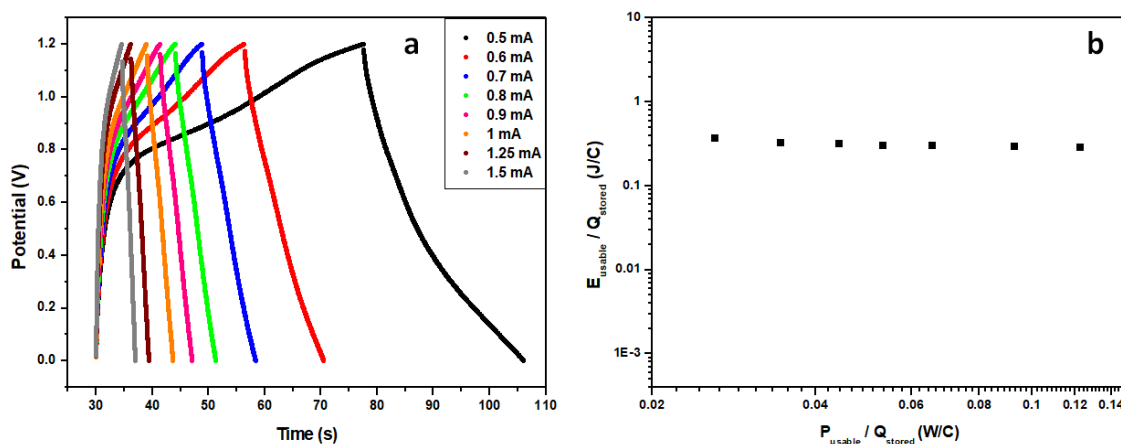


Figure 5.21 – (a) Galvanostatic charge-discharge curves at different currents of NiO/CC-AQD supercapattery , (b) Modified Ragone plot

REFERENCES

- 3555 [1] Daniel M. Teffu, Morongwa E. Ramoroka, Mogwasha D. Makhafola, Katlego Makgopa, Thabiso C. Maponya, Ostar A. Seerane, Mpitloane J. Hato, Emmanuel I. Iwuoha, and Kwena D. Modibane. High-performance supercattery based on reduced graphene oxide/metal organic framework nanocomposite decorated with palladium nanoparticles. *Electrochimica Acta*, 412:140136, April 2022. ISSN 0013-4686. doi: 10.1016/j.electacta.2022.140136.
- 3560 [2] Mengdi Lan, Xixi Wang, Ruijie Zhao, Mengyao Dong, Linxia Fang, and Lingling Wang. Metal-organic framework-derived porous MnNi₂O₄ microflower as an advanced electrode material for high-performance supercapacitors. *Journal of Alloys and Compounds*, 821:153546, April 2020. ISSN 0925-8388. doi: 10.1016/j.jallcom.2019.153546.
- 3565 [3] Siyu Yu, Kamatchi Jothiramalingam Sankaran, Svetlana Korneychuk, Johan Verbeeck, Ken Haenen, Xin Jiang, and Nianjun Yang. High-performance supercatteries using graphite@diamond nano-needle capacitor electrodes and redox electrolytes. *Nanoscale*, 11(38):17939–17946, October 2019. ISSN 2040-3372. doi: 10.1039/C9NR07037K.
- 3570 [4] Saravanakumar Balasubramaniam, Ankita Mohanty, Suresh Kannan Balasingam, Sang Jae Kim, and Ananthakumar Ramadoss. Comprehensive Insight into the Mechanism, Material Selection and Performance Evaluation of Supercatteries. *Nano-Micro Letters*, 12(1):85, April 2020. ISSN 2150-5551. doi: 10.1007/s40820-020-0413-7.
- 3575 [5] Syam G. Krishnan, Arulraj Arunachalam, and Priyanka Jagadish. Chapter twelve - Applications of supercattery. In Numan Arshid, Mohammad Khalid, and Andrews Nirmala Grace, editors, *Advances in Supercapacitor and Supercattery*, pages 311–348. Elsevier, January 2021. ISBN 978-0-12-819897-1. doi: 10.1016/B978-0-12-819897-1.00002-1.
- [6] Wenhua Zuo, Ruizhi Li, Cheng Zhou, Yuanyuan Li, Jianlong Xia, and Jinping Liu. Battery-Supercapacitor Hybrid Devices: Recent Progress and Future Prospects. *Advanced Science*, 4(7):1600539, 2017. ISSN 2198-3844. doi: 10.1002/advs.201600539.
- 3580 [7] Shao-Wen Xu, Ming-Cai Zhang, Guo-Qing Zhang, Jia-Hao Liu, Xin-Zhe Liu, Xuan Zhang, Dan-Dan Zhao, Cai-Ling Xu, and Yong-Qing Zhao. Temperature-dependent performance of carbon-based supercapacitors with water-in-salt electrolyte. *Journal of Power Sources*, 441:227220, November 2019. ISSN 0378-7753. doi: 10.1016/j.jpowsour.2019.227220.

- [8] Ji Hoon Lee, Nokyoung Park, Byung Gon Kim, Dae Soo Jung, Kyuhyun Im, Jaehyun Hur, and Jang Wook Choi. Restacking-Inhibited 3D Reduced Graphene Oxide for High Performance Supercapacitor Electrodes. *ACS Nano*, 7(10):9366–9374, October 2013. ISSN 1936-0851. doi: 10.1021/nn4040734.
- [9] Shashank Sundriyal, Vishal Shrivastav, Harmeet Kaur, Sunita Mishra, and Akash Deep. High-Performance Symmetrical Supercapacitor with a Combination of a ZIF-67/rGO Composite Electrode and a Redox Additive Electrolyte. *ACS Omega*, 3(12):17348–17358, December 2018. doi: 10.1021/acsomega.8b02065.
- [10] Fanbin Meng, Lican Zhao, Yujie Zhang, Jiao Zhai, Yujin Li, and Wei Zhang. Facile synthesis of NiCo₂O₄/rGO microspheres with high-performance for supercapacitor. *Ceramics International*, 45(17, Part B):23701–23706, December 2019. ISSN 0272-8842. doi: 10.1016/j.ceramint.2019.08.085.
- [11] Antoine Bousquet, Marcel Ceccato, Mogens Hinge, Steen Uttrup Pedersen, and Kim Daasbjerg. Redox Grafting of Diazotated Anthraquinone as a Means of Forming Thick Conducting Organic Films. *Langmuir*, 28(2):1267–1275, January 2012. ISSN 0743-7463. doi: 10.1021/la203657n.
- [12] Jean Christophe Lacroix, Gaelle Trippe-Allard, Jalal Ghilane, and Pascal Martin. Electrografting of conductive oligomers and polymers using diazonium electroreduction. *Advances in Natural Sciences: Nanoscience and Nanotechnology*, 5(1):015001, December 2013. ISSN 2043-6262. doi: 10.1088/2043-6262/5/1/015001.
- [13] George Z. Chen. Supercapacitor and supercapattery as emerging electrochemical energy stores. *International Materials Reviews*, 62(4):173–202, May 2017. ISSN 0950-6608. doi: 10.1080/09506608.2016.1240914.
- [14] Jingyuan Zhao and Andrew F. Burke. Electrochemical Capacitors: Performance Metrics and Evaluation by Testing and Analysis. *Advanced Energy Materials*, 11(1):2002192, 2021. ISSN 1614-6840. doi: 10.1002/aenm.202002192.
- [15] Abolhassan Noori, Maher F. El-Kady, Mohammad S. Rahmanifar, Richard B. Kaner, and Mir F. Mousavi. Towards establishing standard performance metrics for batteries, supercapacitors and beyond. *Chemical Society Reviews*, 48(5):1272–1341, March 2019. ISSN 1460-4744. doi: 10.1039/C8CS00581H.
- [16] Dingshan Yu, Qihui Qian, Li Wei, Wenchao Jiang, Kunli Goh, Jun Wei, Jie Zhang, and Yuan Chen. Emergence of fiber supercapacitors. *Chemical Society Reviews*, 44(3):647–662, January 2015. ISSN 1460-4744. doi: 10.1039/C4CS00286E.
- [17] Bengt Sundén. Chapter 4 - Battery technologies. In Bengt Sundén, editor, *Hydrogen, Batteries and Fuel Cells*, pages 57–79. Academic Press, January 2019. ISBN 978-0-12-816950-6. doi: 10.1016/B978-0-12-816950-6.00004-X.

6.1 Conclusion

In my Ph.D. studies, we look at various reactions such as hydrogen evolution reaction (HER), oxygen evolution reaction (OER), and oxygen reduction reaction (ORR). The aim was to develop an efficient and cheap catalyst to improve the response to those reactions.

In chapter 2, we developed manganese oxide nanoparticles through film prepared by electrospinning and submitted to thermal treatment at different temperatures. The manganese oxide synthesized was used to investigate the ORR. The various spectroscopy techniques demonstrated that most of the manganese oxides synthesized were α - Mn_2O_3 . The α - Mn_2O_3 , our manganese oxide, can be found in two forms: α - Mn_2O_3 can be cubic or orthorhombic. The form of α - Mn_2O_3 will impact the catalytic proprieties through the ORR in alkaline media. The electrochemical investigations conducted by rotating ring disk electrode (RRDE) demonstrated that all the samples made had excellent selectivity through the 4 electron pathways. The best sample was the one made at 500°C. It characterizes by the presence of α - Mn_2O_3 and a small fraction of Mn_5O_8 . It presents an electron number exchanged close to 4 electrons and production of the HO_2^- lower than 5 % in the investigated potential window. We also conducted a micro-kinetic study to look deep into the mechanism. We can divide the micro-kinetic studies into two zones. Figure 2.40 shows the evolution of the electron number exchanged and HO_2^- % in both zones. We can see a difference between the two zone studies. This result highlights the role of the nanoparticles' size and demonstrates that the sample made at 500°C exhibits the best performance for 4 electrons ORR.

The other three chapters examine doped nickel oxide foam and demonstrate its trifunctional properties. The doped nickel oxide foam can be a catalyst for HER and OER. Moreover, we can use it as the positive electrode for supercabattery that we assembled in chapter 5.

In chapter 3, we highlighted its response through the HER and observed an excellent electrocatalytic activity. We demonstrated that the response varied as function of the potential. Thanks to this observation, we separated into two zones. The first zone is low overpotential, and the other is large overpotential. With the help of the Tafel plot, we could find the different mechanisms in both zones studied. For the low overpotential zone, we have The Volmer–Heyrovsky mechanism. And for the large overpotential, we have The Volmer-Tafel

mechanism. We also conducted EIS measurements to obtain main electrochemical parameters such as the charge transfer resistance R_{ct} , the electrode polarization resistance R_p , and the resistance of the electrical circuit R'_θ . We demonstrated the correlation between the LSV and EIS investigations.

In chapter 4, we look at the catalytical response of NiOx through OER. Thanks to electrochemical investigations, we demonstrate it is a suitable catalyst. With the Tafel slope analysis, we supposed that the rate-determining steps (RDS) could be due to OH^- adsorption and O–H bond splitting. As seen in chapter 3, we conducted an EIS investigation. We determined the charge transfer resistance R_{ct} , adsorption resistance R_a , and adsorption capacitance C_a . Furthermore, we demonstrated the correlation between the LSV and EIS studies. Thanks to the investigations conducted on HER and OER, we correlated the information obtained to look at water splitting. We used a two-electrode system using Ni foam for NiOx for the anode and cathode. We traced the LSV polarization curve obtained for water splitting to evaluate the system. (Figure 4.18)

Furthermore, in chapter 5, we introduced superbattery. The studies about this type of device in blooming. The interest is increasing due to the battery and supercapacitor properties. We have a device with high power and energy, which translates to a device with longer life and pulse power supply functionalities. We developed a superbattery using the NiOx electrode as the positive and a modified activated carbon cloth as the negative electrode. In these studies, we highlighted the role of electrical flux φ found by the charging/discharging curves. Thanks to electrical flux φ , we can go back to the energy, charge, and power density. These three parameters are essential to estimate the efficiency of the superbattery. With all the parameters, we introduce a modified Ragone plot how the count of the voltage window. (Figure 5.20.(b)) We also introduced the elastance S and the conductance G .

6.2 Perspectives

In this part, we will look at the perspectives linked to the manganese oxide and the nickel oxide studied through my Ph.D. studies.

The use of manganese oxide can be used in biological systems under manganese cluster form in natural media. Our aim with the manganese oxide made during my Ph.D. studies is to be able to work in neutral media. To achieve this goal, the catalysts made will be investigated in less and less basic media to look at the response. We will also develop other types of manganese oxide by playing on the composition of the precursor solution used to make the electrospinning film. This approach will identify the manganese oxide with affinity to neutral media. Thanks to that, we will conduct the electrochemical investigation in parallel with a spectroscopic one, as seen in chapter 2.

For the foam nickel oxide, one approach to boost the catalytic response through HER and OER is introducing or increasing the percentage of heteroatoms or doping the foam. Increasing the catalytic response can improve the catalytic affinity for HER and OER and decrease the Δ_E potential difference (V vs RHE). The Δ_E potential difference is essential; decreasing it will also decrease the energy cost. Our system can reach the 100 mA/cm^2 current density. By following the Δ_E potential difference at 100 mA/cm^2 , we approach the values of the industrial.

Moreover, for the development of superbattery, we can improve both electrode parts. For

the NiOx, we can play on the nanostructure by introducing a dopant on the nickel foam or increasing the size of the NiOx foam used. Furthermore, for the carbon cloth with AQD as the negative electrode, we can increase the size of the electrode. We can also look at the investigation on the neutral media and conduct the same electrochemical investigation. The aim is to increase our system's power and energy.

Summary

The use of non-noble electrocatalysts is an interesting pathway for the development of sustainable energy. In this PhD thesis, the electrocatalytic properties of manganese oxide nanomaterial and doped nickel oxide are investigated for important reactions around oxygen (oxygen evolution reaction and oxygen reduction reaction) and hydrogen (hydrogen evolution reaction) electrochemistry. Indeed, water splitting is an effective approach to producing hydrogen, which is a form of sustainable chemical energy storage. These electrocatalysts are abundant and stable in alkaline media. Also, a supercapattery, an electrochemical energy storage system issued from the marriage of supercapacitor and battery, is studied. Particularly, doped nickel oxide can be viewed as a trifunctional material able to catalyze oxygen evolution and hydrogen evolution reactions and as electrode material for supercapattery.

Keywords: nanomaterials, energy storage, water splitting, electrocatalysis, oxygen evolution reaction, oxygen reduction reaction, hydrogen evolution reaction, supercapattery.

Résumé

L'utilisation d'électrocatalyseurs non nobles est une approche intéressante pour le développement de l'énergie durable. Dans cette thèse de doctorat, les propriétés électrocatalytiques de nanomatériaux à base d'oxyde de manganèse et de l'oxyde de nickel dopé sont étudiées pour des réactions importantes autour de l'électrochimie de l'oxygène (réaction de dégagement d'oxygène et réaction de réduction de l'oxygène) et de l'hydrogène (réaction de dégagement d'hydrogène). En effet, la production d'hydrogène qui est une forme de stockage d'énergie chimique durable via l'électrolyse de l'eau est une approche efficace. Ces électrocatalyseurs sont abondants et stables en milieu alcalin. De même, une supercapatterie qui est un système électrochimique de stockage d'énergie issu du mariage d'un supercondensateur et d'une batterie est étudiée. En particulier, nous montrons que l'oxyde de nickel dopé peut être considéré comme un matériau trifonctionnel apte non seulement à catalyser la réaction de dégagement d'oxygène et la réaction de production d'hydrogène mais également comme matériau d'électrode pour les supercapatteries.

Mots-clés: nanomatériaux, stockage de l'énergie, électrolyse de l'eau, électrocatalyse, réaction de libération d'oxygène, réaction de réduction de l'oxygène, réduction des protons, supercapatterie